Tampere University

RONI LUHTALA

Real-Time Identification and Adaptive Control of Grid-Connected Three-Phase Inverters

Tampere University Dissertations 350

Tampere University Dissertations 350

RONI LUHTALA

Real-Time Identification and Adaptive Control of Grid-Connected Three-Phase Inverters

ACADEMIC DISSERTATION
To be presented, with the permission of
the Faculty of Engineering and Natural Sciences
of Tampere University,
for public discussion in the Auditorium K1702
of the Konetalo Building, Korkeakoulunkatu 6, Tampere,
on 27th of November 2020, at 12 o'clock.

ACADEMIC DISSERTATION
Tampere University, Faculty of Engineering and Natural Sciences
Finland

Responsible supervisor and Custos
Assistant Professor
Tomi Roinila
Tampere University
Finland

Supervisor
Professor
Matti Vilkko
Tampere University
Finland

Pre-examiners
Associate Professor
Marko Hinkkanen
Aalto University
Finland

Dr. Tech.
Mauricio Cespedes
Facebook Inc.
USA

Opponents
Associate Professor
Marko Hinkkanen
Aalto University
Finland

Dr. Tech.
Juha Jokipii
Danfoss Drives
Finland

Cover design: Roihu Inc.

ISBN 978-952-03-1784-3 (print)
ISBN 978-952-03-1785-0 (pdf)
ISSN 2489-9860 (print)
ISSN 2490-0028 (pdf)
http://urn.fi/URN:ISBN:978-952-03-1785-0

PunaMusta Oy – Yliopistopaino
Vantaa 2020

PREFACE

The work was carried out at the Faculty of Engineering and Natural Sciences at Tampere University between 2017 and 2020. The research was mainly funded by Fortum Foundation and Tampere University. In addition, the personal grants from the Walter Ahlström foundation are highly appreciated.

First of all, I wish to express my sincere gratitude to Assistant Professor Tomi Roinila for supervising my thesis and for providing a great environment to start my career as a researcher. His guidance and support in various general and research-related issues have been an irreplaceable part of the thesis, from start to finish. I owe special thanks to Dr. Tech. Tuomas Messo for always making the research work as stress-free and comfortable as possible, and for providing background information on practically everything I know about power electronics. Without his support and guidance, this thesis might never have been finished or even started.

Huge thanks to my closest research fellows for all their support during this research work and for creating a highly enjoyable working atmosphere. I would like to thank M.Sc. Tommi Reinikka and M.Sc. Jussi Sihvo for all the shared moments and thoughts, especially during the first years of our research careers. I am also thankful to M.Sc. Henrik Alenius for sharing the office and, consequently, every research-related difficulty with me during the last few years. I have really appreciated his advice and help (almost) every time. From outside the research community, I also want to thank JeeJee N' That's It -boys for clearing my mind of work stress in my free time.

I want to express my deepest gratitude to my parents Sirpa and Vesa for providing me with a safe and encouraging atmosphere throughout my life. Their support for everything I do and every choice I make have been the most important thing that have helped me to focus, for example, on this thesis and also to enjoy my life. I also want to thank my grandparents - Eeva, Hannu, Matti and Seija - for all their life advice and encouraging words throughout the years. I know that you are or would have been very proud of me and this achievement, which means a lot to me. Finally, loving thanks to the most beautiful and inspiring human being, Minna, and our fur baby Rambo for making our home the best place in the world. Special thanks to Rambo for overflowing sympathy during stressful situations at the home office and for pleasant outdoor activities. Thank you, Minna, for always being there when needed and for sharing all the pleasures and difficulties of life with me.

ABSTRACT

Grid-connected inverters are typically applied to integrate renewable energy, such as solar and wind, to the power system. Therefore, proper operation of the inverters is essential for efficient utilization of the renewable energy. Rapidly increasing the number of grid-connected inverters has started to affect power system dynamics and stability, particularly in areas where the majority of the power is generated through the inverters. One issue studied is the harmonic resonance between the inverter and the grid.

The stability of the grid-connected system can be evaluated by an impedance-based stability analysis, where the system stability is assessed by the ratio between the inverter and the grid impedances. Previous studies have presented multiple methods for designing the grid-connected inverter so that the impedance-based stability issues can be avoided under certain grid conditions. However, the grid impedance usually remains unknown in the inverter design process and may vary over time; this typically means it is not possible to customize the inverter to the grid-connection point or ensure the impedance-based stability.

This thesis has presented methods for real-time measurements of the grid-connected systems. Applying the methods, the grid impedance can be obtained in real time and the impedance-based stability of the grid-connected system can be assessed under varying grid conditions. Additionally, the measurements can be utilized to improve the inverter performance in the grid-connection point. In this thesis, the grid-connected inverter is configured to adaptively re-adjust its own control parameters based on the real-time measurements of the grid conditions. This is shown to effectively avoid the impedance-based stability issues and to improve the inverter control performance under varying grid conditions.

CONTENTS

LIST OF PUBLICATIONS

The thesis is based on the following publications, which are referred to as [P1], [P2], [P3], [P4], [P5] and [P6] in the text. In addition, 13 other publications of the author are applied in the thesis as regular references.

[P1] R. Luhtala, T. Roinila and T. Messo, "Implementation of Real-Time Impedance-Based Stability Assessment of Grid-Connected Systems Using MIMO-Identification Techniques," IEEE Transactions on Industry Applications, vol. 54, no. 5, pp. 5054-5063, 2018.

[P2] R. Luhtala, H. Alenius, T. Messo and T. Roinila, "Online Frequency Response Measurements of Grid-Connected Systems in Presence of Grid Harmonics and Unbalance," IEEE Transactions on Power Electronics, vol. 35, no. 4, pp. 3343-3347, 2020.

[P3] R. Luhtala, T. Reinikka, T. Roinila, T. Messo and J. Sihvo, "Improved Real-Time Stability Assessment of Grid-Connected Converters Using MIMO-Identification Methods," 2018 IEEE Energy Conversion Congress and Exposition, pp. 5322-5329, 2018.

[P4] R. Luhtala, H. Alenius and T. Roinila, “Practical Implementation of Adaptive SRF-PLL for Three-Phase Inverters Based on Sensitivity Function and Real-Time Grid-Impedance Measurements” Energies, vol. 13, no. 5, pp. 1-18, 2020.

[P5] R. Luhtala, H. Alenius and T. Roinila, “Adaptive Optimization of AC-Current Control Loop for Grid-Connected Inverters”, 2020 IEEE Applied Power Electronics Conference and Exposition, 6 pages, 2020.

[P6] R. Luhtala, T. Messo, T. Roinila and G. Spagnuolo, "Adaptive Grid-Voltage Feedforward for Three-Phase Inverters applying Perturb and Observe Algorithm to minimize Current THD,"Annual Conference of the IEEE Industrial Electronics Society, pp. 1591-1596, 2019.

AUTHOR'S CONTRIBUTION

The author was responsible for developing and implementing the frequency-response methods and adaptive control of grid-connected inverters in publications [P1]-[P6]. Assistant professor Tomi Roinila, the supervisor of the thesis, gave constructive insights for the system identification and analysis. Dr. Tech. Tuomas Messo provided extensive background information on dynamics and control of grid-connected inverters. The other authors in publications [P1]-[P6] assisted with laboratory measurements.

SYMBOLS

A	Perturbation amplitude
A_{d}	Amplitude of distortions
A_{pert}	Perturbation amplitude in P&O algorithm
A_{r}	Amplitude of response to perturbation
C	Inverter DC capacitor
C_{f}	LC filter capacitance
$\mathbf{d}$	Inverter duty cycles
D	Steady-state duty cycle
d_{λ}	Distance between eigenvalue and critical point
e	Error signal
$f_{\mathrm{BW\text{-}CC}}$	Crossover frequency of current-control loop
$f_{\mathrm{BW\text{-}PLL}}$	PLL crossover frequency
f_{g}	Grid fundamental frequency
f_{gen}	Generation frequency
f_{m}	Measurable bandwidth
f_{min}	Lowest measured frequency
f_{res}	Frequency resolution
f_{sw}	Switching frequency
$g(t)$	General plant
$\mathbf{G}$	General transfer matrix
$G(j\omega)$	Frequency response function
$G_{\mathrm{Exp}}(j\omega)$	Expected frequency response (reference)
$\mathbf{G}_{\mathrm{c}}$	Current controller
$\mathbf{G}_{\mathrm{cc}}$	Current control loop

$\mathbf{G}_{ci}$	Transfer matrix from duty cycles to input voltage
$\mathbf{G}_{co}$	Transfer matrix from duty cycles to output current
$G_{c\text{-}PLL}$	Internal controller of PLL
$\mathbf{G}_{dc}$	DC voltage controller
$\mathbf{G}_{dec}$	Decoupling matrix
G_{f}	Notch filter
$G_{f\text{-}d}$	Digital notch filter
$\mathbf{G}_{FF}$	Grid-voltage feedforward transfer matrix
$\mathbf{G}_{ff\text{-}ideal}$	Ideal grid-voltage feedforward
$\mathbf{G}_{io}$	Transfer matrix from input current to output current
G_{PLL}	Transfer function for complete PLL effect
$\mathbf{G}_{ri}$	Transfer matrix from current reference to input voltage
$\mathbf{G}_{ro}$	Transfer matrix from current reference to output current
$\mathbf{H}_{in}$	Sensing gain for input voltage
$\mathbf{H}_{io}$	Sensing gain for output currents
$\mathbf{H}_{M}$	Hadamard matrix, M^{th} order
$\mathbf{H}_{PLL}$	Sensing gain for PLL
$\mathbf{H}_{vo}$	Sensing gain for grid voltages
i_{d}	Current d component
$\mathbf{i}_{g}$	Grid currents
i_{in}	Current from DC source
I_{in}	Steady-state current from DC source
i_{Ld}	L filter current d component
I_{Ld}	Steady-state L filter current d component
$\mathbf{i}_{Lg}$	Current through L_{g}
i_{Lq}	Current q component through L filter
I_{Lq}	Steady-state L filter current q component
$\mathbf{i}_{o}$	Inverter output current
i_{od}	Inverter output current d component
i_{oq}	Inverter output current q component
I_{PV}	Current of PV source

i_q	Current q component
i_s	Ideal current source
j	Imaginary unit
k	Sample index in discrete systems
K_c	Transformation gain in Clarke Transformation
K_{FF}	Grid-voltage feedforward gain
K_i	Integral gain of PI controller
$K_{i\text{-}CC}$	Integral gain in current controller
$K_{i\text{-}DC}$	Integral gain in DC voltage controller
$K_{i\text{-}PLL}$	Integral gain in PLL controller
K_p	Proportional gain of PI controller
$K_{p\text{-}CC}$	Proportional gain in current controller
$K_{p\text{-}DC}$	Proportional gain in DC voltage controller
$K_{p\text{-}PLL}$	Proportional gain in PLL controller
K_{PI}	PI controller gain
L	Minor loop gain
L_1	L filter inductance
L_2	Grid-side inductor of LCL filter
L_{CC}	Current-control loop gain
L_{DC}	DC voltage control loop gain
L_{FF}	Grid-voltage feedforward path
L_g	Grid inductance
L_{IN}	Input response of current-control loop
L_{OUT}	Output response of current-control loop
L_{PLL}	PLL loop gain
λ	Eigenvalue
$\lambda(j\omega)$	Eigenloci (GNC loci)
n	Number of bits in shift register (for generating MLBS)
$\mathbf{N}_e$	External disturbance
N_{MLBS}	Length of MLBS
N_{ts}	Length of time series

$n_u(t)$	Disturbance in input signal
$N_u(j\omega)$	Fourier transformed disturbance in input signal
$n_y(t)$	Disturbance in output signal
$N_y(j\omega)$	Fourier transformed disturbance in output signal
M	Number of required uncorrelated sequences
ω	Angular frequency (rad/s)
ω_0	Center frequency of notch filter (rad/s)
ω_c	Critical frequency (rad/s)
ω_g	Fundamental frequency of grid voltages (rad/s)
$\omega_{p\text{-}LCL}$	Resonant pole of LCL filter (rad/s)
ω_Z	Frequency of zero (rad/s)
$\omega_{z\text{-}PI}$	PI-controller zero (rad/s)
P	Number of average periods
P_d	Power of distortions
P_r	Power of response to perturbations
Φ_{MLBS}	Power spectrum of MLBS
q	Index of spectral line
r	Fractional part
R	Integer part
$r(t)$	Excitation sequence
r_1	First excitation
r_2	Second excitation
r_e	Equivalent circuit resistance
r_f	Damping resistance of LC filter
r_g	Grid resistance
r_L	L filter resistance
s	Laplace variable
S	Sensitivity function
S_{det}	Sensitivity function, based on determinant
S_{peak}	Sensitivity peak
σ	Singular value

σ^2	Variance
T_{d}	Time delay
T_{meas}	Measurement time
T_{MLBS}	Measurement time of single MLBS period
$\mathbf{T}_{\mathrm{oi}}$	Transfer matrix from output voltage to input voltage
T_{pert}	Perturbation interval in P&O algorithm
T_{PLL}	Closed PLL loop
T_{s}	Sampling time
ΔT	Time difference
θ_{g}	Phase angle of the grid voltages
Θ_{PM}	Phase margins
$\mathbf{u}$	System input variables
u_1	First measured input signal
u_2	Second measured input signal
$u(k)$	Discrete input signal
$u(t)$	Input signal
$U(j\omega)$	Fourier transformed input signal
$U_{\mathrm{Exp}}(j\omega)$	Expected input signal (reference)
U_{PV}	Voltage of PV source
v_{c}	Voltage over DC capacitor
$\mathbf{v}_{\mathrm{Cf}}$	Voltage over AC filter capacitor
v_{d}	Voltage d component
v_{g}	Grid voltage
v_{in}	Voltage at inverter DC terminal
V_{in}	Steady-state voltage at inverter DC terminal
v_{od}	Voltage d component at inverter AC terminal
V_{od}	Steady-state voltage d component at inverter AC terminal
v_{oq}	Voltage q component at inverter AC terminal
V_{oq}	Steady-state voltage q component at inverter AC terminal
$\mathbf{v}_{\mathrm{PCC}}$	Voltage at PCC
v_{q}	Voltage q component

x	General variable
$\mathbf{x}$	System state variables
$\mathbf{x}^{\alpha\beta}$	Space vector
$\mathbf{x}^{\mathrm{dq}}$	DQ domain vector
$x(kT_s)$	Discrete-time variable
$X(k)$	Discrete Fourier transformed variable
X_g	Grid reactance
$\mathbf{y}$	System output variables
$\mathbf{Y}$	General process output
$y(k)$	Discrete output signal
$y(t)$	Output signal
$Y(j\omega)$	Fourier transformed output signal
$Y_{\mathrm{Exp}}(j\omega)$	Expected output signal (reference)
y_1	First measured output signal
y_2	Second measured output signal
Y_o	Inverter output admittance
$\mathbf{Y}_{o\text{-}o}$	Inverter open-loop output admittance
$\mathbf{Z}$	Impedance matrix
z^{-1}	Unit delay
$\mathbf{Z}_g$	Grid impedance
$\mathbf{Z}_{in}$	Transfer matrix from input current to input voltage

Subscripts

-d	Related to d channel
-dd	dd component
-dq	dq component
DQ	Matrix in DQ domain
-meas	Measured
-o	Open-loop transfer function
-q	Related to q channel
-qd	qd component
-qq	qq component

Superscripts

$*$	Set point
^	Small-signal variable
—1	Inverse
abc	Phase-domain vector
$\alpha\beta$	Space vector
cc	Closed-loop transfer function
DQ	DQ domain vector or matrix
L	Load-affected
ref	Reference value

ABBREVIATIONS

AC	Alternating current
AMP	Power amplifier
CC	Current-control loop
DC	Direct current
DQ	Direct quadrature, Synchronous-reference frame
DFT	Discrete Fourier transform
DIBS	Discrete-interval binary sequence
FPGL	Flexible Power Grid Lab
GHG	Greenhouse gas
GNC	Generalized Nyquist criterion
GV-FF	Grid-voltage feedforward
IPCC	United Nations' Intergovernmental Panel on Climate Change
LC	Filter with inductor and capacitor
LCL	Filter with two inductor and capacitor
LTI	Linear time-invariant
NXOR	Logical complement of XOR
MLBS	Maximum-length binary sequence
MIMO	Multi-input multi-output
MPP	Maximum power point
MPPT	Maximum power-point tracking
OBS	Orthogonal binary sequence
P&O	Perturb-and-observe (algorithm)
PCC	Point of common coupling
PHIL	Power hardware-in-the-loop

PI	Proportional-integral (controller)
PLL	Phase-locked loop
PRBS	Pseudo-random binary sequence
PV	Photovoltaics
PWM	Pulse-width modulation
RHP	Right-half-plane
SVD	Singular value decomposition
SISO	Single-input single-output
SNR	Signal-to-noise ratio
SRF-PLL	Synchronous-reference frame phase-locked loop
THD	Total-harmonic distortion
XOR	Exclusive-or digital logic gate

1 INTRODUCTION

This chapter provides the background for the thesis and introduces the main objectives and challenges of the work. It then reviews previous work related to the topic and lists the scientific contributions of the thesis, before presenting the structure of the thesis.

1.1 Background

Growing concerns about the threatening impacts of climate change have led to means of reducing greenhouse gas (GHG) emission receiving extensive attention over the past decade [1, 2]. To reduce GHG emission in synergy with the sustainable development, action is required especially in the global energy sector [3], in which the fossil fuels contribute the majority of primary power sources (84 percent in 2018 [4]). A significant proportion of these emissions can be reduced by replacing the fossil-fuels based production by GHG-free renewable-energy sources [5]. This has been widely recognized and acted upon; for example, the European Union has set a binding target to produce at least 32 percent of final energy consumption from renewable energy by 2030 [6], and the United Nations' Intergovernmental Panel on Climate Change (IPCC) has proposed that such figures reach about 70-85 percent shares by 2050 [2]. During the past decade, photovoltaics (PV) and wind energy have become price-competitive to fossil-fuel based production [7]. This has accelerated the transition from fossil-fuel based production to renewables [8] meaning that 63 percent of the globally installed capacity were renewables in 2018 [7].

Increasing the amount of renewable energy involves several challenges. From the power-system perspective, renewable energy appears as units that are quite different to the conventional fossil-fuel based power plants. The fossil-fuel based production is most often composed of large and centralized turbines. These turbines produce mechanical power that is converted to electrical power and supplied to the grid, usually through synchronous generators [9]. As the synchronous generator interfaces the grid, the magnetic field of the generator rotor electromechanically couples with the grid voltages and starts rotating at the grid fundamental frequency. This coupling of the rotating mass (rotor) provides inherent inertia and torque that mitigates multiple undesired events in the power system, such as rapid frequency changes, small power imbalances, and high-frequency oscillations [10]. How-

ever, most PV and wind-energy production operates as significantly smaller and distributed units, the power yields of which depend on the local weather conditions with strong daily and seasonal variations [11]. Due to highly varying and uncontrollable power yield, the grid-connecting device must be able to efficiently track and convert the maximum available power of the source to meet the requirements of the power grid. This necessitates a different and much faster reacting device than the synchronous generator in order to facilitate a grid-connection of the PV and wind-energy production [12].

The distributed renewable-energy sources are most commonly connected to the power grid through power-electronics inverters. A power-electronics inverter is a purely electronic device that consists of semiconductor components, and thus does not include mechanics that typically slow down the dynamics. Due to the purely electronic properties of the inverter, a fast-reacting control system is allowed to determine the switching pattern of the semiconductor components, which regulates the source power to match the requirements of the load [13]. This turns the power-electronics inverter into an efficient grid-connecting device for the PV and wind-energy production, as the fast control system can adapt the inverter operation to highly varying power from the renewable source to meet the requirements of the power grid [12].

The power-electronics inverter does not have similar characteristics to the synchronous generators, such as a magnetic field that inherently couples with the grid voltages and provides grid-stabilizing properties. Therefore, the inverter switching must be synchronized with the grid voltages and controlled so that the varying power from the energy source can be efficiently converted to the grid-compatible power. This requires a control system that is able to track the maximum power of the energy source and regulate the power yield through the inverter semiconductor switches into three-phase sinusoidal currents, which are synchronized with the grid voltages. In order to respond rapidly to sudden changes in the operating conditions and to mitigate distortions from the produced power, the high-bandwidth controllers are most desired [14]. The dynamic properties of the inverter are mostly defined by the applied control strategy, which usually means they are significantly faster than the typical dynamics of the devices that mainly consist of mechanical components [15]. Consequently, the inverters are fundamentally different from synchronous generators, which are mostly defined by the relatively slow dynamics of their rotating mass. Therefore, when the fossil-fuel-based production is replaced by the renewable energy in the power system, the number of synchronous generators and their stabilizing properties are reduced [16]. This reduction affects the power system, which will become increasingly time-dependent, vulnerable to system deviations, and more prone to stability issues [17].

The conventional power-system stability analysis can be divided to three main categories: rotor angle stability, frequency stability, and voltage stability [9]. These stability categories are often limited near to the system fundamental frequency (50 Hz or 60 Hz) and are basically related to system power flows and ability to maintain the synchronism. However, in most

power-electronics inverters, the stability analysis becomes much more complex. The reason for this increased complexity relates to the fact that typical dynamics of the inverter control system are prone to stability issues, which may appear at significantly higher frequencies than the system fundamental frequency [18]. These high-frequency stability issues may cause major challenges for the power system robustness, especially in local areas where high levels of the instantaneous power are injected through the inverters. In those areas, the inverter control dynamics dominate and the power system cannot base its operation on the stabilizing properties of the synchronous generators. This results in increased sensitivity to various stability issues in a wide frequency range that may compromise the stability of the whole power system [19]. Thus, the conventional stability analysis is not sufficient for ensuring the stable performance of the future power system with high levels of power-electronics devices [20].

Stability Issues of Grid-Connected Inverters

The stability issues of the grid-connected systems are usually related to the dynamic interactions between the power grid and the interfacing device, such as an inverter. Especially, the grid impedance is an important parameter that significantly affects the stability and control performance of the grid-connected inverter [21]. A mismatch of the grid impedance and the inverter output impedance causes undesired interactions between the inverter and the grid, such as harmonic resonance, which decreases the power quality and may even lead to unstable operations of the grid-connected systems [18]. Consequently, in some areas, these dynamic interactions will become one of the main issues limiting the total share of the PV and wind energy sources connected into the power system [11].

The dynamic interactions between the inverter and the grid can be analyzed by an impedance-based stability analysis [22]. In such an analysis, the stability of the grid-connected inverter can be assessed by a ratio between the grid impedance and the inverter output impedance. The grid-connected system will remain stable if the ratio satisfies the Nyquist stability criterion. Generally, when the grid impedance increases, the stability of the grid connection decreases and the system becomes more sensitive to small disturbances [20]. As the inverter dynamics and its output impedance are mainly determined by the applied control system, a suitable control design can also ensure the impedance-based stability in grids that have a significant grid impedance [23]. In order to ensure the impedance-based stability in the high-impedance grids, relatively slow control dynamics are usually required. However, the suitable control designs for high-impedance grids perform poorly in low-impedance grids where faster control dynamics are most desired for the optimal operation of the grid-connected system.

An underlying problem in guaranteeing the impedance-based stability and desired per-

formance of the grid-connected inverter is that the grid impedance may vary over many parameters and over time [24]. Consequently, when designing the control system without having accurate information about the grid impedance, drastic tradeoffs between the system robustness and the control performance are usually made. Impedance-based stability issues and power quality degradations have already been reported in the grids where high levels of the power are generated through the inverters [18, 25, 26, 27]. Stability issues related to the unknown grid impedance may become more common when the increasing demand for the renewable energy forces new units to be placed in remote areas, where a long grid-connecting cable introduces significant impedance [28]. Thus, the stability cannot be accurately predicted before connecting the device in its grid-connection point; even then, the variations in grid impedance may affect the stability. In order to guarantee the stability and desired performance of the grid-connected inverter under varying grid conditions, the grid dynamics must be measured and analyzed in real time.

Real-Time Methods

In order to assess the impedance-based stability of a grid-connected system, information about the grid impedance is required. The existing impedance-measurement methods can be divided into active and passive methods. Active methods require external excitation to perturb the grid [29], while passive methods are based on existing disturbances or characteristics of the grid and do not require an external perturbation [30]. In most cases, the passive methods cannot be applied to assess the impedance-based stability as the methods usually estimate the grid impedance only at the grid fundamental frequency. In the active methods, however, the system is typically studied at several frequencies [31].

Previous studies have presented a number of active methods for measuring the grid impedance. Particularly, wideband techniques have become popular [32]. In the technique, a broadband perturbation such as an impulse or a multi sine is applied. The perturbation is injected, for example, into the reference of the inverter current control, and the responses both in the grid voltages and currents are measured. Fourier methods are then applied to extract the corresponding frequency components and to determine the grid impedance [33]. As the broadband injection has energy at several frequencies, the grid impedance can be rapidly measured at a wide frequency band.

Recently, one of the most popular broadband perturbation has been the pseudo-random binary sequence (PRBS) [32]. The binary-form PRBS has become superior to other broadband perturbations as its binary sequences have the lowest possible crest factor among all signals. A low crest factor indicates that the perturbation energy is high in relation to the perturbation time-domain amplitude. Therefore, the binary perturbations are well suited for measuring the grid-connected system that are sensitive to nonlinear dynamical phenom-

ena, which are typically triggered by high-amplitude perturbations. Additionally, using a low-amplitude perturbation makes it possible to perform impedance measurements during normal system operation. The PRBS is a deterministic and periodic signal, which makes it possible to average the measurements over multiple injection periods to increase the signal-to-noise ratio (SNR). In addition, the PRBS has a largely controllable spectral energy distribution, so the perturbation is well scalable to different systems. As the sequence is binary, the signal is very easy to implement even with a low-cost controller, whose output can only cope with a small number of signal levels.

Real-time measurements of the grid impedance make it possible to monitor, for example, the system performance and stability margins in varying grid conditions [34]. Accurate and reliable measurements of the grid impedance make it possible to optimize the inverter control system under uncertain and time-varying grid conditions. Therefore, the inverter control system can be tuned closer to maximum performance with less conservative stability margins, which improves the overall system performance and guarantees an adequate power quality [35]. In order to maintain the desired system performance in varying grid conditions, the inverter control system can be configured to autonomously react to the changes in the grid conditions based on the real-time measurements of the grid impedance [36]. Consequently, by applying such a control system, the inverter performance can be continuously optimized to the grid conditions; this ensures a good efficiency, adequate power quality and robustness of the grid-connected system, also in highly varying grid conditions.

1.2 Aim and Scope of the Thesis

The goal of this work is to provide methods for a robust grid-connected system with optimized control performance. Such a system is able to avoid the impedance-based interactions and constantly generate power at an adequate quality under varying grid conditions. To achieve the goal, the inverter control system must be optimized to the unpredictable and time-variant grid conditions. Such optimization requires accurate real-time measurements of the grid impedance and an adaptive control system to continuously optimize the control parameters to the measured grid impedance.

This thesis introduces wideband methods for real-time frequency-response measurements, which can be applied to predict the dynamic performance and to assess the impedance-based stability of a grid-connected system. The methods are based on various pseudo-random sequences and Fourier techniques. The most common issues affecting accuracy of the grid-impedance measurements, such as the grid-voltage unbalance and harmonics, are considered. This thesis introduce a design procedure for the perturbation parameters that effectively mitigate those common issues affecting the measurement accuracy. Measurements of three-phase systems usually require signal-processing and identification tools that are designed es-

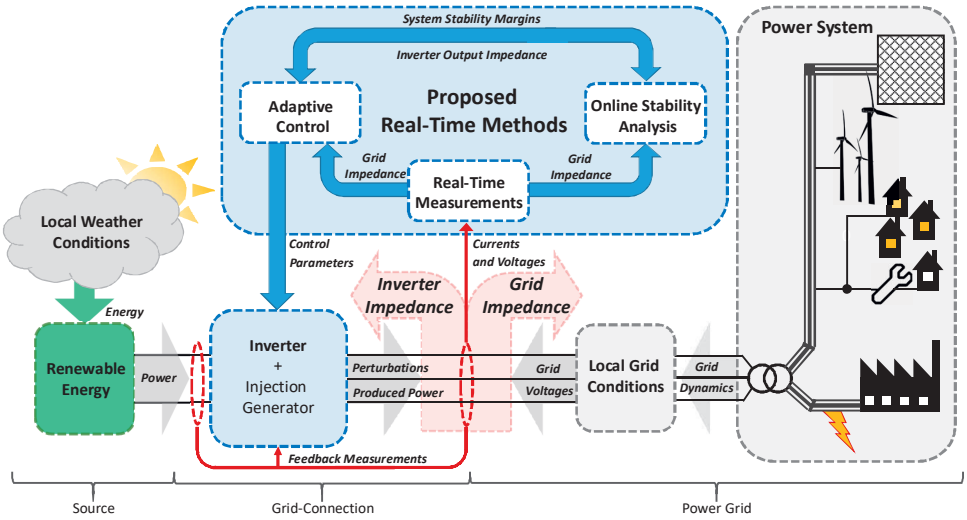

Figure 1.1 Grid-connected inverter with proposed real-time methods.

pecially for systems with multiple inputs and outputs. Therefore, the present thesis also introduces the design and practical implementation of multivariable measurement methods applying orthogonal binary sequences. By applying orthogonal sequences, multiple transfer functions affecting the system dynamics can be measured simultaneously.

This thesis also presents the control tuning procedures that improves the system performance under varying grid conditions. The real-time grid-impedance measurements are applied to re-adjust the inverter control parameters for improved performance under current grid conditions. The proposed adaptive control methods make it possible to keep the impedance-based stability margins constant during changes in the grid conditions by reshaping the inverter impedance, and to provide desired control performance that guarantees adequate power quality in various grid conditions. The adaptive controllers are adjusted to compensate various negative effects of the grid impedance that typically compromise the system stability or degrades the control performance and power quality. The design steps and practical implementation of the proposed adaptive control methods are presented.

Fig. 1.1 shows a graphical abstract of this thesis. The inverter continuously (or at certain intervals) applies an injection, measures the grid impedance, and performs real-time stability analysis. Based on the analysis, the inverter control system is adaptively adjusted to meet the desired stability margins, and, consequently, the desired control performance. The inverter is fully self-supporting and requires no external devices.

The main advantages of the presented methods can be summarized as follows.

- Multiple transfer functions that describe system dynamics can be measured simultaneously in real time using an existing inverter in the system.
- The grid impedance is rapidly obtained under grid-voltage unbalance and harmonics.

- The tradeoff between the system sensitivity and control performance can be optimized by the adaptive grid synchronization, based on real-time grid impedance measurements.
- Improved performance of the current control and enhanced power quality can be achieved by applying the proposed adaptive-control strategies.

Challenges

Real-time measurements and adaptive control of grid-connected systems have multiple challenges that are reviewed briefly here. Some of the challenges are general in many fields of engineering, but others are related especially to the grid-connected systems and their special characteristics.

The main challenges of grid-connected systems are related to the unpredictable and varying grid conditions. In particular, the varying grid impedance has a major effect on the grid-connected inverter by affecting the inverter control performance, triggering the impedance-based interactions, and affecting the local grid voltages. Thus, the grid impedance and its effects must be taken into account in both real-time measurements and adaptive control. Additionally, the stability and performance analyses become highly complicated when the grid impedance includes multiple resonances or is affected by near devices. Consequently, the grid conditions are usually unpredictable and valid generalizations or simplifications are relatively hard to provide. Thus, in order to optimize the performance of the real-time measurements and the adaptive control, a wide range of possible grid characteristics must be considered.

Designing real-time frequency-response measurements of grid-connected systems includes multiple special requirements that must be considered. In general, the applied perturbation must have enough energy at a wide enough frequency band. This is usually achieved by increasing the perturbation amplitude or injecting multiple perturbation periods and applying averaging. However, the injected perturbations appear as distortions from the grid perspective, which decreases the power quality. Therefore, because unnecessary high amplitudes must be avoided, the perturbation amplitude is an important design parameter. Additionally, averaging over multiple periods increases the measurement time and increases the reaction time of the adaptive control. Hence, one of the challenges for real-time measurement is to provide sufficient measurement accuracy within a desired time frame. The desired time frame varies from few tens of milliseconds to a few minutes, depending on the process and application. Furthermore, the measurements must be performed within the computational and memory limits of the hardware, which often restricts the use of some advanced signal-processing and analyzing tools.

Adaptive control of grid-connected inverters has certain challenges, most of which are

related to the impedance-based interactions in varying grid conditions. Due to fast control dynamics of the inverter, a sudden increase in the grid impedance may cause rapidly advancing stability issues. Therefore, the potential time frame to mitigate the stability issues is usually very limited. Within this limited time frame, the advancing stability issues must be first identified by the real-time grid-impedance measurements and, thereafter, the stabilizing actions performed by the adaptive-control system. In order to guarantee good power quality, maintaining the stability is not a sufficient operation of the control system; the desired inverter performance must also be systematically considered. An adequate performance of the inverter is achieved when the control system is continuously adjusted based on the varying grid conditions so that the impedance-based interactions and other disturbances are minimized, maximum power with good efficiency is generated, and rapid control responses to external changes are provided. This becomes complex as the grid conditions set practical limits for the achievable control performance and power quality. Consequently, determining the optimal parameters for the inverter control system is not straightforward, as multiple parameters and cross-effects between the parameters must be considered at the same time.

Research Questions

The main research questions in this thesis can be given as follows.

- What are the injection specifications and practical limitations for frequency-response measurements applied in real-time stability analysis and adaptive control of grid-connected inverter systems?
- How is the operation of a grid-connected inverter affected by varying grid conditions and which grid characteristics should be identified and considered in adaptive control?
- How much can the produced power quality, stability and the control performance of the grid-connected inverter be improved by adaptive control, and what are the limiting issues?

1.3 Review of Previous Studies

Early methods for frequency-response measurements of the grid impedance were introduced in [37, 38]. In both works, a relatively drastic transient was induced to the system by switching a capacitor bank, and the grid impedance was computed from the current and voltage responses applying Fourier techniques. The measurements were performed in order to identify the topology of the power system network and to study the impedance characteristics at a wide frequency range. The measurement technique of the grid impedance was improved in [39, 40], where controllable sinusoidal currents were injected to the grid through an iso-

lation transformer and the responses were processed by a frequency-response analyzer. The impedance data was then applied in power-quality calculations at a specific point of the grid, and to predict the impact of additional loads connected to that point.

In the aforementioned studies, external measurement devices were applied for measuring the grid impedance. The authors in [41] did not apply an external measurement device, but obtained the grid impedance by using an existing power-electronics device to perturb the grid with high-amplitude current spikes. The authors in [42] applied a real PV inverter to inject sinusoidal currents to the grid in order to estimate resistive and inductive components of the grid impedance at the grid fundamental frequency. The method was improved in [43] by fully integrating the excitation generator and impedance calculations to the control system of the PV inverter.

Wideband perturbations were applied to grid-impedance measurements for the first time in [44]. In that method, the duty cycles of the converter PWM were modified to produce current pulses to the grid, the responses were recorded, and the grid impedance was calculated offline. Wideband grid-impedance measurements, performed in real-time, were introduced in [33]. That technique involved measuring the grid impedance by the inverter itself: the inverter injected an impulse current on top of the normal output current, measured the resulting responses in the grid voltage, and applied Fourier analysis to extract the corresponding frequency components in both the voltage and current. The grid impedance was then determined by the ratio between the perturbation voltage and current. The authors in [32] further improved the grid-impedance measurements by using the pseudo-random binary sequence (PRBS) instead of the impulse in the measurements. The PRBS was shown to provide significantly more accurate measurements than the impulse-based method, especially in noisy environments when the injection amplitude is restricted. In [45], a discrete-interval binary sequence (DIBS) was applied to measure the grid impedance. A DIBS is a computer optimized signal where as much power as possible is forced to the specific frequencies without increasing amplitude of the perturbation. The DIBS has weakened frequency resolution compared to the PRBS, but provides significant improvements on the measurement accuracy when the system noise floor is high in contrast to the amplitude of the perturbation.

Recently, orthogonal binary sequences have been introduced for impedance measurements of grid-connected systems [46]. The orthogonal sequences do not have energy at the same frequencies, making it possible to simultaneously measure multiple coupled transfer functions of the system. The method was shown to be particularly useful in the DQ domain analysis in which several (coupled) impedance components are required for the stability analysis. It was shown that the method not only saves overall experimentation time, but also ensures that each impedance component is measured with the system in the same conditions, which may not be the case if sequential perturbations are applied.

Utilizing Grid-Impedance Measurements

The online grid-impedance measurements have enabled various methods that can be applied to improve the system performance, stability, and protection, especially in varying grid conditions. First, such methods utilized an impedance measurement at the grid fundamental frequency to optimize the control tuning of the active filters [47, 48] and to detect grid-impedance variations for the protection purpose [43]. Similar measurements were applied in [49] and [50] to replace static grid-impedance estimations for the independent control of active and reactive powers, and in [51] for the model-predictive control schemes. The authors in [52] applied the wideband measurements of the grid-impedance to locate and identify different grid faults instead of just detecting their occurrence. In [53] the stability of interconnected systems was accurately predicted by utilizing wideband measurements of the source and load impedances. Methods for the real-time stability analysis were introduced in [54] where the stability was assessed by the ratio between the modeled device impedance and the measured grid impedance. The grid impedance was obtained at several frequencies in real time and vector fitting was applied to the measured data.

Real-time grid-impedance measurements have also been utilized in adaptive control of grid-connected inverters. The authors in [36] applied the measurements to improve the impedance-based stability by limiting the control bandwidth of the grid synchronization when the grid impedance increased. In order to mitigate the negative effects of the varying grid impedance to the inverter control performance, the real-time grid-impedance measurements were applied in the adaptive-control strategies that optimize the bandwidth [55] and damping ratio [56] of the controlled system, and also in tuning deadbeat controllers [57]. The impact of the grid-impedance to the dynamics of the LCL filter were considered in [58], where the measured grid impedance was applied in adaptive optimization of the hybrid-damping technique. The adaptive methods have also been applied in DC power systems; the authors in [59] applied real-time measurements of the DC bus impedance for an adaptive control of the system source converters.

1.4 Summary of Scientific Contributions

The main scientific contributions are given as follows.

- A method for practical implementation for real-time measurements of grid impedance applying orthogonal pseudo-random binary sequences.
- A systematic design procedure for a grid-impedance measurement that removes the spectral leakage caused by grid-voltage unbalance and harmonics from the measurements.

- A technique for real-time stability analysis, based on the generalized Nyquist stability criterion and multivariable measurements of the grid impedance.
- An adaptive phase-locked loop that keeps the system sensitivity constant by utilizing the real-time measurements of grid reactance.
- Adaptive grid-voltage feedforward applying perturb-and-observe algorithm in order to minimize the distortions from the produced power.
- Adaptive current-controller and digital Notch filter that compensate the negative impacts of the grid impedance from the inverter innermost control loop.

1.5 Structure of the Thesis

This thesis contains five chapters and publications [P1]-[P6]. The following chapters can be briefly summarized as follows.

Chapter 2: Grid-Connected Three-Phase System

Chapter 2 provides the theoretical background for analyzing the grid-connected three-phase systems. It introduces the synchronous-reference frame (DQ domain) and its most important characteristics, and reviews impedance-based stability and sensitivity analysis based on the generalized Nyquist criterion for the multivariable systems. Also, the small-signal modeling methods of the inverter with the load effect are presented.

Chapter 3: Methods

Chapter 3 presents the proposed methods of the thesis. The methods are divided into two main parts: the real-time measurement methods of the grid-connected systems and adaptive control methods that can be applied to improve the stability and control performance of the grid-connected inverters in varying grid conditions.

The real-time frequency-response measurements of the grid-connected systems are based on the pseudo-random binary sequences and the Fourier techniques. First, the general technique for obtaining frequency responses of the multivariable systems is considered. The binary excitations, suitable for the online-measurements of the grid-connected systems, are reviewed, where the main emphasis is on the orthogonal pseudo-random binary sequences. Finally, the methods and design of the online frequency-response measurements of the grid-connected systems are proposed.

The adaptive-control methods are based on the real-time identifications of the grid impedance, the current control loop, or the generated distortion on the grid. The methods are

proposed for different control loops of the grid-connected inverter in order to improve the stability and control performance of the grid-connected system.

Chapter 4: Implementation and Experimental Verification

Chapter 4 presents implementation of the proposed online measurement and adaptive-control methods for a three-phase grid-connected inverter. Verification of the methods is performed through simulations and power hardware-in-the-loop tests. Accuracy and performance of the online measurement methods are shown and the real-time stability analysis is illustrated. Each proposed adaptive-control method is tested in realistic grid conditions and compared to the conventional implementations.

Chapter 5: Conclusions

Chapter 5 summarizes the thesis and provides the main conclusions. The pros and cons of the proposed methods are critically discussed and their applicability in different conditions is reviewed.

2 GRID-CONNECTED THREE-PHASE SYSTEMS

This chapter presents background information about the three-phase grid-connected systems applied in the thesis. First, the synchronous-reference frame and the impedance-based stability analysis are presented. After that, small-signal modeling of the three-phase inverters is introduced. The impact of the grid impedance is added to the small-signal model by a load-affected transfer functions. Finally, a short discussion of the provided background information is provided.

2.1 Synchronous-Reference Frame

Grid-connected systems are usually analyzed in a sequence domain or in a synchronous-reference frame (DQ domain). The two domains provide relatively similar analyses and predictions about system stability [60]. The sequence domain does not require grid synchronization, but does not provide a steady-state DC operating point either. In a synchronous-reference frame, accurate grid synchronization is required as the frame rotates at the grid fundamental frequency. Due to the synchronized rotating frame, balanced three-phase variables can be represented as two equivalent DC signals whose steady-state operating point can be solved. This makes it possible to use linearized state-space methods and conventional PI-type controllers, which are the main reasons why the DQ domain analysis is applied in this thesis [15].

Three-phase waveforms can be transformed to the synchronous-reference frame in two steps, known as Clarke and Park transformations. First, the three-phase variables (a, b, and c) are transformed to a rotating space vector (α and β) and a zero (0) component using the Clarke transformation. This is achieved by a linear transfer matrix, which can be written as [61]

$$\begin{bmatrix} x_\alpha(t) \\ x_\beta(t) \\ x_0(t) \end{bmatrix} = K_c \begin{bmatrix} 1 & -1/2 & -1/2 \\ 0 & \sqrt{3}/2 & -\sqrt{3}/2 \\ 1/2 & 1/2 & 1/2 \end{bmatrix} \begin{bmatrix} x_a(t) \\ x_b(t) \\ x_c(t) \end{bmatrix} \tag{2.1}$$

where K_c determines the type for the transformation: $K_c = \sqrt{2/3}$ is applied for the power-invariant transformation and $K_c = 2/3$ for the amplitude-invariant transformation that is applied in this thesis. The zero component equals zero when the balanced three-phase variables are transformed.

Next, the frame is synchronized with the grid voltages by Park transformation, and the frame follows the phase angle of the grid voltages, which can be given as $\theta_g = \int_0^t \omega_g \, dt$. Consequently, the frame rotates at the fundamental frequency and the observed variables (appearing at the fundamental frequency) stay still in the frame. The Park transformation for balanced three-phase values can be given as [62]

$$\mathbf{x}^{\mathrm{dq}} = \mathbf{x}^{\alpha\beta} e^{-j\theta_g} = x_{\mathrm{d}} + j\, x_{\mathrm{q}} \tag{2.2}$$

where $\mathbf{x}^{\alpha,\beta}$ is a space-vector representation of the balanced three-phase variables, and the vector in the synchronous-reference frame ($\mathbf{x}^{\mathrm{dq}}$) is divided into direct (x_{d}) and quadrature (x_{q}) components. Therefore, fundamental components of the balanced three-phase waveforms can be represented as DC-valued d- and q-components that are orthogonal to each other.

Considering the DQ domain waveforms, when the frame is accurately synchronized to the balanced three-phase grid voltages, the voltage d-component denotes the amplitude of the grid voltages and the q-component equals zero. As the frame is synchronized to the grid voltages, the phase angle of the grid voltages is applied in transformation of the currents. However, as three-phase voltages and currents are connected through the system impedance, the system reactance causes phase lag (lead) to the current. Thus, the grid current d-component does not equal to the amplitude of the three-phase currents nor the q-components equal to zero. Therefore, the direct components of the currents and voltages are coupled through the system impedance, which must be determined as a multivariable matrix, including direct components (dd and qq) and cross-couplings (dq and qd). The full DQ domain impedances (admittances) are 2 x 2 matrices that can be given as

$$\begin{bmatrix} v_{\mathrm{d}} \\ v_{\mathrm{q}} \end{bmatrix} = \underbrace{\begin{bmatrix} Z_{\mathrm{dd}} & Z_{\mathrm{qd}} \\ Z_{\mathrm{dq}} & Z_{\mathrm{qq}} \end{bmatrix}}_{\mathbf{Z}_{\mathrm{DQ}}} \begin{bmatrix} i_{\mathrm{d}} \\ i_{\mathrm{q}} \end{bmatrix} \tag{2.3}$$

Consequently, systems in the DQ domain are multi-input-multi-output (MIMO) systems.

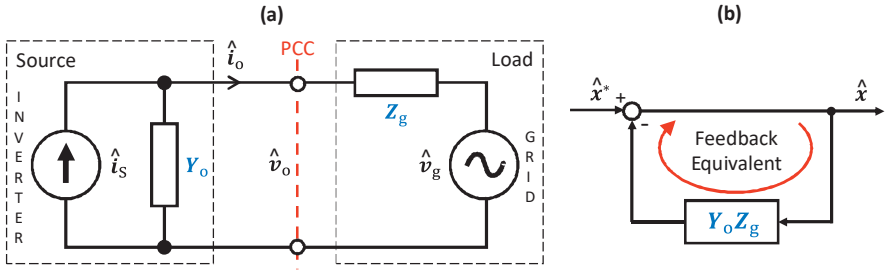

Figure 2.1 Interconnected source-load subsystem (a) and its feedback-system equivalent (b).

2.2 Impedance-Based Stability

In the impedance-based stability analysis of interconnected systems, the stability is determined by the ratio of the source and load impedances or admittances at their point of common coupling (PCC) [22]. Fig. 2.1a shows an equivalent small-signal circuit of a source-load interconnection, where the inverter acts as a source and the grid as a load. The superscript (^) is used to denote small-signal variables of the system. The inverter is modeled as a Norton equivalent by an ideal current source ($\hat{\mathbf{i}}_s$) and shunt admittance (inverter output admittance) $\mathbf{Y}_o$. The inverter output current flows to the grid that is modeled as a Thevenin equivalent, by an ideal voltage sink ($\hat{\mathbf{v}}_g$) and series impedance (grid impedance) $\mathbf{Z}_g$. In the DQ domain analysis, the grid-impedance and the inverter output admittance are analyzed as multivari-able models [53], given as

$$\mathbf{Z}_g(s)=\begin{bmatrix} Z_{g\text{-}dd}(s) & Z_{g\text{-}qd}(s) \\ Z_{g\text{-}dq}(s) & Z_{g\text{-}qq}(s) \end{bmatrix}, \mathbf{Y}_o(s)=\begin{bmatrix} Y_{o\text{-}dd}(s) & Y_{o\text{-}qd}(s) \\ Y_{o\text{-}dq}(s) & Y_{o\text{-}qq}(s) \end{bmatrix} \tag{2.4}$$

The grid and inverter are assumed to be standalone stable; that is, the inverter connected to an ideal grid is stable and the grid without the inverter is stable.

Based on the equivalent circuit shown in Fig.2.1a, the inverter output current can be written as

$$\hat{\mathbf{i}}_o=\left[\mathbf{I}+\mathbf{Y}_o\mathbf{Z}_g\right]^{-1}\hat{\mathbf{i}}_s-\left[\mathbf{I}+\mathbf{Y}_o\mathbf{Z}_g\right]^{-1}\mathbf{Y}_o\hat{\mathbf{v}}_g=\left[\mathbf{I}+\mathbf{Y}_o\mathbf{Z}_g\right]^{-1}\left[\hat{\mathbf{i}}_s-\mathbf{Y}_o\hat{\mathbf{v}}_g\right] \tag{2.5}$$

which is affected by the grid impedance and the inverter output admittance. The term $\left[\hat{\mathbf{i}}_s-\mathbf{Y}_o\hat{\mathbf{v}}_g\right]$ represents an inverter connection to the ideal grid voltages (zero grid impedance), which is assumed to be stable in all conditions. The residual term $\left[\mathbf{I}+\mathbf{Y}_o\mathbf{Z}_g\right]^{-1}$ affects stability and resembles a closed-loop transfer function for a multivariable negative feedback system. The stability of such a system is assessed if the system minor loop gain

$$\mathbf{L}(s)=\mathbf{Y}_o(s)\mathbf{Z}_g(s) \tag{2.6}$$

satisfies the generalized Nyquist criterion (GNC) [63].

Fig. 2.1b illustrates the feedback-system equivalent for the interconnected grid and inverter subsystems. The forward gain equals one, and feedback gain is a product of the inverter output admittance and the grid impedance that is the system minor loop gain (2.6). The closed-loop transfer function for the feedback system can be written as

$$\left[\mathbf{I}+\mathbf{Y}_{\mathrm{o}}\mathbf{Z}_{\mathrm{g}}\right]^{-1}=\frac{\mathrm{adj}\left[\mathbf{I}+\mathbf{Y}_{\mathrm{o}}\mathbf{Z}_{\mathrm{g}}\right]}{\det\left[\mathbf{I}+\mathbf{Y}_{\mathrm{o}}\mathbf{Z}_{\mathrm{g}}\right]} \tag{2.7}$$

where the inverse matrix is divided to the determinant (det) and the adjugate (adj) terms. A necessary and sufficient condition for the feedback system stability is that $\det\left[\mathbf{I}+\mathbf{Y}_{\mathrm{o}}\mathbf{Z}_{\mathrm{g}}\right]$ satisfies the generalized Nyquist stability criterion [64].

Stability Margins and System Sensitivity Function

The stability of the multivariable grid-connected system can be assessed by the eigenvalues of the minor loop gain. The stability margins of the feedback-system equivalent (Fig. 2.1b) can be evaluated through the eigenvalue loci (eigenvalues for each frequency $j\omega$) of the minor loop gain [63]. Assuming the minor loop gain has no zeros with a positive real part, the system is stable if the eigenvalue loci does not encircle the critical (-1 + j0) point in the complex plane and the stability margins can be then evaluated by the shortest distance to that critical point. The eigenvalues (λ) for each frequency can be solved from

$$\det\left[\lambda(j\omega)\mathbf{I}-\mathbf{Y}_{\mathrm{o}}(j\omega)\mathbf{Z}_{\mathrm{g}}(j\omega)\right]=\det\left[\lambda(j\omega)\mathbf{I}-\mathbf{L}(j\omega)\right]=0 \tag{2.8}$$

This yields a second-order equation for the minor loop gain (2x2 matrix), given as

$$\lambda^2-\lambda(L_{11}+L_{22})+(L_{11}L_{22}-L_{12}L_{21})=0 \tag{2.9}$$

The solution of such a second-order equation returns a pair of complex eigenvalues for each frequency $j\omega$. Consequently, two eigenvalue loci ($\lambda_1(j\omega)$ and $\lambda_2(j\omega)$) are plotted in the complex plane, where both loci must satisfy the GNC [53]; that is, they must not encircle the critical point in a clockwise direction.

The system's robustness can be evaluated by the proximity of the eigenvalue loci to the critical point. The shorter the distance, the more sensitive is the system to external distortions [65]. For a given eigenvalue ($\lambda(j\omega)=\alpha+j\beta$), distance to the critical point can be written as

$$d_{\lambda(j\omega)}=\sqrt{(1+\alpha)^2+\beta^2} \tag{2.10}$$

The closest eigenvalue determines the most sensitive frequency of the system, denoted by

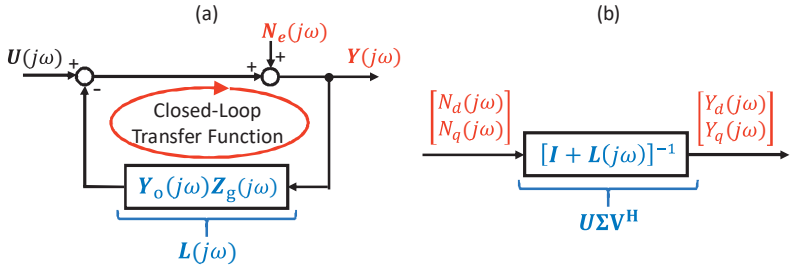

Figure 2.2 Multivariable feedback equivalent (a) and definition (b) of impedance-based sensitivity.

the critical frequency ω_c. The closest acceptable distance can be adjusted by drawing a circle around the critical point, where the radius of the circle is considered as a stability margin that determines the minimum system attenuation for external disturbances. Correspondingly, the impedance-based stability margins can be considered by a transfer function from external disturbances to the system output; this is known as a system sensitivity function. This approach was presented in [65] for a impedance-based stability analysis of a DC-DC system. For such a single-input single-output (SISO) system, the system sensitivity function is straightforwardly defined as an inverse of the distance between the eigenvalue loci and the critical point.

A sensitivity function for a multivariable system is more complex than for the SISO systems, as multiple eigenvalue loci are coupled [64]. Fig. 2.2a depicts the system sensitivity, determined by a closed-loop transfer function from external disturbance $\mathbf{N}_e(j\omega)$ to the process output $\mathbf{Y}(j\omega)$, where the feedback gain represents the minor loop gain (2.6) and mostly determines the system sensitivity. Fig. 2.2b shows the closed-loop system from $\mathbf{N}_e(j\omega)$ to $\mathbf{Y}(j\omega)$, from which the system sensitivity can be determined by singular value decomposition (SVD). The SVD can be written as [66]

$$\left[\mathbf{U}\boldsymbol{\Sigma}\mathbf{V}^{\mathbf{H}}\right](j\omega) = SVD(\left[\mathbf{I}+\mathbf{Y}_o(j\omega)\mathbf{Z}_g(j\omega)\right]^{-1}) = SVD(\left[\mathbf{I}+\mathbf{L}(j\omega)\right]^{-1}) \tag{2.11}$$

where the closed-loop transfer matrix is divided into three parts: matrices $\mathbf{U}$ and $\mathbf{V}^{\mathbf{H}}$ represent the rotation of the matrix, while diagonal matrix $\boldsymbol{\Sigma}$ represents the scaling of the final transfer matrix. Therefore, components of the $\boldsymbol{\Sigma}$ are the system singular values ($\sigma_1(j\omega)$ and $\sigma_2(j\omega)$) that determine absolute (frequency depended) gains through the closed-loop feedback and, thus, define the system sensitivity for external disturbances. Further analysis of the SVD is beyond the scope of this thesis, as only the impedance-based system sensitivity is considered by the system singular values (sensitivity function).

The greater of the two singular values ($\sigma_1(j\omega)$ and $\sigma_2(j\omega)$) represents the system sensitivity; that is, the maximum frequency-dependent gain (in Fig. 2.2) for the external disturbances [64]. The maximum of the singular values is usually considered as the principal gain of the multivariable system [67], which determines the maximum absolute gain of the closed-loop system for disturbances arising from any directions. In the DQ domain this means any dis-

turbances from the d-channel, q-channel, or combinations thereof. Based on this definition, the impedance-based sensitivity function can be given as

$$S(j\omega) = \max(\Sigma(j\omega)) \tag{2.12}$$

with which the system robustness at each frequency can be determined by a single real-valued number.

The stability of the multivariable feedback system can be assessed if the determinant of the closed-loop transfer function (2.7) satisfies the GNC. The inverse determinant term is a product of the system singular values for a 2 x 2 matrix, given as [64]

$$\frac{1}{\det[\mathbf{I}+\mathbf{L}(j\omega)]} = \prod_{i=1}^{2} \sigma_i(j\omega) = \sigma_1(j\omega)\sigma_2(j\omega) \tag{2.13}$$

and thus, provides a straightforward indicator of the overall system sensitivity. Use of the determinant term instead of the SVD analysis simplifies the analysis and eases computational burden. Thus, in this thesis, the impedance-based sensitivity function of the multivariable grid-connected system is defined by a determinant term, given as

$$S_{\det}(j\omega) = \frac{1}{\det[\mathbf{I}+\mathbf{L}(j\omega)]} \tag{2.14}$$

The maximum absolute value of $S_{\det}(j\omega)$ is denoted as a sensitivity peak, given as

$$S_{\text{peak}} = \max_{0\le\omega\le\infty} |S_{\det}(j\omega)| = \max_{0\le\omega\le\infty} \left| \frac{1}{\det[\mathbf{I}+\mathbf{L}(j\omega)]} \right| \tag{2.15}$$

The sensitivity peak rises to infinity when either of the system singular values (or eigenvalue loci) approaches instability. Low values for S_{peak} are desirable in order to mitigate harmonics and avoid stability issues. Thus, the sensitivity peak, defined by the determinant term, can be applied as an indicator of system robustness. The desired robustness level can be adjusted by limiting the maximum allowed sensitivity peak.

For the stability and robustness assessment, the first step is to assess the absolute stability by applying both the system eigenvalue loci and then the stability margins by the system sensitivity function. By defining the system sensitivity function as (2.12) or (2.14), the sensitivity function can be considered to represent the distance of the eigenvalue loci from the critical point rather than to return information about possible encirclement of the critical point. Consequently, the sensitivity function may have low values that indicate a robust system, even though the actual eigenvalue loci encircles the critical point, and thus, the system does not satisfy the generalized Nyquist criterion.

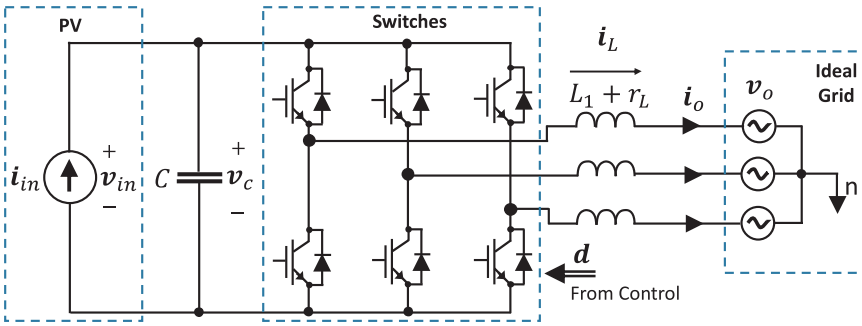

Figure 2.3 Three-phase inverter connected to ideal grid.

2.3 Inverter Small-Signal Model and Output Admittance

In this section, a small-signal model of the inverter output admittance in the DQ domain is constructed. The model is based on the linearized state-space averaging [68] and closed-loop transfer functions. The modeling method was originally developed for the filters and the DC-DC converter, where the system can be linearized around the DC-valued operating point. However, voltages and currents in AC systems are sinusoidal and the DC-valued operating point does not occur. Here, the DQ domain analysis becomes superior over stationary frames (such as sequence domain) as the balanced three-phase variables are transformed to two DC-valued signals, which can be linearized around the steady-state operating point by first-order derivatives of the Taylor series.

Fig. 2.3 shows a grid-connected inverter that connects the photovoltaic source to the ideal grid voltages through an L filter. Equations for the inductor voltage (derivative of the current) and capacitor current (derivative of the voltage) are formed by applying the conventional Kirchoff's circuit laws. The signals are transformed to the DQ domain and averaged over a switching period, determined by the duty cycle **d**. The yielding averaged model can be given as [69]

$$\begin{aligned}
\frac{d\langle i_{\mathrm{Ld}}\rangle}{dt} &= \frac{1}{L_1}\left(-r_{\mathrm{L}}\langle i_{\mathrm{Ld}}\rangle + \omega_{\mathrm{g}} L_1 \langle i_{\mathrm{Lq}}\rangle + d_{\mathrm{d}}\langle v_{\mathrm{c}}\rangle - \langle v_{\mathrm{od}}\rangle\right) \\
\frac{d\langle i_{\mathrm{Lq}}\rangle}{dt} &= \frac{1}{L_1}\left(\omega_{\mathrm{g}} L_1 \langle i_{\mathrm{Ld}}\rangle - r_{\mathrm{L}}\langle i_{\mathrm{Lq}}\rangle + d_{\mathrm{q}}\langle v_{\mathrm{c}}\rangle - \langle v_{\mathrm{oq}}\rangle\right) \\
\frac{d\langle v_{\mathrm{c}}\rangle}{dt} &= \frac{1}{C}\left(-\frac{3}{2} d_{\mathrm{d}}\langle i_{\mathrm{Ld}}\rangle - \frac{3}{2} d_{\mathrm{q}}\langle i_{\mathrm{Lq}}\rangle + \langle i_{\mathrm{in}}\rangle\right) \\
\langle v_{\mathrm{in}}\rangle &= \langle v_{\mathrm{c}}\rangle, \langle i_{\mathrm{od}}\rangle = \langle i_{\mathrm{Ld}}\rangle, \langle i_{\mathrm{oq}}\rangle = \langle i_{\mathrm{Lq}}\rangle
\end{aligned} \tag{2.16}$$

where the variables shown in the Fig. 2.3 are transformed to the DQ domain and ω_{g} represents the grid-fundamental (angular) frequency.

The steady-state values are determined by the grid voltages and power yield of the DC power source. Additionally, the output current q component (reactive power) is regulated to zero as the intentional production of reactive power is not considered in this thesis. For other variables, the steady-state can be solved from the average model as the derivatives settle to zero at the steady state. The steady-state variables can be written as

$$\begin{aligned} D_d &= \frac{V_{od} + \sqrt{{V_{od}}^2 + \frac{8}{3} V_{in} r_e I_{in}}}{2V_{in}} \\ D_q &= \frac{2I_{in} L_1 \omega_g}{3D_d V_{in}} \\ I_{Ld} &= \frac{2I_{in}}{3D_d} \end{aligned} \tag{2.17}$$

The equations are linearized around the steady-state operating point. In the linearized model, the small-signal variables are gathered into input (**u**), output (**y**), and state (**x**) vectors. The yielding linearized equations are gathered into state matrices (**A**, **B**, **C**, and **D**), representing the inverter dynamics, as [70].

$$\underbrace{\frac{d}{dt}\begin{bmatrix} \hat{i}_{Ld} \\ \hat{i}_{Lq} \\ \hat{v}_c \\ 0 \end{bmatrix}}_{\mathbf{x}} = \underbrace{\begin{bmatrix} -\frac{r_L}{L_1} & \omega_g & \frac{D_d}{L_1} & 0 \\ -\omega_g & -\frac{r_L}{L_1} & \frac{D_q}{L_1} & 0 \\ -\frac{3}{2}\frac{D_d}{C} & -\frac{3}{2}\frac{D_q}{C} & 0 & 0 \\ 0 & 0 & 0 & 0 \end{bmatrix}}_{\mathbf{A}} \underbrace{\begin{bmatrix} \hat{i}_{Ld} \\ \hat{i}_{Lq} \\ \hat{v}_c \\ 0 \end{bmatrix}}_{\mathbf{x}} + \underbrace{\begin{bmatrix} 0 & 0 & -\frac{1}{L_1} & 0 & \frac{V_{in}}{L_1} & 0 \\ 0 & 0 & 0 & -\frac{1}{L_1} & 0 & \frac{V_{in}}{L_1} \\ \frac{1}{C} & 0 & 0 & 0 & -\frac{3}{2}\frac{I_{Ld}}{C} & -\frac{3}{2}\frac{I_{Lq}}{C} \\ 0 & 0 & 0 & 0 & 0 & 0 \end{bmatrix}}_{\mathbf{B}} \underbrace{\begin{bmatrix} \hat{i}_{in} \\ 0 \\ \hat{v}_{od} \\ \hat{v}_{oq} \\ \hat{d}_d \\ \hat{d}_q \end{bmatrix}}_{\mathbf{u}}$$

$$\underbrace{\begin{bmatrix} \hat{v}_{in} \\ 0 \\ \hat{i}_{od} \\ \hat{i}_{oq} \end{bmatrix}}_{\mathbf{y}} = \underbrace{\begin{bmatrix} 0 & 0 & 1 & 0 \\ 0 & 0 & 0 & 0 \\ 1 & 0 & 0 & 0 \\ 0 & 1 & 0 & 0 \end{bmatrix}}_{\mathbf{C}} \underbrace{\begin{bmatrix} \hat{i}_{Ld} \\ \hat{i}_{Lq} \\ \hat{v}_c \\ 0 \end{bmatrix}}_{\mathbf{x}} + \underbrace{0}_{\mathbf{D}} \underbrace{\begin{bmatrix} \hat{i}_{in} \\ 0 \\ \hat{v}_{od} \\ \hat{v}_{oq} \\ \hat{d}_d \\ \hat{d}_q \end{bmatrix}}_{\mathbf{u}} \tag{2.18}$$

where uppercase denote the steady-state values. In the Laplace (frequency) domain, the open-loop transfer functions from the input vector to the output vector can be solved as [71]

$$\mathbf{Y}(s) = \left[\mathbf{C}(s\mathbf{I} - \mathbf{A})^{-1}\mathbf{B} + \mathbf{D}\right]\mathbf{U}(s) \tag{2.19}$$

The yielding transfer matrix **G** represents the inverter small-signal dynamics at the steady-state operating point, given as

$$\underbrace{\begin{bmatrix} \hat{v}_{in} \\ 0 \\ \hat{i}_{od} \\ \hat{i}_{oq} \end{bmatrix}}_{\mathbf{Y}} = \underbrace{\begin{bmatrix} Z_{\text{in-o}} & 0 & T_{\text{oid-o}} & T_{\text{oiq-o}} & G_{\text{cid-o}} & G_{\text{ciq-o}} \\ 0 & 0 & 0 & 0 & 0 & 0 \\ G_{\text{iod-o}} & 0 & -Y_{\text{odd-o}} & -Y_{\text{oqd-o}} & G_{\text{codd-o}} & G_{\text{coqd-o}} \\ G_{\text{ioq-o}} & 0 & -Y_{\text{odq-o}} & -Y_{\text{oqq-o}} & G_{\text{codq-o}} & G_{\text{coqq-o}} \end{bmatrix}}_{\mathbf{G}} \underbrace{\begin{bmatrix} \hat{i}_{in} \\ 0 \\ \hat{v}_{od} \\ \hat{v}_{oq} \\ \hat{d}_{d} \\ \hat{d}_{q} \end{bmatrix}}_{\mathbf{U}} \tag{2.20}$$

To simplify further analysis, the DQ domain transfer functions appearing in **G** are grouped as 2 x 2 matrices

$$\mathbf{Z}_{\text{in-o}} = \begin{bmatrix} Z_{\text{in-o}} & 0 \\ 0 & 0 \end{bmatrix}, \mathbf{T}_{\text{oi-o}} = \begin{bmatrix} T_{\text{oid-o}} & T_{\text{oiq-o}} \\ 0 & 0 \end{bmatrix}, \mathbf{G}_{\text{ci-o}} = \begin{bmatrix} G_{\text{cid-o}} & G_{\text{ciq-o}} \\ 0 & 0 \end{bmatrix}$$

$$\mathbf{G}_{\text{io-o}} = \begin{bmatrix} G_{\text{iod-o}} & 0 \\ G_{\text{ioq-o}} & 0 \end{bmatrix}, \mathbf{Y}_{\text{o-o}} = \begin{bmatrix} Y_{\text{odd-o}} & Y_{\text{oqd-o}} \\ Y_{\text{odq-o}} & Y_{\text{oqq-o}} \end{bmatrix}, \mathbf{G}_{\text{co-o}} = \begin{bmatrix} G_{\text{codd-o}} & G_{\text{coqd-o}} \\ G_{\text{codq-o}} & G_{\text{coqq-o}} \end{bmatrix}$$

Closed-Loop Output Admittance Model

In this section, the control loops are closed and the multivariable inverter output admittance at the closed loop is presented with the linearized transfer functions. The grid-connected inverter, which connects renewable energy to the grid, usually utilizes a cascaded control system [15]. Fig. 2.4 shows such a control structure, implemented in the DQ domain. The inner control loop regulates the AC currents and provides the duty cycles for the inverter switching. The d and q components are coupled through reactance within the feedback loop. Therefore components of the inverter output current couple through the AC-side filter, which can be mitigated by applying decoupling gains. In the renewable-energy applications, the DC voltage must be controlled in order to achieve the maximum power point of the renewable source [72]. Therefore, the outer loop of the cascaded control system controls the DC voltage. The DC voltage control removes the need for an additional DC-DC con-

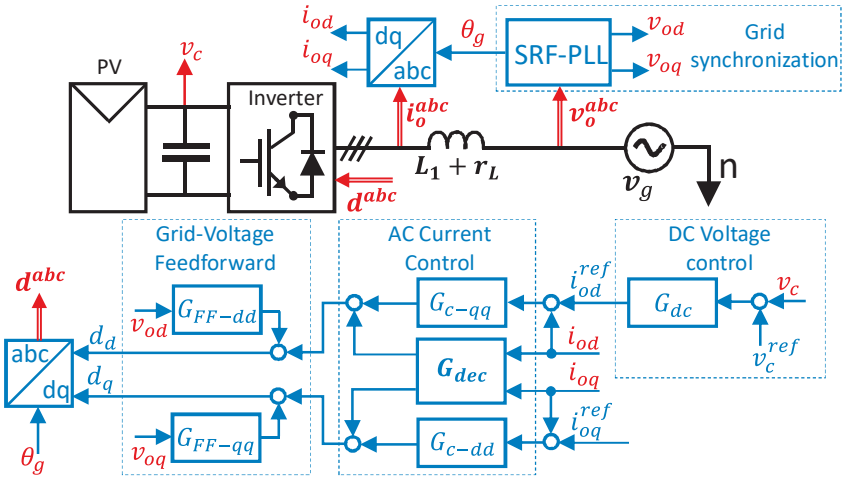

Figure 2.4 Grid-connected inverter utilizing cascaded control system.

verter between the source and the inverter. The inverter control system is synchronized to the grid voltages using a synchronous-reference-frame phase-locked loop (SRF-PLL). Additionally, a grid-voltage feedforward is utilized in order to improve mitigation of the low-order harmonics from the produced currents [73].

The fact that real switches cannot change their state instantaneously must be considered when implementing the pulse-width modulation (PWM) in order to avoid short-circuiting the DC capacitor. Therefore, the switches' turn-on signals are delayed by a few percent of the switching cycle. This is known as dead time. The phenomenon has highly non-linear characteristics and complex dependency of many parameters [74], so it is not included in the linearized inverter model. However, the impact of the dead time to the power quality is considered when the grid-voltage feedforward is adjusted in Section 3.

Fig. 2.5 shows a block diagram, which represents the inverter small-signal behavior when the PLL, grid-voltage feedforward, and the decoupled AC current control loops are closed. The DC voltage control loop is not included, but will be added in the model later.

First the AC current control loop $\mathbf{L}_{cc}$ is closed. The output currents are sensed and fed to the corresponding channels (separate d- and q-channels) through sensing gain, given as

$$\mathbf{H}_{io} = \begin{bmatrix} 1 & 0 \\ 0 & 1 \end{bmatrix} \tag{2.21}$$

The current control $\mathbf{G}_c$ includes separate controllers in the current d- and q-channels. The d-channel controls the active power and reactive power is controlled in the q-channel. However, the current d- and q-components are coupled through the reactance within the feedback loop and characteristics of the control system [75]. In order to mitigate these couplings, the decoupling matrix ($\mathbf{G}_{dec}$) is applied in the current-control. Gains in the decoupling matrix

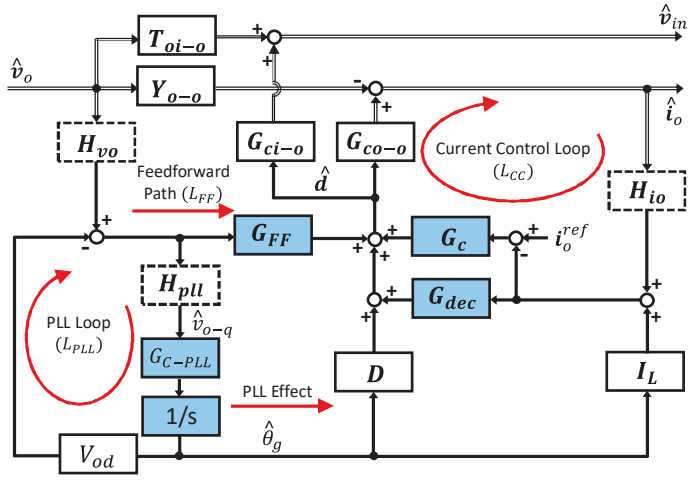

Figure 2.5 Inverter dynamics with PLL, grid-voltage feedforward, and AC current control.

are tuned by (2.16) in order to compensate the effect of i_{Ld} to the i_{Lq}, and opposite. The cross-couplings, caused by the L filter, can be compensated by the decoupling matrix, given as [15]

$$\mathbf{G}_{dec} = \begin{bmatrix} 0 & -\omega_g L_1 / V_{in} \\ \omega_g L_1 / V_{in} & 0 \end{bmatrix} \tag{2.22}$$

The decoupled current-control loop gain (feedback loop not closed yet) can be written as

$$\mathbf{L}_{CC} = \mathbf{G}_{co\text{-}o}(\mathbf{G}_c - \mathbf{G}_{dec})\mathbf{H}_{io} \tag{2.23}$$

By closing the feedback loop, the AC current control loop is formed as

$$\mathbf{G}_{cc} = \mathbf{L}_{CC}(\mathbf{I} + \mathbf{L}_{CC})^{-1} \tag{2.24}$$

Next the SRF-PLL loop is closed, which synchronizes the DQ domain control system with the grid voltages. Thus, the PLL provides the synchronization angle (θ_g) for the DQ transformation of the currents and voltages, and reverse transformation for the duty cycles. The grid voltages are sensed and fed to corresponding channels of the control system as

$$\mathbf{H}_{vo} = \begin{bmatrix} 1 & 0 \\ 0 & 1 \end{bmatrix} \tag{2.25}$$

The SRF-PLL synchronizes the DQ control frame to the grid voltages (grid reference frame) by regulating the sensed output voltage q component to zero. Therefore, only the voltage q

component is sensed for the PLL as

$$\mathbf{H}_{\text{PLL}} = \begin{bmatrix} 0 & 0 \\ 0 & 1 \end{bmatrix} \tag{2.26}$$

The internal controller of the PLL ($G_{\text{c-PLL}}$) and the plant ($V_{\text{od}}(s)^{-1}$) are scalar transfer functions, as only the voltage q component is regulated. The PLL loop gain can be given as [70]

$$\mathbf{L}_{\text{PLL}} = V_{\text{od}}(s)^{-1} G_{\text{c-PLL}} \mathbf{H}_{\text{PLL}} \tag{2.27}$$

where V_{od} is the steady-state value of the grid-voltage d component. The PLL loop is formed as

$$\mathbf{T}_{\text{PLL}} = (V_{\text{od}})^{-1} \mathbf{L}_{\text{PLL}} (\mathbf{I} + \mathbf{L}_{\text{PLL}})^{-1} \tag{2.28}$$

the input of which is the grid voltages and output is the synchronization angle θ_{g}. The small-signal variation in the synchronization angle affect the DQ domain control system. The small-signal angle can be written as [76]

$$\hat{\theta}_{\text{g}} = \mathbf{T}_{\text{PLL}} \hat{v}_{\text{oq}} \tag{2.29}$$

As the three-phase variables in the DQ domain are presented by two DC-valued signals that are orthogonal to each other, the small variations in the synchronization angle (a small errors in DQ transformation) cause coupling between the d and q components. The small variations in the synchronization angle affect the inverter currents and duty cycles through the steady-state values, as

$$\mathbf{D} = \begin{bmatrix} 0 & -D_{\text{q}} \\ 0 & D_{\text{d}} \end{bmatrix} \tag{2.30}$$

$$\mathbf{I}_{\text{L}} = \begin{bmatrix} 0 & I_{\text{Lq}} \\ 0 & -I_{\text{Ld}} \end{bmatrix} \tag{2.31}$$

This increases the coupling between the d and q channels. The complete effect of the PLL to dynamics of the inverter innermost control loop (the current-control loop) can be given as a transfer matrix

$$\mathbf{G}_{\text{PLL}} = [\mathbf{L}_{\text{cc}} \mathbf{I}_{\text{L}} - \mathbf{G}_{\text{co-o}} \mathbf{D}] \mathbf{T}_{\text{PLL}} \tag{2.32}$$

Next, the grid-voltage feedforward path is closed. The purpose of the grid-voltage feedforward is to compensate the open-loop output admittance ($\mathbf{Y}_{\text{o-o}}$) [77]. The feedforward path is implemented by scaling the sensed grid voltages by appropriate feedforward gains ($K_{\text{FF-dd}}$ and $K_{\text{FF-qq}}$) and adding the scaled signals to the duty ratios from the current control. The

feedforward gains are included in the transfer matrix as [73]

$$\mathbf{G}_{\text{FF}} = \begin{bmatrix} K_{\text{FF-dd}} & 0 \\ 0 & K_{\text{FF-qq}} \end{bmatrix} \tag{2.33}$$

The closed feedforward path can be written as

$$\mathbf{L}_{\text{FF}} = \mathbf{G}_{\text{co-o}}\mathbf{G}_{\text{FF}}(\mathbf{I}+\mathbf{L}_{\text{PLL}})^{-1}\mathbf{H}_{\text{vo}} \tag{2.34}$$

where the grid voltages are sensed by $\mathbf{H}_{\text{vo}}$ and the PLL affect the voltage q component.

At this point, each loop shown in Fig. 2.5 is closed and corresponding transfer matrices are modeled. In order to clarify the further modeling, the previously modeled transfer matrices are gathered into the four auxiliary closed-loop transfer matrices that include the SRF-PLL, the current-control loop, and the grid-voltage feedforward path. The closed-loop transfer matrix from $\hat{v}_{\text{o}}$ to $\hat{i}_{\text{o}}$ can be given as

$$\mathbf{Y}_{\text{o}}^{\text{cc}} = (\mathbf{I}+\mathbf{L}_{\text{CC}})^{-1}(\mathbf{Y}_{\text{o-o}} - \mathbf{L}_{\text{FF}} - \mathbf{G}_{\text{PLL}}) \tag{2.35}$$

From the AC current reference ($\hat{i}_{\text{o}}^{ref}$) to $\hat{i}_{\text{o}}$ is given as

$$\mathbf{G}_{\text{ro}}^{\text{cc}} = (\mathbf{I}+\mathbf{L}_{\text{CC}})^{-1}\mathbf{G}_{\text{co-o}}\mathbf{G}_{\text{c-out}} \tag{2.36}$$

From $\hat{v}_{\text{o}}$ to $\hat{v}_{\text{in}}$ is

$$\mathbf{T}_{\text{oi}}^{\text{cc}} = \mathbf{T}_{\text{io-o}} + \mathbf{G}_{\text{ci-o}}\mathbf{G}_{\text{co-o}}^{-1}(\mathbf{G}_{\text{cc}}(\mathbf{Y}_{\text{o-o}}+\mathbf{G}_{\text{PLL}}) - \mathbf{G}_{\text{PLL}}) \tag{2.37}$$

and from $\hat{i}_{\text{o}}^{ref}$ to $\hat{v}_{\text{in}}$ is

$$\mathbf{G}_{\text{ri}}^{\text{cc}} = \mathbf{G}_{\text{ci-o}}(\mathbf{G}_{\text{co-o}})^{-1}(\mathbf{I}-\mathbf{G}_{\text{cc}})\mathbf{L}_{\text{cc}}(\mathbf{H}_{\text{io}})^{-1} \tag{2.38}$$

Fig. 2.6 shows the AC-side dynamics of the inverter, when the DC voltage control loop is closed and the auxiliary closed-loop transfer matrices (2.35-2.38) are applied. The DC voltage control adjusts the current reference for the output current d-component, and the current q-component is regulated to zero as intentional production of reactive power is not considered in this thesis. The DC voltage is sensed and fed to the d-channel of the control system through sensing gain, given as

$$\mathbf{H}_{\text{in}} = \begin{bmatrix} 1 & 0 \\ 0 & 0 \end{bmatrix} \tag{2.39}$$

Therefore, the DC voltage controller G_{dc} affects directly only the d-component. The DC

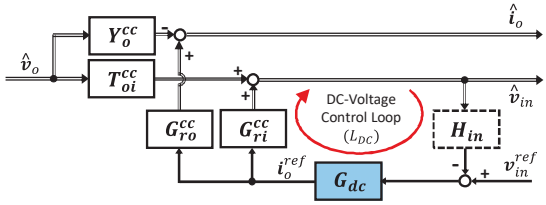

Figure 2.6 Inverter dynamics with DC voltage control included.

voltage control loop gain can be given as

$$\mathbf{L}_{\mathrm{DC}} = \mathbf{G}_{\mathrm{ri}}^{\mathrm{cc}} G_{\mathrm{dc}} \mathbf{H}_{\mathrm{in}} \tag{2.40}$$

Finally, all the applied control loops of the cascaded control system are closed. The complete DQ domain inverter output admittance can be solved from Fig. 2.6 as transfer matrix from $\hat{v}_{\mathrm{o}}$ to $\hat{i}_{\mathrm{o}}$, and given as [73]

$$\mathbf{Y}_{\mathrm{o}} = \mathbf{Y}_{\mathrm{o}}^{\mathrm{cc}} + \mathbf{G}_{\mathrm{ro}}^{\mathrm{cc}} \mathbf{G}_{\mathrm{dc}} \mathbf{H}_{\mathrm{in}} (\mathbf{I} + \mathbf{L}_{\mathrm{DC}})^{-1} \mathbf{T}_{\mathrm{oi}}^{\mathrm{cc}} \tag{2.41}$$

The PLL transfer matrix (2.32) is included to $\mathbf{Y}_{\mathrm{o}}^{\mathrm{cc}}$ and $\mathbf{T}_{\mathrm{oi}}^{\mathrm{cc}}$. The grid-voltage feedforward affects the $\mathbf{Y}_{\mathrm{o}}^{\mathrm{cc}}$. The current-control loop acts as the innermost loop, and thus, affects all closed-loop transfer matrices related to the inverter output current and, consequently, the output admittance. Additionally, when the switching frequency f_{sw} of the modeled inverter is defined, the unity sensing gains and PWM are replaced by a third-order Pade approximation of the time delay ($T_{\mathrm{d}} = 1.5/f_{\mathrm{sw}}$). Alternatively, control delays and effect of the discrete data sampling, synchronized with the PWM, can be accurately taken into account by applying discrete-time modeling methods [78]. However, analysis of the grid-connected systems in this thesis is based on the presented continuous-time methods.

The presented small-signal model of the grid-connected inverter can be applied in the impedance-based stability analysis, but also in design process of the inverter control system. Each loop of the cascaded control system is included in the inverter model with a transfer function that makes it possible to tune the control parameters properly and to observe impact of the different parameters in various operating conditions. Therefore, the control indicators, such as bandwidth and phase margins, can be observed and properly adjusted by applying the presented small-signal model.

2.4 Load-Affected Model

As the inverter is connected to the real grid, the grid impedance is present and results in a load effect. The load effect appears as the output current affects the grid voltage through the grid impedance ($\mathbf{Z}_{\mathrm{g}}$). Consequently, the grid voltage affects the currents through the inverter

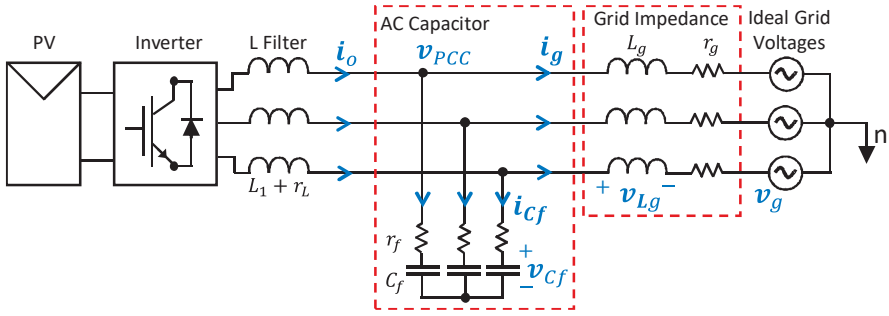

Figure 2.7 Inverter connected to grid with impedance.

output admittance ($\mathbf{Y}_{o\text{-}o}$). As a combination of these two effects, an additional term appears in the inverter transfer functions. This term resembles a feedback loop and can be written as $\left[\mathbf{I}+\mathbf{Y}_{o\text{-}o}\mathbf{Z}_g\right]^{-1}$. A similar transfer function is analyzed in the impedance-based stability and sensitivity analysis [22].

The load-affected modeling becomes a practical option for assessing the system stability and predicting its control performance, as effect of the load can be added to the system open-loop transfer functions. For example, the load-affected transfer function from the duty ratios to the output current ($\mathbf{G}_{co\text{-}o}$) can be written as [21]

$$\mathbf{G}^{L}_{co\text{-}o} = \mathbf{G}_{co\text{-}o}\left[\mathbf{I}+\mathbf{Y}_{o\text{-}o}\mathbf{Z}_g\right]^{-1} \tag{2.42}$$

Grid-Side Impedance

The main challenge in assessing the impedance-based stability is the fact that the grid characteristics can be complex and time-varying [79], which means that generalized models cannot be usually presented. Therefore in this thesis, the real-time measurements of the grid impedance will be applied to assess the stability and to remove the need for modeling the grid. However, a small-signal model of the grid impedance model becomes practical in analytical studies of the load-affected inverter performance and stability under certain grid conditions. Additionally, AC-side filters can be added into the model and properly designed. Therefore, this section briefly presents a simple grid impedance model that includes inductive/resistive components and impedance of the AC filter with capacitor.

Fig. 2.7 shows an inverter, connected through an LC filter to the inductive grid impedance. The inverter itself is modeled with the L filter. Therefore, for the impedance-based stability analysis, the filter capacitor is considered as part of the grid impedance. The grid inductance (L_g) can be considered to also include the grid-side inductor (L_2) if an LCL filter is applied.

A linearized small-signal model of the grid is produced by applying the similar state-space analysis as performed for the inverter. The input variables are defined as inverter output currents and the grid voltages. The output variables of the model are the PCC voltages

and the current flowing to the grid. The grid-side inductor currents and the filter capacitor voltages are applied as state variables. The linearized state-space model can be given as [69].

$$\frac{d}{dt}\begin{bmatrix}\hat{i}_{\text{Lg-d}}\\ \hat{i}_{\text{Lg-q}}\\ \hat{v}_{\text{Cf-d}}\\ \hat{v}_{\text{Cf-q}}\end{bmatrix}=\begin{bmatrix}-\frac{(r_\text{f}+r_\text{g})}{L_\text{g}} & \omega_g & \frac{1}{L_\text{g}} & 0\\ -\omega_g & -\frac{(r_\text{f}+r_\text{g})}{L_\text{g}} & 0 & \frac{1}{L_\text{g}}\\ -\frac{1}{C_\text{f}} & 0 & 0 & \omega_g\\ 0 & -\frac{1}{C_\text{f}} & -\omega_g & 0\end{bmatrix}\begin{bmatrix}\hat{i}_{\text{Lg-d}}\\ \hat{i}_{\text{Lg-q}}\\ \hat{v}_{\text{Cf-d}}\\ \hat{v}_{\text{Cf-q}}\end{bmatrix}+\begin{bmatrix}\frac{r_\text{f}}{L_\text{g}} & 0 & -\frac{1}{L_\text{g}} & 0\\ 0 & \frac{r_\text{f}}{L_\text{g}} & 0 & -\frac{1}{L_1}\\ \frac{1}{C_\text{f}} & 0 & 0 & 0\\ 0 & \frac{1}{C_\text{f}} & 0 & 0\end{bmatrix}\begin{bmatrix}\hat{i}_{\text{od}}\\ \hat{i}_{\text{oq}}\\ \hat{v}_{\text{g-d}}\\ \hat{v}_{\text{g-q}}\end{bmatrix}$$

$$\begin{bmatrix}\hat{v}_{\text{PCC-d}}\\ \hat{v}_{\text{PCC-d}}\\ \hat{i}_{\text{g-d}}\\ \hat{i}_{\text{g-q}}\end{bmatrix}=\begin{bmatrix}-r_\text{f} & 0 & 1 & 0\\ 0 & -r_\text{f} & 0 & 1\\ 1 & 0 & 0 & 0\\ 0 & 1 & 0 & 0\end{bmatrix}\begin{bmatrix}\hat{i}_{\text{Lg-d}}\\ \hat{i}_{\text{Lg-q}}\\ \hat{v}_{\text{Cf-d}}\\ \hat{v}_{\text{Cf-q}}\end{bmatrix}+\begin{bmatrix}r_\text{f} & 0 & 0 & 0\\ 0 & r_\text{f} & 0 & 0\\ 0 & 0 & 0 & 0\\ 0 & 0 & 0 & 0\end{bmatrix}\begin{bmatrix}\hat{i}_{\text{od}}\\ \hat{i}_{\text{oq}}\\ \hat{v}_{\text{g-d}}\\ \hat{v}_{\text{g-q}}\end{bmatrix} \tag{2.43}$$

The impedance dynamics are gathered into the matrix by applying (2.19) and can be written as

$$\begin{bmatrix}\hat{v}_{\text{PCC-d}}\\ \hat{v}_{\text{PCC-d}}\\ \hat{i}_{\text{g-d}}\\ \hat{i}_{\text{g-q}}\end{bmatrix}=\begin{bmatrix}Z_{\text{g-dd}} & Z_{\text{g-qd}} & T_{\text{g-dd}} & T_{\text{g-qd}}\\ Z_{\text{g-dq}} & Z_{\text{g-qq}} & T_{\text{g-dq}} & T_{\text{g-qq}}\\ G_{\text{g-dd}} & G_{\text{g-qd}} & -Y_{\text{g-dd}} & -Y_{\text{g-qd}}\\ G_{\text{g-dq}} & G_{\text{g-qq}} & -Y_{\text{g-dq}} & -Y_{\text{g-qq}}\end{bmatrix}\begin{bmatrix}\hat{i}_{\text{od}}\\ \hat{i}_{\text{oq}}\\ \hat{v}_{\text{g-d}}\\ \hat{v}_{\text{g-q}}\end{bmatrix} \tag{2.44}$$

where the transfer functions from inverter output currents ($\hat{i}_{\text{od}}$ and $\hat{i}_{\text{oq}}$) to the PCC voltages ($\hat{v}_{\text{PCC-d}}$ and $\hat{v}_{\text{PCC-q}}$) are components of the DQ domain grid impedance ($\mathbf{Z}_\text{g}$), seen by the inverter. Typically, the filter parameters (L_2, C_f, and r_f) are known, but the grid impedance (L_g and r_g) remains unknown and varies over time. However, this simple model can be used to analyze the dynamics of common AC filters and include the grid impedance into the load-affected models.

AC Filter

A parallel capacitor is usually added to the AC filter in order to mitigate high-frequency distortions caused by inverter switching [80]. The most common topologies are the LC and LCL filters, where the inverter-side inductor (L_1), the AC capacitor (C_f), damping resistor (r_f), and the possible grid-side inductor (L_2) are known by the design process. However, as the inverter is connected to the grid, the grid impedance is present and affects the filter characteristics. As the grid impedance is usually mainly inductive, the grid-side inductance is increased. Additionally, the LC filter and the interfaced grid inductance (L_g) form an LCL

circuit. Thus, the properties of the AC filters depend on the grid impedance.

The resonant pole of the LCL filter (without damping) appears at

$$\omega_{\text{p-LCL}} = \sqrt{\frac{L_1 + L_g}{C_i L_1 L_g}} \tag{2.45}$$

where L_g is usually unknown. The value of L_g depends on the connection point and may vary over time. In general, increasing grid inductance decreases the frequency of the pole. The pole appears as a resonant peak and is usually designed to locate at significantly higher frequencies than the control bandwidths. In high frequencies, the control delays usually decreases the phase of the inverter output impedance so that the passivity is lost (phase below -90 degrees) [81]. Therefore, the impedance-based interactions between the inverter and the grid may be triggered by resonance of the LCL filter. The stability issues may occur especially in weak grids, where the grid inductance has a significant effect on the resonant pole of the LCL filter. Therefore, the impedance-based stability must also be assessed at significantly higher frequencies than the control bandwidths.

2.5 Discussion

This chapter has presented background information on the analysis of grid-connected systems, upon which the proposed methods in this thesis are based. Fig. 2.8 shows a grid-connected three-phase inverter and role of the methods, presented in this chapter. In this thesis, the analysis, modeling, and measurements of grid-connected systems are performed in the DQ domain. System stability is assessed by the impedance-based stability analysis and the stability margins are assessed by the system sensitivity function. Although the thesis does not provide novel methods or significant improvements into modeling of the grid-connected power electronics, small-signal modeling of the three-phase grid-connected

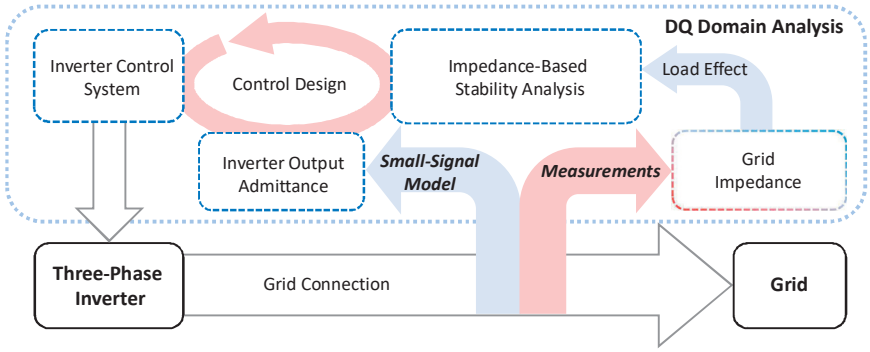

Figure 2.8 Grid-connected three-phase inverter.

inverter has been introduced in this chapter. The accurate small-signal model will be applied in the impedance-based stability analysis of the grid-connected systems and to design the inverter control system. In the design process, the control parameters can be appropriately adjusted by observing their impacts on the small-signal model. Additionally, the system stability and performance in various grid conditions with different control parameters can be predicted by applying the load-affected inverter models. Consequently, the background information and modeling methods presented in this chapter are required in the following sections, where the adaptive control system is designed for the grid-connected three-phase inverter, and impedance-based stability of the grid-connected system is considered by the real-time grid-impedance measurements.

3 METHODS

This chapter is divided into two sections. The first section presents methods for real-time measurements of the grid-connected systems and the second section proposes multiple methods for adaptive control of the grid-connected inverters.

Non-parametric methods for obtaining frequency-response measurements of the grid-connected systems are reviewed in this chapter. The methods are based on the pseudo-random binary sequences and Fourier techniques. The special characteristics of the grid-connected systems are considered and suitable design process for online measurements is proposed.

The second section discusses the control-design process for the SRF-PLL, the current-control loop with its auxiliary functions, and the DC voltage control. Additionally, the adaptive-control methods are proposed for different control loops. The adaptive control strategies are based on the inverter small-signal model and the identified characteristics of the interfaced grid conditions.

3.1 Real-Time Analysis of Grid-Connected Systems

Grid-connected systems can usually be considered as linear time-invariant (LTI) systems for small signal variations [57]. According to control theory, a LTI system can be characterized in the time domain by its impulse responses and in the frequency domain by a frequency response. The frequency response is the Fourier transform of the impulse response [29].

Fig. 3.1 shows a general setup for measuring a frequency response of the plant ($g(t)$). The input signal of the plant is perturbed by a device whose actuator follows a generated excitation sequence ($r(t)$). In order to obtain the frequency response of the plant, the input ($u_1(t)$) and output ($y_1(t)$) signals are measured during the perturbations. However, the input and output signals are corrupted by external distortions ($n_u(t)$ and $n_y(t)$) that include white noise and other distortions arising from the system characteristics. Therefore, the measured input and output signals can be given as

$$\begin{aligned} u_1(t) &= u(t) + n_u(t) \\ y_1(t) &= y(t) + n_y(t) \end{aligned} \tag{3.1}$$

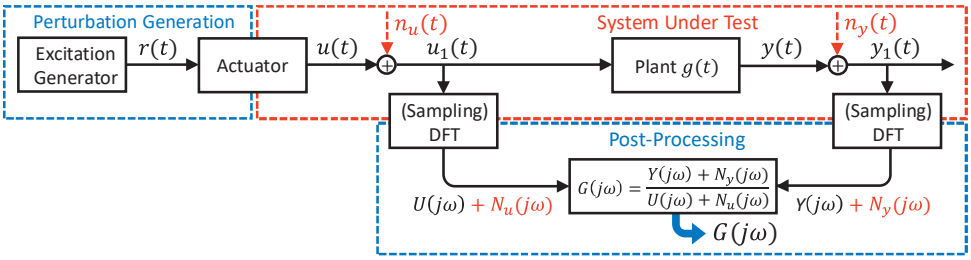

Figure 3.1 General measurement setup.

where $u(t)$ and $y(t)$ are considered as disturbance-free input and output signals, respectively. The measured signals are transformed to the frequency domain by a discrete Fourier transform (DFT) and the frequency response ($G(j\omega)$) between signals is computed as [31]

$$G(j\omega) = \frac{Y(j\omega) + N_y(j\omega)}{U(j\omega) + N_u(j\omega)} \tag{3.2}$$

where $U(j\omega)$, $Y(j\omega)$, $N_u(j\omega)$ and $N_y(j\omega)$ denote Fourier-transformed input and output signals, and the corresponding distortions, respectively.

3.1.1 Pseudo-Random Binary Sequences

Pseudo-random binary sequences (PRBS) have become popular excitation signals in frequency-response measurements of grid-connected systems. The PRBS is a broadband signal with which the frequency response can be measured at multiple frequencies simultaneously. The binary signals have the lowest possible crest factor among all signals, which means that the signal's total energy is very high in relation to its time-domain amplitude [31]. This makes it possible to minimize the system interference during the measurements. Additionally, due to binary form of the PRBS, it is also easy to generate with low-cost devices that can cope with limited signal levels.

Maximum-length binary sequence (MLBS) is the most common form of the PRBS. The MLBS is a periodic excitation signal, which appears at certain sequence lengths $N_{\text{MLBS}} = 2^n - 1$, where n is an integer [82]. The MLBS is easy to generate by an n-bit shift register and XOR-feedback [32], which yields a periodic binary sequence varying between values 0 and 1. In order to produce symmetrical perturbation with an average close to zero, the binary values are mapped as A and $-A$, corresponding to the time-domain amplitude.

The spectrum of the MLBS is linearly spaced with a constant frequency resolution of $f_{\text{res}} = f_{\text{gen}}/N_{\text{MLBS}}$, where f_{gen} is the signal generation frequency. The power spectrum of the continuous MLBS can be written as [31]

$$\Phi_{\text{MLBS}}(q) = A^2 \frac{N_{\text{MLBS}} + 1}{N_{\text{MLBS}}^2} \frac{\sin^2(\pi q/N_{\text{MLBS}})}{(\pi q/N_{\text{MLBS}})^2} \tag{3.3}$$

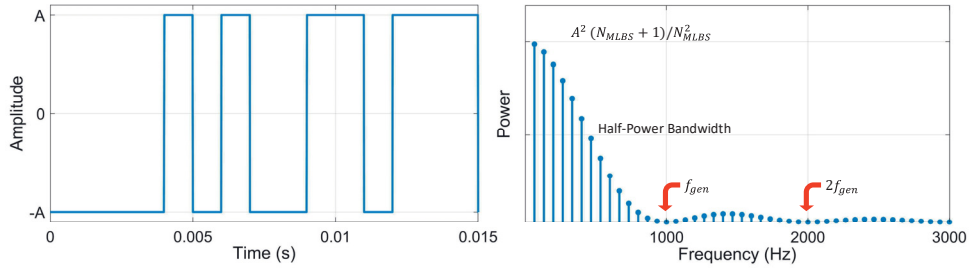

Figure 3.2 MLBS in time domain its power spectrum in frequency domain.

where q is integer that represents index for a spectral line (harmonic). The power spectrum follows $\mathrm{sinc}^2(q) = \sin^2(q)/q^2$ function, whose absolute values are determined by the MLBS amplitude A and length N_{MLBS} [83].

Fig. 3.2 shows an example of MLBS, where $N_{\mathrm{MLBS}} = 15$ ($n = 4$) and $f_{\mathrm{gen}} = 1$ kHz. The power of the MLBS drops to zero at generation frequency f_{gen} and its multipliers. The half-power bandwidth of sinc^2 function is usually applied as measurable bandwidth for the given MLBS, which lies approximately at $f_{\mathrm{m}} \approx 0.44 f_{\mathrm{gen}}$. The measurement time for a single MLBS period can be defined by generation frequency and sequence length as

$$T_{\mathrm{MLBS}} = \frac{N_{\mathrm{MLBS}}}{f_{\mathrm{gen}}} = \frac{1}{f_{\mathrm{res}}} \tag{3.4}$$

The MLBS is a deterministic signal that enables multiple repeated sequences to be injected and the obtained results to be averaged. Averaging increases the measurement time proportionally to the number (P) of averaged (repeated) periods [84].

3.1.2 Identification of Multi-Input Multi-Output Systems

A general multivariable or multi-input multi-output (MIMO) system includes n inputs and m outputs. Therefore, the system to be identified is an n x m transfer matrix. The simplest way of identifying such a system is to perturb system inputs (n) one at time and to measure the responses at all system outputs (m) in turn [53]. This must be performed for each input-output combination, which may become time-consuming when the number of inputs increases. Additionally, the operating conditions may vary between sequential measurements. An alternative to sequential measurements is to simultaneously measure all the system input-output combinations (components) by applying uncorrelated sequences [85]. The uncorrelated sequences have energy at different frequencies, which means that several frequency responses can be measured simultaneously during a single measurement cycle. This technique saves time compared to the sequential approach and allows the frequency responses to be measured under the same operating conditions [P1].

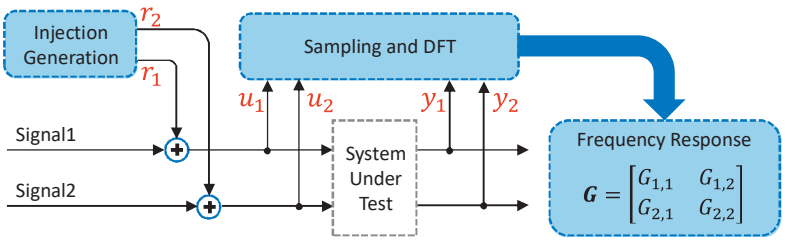

Figure 3.3 Typical setup for MIMO measurements.

Fig. 3.3 depicts a typical frequency response measurement setup for MIMO identification. The system under test is a 2 x 2 matrix that has two inputs and two outputs, from which each input signal is coupled to both outputs. In the setup, two system signals are perturbed by separate injections (r_1 and r_2), the system responses are measured, and the frequency response is calculated as a ratio between responses using Fourier methods. In order to measure the frequency responses of such a MIMO system, the sequential measurement approach using the conventional MLBS requires at least two separate measurements. The identification can be performed as simultaneous measurements by applying uncorrelated sequences r_1 and r_2 that perturb different frequencies $j\omega_1$ and $j\omega_2$, respectively [P1]. Perturbing the first input signal (u_1) with $r_1(j\omega_1)$ causes a response in both output signals y_1 and y_2 at $j\omega_1$. This makes it possible to calculate frequency responses $G_{1,1}(j\omega_1)$ and $G_{2,1}(j\omega_1)$. Correspondingly, the second input signal (u_2) is perturbed at $j\omega_2$, which also results in a response in both output signals, but at different frequency $j\omega_2$. This makes it possible to calculate the frequency response of $G_{1,2}(j\omega_2)$ and $G_{2,2}(j\omega_2)$. Therefore, the measured MIMO transfer matrix can be written as

$$\begin{bmatrix} y_1(j\omega_{1,2}) \\ y_2(j\omega_{1,2}) \end{bmatrix} = \underbrace{\begin{bmatrix} G_{1,1}(j\omega_1) & G_{1,2}(j\omega_2) \\ G_{2,1}(j\omega_1) & G_{2,2}(j\omega_2) \end{bmatrix}}_{\mathbf{G}(j\omega_{1,2})} \begin{bmatrix} u_1(j\omega_1) \\ u_2(j\omega_2) \end{bmatrix} \tag{3.5}$$

where columns of $\mathbf{G}(j\omega_{1,2})$ are identified at different frequencies, determined by the applied uncorrelated perturbations $r_1(j\omega_1)$ and $r_2(j\omega_2)$ [P3].

The uncorrelated sequences can be produced from conventional MLBS by applying a Hadamard modulation [85]. The technique is based on modulating original MLBS with rows of a Hadamard matrix, which is a 2^M x 2^M matrix, where M denotes the number of required uncorrelated sequences. A general Hadamard matrix can be given as

$$\mathbf{H}_M = \begin{bmatrix} H_{M-1} & H_{M-1} \\ H_{M-1} & -H_{M-1} \end{bmatrix} \tag{3.6}$$

where the first-order ($M = 1$) matrix is $H_1 = [1]$ and higher-order matrices can be produced recursively. For generating two uncorrelated sequences ($M = 2$), the Hadamard matrix can be given as

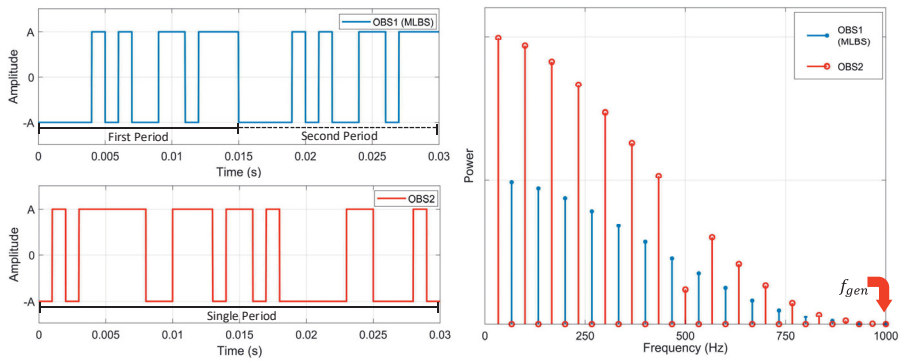

Figure 3.4 OBS1 (MLBS) and OBS2 in time domain and their power spectra in frequency domain.

$$\mathbf{H}_2 = \begin{bmatrix} H_1 & H_1 \\ H_1 & -H_1 \end{bmatrix} = \begin{bmatrix} 1 & 1 \\ 1 & -1 \end{bmatrix} \tag{3.7}$$

The length of the modulating sequence doubles after each increase in number of generated uncorrelated sequences. As a result, the sequence length of the i^{th} orthogonal sequence is doubled compared to the length of the $(i-1)^{\text{th}}$ sequence. Due to the inverse-repeating property of the Hadamard modulation, the even-order harmonics of each uncorrelated sequence are mitigated to zero. Mitigation of the even-order harmonics provides uncorrelated characteristics of the sequences, because those even-order harmonics are included in the spectrum of the other sequences [85].

Fig. 3.4 shows an example of two orthogonal sequences obtained by the Hadamard modulation. Both sequences are generated at 1 kHz with equal time-domain amplitudes. The first sequence (OBS1) is a conventional 15-bit-long MLBS and the second sequence (OBS2) is obtained by modulating the original MLBS with rows of the Hadamard ($\mathbf{H}_2$) matrix, which is equivalent to inverting every other digit [86]. The resulting second sequence is orthogonal with respect to the original MLBS and has inverse-repeated characteristics; that is, the even-order harmonics are mitigated. Fig. 3.4 shows the power spectra of the orthogonal sequences, including a 15-bit-long OBS1 (blue) and corresponding OBS2 (red). The power spectrum of both orthogonal sequences follows the sinc^2 function in which the power drops to zero at the generation frequency [85]. The frequency resolution of two orthogonal sequences equals to each other, but the lowest frequency of OBS2 is halved compared to OBS1. As a result, the sequences have different frequencies over the spectrum. As the sequence length and amplitude define the energy content of the binary signal, the power of the double length OBS2 is approximately doubled at certain harmonics compared to single period of the OBS1. However, this is compensated over the common period of the orthogonal binary sequences, as two periods of the OBS1 can be repeated during a single period of the OBS2 [P1].

3.1.3 Accuracy of Frequency-Response Measurements

The accuracy of the frequency-response measurements can be assessed, for example, by variance σ^2, where σ denotes variation around the expected value of variable. Higher variance indicates increased variability between consecutive measurements and errors around the expected value. As the frequency response is a ratio between the input and the output signals ($G(j\omega) = Y(j\omega)/U(j\omega)$), variance of the frequency-response measurements can be considered as a combination of variations in the signals $Y(j\omega)$ and $U(j\omega)$ [29].

Considering the measured responses (3.1), the system distortions are always present and cause steady-state variation in measured input and output signals. By increasing the perturbation amplitude A, the proportion of the system distortions is reduced in the measured responses ($u_1(t)$ and $y_1(t)$). The signal-to-noise ratio (SNR) is defined as a power ratio between the desired signal and the system distortions, as

$$SNR = \frac{P_\mathrm{r}}{P_\mathrm{d}} = \left(\frac{A_\mathrm{r}}{A_\mathrm{d}}\right)^2 \tag{3.8}$$

where P_r and P_d are power of the response and distortions, respectively. This can also be given by the ratio of squared amplitudes (A_r and A_d). If the system noise level remains constant, doubling the excitation amplitude increases the SNR by a factor of four. The measurement variance is inversely proportional to the SNR, so higher perturbation amplitude increases the measurement SNR and mitigates variance between the consecutive frequency-response measurements. It should be noted that the output signal depends on magnification of the system under test ($Y(j\omega) = G(j\omega)U(j\omega)$). Therefore, the transfer functions with a significant attenuation produces low output SNR, even for high perturbation amplitudes, which makes them more difficult to measure [87].

Periodic excitations allow the measured data to be averaged over multiple repeated periods (P). By averaging measurements over P periods, the impact of the non-periodic disturbances can be reduced. This decreases the variance of the measured frequency response, which can be written as [29].

$$\sigma^2 = \frac{1}{P}\sum_{p=1}^{P} |G_\mathrm{Exp}(j\omega) - G_\mathrm{p}(j\omega)|^2 = \frac{1}{P}\sum_{p=1}^{P} \left[Y_\mathrm{Exp}(j\omega) - Y_\mathrm{p}(j\omega)\right]\left[\overline{U}_\mathrm{Exp}(j\omega) - \overline{U}_\mathrm{p}(j\omega)\right] \tag{3.9}$$

where subscript p denotes order of the periods and Exp denotes the expected (reference) value. Therefore, the variance is proportional to the inverse number of averaged periods, assuming that all periods are measured in steady-state conditions without transients.

In conclusion, measurement accuracy depends on system disturbances, perturbation design, and magnification of the measured system. Accuracy can be evaluated by the measurement variance, which is inversely proportional to the SNR. Dependency of the measurement

variance to the SNR value, and adjustable perturbation amplitude A and averaged periods P, can be written as

$$\sigma^2 \sim \frac{1}{SNR} \sim \frac{1}{A^2} \quad \text{and} \quad \frac{1}{P} \tag{3.10}$$

3.1.4 Injection Design for Grid-Connected Systems

The design of the injection required for the frequency-response measurement of a grid-connected system can be divided into two parts. In the first part, the following specification variables are defined:

- Measurable bandwidth (f_{m})
- Frequency resolution (f_{res})
- Measurement time (T_{meas})
- Measurement quality, approximated by variance (σ^2) or SNR
- Impact of the perturbation to the grid currents and voltages, for example, by produced total-harmonic distortion (THD)

In the second part, the injection parameters are adjusted so that the desired specification parameters are satisfied. The design parameters for the MLBS-based frequency-response measurements can be given as:

- Generation frequency (f_{gen})
- Sequence length (N_{MLBS})
- Perturbation amplitude (A)
- Number of averaged periods (P)

The spectral properties of the MLBS mainly depend on the sequence length and generation frequency. The generation frequency determines the measurable frequency band ($\approx 0.44 f_{\mathrm{gen}}$). Thus, the generation frequency must be set high enough to obtain accurate measurements from a wide enough frequency band. If an unnecessarily high generation frequency is applied, a greater amount of the MLBS energy will be injected to frequencies out of the interesting frequency band. The sequence length must be adjusted so that both the frequency resolution and the lowest measured frequency ($f_{\mathrm{res}} = f_{\mathrm{min}} = f_{\mathrm{gen}}/N_{\mathrm{MLBS}}$) are satisfied. The measurement time is proportional to the sequence length. As the MLBS exist in relatively limited lengths ($N_{\mathrm{MLBS}} = 2^n - 1$), the use of longer sequences must be carefully considered because it significantly increases the measurement time [77].

In general frequency-response measurements, high SNR is the most desired in order to obtain accurate measurements. The SNR is typically increased by applying higher injection

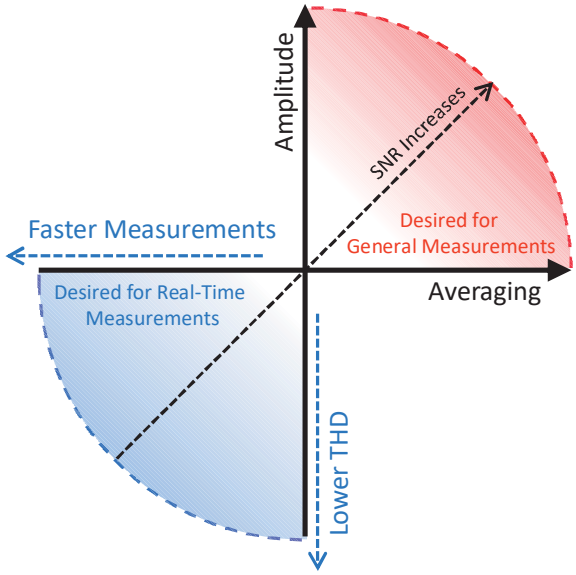

Figure 3.5 Impact of injection amplitude and averaged periods to measurement properties.

amplitude or averaging the measurements over multiple periods as shown in (3.10). However, increasing the injection amplitude or the number of averaged periods causes an unavoidable tradeoff between the measurement accuracy (SNR) and performance of the online measurements or generated distortions of the grid-connected inverter [34]. This is illustrated in Fig. 3.5, where a red sector represents the desired characteristics for the general frequency-response measurements and the blue sector shows the real-time measurements of the grid-connected systems. Increasing SNR by applying higher excitation amplitude causes more distortions (THD) to the grid and averaging over multiple periods increase the measurement time, which is not desirable in real-time measurements [P3]. Therefore, the tradeoff between measurement accuracy and performance of the online measurements system must be considered in the design process [87].

Spectral Leakage

In the frequency-response measurements, the measured signals are transformed into the frequency domain, which is usually performed by the discrete Fourier transform (DFT). The measured signals are sampled at certain time intervals T_s (sampling time) and buffered to time series with a length of $N_{ts} = kT_s$ where k is number of samples. For a given time series $x(kT_s)$, where $k = 0, 1...N_{ts} - 1$, the discrete Fourier transform can be given as

$$X(k) = \frac{1}{\sqrt{N_{ts}}} \sum_{k=o}^{N_{ts}-1} x(kT_s) e^{-j2\pi kT_s/N_{ts}} \tag{3.11}$$

where $X(k)$ is the given time series transformed to the frequency domain. Due to the discrete-time data and use of the DFT, $X(k)$ include frequencies $f(k) = k/(T_s N)$, where $k = 0, 1...N_{ts} - 1$ [88].

The applied perturbation and the DFT must be synchronized so that the discrete spectrum of the DFT (3.11) includes the frequencies that are perturbed, for example, by the MLBS. This is achieved by adjusting the sampling time as $T_s = 1/(b_1 f_{gen})$ where b_1 is an integer, and the length of the buffered time series as $N_{ts} = b_2 N_{MLBS}$ where b_2 is an integer. The lack of frequency synchronism causes perturbation energy to leak other frequencies through the DFT. This is known as spectral leakage and it degrades the measurement accuracy [89].

Periodic system disturbances may also cause spectral leakage through the DFT, if they do not appear at frequencies of the discrete spectrum of the DFT. In the grid-connected systems, the periodic disturbances typically arise from the grid harmonics (harmonics of the fundamental grid frequency f_g). Therefore, the periodic system disturbances can be taken into account in the measurement-design process. The spectral leakage of the grid harmonics can be minimized by designing the measurement setup so that the integer number of the grid fundamental cycles (and thereby its harmonics) occurs in the obtained time series that are being Fourier-transformed. The number of the grid fundamental cycles that occur during the measurement time can be given as [P2]

$$\frac{N_{MLBS}}{f_{gen}} P f_g = (R + r) \tag{3.12}$$

where the perturbation (MLBS) is generated at f_{gen} and averaged over P periods, and f_g is a grid fundamental frequency. The number of grid fundamental cycles is divided into the integer part (R) and the fractional part (r), from which the non-zero r indicates that the spectral leakage will appear in the frequency-response measurements. The time difference ΔT between the measurement time and the nearest multiple of the periodic cycle can be given as [P2]

$$\Delta T = \mathrm{abs}\left[\frac{N_{MLBS}}{f_{gen}} P f_g - \mathrm{round}(\frac{N_{MLBS}}{f_{gen}} P f_g)\right]\frac{1}{f_g} \tag{3.13}$$

where the operator $round$ gives the nearest integer of the grid fundamental. By varying design parameters affecting the measurement time, such as the number of averaged periods, the local minimum of the spectral leakage is expected when $\Delta T(P)$ (and r) is minimized, representing the proposed measurement design.

For the MLBS-based frequency-response measurements, the following design procedure yields parameters to minimize the spectral leakage [P2].

1. Adjust $f_{gen} = m(2f_g)$, where m is an integer.
    - Converter switching frequency f_{sw} may restrict the possible choices as $f_{gen} = f_{sw}/e$, where e is an integer.

2. Choose $P = f_{gen}/f_g$ or a multiple thereof.

   - $T_{meas} = P(N_{MLBS}/f_{gen}) = a(1/f_g)$, where a is an integer.
   - This results in $a = N_{MLBS}$ and, thus, T_{meas} includes exactly $R = N_{MLBS}$ fundamental grid cycles and r =0.

3. N_{MLBS} can be chosen without restrictions to satisfy the desired measurement characteristics.

As a result of the proposed design procedure, an integer amount of the grid fundamental cycles (and consequently, its harmonics) are being measured. Therefore, the spectral leakage caused by grid-voltage harmonics is avoided. The same design process applies for the multivariable measurements performed by the orthogonal sequences, but the averaged periods P of the original MLBS must be adjusted so that the total measurement time includes the common periods of the applied orthogonal sequences.

3.2 Adaptive Control of Grid-Connected Inverters

The remainder of this chapter introduces control design for the grid-connected inverter and proposes methods for adaptive operations. In this thesis, a cascaded control system for the grid-connected inverter is applied and a design process for each control loop of the cascaded control system is introduced, including

- Synchronous reference frame phase-locked loop (SRF-PLL)
- AC current control loop with digital notch filter
- Grid-voltage feedforward
- DC voltage control loop

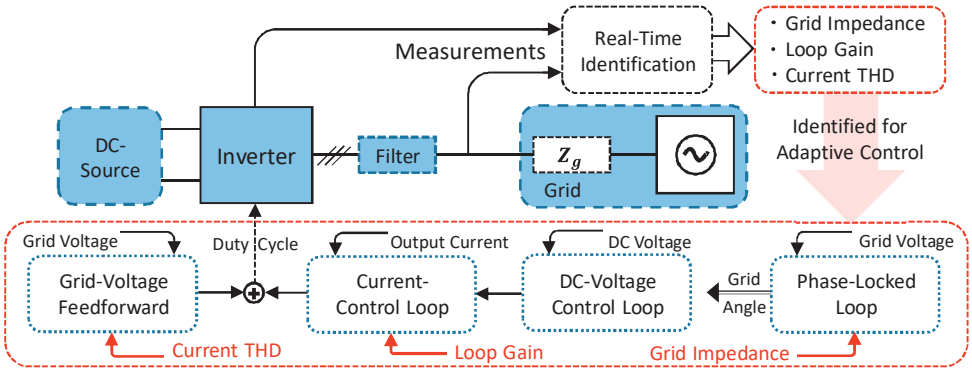

Figure 3.6 Simplified adaptive control scheme of grid-connected inverter.

Fig. 3.6 shows a simplified control system of the three-phase grid-connected inverter that is synchronized to the grid voltages by a phase-locked loop (PLL). The control-design procedure is mainly based on the inverter small-signal model, introduced in Chapter 2. The grid characteristics are identified in real time, and compensated by the adaptive methods. The grid impedance is identified for adaptive control of the PLL, online loop-gain measurements of the current-control loop are performed for the adaptive current control, and output current THD is observed for adjusting the gains of the grid-voltage feedforward. The DC voltage controller is not significantly affected by the grid-conditions, and is therefore not adaptively controlled by grid measurements in this thesis.

In each feedback loop of the cascaded control system, the conventional PI-type controllers are applied. The transfer function for the PI-type controller can be written as [71]

$$G_{\mathrm{PI}} = K_{\mathrm{p}} + \frac{K_{\mathrm{i}}}{s} = \frac{K_{\mathrm{p}} s + K_{\mathrm{i}}}{s} = \frac{K_{\mathrm{PI}}(s/(\omega_{\text{z-PI}}) + 1)}{s} \tag{3.14}$$

where the K_{p} and K_{i} are the proportional and integral gains respectively or, alternatively, the controller can be tuned by the controller gain K_{PI} and the controller zero $\omega_{\text{z-PI}}$.

3.2.1 Phase-Locked Loop

The inverter control system is typically synchronized to the grid by means of the PLL. Control design of the PLL has a major effect on the impedance-based stability margins of the grid-connected system, as the PLL dominates the inverter output admittance (2.41) within the control bandwidth, determined by the PLL loop (2.29). Below the PLL bandwidth, the qq-component of the inverter output admittance loses its passivity as the phase stays at 180 degree and the magnitude constant, approximately at $I_{\mathrm{Ld}}/V_{\mathrm{od}}$ [73]. This is often referred to a negative-resistance-like behavior of the inverter output admittance, which may cause impedance-based stability issues when the inverter is connected to a grid with significant (inductive) grid impedance. Phase response of mainly inductive grid impedance is close to 90 degrees, which causes high phase difference (a maximum of 270 degrees) in impedance-based stability analysis. The stability issues occur when high PLL bandwidth is connected to a significant grid impedance, where the system minor loop gain $\mathbf{Y}_{\mathrm{o}}(j\omega)\mathbf{Z}_{\mathrm{g}}(j\omega)$ (2.6) has significant magnitude at frequencies within the PLL bandwidth [90].

Considering the PLL loop gain (2.29), the actual plant consists of an integrator ($1/s$) with a constant gain (V_{od}) that depends on the voltage level of the grid. This simple structure makes it possible to provide straightforward control-tuning procedure, where the PLL loop gain phase margin (Θ_{PM}) and crossover frequency ($f_{\text{BW-PLL}}$) can be fixed. The proposed tuning procedure considers the loop characteristics at $f_{\text{BW-PLL}}$, where the loop magnification is 0 dB

and $s = j2\pi f_{\text{BW-PLL}}$. This yields the following equation group [P4]

$$\begin{cases} \cot(-180^\circ + \Theta_{\text{PM}}) = \dfrac{\left(\dfrac{V_{\text{od}}}{4\pi^2 f_{\text{BW-PLL}}^2}\right) K_{\text{i-PLL}}}{\left(\dfrac{V_{\text{od}}}{2\pi f_{\text{BW-PLL}}}\right) K_{\text{p-PLL}}} \\ 1\angle(-180^\circ + \Theta_{\text{PM}}) = \left(K_{\text{p-PLL}} + \dfrac{K_{\text{i-PLL}}}{2\pi f_{\text{BW-PLL}}}\right) \dfrac{V_{\text{od}}}{2\pi f_{\text{BW-PLL}}} \end{cases} \tag{3.15}$$

where the desired phase margin Θ_{PM} determines the ratio between the imaginary and real parts of the PLL loop gain, while the final control gains set the loop magnification (0 dB) at $f_{\text{BW-PLL}}$. By solving the equation group, the controller gains defined by the desired PLL control bandwidth can given as [P4]

$$\begin{cases} K_{\text{i-PLL}} = K_{\text{p-PLL}} 2\pi \cot(-180^\circ + \Theta_{\text{PM}}) f_{\text{BW-PLL}} \\ K_{\text{p-PLL}} = \dfrac{2\pi}{V_{\text{od}} \sqrt{\cot(-180^\circ + \Theta_{\text{PM}})^2 + 1}} f_{\text{BW-PLL}} \end{cases} \tag{3.16}$$

The tuning procedure can be applied in adjusting the PLL control bandwidth suitable to the grid conditions. As the phase margin of the controlled closed-loop system is clearly linked with overshoot of the control responses [71], the constant phase margin and adjustable bandwidth make the PLL responses more predictable.

Adaptive SRF-PLL Based on Sensitivity Function

Due to possible impedance-based stability issues caused by negative-resistance-like characteristics of the inverter output admittance and high grid impedance, overly high PLL bandwidth must be avoided when the inverter is connected to a weak grid [36]. However, overly conservative PLL tuning decreases the voltage tracking performance, which affects accuracy of the grid synchronization and the overall control performance of the grid-connected inverter. Consequently, designing the PLL bandwidth is a tradeoff between the inverter control performance and the system robustness, because the high bandwidth is the most desired in low-impedance grids, but causes impedance-based stability issues in high-impedance grids. Therefore, the adaptive control of the PLL based on the real-time grid-impedance measurements is proposed [P4]. In the adaptive-control scheme, the impedance-based stability is improved in weak grids by decreasing the bandwidth. Correspondingly, the control performance is improved in strong grids by increasing the bandwidth.

Design of the adaptive PLL is based on the sensitivity function (2.14), which can be applied as an indicator for the robustness of the grid-connected system and, in this case, for the control performance. When the inverter small-signal model is known, the system sensitivity

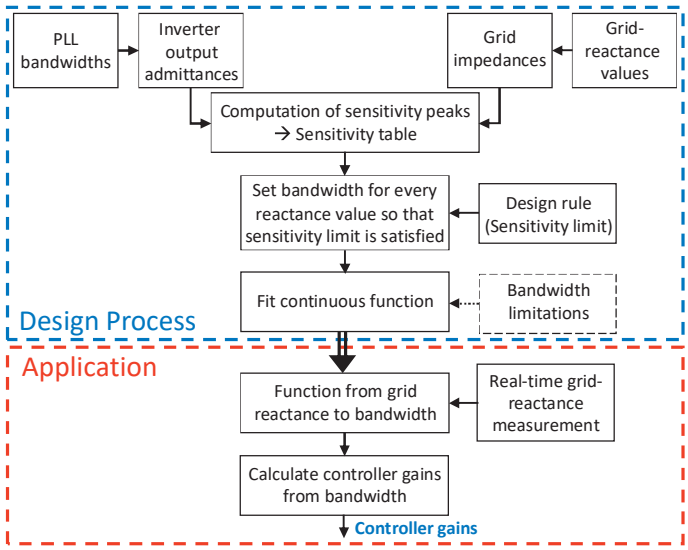

Figure 3.7 Flowchart of adaptive PLL design process and application.

function can be evaluated by the real-time measurements of the grid impedance. Desired system robustness can be assessed by limiting the sensitivity peak (2.15). The sensitivity limit can be chosen arbitrarily as a good trade-off between the control performance and robustness; the higher limit allows the use of higher PLL bandwidths, but also an increased amount of distortions. By adaptively re-adjusting the PLL control parameters based on the real-time grid-impedance measurements, the maximal PLL bandwidth in chosen stability boundaries can be achieved. Consequently, the system sensitivity peak is kept constant in varying grid conditions and the maximal voltage-tracking performance under each grid impedance is provided.

The proposed design process for the adaptive PLL yields a continuous function from the grid-impedance measurements to the PLL bandwidth. Fig. 3.7 shows a flowchart of the design process and application of the adaptive PLL, proposed in [P4]. The design process begins by modeling the grid impedance (2.43) over a wide range of inductive reactance values and the inverter output admittance (2.41) over a wide range of PLL bandwidths (3.16). The sensitivity peak is computed for each modeled pair of the PLL bandwidth and grid-impedance value. Next, the sensitivity limit is chosen, which operates as a design rule for the adaptive PLL. Based on the chosen sensitivity limit, the desired PLL bandwidth for each grid-impedance value is selected from computed sensitivity peaks so that the chosen sensitivity limit is satisfied under every grid impedance. In the last step of the design process, a continuous function is fitted to the discrete pairs of the PLL bandwidth and grid-impedance values. In the application, the PLL parameters are adaptively re-adjusted based on the real-time grid-impedance measurements. Therefore, dynamical performance of the adaptive control depends heavily on the accuracy and update time of the real-time measurements.

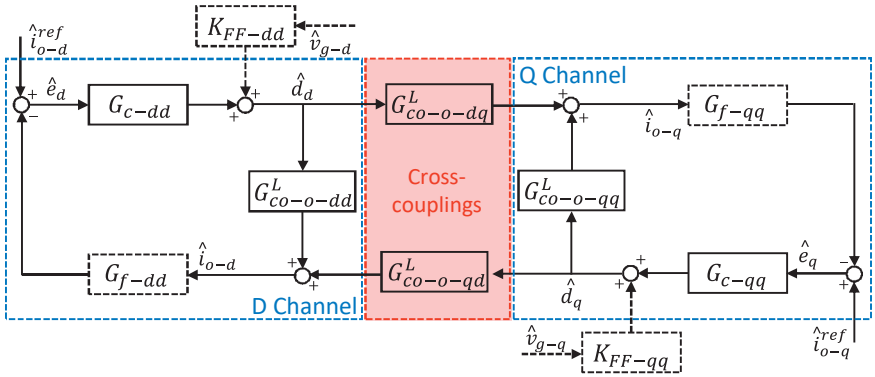

Figure 3.8 Current-control loop with digital filter and grid-voltage feedforward.

3.2.2 Current-Control Loop

The current-control loop acts as the innermost control loop of the cascaded control system and has a major effect on the quality of the produced power. Fig. 3.8 shows the block-diagram representation and related transfer functions of the load-affected current-control loop, from which the system stability can be assessed similar to the impedance-based stability analysis [91]. The transfer matrices are divided into direct (dd and qq) and cross-coupling components (dq and qd). The load effect (2.42) is added into the open-loop transfer functions and denoted by superscript L. The current controllers are denoted as $G_{\text{c-dd}}$ and $G_{\text{c-qq}}$ for the d and q channels, respectively. Additional digital filters in the loop are denoted by $G_{\text{f-dd}}$ and $G_{\text{f-qq}}$. The DC voltage controller and grid synchronization are omitted from the model as they have significantly lower bandwidth than the current-control loop. The current-control loop gains can be written as

$$L_{\text{CC-d}} = G_{\text{c-dd}} G_{\text{co-o-dd}}^{\text{L}} G_{\text{f-dd}} - \frac{G_{\text{c-dd}} G_{\text{co-o-dq}}^{\text{L}} G_{\text{f-qq}} G_{\text{c-qq}} G_{\text{co-o-qd}}^{\text{L}} G_{\text{f-dd}}}{(1 + G_{\text{c-qq}} G_{\text{co-o-qq}}^{\text{L}} G_{\text{f-qq}})} \tag{3.17}$$

$$L_{\text{CC-q}} = G_{\text{c-qq}} G_{\text{co-o-qq}}^{\text{L}} G_{\text{f-qq}} - \frac{G_{\text{c-qq}} G_{\text{co-o-qd}}^{\text{L}} G_{\text{f-dd}} G_{\text{c-dd}} G_{\text{co-o-dq}}^{\text{L}} G_{\text{f-qq}}}{(1 + G_{\text{c-dd}} G_{\text{co-o-dd}}^{\text{L}} G_{\text{f-dd}})} \tag{3.18}$$

The inverter is able to effectively mitigate distortions from the output current within the control bandwidth of the current-control loop. However, overly high control bandwidth or magnitude of the loop gain magnifies the switching ripple or may cause impedance-based stability issues. Therefore, PI-controller gains of the $G_{\text{c-dd}}$ and $G_{\text{c-qq}}$ must be adjusted so that the loop provides the desired mitigation of the distortions, but avoids magnifying the switching ripple and causing impedance-based stability issues. The grid impedance significantly affects the current-control loop through the load effect and weakens its control performance; for example, the ability to mitigate distortions from the produced currents. Additionally, if the LC (LCL) filter is applied as an AC filter, stability issues may arise in weak grids where the

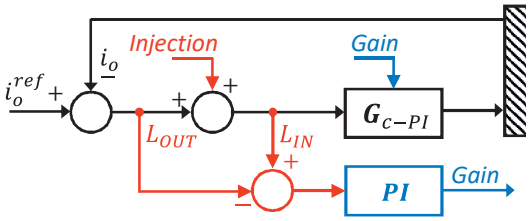

Figure 3.9 Adaptive current controller based on online loop-gain measurements.

grid inductance magnifies the LCL-resonance peak and affects its frequency (2.45) [35].

Adaptive Current Control Based on Loop-Gain Measurements

In order to avoid the stability issues caused by the grid-affected LCL resonance, a digital notch filter can be added to the current-control loop ($G_{\text{f-dd}}$ and $G_{\text{f-qq}}$ in Fig. 3.8) to mitigate the resonance peak [92]. In this thesis, a second-order notch filter with a unity quality factor is applied. The transfer function of such a filter can be written as

$$G_{\text{f}} = \frac{s^2 + \omega_0^2}{s^2 + \omega_0 s + \omega_0^2} \tag{3.19}$$

where ω_0 is center frequency of the notch filter. To effectively mitigate possible stability issues, the center frequency of the notch filter should be adjusted as near to the LCL-resonance peak (2.45) as possible. Due to the narrow frequency band of the notch filter and the possibly varying frequency of the grid-affected LCL-resonance [35], adaptive adjustment of the notch filter based on online measurements of the current-control loop gain is proposed in [P5]. The stability issues in a weak grid can be avoided by accurately adjusting the central frequency of the notch filter to the high-frequency maximum of the measured current-control loop. Additionally, the use of the notch filter allows higher gains for the current control loop, and thus improved performance of the current control.

As increased grid-impedance decreases the bandwidth of the current-control loop, the control gains must be re-adjusted in a weak grid in order to achieve the desired control performance and adequate power quality. The proposed self-tuning technique in [P5] is to perturb the current-control loop at the selected bandwidth frequency ($f_{\text{BW-CC}}$) and adaptively re-adjust the controller gain so that the loop magnification is 0 dB at that frequency. Selection of the bandwidth can be made arbitrarily, depending on the desired loop characteristics. However, in order to achieve similar control performance in very weak grids as in a strong grid, the control gains may have to be increased to values that make the controller output to saturate. This usually sets practical limitations to the controller. Additionally, applying higher gains magnify external disturbances in the system, which must be taken into account when determining the desired loop characteristics.

Fig. 3.9 shows the adaptive procedure based on the online loop responses ($|L_{\text{IN}}|$ and $|L_{\text{OUT}}|$) at the perturbation frequency $f_{\text{BW-CC}}$. The adaptive procedure is implemented by a feedback controller that regulates the magnitude difference of the responses to zero by re-adjusting gain of the current controller. When the magnitude difference is zero, the loop magnification at $f_{\text{BW-CC}}$ is 0 dB, so the desired bandwidth of the current-control loop is achieved. Applying the adaptive current controller and adaptive notch filter in the current-control loop can mitigate the high-frequency stability issues, improve the performance of the current-control loop, and, consequently, enhance the produced power quality.

3.2.3 Grid-Voltage Feedforward

The grid-voltage feedforward is applied to mitigate circulation of the grid-voltage harmonics to the inverter output currents. The grid-voltage harmonics circulate to the inverter output currents through the inverter open-loop output admittance ($\mathbf{Y}_{\text{o-o}}$), which can be mitigated by the grid-voltage feedforward [77]. This is achieved by an additional feedforward path ($\mathbf{L}_{\text{FF}}$) for grid voltages, as shown in Fig. 2.5. In the ideal case, without impact of, for example, the control delay and effect of the PLL, the feedforward matrix can be calculated as

$$\mathbf{G}_{\text{ff-ideal}} = \begin{bmatrix} G_{\text{codd-o}} & G_{\text{coqd-o}} \\ G_{\text{codq-o}} & G_{\text{coqq-o}} \end{bmatrix}^{-1} \begin{bmatrix} -Y_{\text{odd-o}} & -Y_{\text{oqd-o}} \\ -Y_{\text{odq-o}} & -Y_{\text{oqq-o}} \end{bmatrix} \tag{3.20}$$

Solving the equation yields a second-order transfer function for the inverter with the L filter [73].

Generally, the feedforward schemes are sensitive to disturbations, especially due to derivative terms introduced by higher-order transfer functions. Therefore, analytically defined high-order feedforward gains do not operate well in the realistic conditions where background noise and disturbations are present [93]. Due to that, equations are simplified and the higher-order feedforward transfer functions are reduced to proportional gains, which are less sensitive for the external disturbances.

By neglecting the cross-coupling components of small-signal model of the inverter output admittance (2.41), the model can be simplified and the ideal feedforward gains for direct components can be given as

$$K_{\text{FF-dd}} = \frac{-Y_{\text{odd-o}}}{G_{\text{codd-o}}} = \frac{s^2 + \frac{r_{\text{L}}}{L_1}s + \frac{3D_{\text{q}}^2}{2CL_1}}{\underbrace{V_{\text{C}}\left(-s^2 - \frac{r_{\text{L}}}{L_1}s - \frac{3D_{\text{q}}^2}{2CL_1}\right)}_{=O_{\text{1-dd}}} + \underbrace{\frac{3I_{\text{Ld}}}{2C}\left(D_{\text{d}}s + \omega_{\text{g}}D_{\text{q}} + \frac{D_{\text{d}}r_{\text{L}}}{L_1}\right)}_{=O_{\text{2-dd}}}}$$

$$K_{\text{FF-qq}} = \frac{-Y_{\text{oqq-o}}}{G_{\text{coqq-o}}} = \frac{s^2 + \frac{r_{\text{L}}}{L_1}s + \frac{3D_{\text{d}}^2}{2CL_1}}{\underbrace{V_{\text{C}}(-s^2 - \frac{r_{\text{L}}}{L_1}s - \frac{3D_{\text{d}}^2}{2CL_1})}_{=O_{\text{1-qq}}} + \underbrace{\frac{3I_{\text{Lq}}}{2C}(D_{\text{q}}s + \omega_{\text{g}}D_{\text{d}} + \frac{D_{\text{q}}r_{\text{L}}}{L_1})}_{=O_{\text{2-qq}}}} \tag{3.21}$$

where denominators are divided to two parts. The first part ($O_{\text{1-dd}}$ and $O_{\text{1-qq}}$) is second-order function and dominates the function characteristics. The second part ($O_{\text{2-dd}}$ and $O_{\text{2-qq}}$) has a relatively small effect compared to the first part and depends on the output currents (produced power). Active power affects the d-component and reactive power affects the q component; both are equal to zero when no power is generated. Due to the small effect and dynamics that depend on the typically highly varying power, the second part of the denominator ($O_{\text{2-dd}}$ and $O_{\text{2-qq}}$) is omitted from the analysis.

The simplified modeling yields symmetrical proportional feedforward gains for both channels, solved as

$$K_{\text{FF-dd}} = \frac{s^2 + \frac{r_{\text{L}}}{L_1}s + \frac{3D_{\text{q}}^2}{2CL_1}}{V_{\text{C}}(-s^2 - \frac{r_{\text{L}}}{L_1}s - \frac{3D_{\text{q}}^2}{2CL_1})} = -\frac{1}{V_{\text{C}}}$$

$$K_{\text{FF-qq}} = \frac{s^2 + \frac{r_{\text{L}}}{L_1}s + \frac{3D_{\text{d}}^2}{2CL_1}}{V_{\text{C}}(-s^2 - \frac{r_{\text{L}}}{L_1}s - \frac{3D_{\text{d}}^2}{2CL_1})} = -\frac{1}{V_{\text{C}}} \tag{3.22}$$

The proportional gains compensate the inverter output admittance at low frequencies and are not very sensitive to the external disturbances. Thus, the proportional gains improve the power quality in realistic conditions by mitigating the low-order harmonics that arise from the distorted grid voltages [77]. In high frequencies, the control delays weaken the performance of the grid-voltage feedforward. Varying power, quality of the grid voltages, inverter dead time and grid impedance also affect the feedforward performance [94].

Adaptive Grid-Voltage Feedforward Based on Perturb-and-Observe Algorithm

Although the proportional grid-voltage feedforward is not particularly sensitive to disturbances, it still has a dualistic impact on quality of the produced power: it effectively mitigates low-order harmonics arising from distorted grid voltages, but is also shown to magnify inverter internal distortions caused, for example, by the dead time [94]. Therefore, in the ideal grid conditions, the feedforward merely magnifies the inverter internal disturbances, thereby decreasing the quality of the produced power. However, when the inverter is ideal or connected to highly distorted grid voltages, the feedforward effectively improves the power quality. As a consequence, the optimal gain for the feedforward path, that minimizes the THD from the produced power, depends on the inverter characteristics and grid conditions.

The THD-minimizing gain for the proportional grid-voltage feedforward depends on multiple parameters of the grid-connected system that usually vary over time; for example, the amount of generated power, quality of the grid-voltages, and the grid impedance. Additionally, the inverter model does not include the dead-time effect that mainly causes the internal disturbances, and therefore has an important impact on the THD-minimizing gain. Consequently, analytical assessment of the THD-minimizing gain is relatively difficult and may vary over time. Therefore, the adaptive control based on the perturb-and-observe (P&O) algorithm is proposed in [P6] for improving the performance of the grid-voltage feedforward, thus enhancing the produced power quality. The P&O algorithm is widely used in PV systems' maximum power-point tracking (MPPT) for optimizing the energy yield [95]. The popularity of the algorithm is based on its simple implementation, where the PV-array voltage is perturbed and the output power is observed. The direction of the next voltage step is defined based on an observed effect on the output power. Therefore, the P&O algorithm does not require prior knowledge of the system.

In the proposed adaptive feedforward, the feedforward gain is perturbed and the effect on the output current THD is observed. The proportional gain is perturbed by step-wise changes $A_{\text{pert}} = X_{\text{pert}}/V_{\text{C}}$, where X_{pert} is a constant between 0 and 1 and determines the step size. During the adaptive process, the gain of the proportional grid-voltage feedforward can be written as

$$K_{\text{FF}}^{i} = K_{\text{FF}}^{i-1} \pm A_{\text{pert}} \tag{3.23}$$

where i is integer (index for consecutive steps) and K_{FF}^{i-1} denotes the previous gain value. The direction for the next step ($\pm A_{\text{pert}}$) is defined by the observed effect of the previous step to the output current THD. If the THD decreases (power quality enhances), the next step is taken in the same direction; if the THD is increased, the next step is taken in the opposite direction [P6]. The proposed adaptive feedforward has a plug-and-play feature, as it reaches the THD-minimizing gain autonomously without accurate models of the system under test.

A drawback of the algorithm is that it continues perturbations even when the optimal value has been found. Thus, the algorithm makes the perturbed variable oscillate around the desired value [95]. The oscillation amplitude is equal to the applied perturbation-step size (A_{pert}). A lower step size indicates slow tracking in changing conditions, whereas higher steps increase oscillations. The step size should be high enough to perturb the system so that the increase or decrease in the observed value can be detected. Another critical value of the P&O algorithm is the time interval between the perturbations (T_{pert}), which should be longer than the system settling time, caused by the perturbation, to avoid misleading observations. However, longer time intervals make the P&O algorithm slower in terms of finding the desired values after a change in operation conditions or during start-up.

3.2.4 DC Voltage Control

The DC voltage control acts as the outer loop of the cascaded control system. The DC voltage control removes the necessity of an additional DC-DC converter between the source and the inverter, and adjusts reference for the output current d-component. The DC voltage controller is adjusted so that the loop stability is ensured and impact of the grid harmonics are mitigated from the DC voltage reference. This determines the higher and lower limits for the bandwidth design of the DC voltage control loop (2.40), which is considered when tuning the DC voltage controller.

Stability of the DC voltage control loop may be compromised when the PV operates at lower voltages than MPP. The PV generator has an output impedance that depends on the operating-point and introduces a source effect for the inverter, similarly to how the grid impedance causes the load effect. When the operation voltage of the PV is low, the right-hand-plane (RHP) zero appears in the inverter transfer functions through the source effect [96]. The RHP zero becomes an unstable pole when the loop is closed. However, by adjusting the bandwidth of the control loop higher than the RHP zero (closed-loop pole), the system can be stabilized [64]. Therefore, the maximum frequency of the zero is an important design parameter for the DC voltage control loop. The frequency at which the zero is located depends on the operating point and can be approximated as [76]

$$\omega_{\mathrm{Z}} = \frac{I_{\mathrm{PV}}}{U_{\mathrm{PV}} C} \tag{3.24}$$

where the I_{PV} and U_{PV} are the DC-side current and voltage, and C is the DC capacitor. The frequency reaches the maximum value when the operating voltage of the PV generator is at its minimum and the current is at its maximum. The absolute minimum for the DC voltage is two times the amplitude of the grid voltages. The maximum current can be approximated by the short-circuit current of the PV generator or rated power of the inverter. Applying these considerations makes it possible to determine the lower limit for the bandwidth of the DC voltage control loop.

In the DQ domain, unbalanced grid voltages produce double grid-frequency oscillations into the control system. These oscillations circulate to the DC voltage, and thereby to the current d-component reference if not mitigated in the DC voltage control loop. Therefore, the bandwidth of the DC voltage control loop should be adjusted so that the sufficient attenuation at the second grid harmonic is provided. This introduces the higher limit for the bandwidth of the DC voltage control loop.

4 IMPLEMENTATION AND VERIFICATION

This chapter introduces the practical implementation of the proposed methods and presents the most important results obtained. The first section introduces the experimental power hardware-in-the-loop (PHIL) setups. Implementation and verification of the proposed methods are divided into two parts: the real-time measurement methods and the adaptive-control methods.

The second section presents the practical implementation of the real-time identification methods. Performance of the real-time measurement methods is introduced by three experimental sets, given as follows.

Experiment 1:
Measurement setup for the real-time measurements of the DQ domain grid impedance is introduced [P1]. The applied perturbation design is presented and the accuracy of the obtained results is analyzed. The results illustrate benefits of the proposed design procedure that minimizes the spectral leakage caused by the grid harmonics [P2].

Experiment 2:
Implementation for the stability analysis is presented, where the impedance-based stability of a grid-connected system is based on the real-time grid impedance measurements and the analytical inverter output admittance is performed. The results are visualized by the GNC loci, which is updated in real time. Obtained GNC loci are applied to assess the system stability and to predict stability with different control designs of the inverter [P3].

Experiment 3:
The real-time loop-gain measurements are performed and the current-control loop of a grid-connected inverter is measured under different grid impedances. The results illustrate how the increased grid impedance decreases control bandwidth of the current-control loop and affects the high-frequency resonance peak of the applied LC-filter [P5].

The third section introduces the design process and implementation of the proposed adaptive-control methods for the grid-connected inverter. Each proposed method is verified through simulations or experimental tests and the control performance, achieved by the proposed

adaptive methods, is compared to the conventional control designs. The adaptive methods are presented and verified as follows.

Experiment 4:
Implementation of the grid-voltage feedforward applying P&O algorithm is introduced. The algorithm adaptively adjusts the feedforward gains so that THD in the inverter output current is minimized. The obtained results and produced power quality are compared to the conventional grid-voltage feedforward implementations [P6].

Experiment 5:
Practical operation of the proposed self-tuning method for the current-control loop and adaptive adjustment of the digital notch filter are presented. Both methods are based on the loop-gain measurements and re-shape the current-control loop so that the system stability and control performance are improved. During the adaptive process, online loop-gain measurements of the current-control loop are presented and the control performance of the adaptively adjusted loop is analyzed [P5].

Experiment 6:
The design process for the adaptive PLL based on the system sensitivity function is introduced. In the practical implementation, the low-frequency sensitivity peak of the grid-connected system is kept constant by adaptively re-adjusting the PLL parameters based on the real-time grid-impedance measurements. The experimental results show the improved system stability and voltage-tracking performance of the PLL under varying grid-conditions [P4].

4.1 Experimental Setups

Two different experimental setups are applied; Experimental Setup 1 operates at high power (200 kVA) and Experimental Setup 2 at down-scaled power (2.7 kVA). Both of the setups are power hardware-in-the-loop (PHIL) setups designed for testing the three-phase grid-connected PV inverter with real power and hardware.

Experimental Setup 1

Experimental verification of the real-time measurement methods with higher power was performed at DNV GL Flexible Power Grid Lab (FPGL). Fig. 4.1 shows the PHIL setup, which is made up of 200 kVA Egston power amplifiers and driven by an OPAL-RT real-time simulator. An individual power amplifier consists of six parallel half-bridge converters with an equivalent switching frequency of 125 kHz. The closed-loop bandwidth of the power amplifiers is 5 kHz, which means they can be applied to emulate three-phase inverters, as

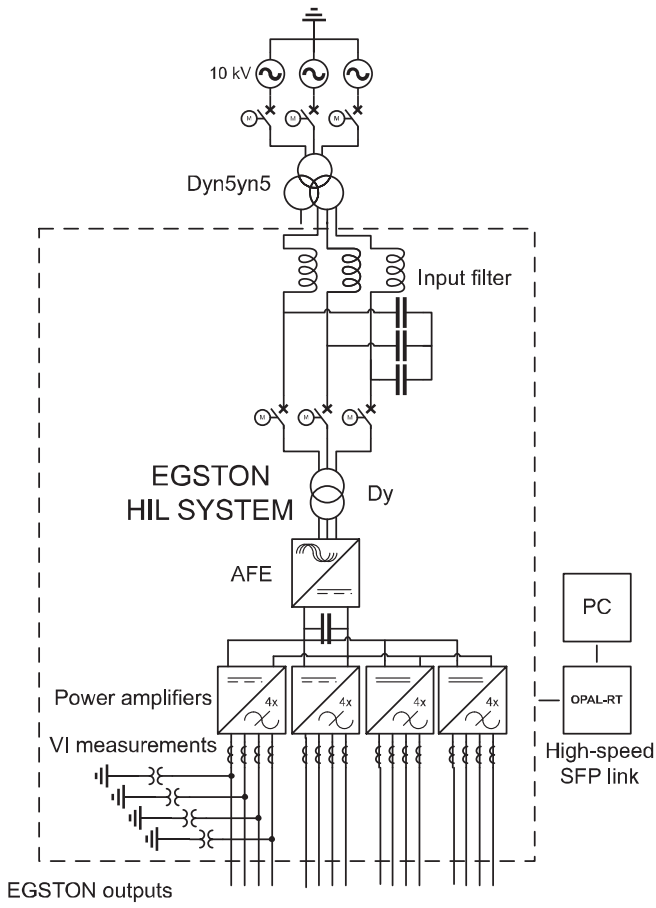

Figure 4.1 PHIL setup in DNV GL Flexible Power Grid Lab.

shown in [97]. The power amplifiers can be freely configured to act as sources or loads depending on what kind of power system architecture is studied. Hardware impedance can be placed between amplifiers, for example, to emulate the grid impedance.

Experimental Setup 2

Fig. 4.2 shows the PHIL setup that includes a three-phase grid emulator (linear amplifier, Spitzenberger Spies PAC 15000), a PV emulator (Spitzenberger Spies PVS7000), a three-phase inverter (Myway Plus MWINV-9R144), an isolation transformer, and a set of passive components with a relay in order to vary the grid impedance. A real-time simulator (dSPACE) runs the control system of the inverter, which enables testing of the proposed control schemes with the real hardware. Additionally, a measurement card (NI USB-3636) is applied in some experiments to gather and store the measured data.

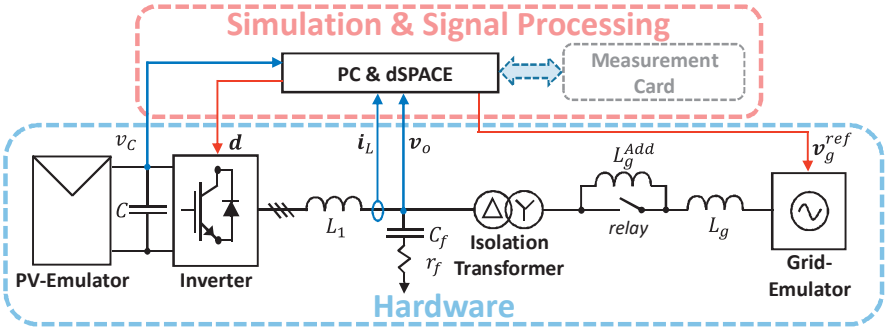

Figure 4.2 PHIL setup for experimental tests.

Table 4.1 Steady-state parameters of the inverter at nominal power.

V_c	414 V	I_{in}	6.6 A	ω_g	$2\pi \cdot 60$ rad/s	P_n	2.7 kVA
V_{od}	$\sqrt{2} \cdot 120$ V	V_{oq}	0 V	f_{sw}	8 kH	r_f	1.8 Ω
I_{Ld}	10.6 A	D_d	0.4122	D_q	0.0213	C_f	10 μF
C	1.5 mF	r_L	0.1 Ω	L_1	2.2 mH		

Table 4.2 Control parameters.

	DC Voltage		Current Control		PLL		Feedforward
	$K_{p\text{-}DC}$	$K_{i\text{-}DC}$	$K_{p\text{-}CC}$	$K_{i\text{-}CC}$	$K_{p\text{-}PLL}$	$K_{i\text{-}PLL}$	Gain
Set1 (Reference)	0.0962	1.209	0.0149	23.44	0.6723	38.0189	0
Set2 (PLL)	0.0962	1.209	0.0149	23.44	**3.315**	**1000**	0
Set3 (CC)	0.0962	1.209	**0.0224**	**35.16**	0.6723	38.0189	0
Set4 (GV-FF)	0.0962	1.209	0.0149	23.44	0.6723	38.0189	**0.0012**

The inverter operating point, at nominal power (2.7 kVA) and connected to (120 V / 60 Hz) grid, is given in Table 4.1. Four examples of the control-parameter sets are given in Table 4.2. Parameter Set1 (Reference) is applied as a reference for comparing the results, obtained by the adaptive control. Higher PLL bandwidth (100 Hz) is applied in Set2. Controller gains of the symmetrical (d and q channels) current controllers are increased in Set3. The grid-voltage feedforward is applied in Set4, where the feedforward gain is set to $0.5/V_c$.

4.2 Experiment 1: Grid-Impedance Measurements

Considering the grid-connected systems in the DQ domain, full-order transfer functions are represented as 2 x 2 matrices that include direct (dd and qq) and cross-coupling (dq and qd) components. In order to simultaneously measure full DQ domain transfer matrices, two uncorrelated sequences must be applied to perturb both d and q channels as presented in [P1, P2, P3].

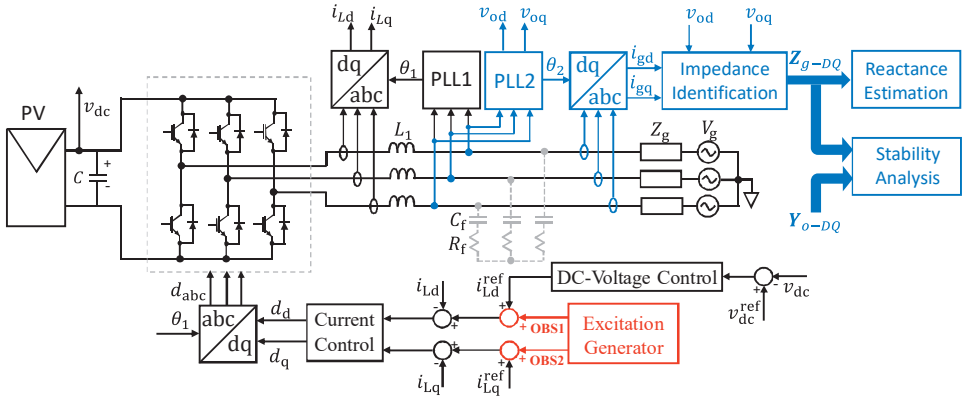

Figure 4.3 Grid-connected three-phase inverter including online grid-identification methods.

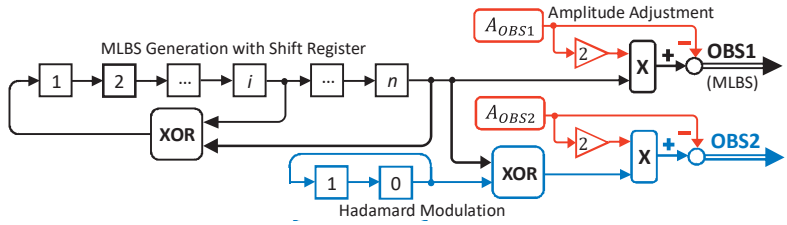

Figure 4.4 Generation of two orthogonal binary sequences, OBS1 and OBS2.

Fig. 4.3 shows a grid-connected three-phase inverter that is configured to identify frequency response of the DQ domain grid impedance. Fig. 4.4 shows practical implementation of the excitation generator, which is included in the inverter control system. The excitation generator continuously generates two orthogonal binary sequences (OBS1 and OBS2), which are injected on top of the current reference d- and q-components. Consequently, the inverter generates current perturbations to the grid. From measured responses in the grid voltages and currents, the frequency response of the DQ domain grid impedance can be obtained in real-time, during otherwise normal system operation [P1]. The real-time measurement can be applied for stability analysis [P3] or for estimating grid indicators, such as grid reactance [P4].

In the practical implementation, illustrated in Fig. 4.3, a second PLL (PLL2) is used for DQ transformation in the real-time identifications [P1]. PLL2 has lower bandwidth than the lowest measured frequency by OBS1 or OBS2 because the applied PLL regulates the obtained voltage q-component zero within its bandwidth, and thus, degrades the grid-impedance measurements inside the bandwidth [86]. PLL1 does not affect the measurements; it can have higher bandwidth and is applied for grid-synchronization of the inverter control system.

The real-time grid-impedance measurements are performed with high power levels applying the Experimental Setup 1. In the experiments, a simple power-system architecture is studied, where a single inverter is connected to the power grid through an impedance. Therefore, two power amplifiers are used; one (AMP1) is configured to emulate a three-phase

inverter and the other (AMP2) emulates (230 V, 50 Hz) a three-phase grid. A three-phase inductive component ($\approx$ 0.5 mH) is placed between the power amplifiers as a hardware grid impedance. Voltages of AMP2 (representing the grid voltages) are highly distorted by white noise and periodic oscillations. The periodic oscillations are generated as follows. A single phase is in 20 % unbalance and all phases include 5 % of positive sequence 2^{nd} and 7^{th} harmonic as well as negative sequence 2^{nd} and 5^{th} harmonic. In the DQ domain (50 Hz grid), the unbalance occurs at 50 and 100 Hz and harmonics at 50, 150, and 300 Hz.

For the full DQ domain grid-impedance measurements, the current injections are generated to the grid by continuously injecting OBS1 and OBS2 on top of the current reference d and q components of AMP1, as illustrated in Fig. 4.3. The length of OBS1 (MLBS) is 2047 bits and the corresponding OBS2 4094 bits. Both sequences are generated at 5 kHz, so the frequency resolution is 2.44 (5000/2047) Hz. The currents and voltages are measured from the output terminal of the power amplifier that emulates the inverter (AMP1). The data is captured by a measurement card (NI USB-6363) and operated by the MATLAB/Data Acquisition Toolbox.

In order to illustrate importance of the measurement design process (3.1.4) in minimizing spectral leakage caused by the periodic oscillations, the number of averaged periods is varied between measurements. Fig. 4.5 shows the measured grid impedance with two different numbers of averaged periods. The blue lines represents one of the proposed measurement parametrizations ($P = 100$), where the spectral leakage of the grid harmonics is minimized as the sampled data (measurement time) include exactly full periods of the grid fundamental frequency (50 Hz) and harmonics. The red line represents otherwise similar parametrizations, but the number of the averaged periods is increased ($P = 108$). A higher number of averaged periods increases SNR but, in this case, the measurement time does not include exactly full periods of the grid fundamental frequency when $P = 108$. Therefore, the DFT (3.11) does not produce the spectral line at 50 Hz and its harmonics, the periodic oscillation leak to other frequencies; therefore, the grid-voltage unbalance and harmonics deteriorate the measurements through the spectral leakage.

Grid-impedance measurements were performed with a high number of averaged periods ($P = 200$). Sampled voltages and currents were divided to sub-records with the length of varying averaged periods ($P = 2k$, where k is an integer), and the grid impedance was computed by Fourier methods. Fig. 4.6 shows the variance sum of each DQ domain component to their reference, an averaging trend line, and the time difference (3.13) to grid fundamental frequency ($\Delta T(50Hz)$) and second harmonic ($\Delta T(100Hz)$) with varying number of averaged periods P. The variance follows the averaging trend line, but significantly decreases at local minimums of $\Delta T(50Hz)$. Therefore, the local minimums of $\Delta T(50Hz)$ determine the proposed measurement parametrization, so it is strongly recommended that the design rules given in Section 3.1.4 be followed in order to avoid spectral leakage in the measurements [P2].

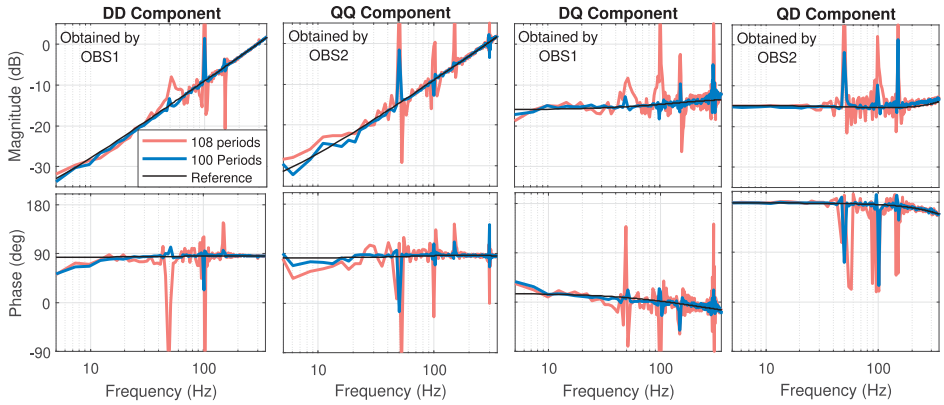

Figure 4.5 Measured grid impedance using orthogonal injections.

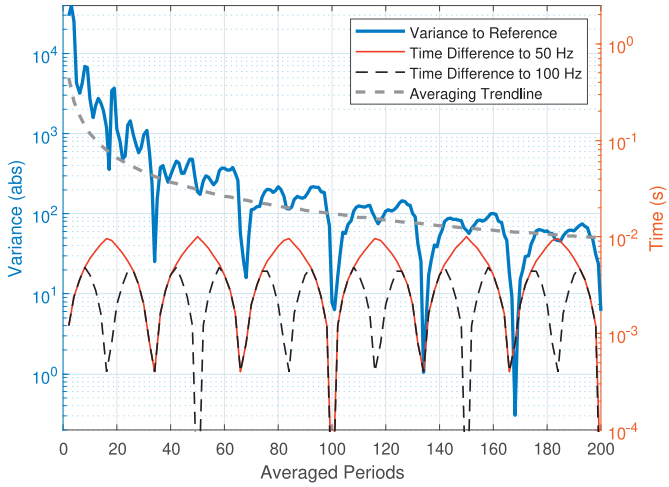

Figure 4.6 Variance over different averaging periods.

In order to illustrate the appearance of the spectral leakage more efficiently, Fig. 4.7 shows the measurement variance as a function of frequency with three different P. The red bars ($P = 184$) show variance when measurement parameters are chosen as local minimum of ΔT(100 Hz), which mitigates the spectral leakage of even-order grid harmonics (here 100 and 300 Hz). The blue bars ($P = 176$) represent parameters where the spectral leakage is not considered. Finally, the black bars ($P = 168$) show variance when the measurement parameters are chosen from the local minimum of both ΔT(50 Hz), and consequently ΔT(100 Hz). This mitigates the spectral leakage from all grid-harmonic frequencies, which represents one of the proposed measurement designs.

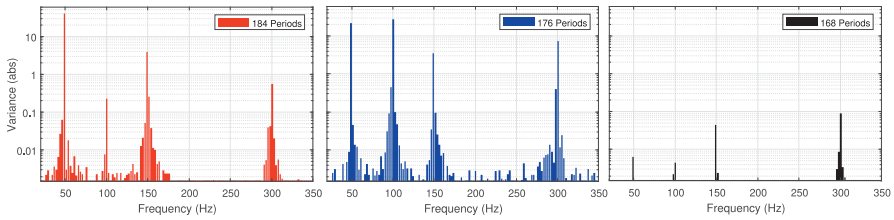

Figure 4.7 Variance over frequency spectrum with different number of averaged periods.

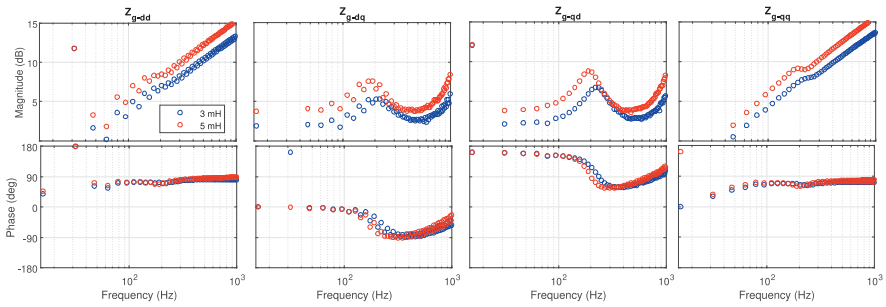

Figure 4.8 Real-time measurements of two grid impedances.

4.3 Experiment 2: Real-Time Stability Analysis

Verification of the real-time stability analysis is performed applying Experimental Setup 2 (shown in Fig. 4.2), where the hardware grid impedance can be varied by switching the by-pass relay of additional impedance components in the grid-side. The stability analysis is based on the analytical inverter output admittance and the real-time measurement of the multivariable grid impedance. The impedance-based stability is assessed by the real-time GNC loci (2.9) that is updated when new grid-impedance measurement is obtained. Therefore, the accuracy and updating time of the GNC loci depends on the real-time measurements of the grid impedance.

The grid-impedance measurements are performed similar to Experiment 1; the current perturbations are generated to the grid by injecting orthogonal sequences on top of the inverter current references. However, the GNC loci requires information from all DQ domain components at each studied frequency. Therefore, all of the DQ domain components are measured by both sequences (OBS1 and OBS2) during a single measurement cycle. This is implemented by first injecting the OBS1 to the d-component (OBS2 to the q-component), and in the middle of the measurement cycle, the order of the sequences is changed so that the OBS1 is injected to the q-component (OBS2 to the d-component). Consequently, each component of DQ domain grid impedance is measured by both OBS1 and OBS2, and the GNC-loci can be computed.

In this experiment, the measurements are performed by a 127-bit-long OBS1 and the corresponding OBS2 with symmetrical 0.3 A (less than 3 % of nominal current). Both sequences

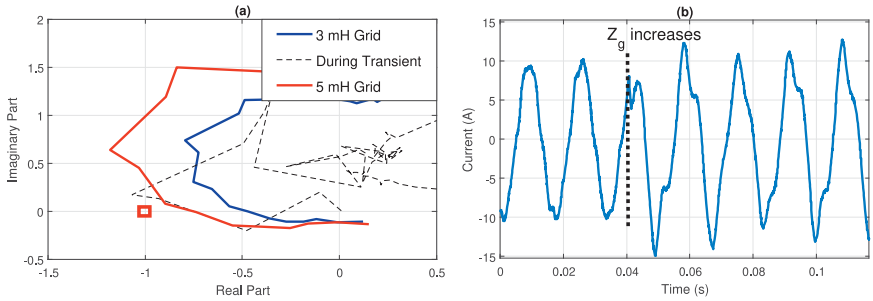

Figure 4.9 Real-time GNC loci (a) and current during grid transient (b).

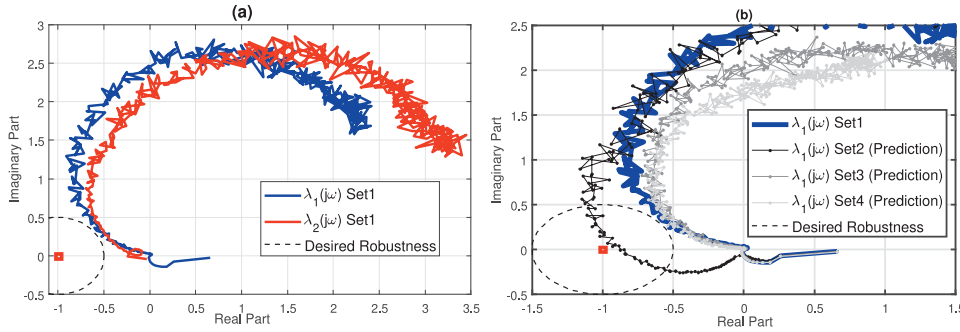

Figure 4.10 Real-time GNC loci (a) and stability predictions of different control-parameter sets (b).

are generated at 4 kHz. All components of the DQ domain grid impedance are measured by both sequences, so the combined frequency resolution equals to 15.75 ($4000/(2 \times 127)$) Hz. The number of averaged OBS1 periods (for each component) is $P = 20$, so double-length OBS2 is averaged over 10 periods. Fig. 4.8 shows real-time measurements ($T_{\text{meas}} \approx 1.27$ s) of the multivariable grid impedance with two grid-inductance values $L_{\text{g-1}} = 3$ mH and $L_{\text{g-2}} = 5$ mH, which translates to the equivalent short-circuit ratio (SCR) of 14.1 and 8.5, respectively.

A grid transient from relatively strong to relatively weak grid is performed when high PLL bandwidth (control-parameter Set2 in Table 4.2) is applied. Fig. 4.9a shows the critical GNC loci based on the real-time grid-impedance measurements given in Fig. 4.8. In the experiment, the grid inductance equals to 3 mH (SCR = 14.1), then the bypass relay is switched off and the grid inductance increases to 5 mH (SCR = 8.5). Changed grid-impedance deteriorates the measurements during the transient, which means that the GNC loci obtained during the transient cannot be applied to assess the stability. After the transient, the inverter is connected to 5 mH grid and the obtained GNC loci is close to critical (-1 + j0) point. This indicates low stability margins, verified in Fig. 4.9b by the phase current, recorded during the change in the grid impedance. The harmonic resonance occur after the grid-impedance transient and verifies low stability margins, which is caused here by overly high PLL bandwidth and high (inductive) grid impedance.

In the next experiment, the obtained GNC loci of the grid-connected system is applied as an aid for the control tuning procedure of the inverter. In order to achieve accurate sta-

bility analysis of the system, the GNC is based on online grid-impedance measurement, where measurement accuracy and frequency resolution are improved at the expense of increased measurement time. A 2047-bit-long OBS1 and corresponding OBS2 are applied to measure each component of the DQ domain grid impedance, similarly as in the previous experiment. Both sequences are generated at 4 kHz and the combined frequency resolution is 0.98 ($4kHz/(2\times2047)$) Hz. OBS1 is averaged over 20 periods (OBS2 over 10 periods) for each component. This yields a relatively long measurement time $T_{\text{meas}} \approx 40$ s, which means it cannot usually be considered as a real-time measurement. Fig. 4.10a shows both GNC loci ($\lambda_1(j\omega)$ and $\lambda_2(j\omega)$) of the inverter applying control-parameter Set1 (Table 4.2) and connected to 7 mH (SCR = 6.1) grid impedance. The circle around the critical point determines the desired stability margins by limiting the shortest allowed distance of the GNC loci to the critical point (2.10). Here the distance is limited to $d_\lambda = 1/2$ but can be adjusted arbitrarily. Fig. 4.10b shows the online stability analysis for control-parameter Set1 and stability prediction for other control-parameter sets from Table 4.2. The stability predictions are based on the analytical models of the inverter output admittances with different control parameters (Set2, Set3 and Set4 given in Table 4.2) and the online measurements of grid impedance at current inverter operating conditions. Set3 (increased gain in current controllers) and Set4 (grid-voltage feedforward applied) would satisfy the adjusted stability limit, but increasing the PLL bandwidth (Set2) violates the stability limit, so it is not proposed in these grid conditions.

4.4 Experiment 3: Online Loop-Gain Measurements

Online loop-gain measurements of the current-control loop reveal impedance-based stability information and the inverter performance can be predicted. This experiment is performed by applying Experimental Setup 2, where the LC-filter is applied. In the experiment, a 2047-bit-long MLBS is generated at 4 kHz, which provides a frequency resolution of 1.95 Hz.

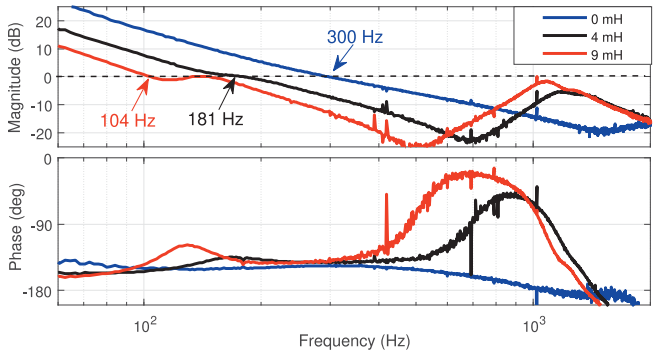

Figure 4.11 Online measurements of current-control loop gain under various inductive grid impedances.

The MLBS is injected to the loop and the loop responses are measured as shown in Fig 3.9. Fig. 4.11 shows the online measurements of the current-control loop under three different grid impedances. In the control-design process the loop bandwidth is set to 300 Hz. The blue line represents online measurement in nearly ideal grid conditions (0 mH grid), where the effect of the grid impedance is negligible. Black (4 mH grid) and red (9 mH grid) lines represents the loop gains when significant grid impedance is present and affects the loop characteristics. For example, when the inverter is connected to a 9 mH grid (red line), the bandwidth is decreased to as low as 104 Hz. Additionally, higher grid impedance affects the LC resonance ,which is magnified, and the peak appears at lower frequency.

4.5 Experiment 4: Adaptive Grid-Voltage Feedforward

In this section, practical implementation of the adaptive grid-voltage feedforward based on the P&O algorithm is applied. The algorithm adaptively adjusts the THD-minimizing gains in different conditions by observing the produced inverter output currents. The obtained results are compared to the conventional implementations in different grid conditions.

The grid-voltage feedforward gains have a dualistic impact on quality of the produced output current: higher gains mitigate impact of the grid voltage harmonics, but magnify inverter internal distortions caused, for example, by the dead time. Therefore, THD-minimizing gain is a tradeoff between the dualistic impact. The THD-minimizing gain equals zero from the dead-time perspective and $1/V_{\mathrm{C}}$ to most effectively mitigate the grid-voltage distortions. The P&O algorithm is proposed to adaptively adjust the THD-minimizing gain of the grid-voltage feedforward during the otherwise normal operation of the inverter. Fig. 4.12 shows a block diagram of the adaptive-control scheme and the applied P&O algorithm. In the implementation, the grid-voltage feedforward gain is perturbed by A_{pert} at certain time intervals T_{pert}, and THD of the output current is observed after the perturbation. Direction of the next perturbation step of the feedforward gains is based on the observed THD so that the increased THD always changes the direction. The feedforward gains are symmetrically adjusted for the d and q channels.

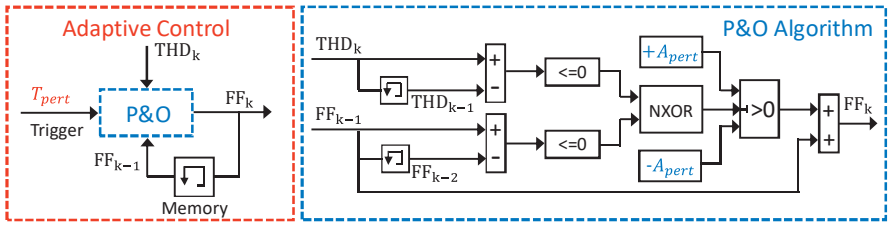

Figure 4.12 Implementation of P&O algorithm that minimizes output current THD.

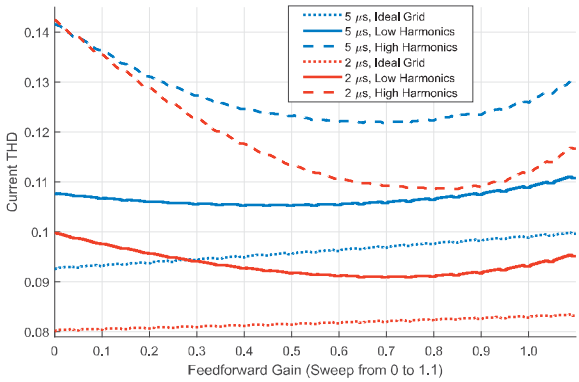

Figure 4.13 Impact of grid-voltage feedforward gain in different operating conditions.

The proposed approach for the adaptive grid-voltage feedforward is tested with a switching model of the three-phase grid-connected inverter in MATLAB/Simulink, simulating Experimental Setup 2. The operating conditions are given in Table 4.1 and the control parameters (Set1) are given in Table 4.2, where the grid-voltage feedforward gains are obviously varied by the P&O algorithm. The inverter dead time is included in the model by delaying the turn-on signals of the inverter switches. The grid impedance is kept constant in each simulation ($r_g = 0.4\ \Omega$, $L_g = 0.9$ mH) and the grid disturbances are realized by introducing harmonics to grid voltages. The DC voltage is kept at the maximum-power point (414 V). In the simulations, the perturbation size of the P&O algorithm is chosen as $A_{pert} = 0.05/V_C$. The interval between perturbations is $T_{pert} = 0.2$ s and the THD is averaged over 0.15 s in order to reduce misleading predictions during the adaptive process.

Fig. 4.13 illustrates the dualistic impact of the grid-voltage feedforward. The proportional feedforward gain is scanned from 0 to $1.1/V_C$, and the output current THD is observed. Two different inverter dead times 2 μs and 5 μs (representing 1.6 % and 4 % of the inverter switching frequency, respectively) are applied. In the ideal grid, the THD-minimizing gain of the grid-voltage feedforward equals zero as higher gain increases the THD of the output currents. However under non-ideal grid voltages, the THD-minimizing gain of the grid-voltage feedforward varies between 0 and $1/V_C$. This THD-minimizing gains can be adaptively found by observing the THD of the output currents, as proposed in [P6].

The implementation has a plug-and-play feature, as the P&O algorithm independently finds the THD-minimizing gains in interfaced grid conditions. Fig. 4.14 shows the output current THD and the feedforward gain during the inverter start-up in two different grid conditions. The inverter is connected to a grid with low (a) and high (b) harmonic content. Dead time of 5 μs is applied in both tests. In order to avoid first transients, the P&O algorithm is enabled 0.6 s after the inverter is connected to the grid. The feedforward gain increases by $0.05/V_C$ at 0.2 s intervals until the THD-minimizing gain is achieved. The THD-minimizing gains equals to $0.5/V_C$ (in 1.8 seconds) and $0.7/V_C$ (in 2.4 seconds) for grids with low and high

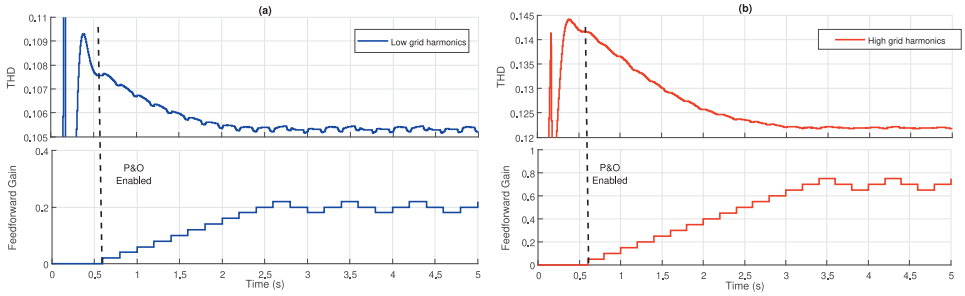

Figure 4.14 Adaptive performance during inverter start-up under relatively low (a) and high (b) grid-voltage distortions.

harmonics, respectively. Compared to the zero feedforward gain (observed at 0.5 s), the adaptively adjusted grid-voltage feedforward decreases the output current THD by 3 % in grids with low harmonic content and by 14 % in those with high harmonic content.

Fig. 4.15a shows the adaptive process under varying grid conditions, and compares performance between the conventional (zero and $1/V_C$ gains) grid-voltage feedforward implementations. The inverter is started up under ideal grid voltages and the adaptively adjusted feedforward gain (blue line) oscillates around zero. The observed THD is obviously similar to the zero gain (red dots), but 5 % higher with $1/V_C$ gain (grey dashed line), in which the internal distortions of the inverter are magnified through unnecessarily high gains in the grid-voltage feedforward. At 2 s and 10 s the grid-voltage harmonics are increased. After the first increase in harmonics, it takes 2.4 s for the P&O algorithm to reach the THD-minimizing gain of $0.6/V_C$ under slightly distorted grid voltages. The adaptive implementation produces 8 % lower THD than both conventional implementations, which produce approximately equal THD. After the second transient, it takes 1.6 s for the P&O algorithm to reach the new THD-minimizing gain ($0.9/V_C$). Due to highly distorted grid voltages, the zero gain produces significantly higher current THD than the constant $1/V_C$. However, the THD-minimizing gain produces THD that is more than 7 % lower than $1/V_C$ gain and 21 % lower than zero gain. The drawback of the P&O algorithm is that the gains start oscillating around the THD-minimizing gain by A_{pert}. The feedforward gain remains at the THD-minimizing gain half of the oscillation cycle (4 T_{pert}), while the gain is improperly adjusted by A_{pert} during the other half of the cycle. However, the effect on the output current THD is negligible compared to the benefits of the adaptive grid-voltage feedforward.

Figures 4.15b and 4.15c show individual harmonics of the output current, obtained between 7-9 s and 12-14 s during the experiment (Fig. 4.15a). Higher feedforward gain effectively mitigates the low-order harmonics, arising from the grid voltages, especially 3^{rd} and 5^{th}. For example, under high grid harmonics, the 3 rd harmonic can be mitigated over 70 % by using $1/V_C$ gain, and over 60 % with adaptive ($\approx 0.9/V_C$) gain compared to the constant zero gain. However, high feedforward gain magnifies higher-order harmonics arising from the inverter internal distortions.

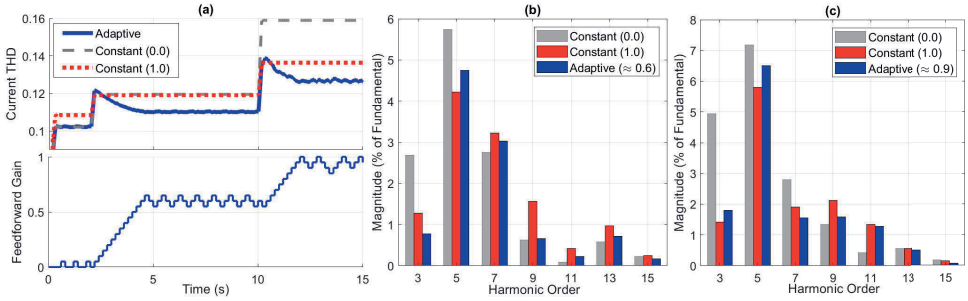

Figure 4.15 Performance comparison during grid transients (a), current harmonics under slightly distorted grid (b) and highly distorted grid (c).

4.6 Experiment 5: Adaptive Current-Control Loop

In this section, adaptive methods for the current-control loop and the digital notch filter are implemented inside the inverter control system. Methods are based on the online loop-gain measurements and re-shaping of the current-control loop. The impact on the current-control loop is illustrated and improvements in the power quality are verified through experimental tests.

The adaptive procedure of the current-control loop adjusts the controller parameters so that the loop magnification is 0 dB at the chosen bandwidth frequency $f_{\text{BW-CC}}$; that is, the bandwidth is kept constant under varying grid conditions. The selection of the bandwidth can be made arbitrarily, depending on the desired loop characteristics. System delays and the LCL resonance between the filter and the grid impedance usually set the upper limit for the gains, which can be increased significantly by applying the proposed adaptive notch filter. However, in order to achieve high bandwidth in weak grids, very high controller gains are required. High controller gains magnify external disturbances and may saturate output of the current controller, which must be considered when determining the desired loop characteristics and maximum controller gains.

During the inverter start-up, the online measurements of the current-control loop are performed by the MLBS. Fig. 4.11 has provided examples of the MLBS-based loop measurement under three different grid impedances. Based on the measured current-control loop, the center frequency (ω_o) of the adaptive notch filter (3.19) is adjusted to the frequency in which the high-frequency resonance peak appears. This high-frequency resonance peak is caused by the resonant pole of the LCL filter (2.45). Here the resonance peak is observed above 1000 Hz because the lowest possible frequency of the LCL resonant pole between the applied LC filter and the grid inductance (that corresponds to SCR value of 1.0) is approximately 1100 Hz. However, frequency of the resonant pole depends on the applied LC or LCL filter and must be re-considered for different systems.

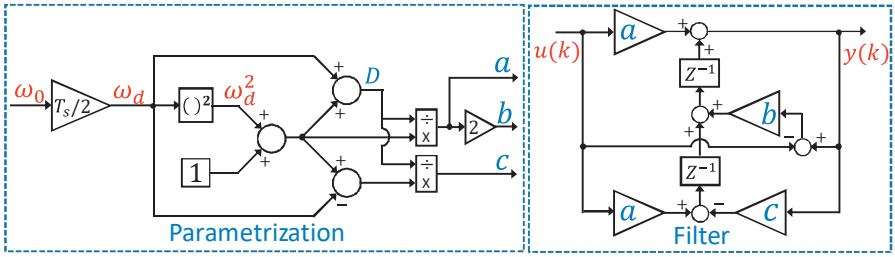

Figure 4.16 Implementation of adaptive notch filter.

For a practical implementation, the notch filter (3.19) must be discretized. This can be performed by the Tustin approximation, yielding

$$G_{\text{f-d}} = u(k)\left[a - bz^{-1} + az^{-2}\right] - y(k)\left[-bz^{-1} + cz^{-2}\right] \tag{4.1}$$

where z^{-1} is the unit delay, determined by the sampling time T_s of the control system, defined here by the inverter switching frequency $f_{\text{sw}} = 8$ kHz. Based on the determined central frequency, the parameters for the digital notch filter can be adjusted as

$$\begin{aligned} \omega_d &= \omega_0 T_s/2 \\ D &= 1 + \omega_d + \omega_d^2 \\ a &= \frac{1+\omega_d^2}{D} \\ b &= \frac{2(1+\omega_d^2)}{D} \\ c &= \frac{1-\omega_d+\omega_d^2}{D} \end{aligned} \tag{4.2}$$

Fig. 4.16 shows a block-diagram presentation of the parametrization process of the discrete notch filter, where the center frequency ω_0 is determined by the online loop measurement.

After the start-up process and adjustment of the digital notch filter, the adaptive process of the current controller is launched. Fig. 4.17 shows a practical implementation of the adaptive process. First, the desired bandwidth ($f_{\text{BW-CC}}$) is determined and the loop perturbed by a small-amplitude sinusoidal current at $f_{\text{BW-CC}}$. The loop responses (L_{IN} and L_{OUT}) are measured and fed to the adaptive controller where they are compared in a synchronous frame, rotating at f_{BW}. In the synchronous frame, amplitudes of the loop responses can be observed. The amplitude difference ($|L_{\text{IN}}(f_{\text{BW-CC}})| - |L_{\text{OUT}}(f_{\text{BW-CC}})|$) is regulated to zero by the PI-controller, whose output adjusts the current-controller gains, thereby affecting particularly to the amplitude of $L_{\text{OUT}}(f_{\text{BW-CC}})$. Consequently, magnification of the current-control loop is regulated to 0 dB at the frequency of the desired bandwidth when the amplitude difference is regulated

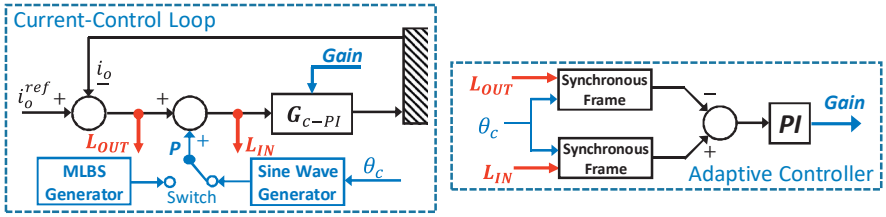

Figure 4.17 Implementation of adaptive process.

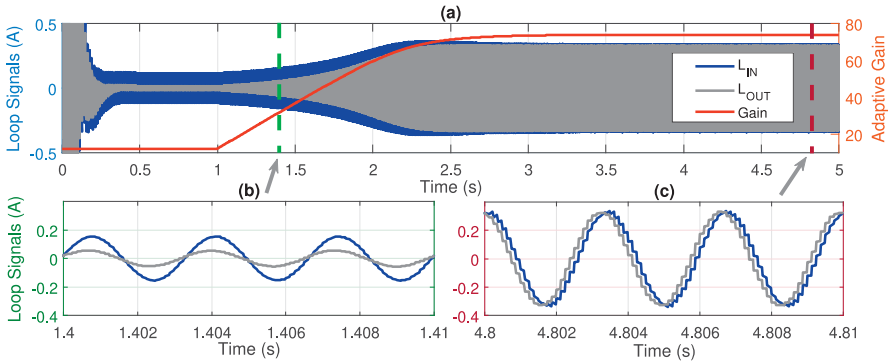

Figure 4.18 Operation of the adaptive control.

to zero. Symmetrical controllers are applied in the d and q channels.

Basic operation of the proposed adaptive re-adjustment of the current controller is illustrated through the simulation in MATLAB/Simulink. The Experimental Setup 2 is simulated, the system parameters are given in Table 4.1, and the inverter control parameters of Set1 (given in Table 4.2) are applied, where gains of the current controller are adaptively re-adjusted. Fig. 4.18a shows the adaptive operation during the inverter start-up. During the first second, the MLBS measurement of the current-control loop gain is performed and the notch filter is adjusted. Here, the desired loop bandwidth is chosen to be 300 Hz, so the loop is perturbed by sinusoidal current at that frequency. The PI-controller adjusts the current controller gains so that the amplitude difference of $L_{\text{OUT}}(300Hz)$ (grey line) and $L_{\text{IN}}(300Hz)$ (blue line) is regulated to zero, which means the desired bandwidth is reached. The suitable controller gains are found approximately at 3 s when the amplitude of $L_{\text{OUT}}(300Hz)$ equals to $L_{\text{IN}}(300Hz)$ amplitude. The lower parts of the figure illustrate the amplitude difference during the adaptive process at 1.4 s (b) and after the current-controller gain is properly adjusted at 4.8 s (c).

The experimental verification of the proposed methods is performed applying Experimental Setup 2. The adaptive process is performed similarly as in the simulations and the 300 Hz bandwidth is adaptively adjusted. In order to illustrate re-shaping property of the adaptive method, the online measurements of the current-control loop gain are obtained after each step of the adaptive process, given as

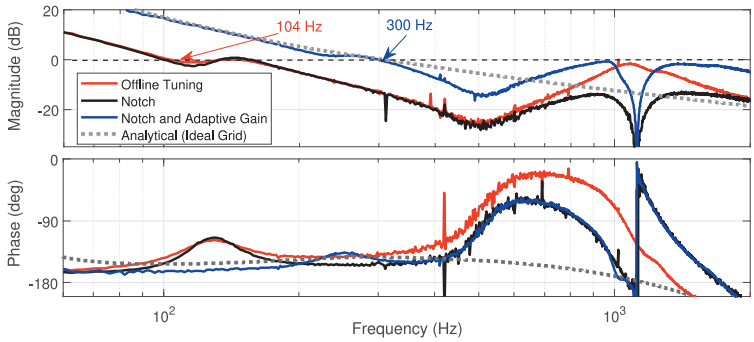

Figure 4.19 Measured loop gains during adaptive process.

- After grid connection, with control-parameter Set1 (Table 4.2).
- When the adaptive notch filter is adjusted based on the high-frequency maximum of the previous loop-gain measurement.
- When bandwidth of the current-control loop is adaptively adjusted.

The measurements are performed by a 2047-bit-long MLBS, generated at 4 kHz, yielding 1.95 Hz frequency resolution.

Fig. 4.19 shows MLBS-based online loop-gain measurements during the adaptive process when the inverter is connected to a weak (9 mH, SCR = 4.7) grid. The grey dashed line represents the analytical loop gain when the load effect is neglected from the analysis and the bandwidth is set to 300 Hz. The red line shows the online loop measurements when the inverter is connected to the grid but the adaptive process is not launched. The bandwidth is significantly decreased when the grid impedance is present. Based on the measurement, the central frequency of the notch filter is adjusted to 1150 Hz, where the load-affected LC-resonance peak occurs. The black line shows the loop gain when the notch filter is added to the loop, and the resonance peak is clearly mitigated. After adjusting the notch filters, the bandwidth is adaptively adjusted to 300 Hz, as illustrated in Fig. 4.18. The blue line shows the final current-control loop gain, when the notch filter has mitigated the resonance peak and the adaptive process has adjusted the desired 300 Hz bandwidth. Without a properly adjusted notch filter, increasing gains of the current controller cause impedance stability issues and harmonic resonance around the LC-resonance peak.

The control performance of different current-control loops is tested in a weak grid, where high grid impedance usually decreases control performance. In the experiment, an inverter is connected to a similar grid impedance (9 mH, SCR = 4.7), as in the previous experiment. A slight unbalance and third harmonic are generated to the grid voltages in order to produce distortions at 120 Hz and 180 Hz. Under such conditions, the distortion-mitigating ability of different current-control loops are tested. The upper part of Fig. 4.20 shows the magnitudes of each tested current-control loop, obtained by the online loop-gain measurements. The

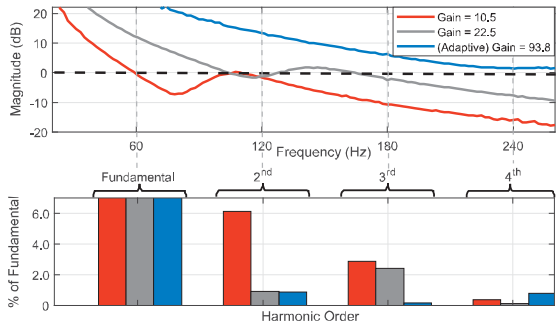

Figure 4.20 Effect of the loop gain under a weak grid with 3^{rd} harmonic and voltage unbalance.

blue line represents the proposed method, where the bandwidth is adaptively set to 300 Hz. The other two lines represent control designs that yield loop bandwidths below 180 Hz (grey line) and 120 Hz (red line) under such grid conditions. The lower part of the figure shows output current harmonics (2^{nd}, 3^{rd}, and 4^{th}) observed during normal operation of each tested current-control loops, where the colors match the loop magnitudes in the upper part of the figure. It can be seen that the harmonics are effectively mitigated within the bandwidth of the current-control loop. With the lowest bandwidth (red line) of 110 Hz, a significant amount of 120 Hz (2^{nd} harmonic) and 180 Hz (3^{rd} harmonic) distortions are produced. The loop (grey line) with a 160 Hz bandwidth is able to mitigate 2^{nd} harmonic distortion but not the 3^{rd} harmonic. The adaptive loop (blue line) with 300 Hz bandwidth effectively mitigates all present low-frequency distortions.

4.7 Experiment 6: Adaptive Control of Phase-Locked Loop

This section presents practical implementation of the adaptive SRF-PLL based on the real-time grid-impedance measurement. The resulting improvements in the inverter control performance in varying grid conditions are verified through the experimental tests. The results show that adjusting the PLL bandwidth with respect to the grid conditions is highly beneficial for system performance and stability.

The design of the adaptive SRF-PLL is based on the system sensitivity function (2.14), which can be applied as an indicator for the robustness and, in this case, for the control performance. By adaptively re-adjusting the PLL bandwidth based on the observed changes in the grid impedance, the sensitivity peak (2.15) can be kept at a constant value. The sensitivity limit should be carefully chosen as a good trade-off between the control performance and robustness; a higher limit allows the use of higher PLL bandwidths, but also an increased amount of distortions.

Fig. 4.21 shows analytical sensitivity functions, computed for the Experimental Setup 2, below 300 Hz when the inductive grid reactance (a), grid resistance (b), and the PLL band-

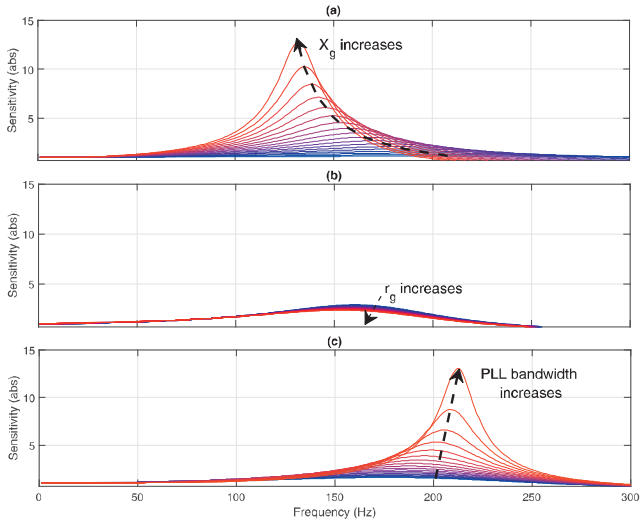

Figure 4.21 System sensitivity functions as (a) inductive grid reactance increases, (b) grid resistance increases, and (c) PLL bandwidth increases.

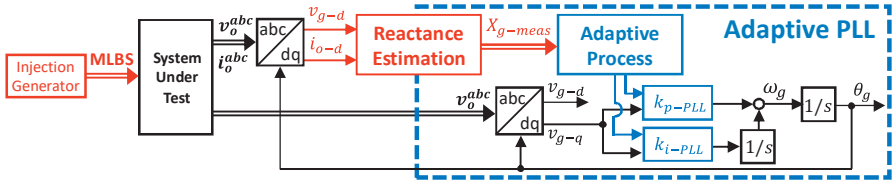

Figure 4.22 Implementation of adaptive SRF-PLL.

width (c) are increased. When the inverter control system is kept constant, the grid reactance clearly increases the sensitivity peak (2.15), but the resistance has a negligibly small effect. Higher PLL bandwidth in constant grid conditions increases the sensitivity peak, so this adjustable system parameter has a major effect in the system robustness. Consequently, when the inverter model is known, the low-frequency sensitivity function can be evaluated by the grid-reactance measurements. Therefore, the system sensitivity peak can be kept constant by adaptively re-adjusting the PLL bandwidth based on the grid-reactance measurements. Fig. 4.22 shows a general-level implementation of the adaptive process, where the measured grid reactance is applied in adaptive control of the PLL.

The PLL bandwidth can be adjusted by its PI-controller gains, shown in Fig. 4.22. The control gains depend on the voltage level of the grid, so the tuning procedure is performed for the Experimental Setup 2 ($V_{od} = \sqrt{2} \times 120V$). The PLL controller is tuned so that the phase margin of the PLL loop gain remains at 65 degrees for every bandwidth. By substituting $V_{od} = \sqrt{2} \times 120V$ and $\Theta_{PM} = 65°$ into (3.16), the controller gain can be computed as

$$\begin{aligned} K_{\text{p-PLL}} &= 0.0336 f_{\text{BW-PLL}} \\ K_{\text{i-PLL}} &= 0.0983 f_{\text{BW-PLL}}^2 \end{aligned} \tag{4.3}$$

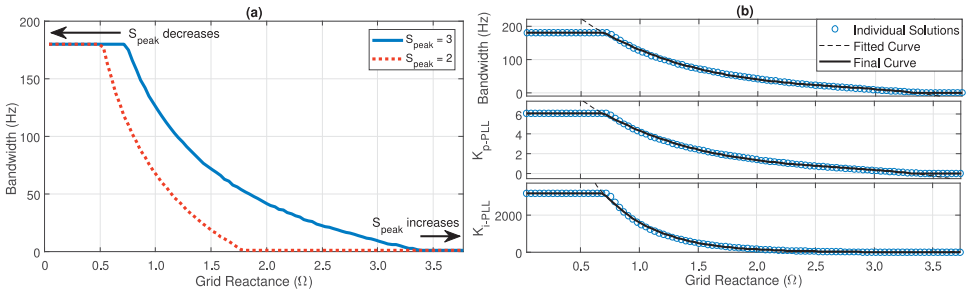

Figure 4.23 PLL bandwidths that satisfy chosen sensitivity limit (a) and fitted function from reactance to control gains (b).

where the proportional gain ($K_{\text{p-PLL}}$) is linearly depended on the desired PLL bandwidth while the integral gain ($K_{\text{i-PLL}}$) has squared dependency.

The function from the grid reactance to the PLL bandwidth is determined based on the analytical sensitivity peaks below 300 Hz (see Fig. 4.21). The sensitivity peaks are computed for various inverter output admittances and grid impedances by substituting them as pairs into equation for the sensitivity function (2.15). Here the grid impedance is modeled with inductive reactance values varying from 0.038 to 4.0 Ω (resolution 0.038 Ω), which corresponds to equivalent SCR from 421 to 4. The grid resistance is kept constant ($r_g = 0.1\ \Omega$) due to its negligibly small impact on the system sensitivity (see Fig. 4.21). The inverter output admittance is modeled with a PLL bandwidth resolution of 1 Hz and limited between 1 and 180 Hz. An appropriate PLL bandwidth is determined for every grid-reactance value, so that the bandwidth-reactance pair satisfies the chosen sensitivity limit. For example, Fig. 4.23a shows the PLL bandwidths that satisfy most accurately the sensitivity limit of two (red line) and three (blue line).

In the final step of the design process, the continuous function from the grid reactance to the PLL bandwidth is fitted based on the reactance-bandwidth pairs. In these experiments, the sensitivity limit of three is chosen as the adaptive rule, representing the blue line in Fig. 4.23a, to which the continuous function is fitted. A least-square regression and third-degree polynomial function are applied in the curve fitting process. Fig. 4.23b shows the fitted third-order function (black dashed line), which can be written as

$$f_{\text{BW-PLL}} = -13.43X_g^3 + 111.24X_g^2 - 327.03X_g + 357.90 \tag{4.4}$$

The final controller gains are generated by substituting (4.4) into (4.3) as

$$\begin{aligned} K_{\text{p-PLL}} &= 0.0336(-13.43X_g^3 + 111.24X_g^2 - 327.03X_g + 357.90) \\ K_{\text{i-PLL}} &= 0.0983(-13.43X_g^3 + 111.24X_g^2 - 327.03X_g + 357.90)^2 \end{aligned} \tag{4.5}$$

The real-time measurement system determines important properties of the adaptive per-

formance, such as, reaction time to the grid-impedance transients. A rapid increase in grid impedance may destabilize the system, so the fast reaction time is required from the measurement system. The grid-impedance is measured by the MLBS, from which the grid reactance at fundamental grid frequency can be computed as

$$X_{\mathrm{g}} = \frac{\mathrm{Im}[Z_{\mathrm{g}}(\omega)]}{\omega} \times \omega_{\mathrm{g}} \tag{4.6}$$

where $\mathrm{Im}[Z_{\mathrm{g}}(\omega)]$ is imaginary part (reactance) of the measured grid impedance, ω is the angular frequency, and ω_{g} is the fundamental frequency ($2\pi 60$ Hz). The reactance can be estimated at multiple frequencies of the grid-impedance measurement. Therefore, results from different frequencies can be considered as individual estimates, which are not polluted by same disturbances. Because the estimation procedure (4.6) cannot process high resonance peaks correctly, the reactance estimations are obtained below 400 Hz, where high resonance peaks are considered to rarely appear. Additionally, identified frequencies are chosen so that dominating periodic distortions are avoided, which in the DQ domain (60 Hz grid) are unbalanced grid voltages (oscillations at 120 Hz) and the fifth harmonic (appears at 360 Hz). The third (in-phase) harmonic occurs only in the zero component and does not affect the measured d component. The final reactance value is given as a median from estimates at multiple frequencies. This reduce measurement errors, but does not increase the measurement time similar to conventional averaging over many measurement cycles.

The performance of the adaptive PLL is verified by experimental tests applying Experimental Setup 2. Grid-side impedance is varied by switching the by-pass relay of the additional hardware inductance located between the inverter and the grid emulator. The relay is located very near to the inverter output terminals, which means that switching produces drastic transient in the grid conditions; for example, to PCC voltage and the actual impedance. Thus, the experimental test are performed in extremely challenging conditions for the adaptive performance.

In the experiments, a 31-bit-long MLBS is generated at 1 kHz and injected on top of the current reference d-component with 0.1 A ($<$ 1 % of the nominal current) injection amplitude. This provides a frequency resolution of 32.3 Hz and measurement time of 31 ms. The grid reactance is given as a median from estimates at five different frequencies, chosen as 193.5 Hz, 225.8 Hz, 258.1 Hz, 290.3 Hz, and 322.6 Hz. These frequencies are below 400 Hz and are not significantly polluted by neither 120 Hz nor 360 Hz oscillations. The grid-reactance measurement is filtered through a first-order low-pass filter with a time constant of 1 s in order to reduce fluctuations of the PLL bandwidth at the steady state. However, the slow time-domain filtering is by-passed when a rapid change in grid impedance occurs. If the measured grid reactance (prior filtering) is 0.5 Ω greater than the filter output, the control interprets this as an rapid grid-impedance change and injects an impulse-like signal (multiplies the latest estimation by 10) to the measured grid reactance. This decreases the PLL band-

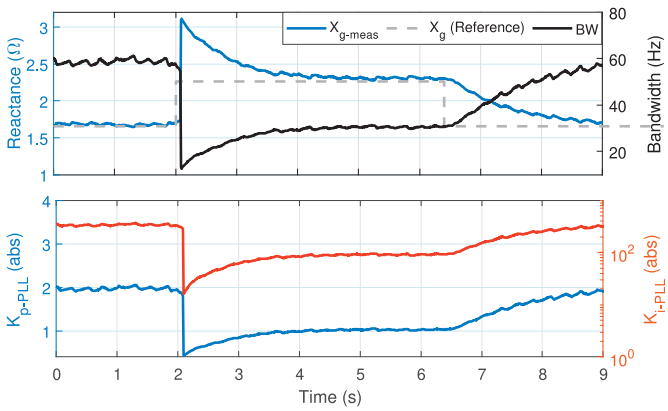

Figure 4.24 Adaptive control during changes in grid impedance.

width within tens of ms, so that the stability is preserved even in drastic grid impedance changes, such as grid faults.

Fig. 4.24 illustrates the operation of the adaptive control and shows how the PLL control parameters follow the grid-reactance estimates under varying grid impedance. The system is connected to a relatively strong grid (SCR $\approx$ 10.0), the grid-reactance measurement is settled around 1.65 Ω, and the PLL bandwidth is adaptively adjusted approximately to 60 Hz. At 2 s, a sudden increase in grid impedance (SCR $\approx$ 6.7) occurs that triggers the overshooting by-pass of the slow reactance-estimation filtering, thereby decreasing the PLL bandwidth rapidly. After the overshoot, the reactance estimation settles around 2.35 Ω and the PLL bandwidth to 29 Hz. The grid-reactance measurement decreases back to 1.65 Ω at 6.5 s. Decrease in the grid impedance does not trigger the by-passing operation of the slow filtering, meaning that the original steady-state bandwidth ($\approx$ 60 Hz) is adjusted after approximately two seconds.

Fig. 4.25 shows the performance comparison between two constant-bandwidth (40 and 50 Hz) PLLs and the adaptive PLL during a drastic increase in the grid impedance (grid fault). First, the inverter is connected to a grid with approximately 2.1 Ω grid reactance (SCR $\approx$ 7.6) where the PLL bandwidth is adaptively adjusted around 40 Hz. The grid reactance is suddenly increased to approximately 3.45 Ω (SCR $\approx$ 4.5) at 0.1 s, where the adaptive control proposes 2 Hz PLL bandwidth. The rapid increase in the grid impedance is noticed 50 ms after the transient, which triggers by-passing operation of the reactance-estimation filter. Due to overshoot in the reactance estimation, the adaptive implementation (blue lines) decreases the bandwidth from 40 Hz to its lower limit 1 Hz. With the adaptively controlled PLL, the oscillations in i_{oq} and v_q (blue lines, figures in the middle) are effectively mitigated. With a constant 40 Hz PLL (red lines), the voltages and currents continue to oscillate after the transient, which indicates insufficient stability margins. The inverter with a constant 50 Hz PLL (gray lines) becomes unstable (or marginally stable) after the transient, extremely high oscillations appear in the waveforms, and the system cannot recover from the grid-

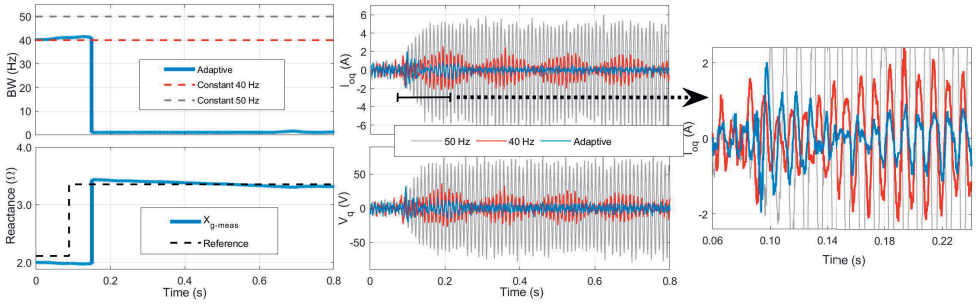

Figure 4.25 Performance comparison of adaptive PLL and conventional constant-bandwidth PLLs during grid transient.

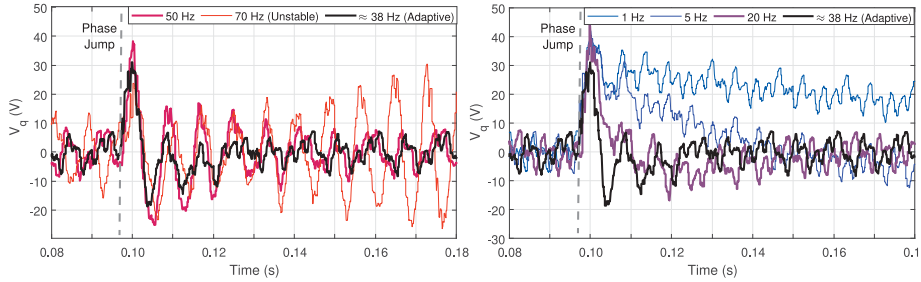

Figure 4.26 Performance comparison of different PLLs during phase jump in grid voltages.

impedance transient. The right-hand side of the figure takes a closer look at i_{oq} during the grid-impedance transient.

Fig. 4.26 shows the transient response in v_q during a 30-degree phase jump in grid voltages. Different PLL bandwidths are compared in a grid with approximately 2.1 Ω grid reactance (SCR ≈ 7.6). For a chosen sensitivity limit of three, the adaptive procedure proposes approximately 38 Hz bandwidth. In order to illustrate the sensitivity peak (limit) as an indicator of robustness and control performance, the adaptive PLL is compared to higher (50 and 70 Hz) and lower (1, 10, and 20 Hz) bandwidths. As shown in the left-hand side of the figure, oscillations are magnified when higher PLL bandwidths are applied. This indicates increased system sensitivity, and therefore insufficient stability margins. The oscillations are mitigated by using a lower PLL bandwidth. However, a lower bandwidth decreases the voltage-tracking performance as the settling time of v_q is increased. Here, the non-zero v_q means a momentary loss of the optimal grid synchronization that affects the whole DQ domain control performance of the inverter. Therefore, a good trade-off between high and low bandwidths can be achieved by considering the desired value of the system sensitivity peak.

These experimental tests are chosen to demonstrate the performance of the proposed adaptive re-adjustment of the PLL bandwidth based on the real-time grid reactance estimation. Consequently, any specific fault types are not considered; instead, general-level behavior of the proposed sensitivity-function-based approach for adaptive SRF-PLL is demonstrated.

5 CONCLUSIONS

The number of grid-connected inverters used for grid integration of the renewable energy has increased rapidly, which has started to affect the power-system dynamics, particularly in areas where majority of the power is generated through the inverters. One of the main issues arising from interactions between the inverters and the local power-system dynamics is the harmonic resonance that indicates poor stability margins, leading to poor or even unstable operation of the grid-connected system.

Stability of the grid-connected system can be assessed by an impedance-based stability analysis, where system stability is assessed by a ratio between the grid impedance and the inverter output impedance. The inverter output impedance is mostly determined by the applied control system. However, the grid impedance usually remains unknown, which prevents the inverter output impedance from being customized, so that the impedance-based stability is ensured in the grid-connection point. Additionally, the grid conditions typically vary over time, which makes the offline measurements and general models of the grid impedance inefficient in terms of assessing the system stability. Therefore, in order to ensure proper operation of a grid-connected system in varying grid conditions, real-time methods for assessing and improving the system stability are preferred. One effective method is the inverter adaptive control based on real-time measurements of the grid impedance.

Previous studies have presented broadband methods for frequency response measurements that can be utilized in real-time measurements of the grid-impedance. In these methods, a broadband sequence such as an impulse or a pseudo-random binary sequence (PRBS) is injected, for example, on top of the inverter control reference. The inverter output currents and grid voltages are measured and Fourier techniques are applied to obtain the grid impedance. Such measurements are generally quite simple. However, real-time measurements of the grid impedance present several challenges that arise from the special characteristics of the grid-connected systems. One of the main issues is related to the grid voltages, whose harmonics, unbalance, and other distortions affect the measurements. Another challenge is the impact of the perturbations to the generated power quality, which becomes particularly important when the real-time measurements are continuously performed. A common way of improving the accuracy of the frequency response measurements is to increase the perturbation amplitude or number of averaged periods. However, the measurement time and induced interference to the grid are usually strictly limited in the grid-connected system,

which prevents the application of a high number of averaged periods or high perturbation amplitude.

This thesis has investigated methods for fast online measurements of grid-connected systems that can be performed in real time. The pseudo-random sequences, such as maximum-length binary sequence (MLBS), are applied as perturbations in the measurements. The MLBS has widely modifiable spectral properties for different applications, and the sequence itself has multiple good characteristics; for example, the sequence is easy to generate using a simple shift-register circuit. In addition, the MLBS has a very low crest factor, which means that the signal energy is very high with respect to the signal time-domain amplitude. Furthermore, the MLBS is deterministic, which makes it possible to average the obtained results over multiple repeated periods. Another type of pseudo-random sequences applied in the thesis is orthogonal binary sequences. Such sequences do not have energy at common frequencies, making them useful for measuring several frequency responses at the same time. The sequences are useful particularly in the DQ-domain measurements of three-phase grid-connected systems. Such measurements are typically composed of several different (coupled) components. By applying the orthogonal sequences, the components can be simultaneously measured during a single measurement cycle. This approach not only saves overall experimentation time, but also ensures that each component is measured with the system in the same conditions, which may not be the case if sequential perturbations are applied

The real-time measurements of the grid characteristics, such as the grid impedance, can be applied to monitor and to adaptively improve the performance of the grid-connected systems. The stability-analysis method applied in the thesis is based on the generalized Nyquist stability criterion and the real-time measurements of the grid impedance. The applied adaptive methods for the grid-connected inverter can be summarized as follows.

- The grid-reactance measurements are applied in adaptive control of the PLL. The impedance-based sensitivity function is kept constant by adaptively re-adjusting the PLL bandwidth based on the real-time measurements of the grid impedance. The method ensures the system stability and the adequate voltage-tracking performance in wide range of grid impedance values by maximizing the PLL bandwidth under certain stability limits.
- Online loop-gain measurements of the current-control loop are applied for the self-tuning method, where current-control gains are re-adjusted online so that the desired bandwidth under varying grid impedance is achieved. Similar measurements are used to adjust the adaptive parameters of the digital Notch filter, which is added into the loop to mitigate resonance peak between the applied AC filter and the grid impedance. This improves the high-frequency stability and enables higher gains in the current-control loop. As the grid-voltage harmonics are effectively mitigated within the control bandwidth of the current-control loop, the proposed method improves the power

quality and makes the inverter performance more predictable.

- The produced output-current THD is observed in real time for adaptive control of the grid-voltage feedforward. The adaptive method is based on the perturb-and-observe algorithm that adaptively adjusts the feedforward gain so that the observed current THD is minimized. The increased feedforward gain is shown to mitigate low-frequency disturbances from the grid side, but to magnify the inverter internal disturbances. Consequently, the THD-minimizing gain is a tradeoff between this dualistic impact of the grid-voltage feedforward, which depends on quality of the grid voltages. The method has a plug-and-play feature and does not require any prior knowledge about the grid conditions.

The proposed real-time measurement and adaptive-control methods were verified by numerous experimental power hardware-in-the-loop tests with real power and hardware. The experiments demonstrated the performance of the real-time measurement methods and the importance of the systematic measurement design. The adaptive operations were shown to improve the inverter stability, produced power quality and transient performance when the grid conditions experience drastic changes, such as grid faults.

Discussion and Criticism

The proposed measurement methods applying pseudo-random binary sequences were originally designed for measuring the linear systems. However, in some cases, the inverter and grid dynamics may be highly nonlinear, especially when the local grid-connection point include multiple power-electronics devices nearby. The non-linear characteristics are not considered in this thesis, and they may decrease the measurement accuracy. To solve this issue, recent studies have presented multilevel perturbation sequences, such as ternary sequences, that perform more efficiently under non-linear conditions [98].

Although the methods presented in this thesis are applicable to a wide range of different grid-connected systems, some drastic grid faults may cause overly high and sudden variations in the grid impedance that prevent the presented methods from being applied as intended. In such conditions, the impedance-based stability is not accurately assessed and the adaptive operations may fail to react to the changes.

It may be obvious that, in many local areas, the grid conditions remain approximately constant over time. In such cases there may be no need to apply continuous stability assessment or adaptive control. However, the presented methods are still applicable, for example, during start-up processes of the systems.

In the present thesis, the adaptive methods are implemented only for a single grid-connected inverter. However, adaptive control of a single device does not significantly improve the local power quality if other nearby devices perform poorly. Additionally, in adaptive

control of multiple devices, some communication between the devices should be applied. This is mainly because multiple devices should not simultaneously inject current injections to the same grid-connection point and measure the same grid impedance.

5.1 Summary of Publications

[P1]
The paper presents a practical method for measuring the DQ domain grid impedance by using an existing inverter. The measurements are based on the orthogonal binary sequences and can be performed in real time. In the methods, the orthogonal binary sequences are added on top of the inverter current references, and thereby injected to the grid as current perturbations. This makes it possible to obtain frequency response measurement of the grid impedance from the inverter output currents and grid voltages, which are already measured for the inverter control purposes. Thus, the methods do not require any additional measurement devices.

[P2]
The paper presents a perturbation design process to mitigate the effect of the grid-voltage unbalance and harmonics from the frequency response measurements of the grid-connected systems. The design method ensures that the integer amount of the grid fundamental cycles is included in the total measurement time; this minimizes the spectral leakage caused by grid-voltage harmonics and improves the obtained results, especially under poor grid voltages. The effectiveness of the design method is verified by analyzing the total variance of DQ domain grid-impedance measurements with different perturbations designs.

[P3]
The paper introduces a method for assessing the impedance-based stability in real time. The method is based on the real-time measurement of the DQ domain grid impedance, multivariable small-signal model of the inverter output admittance, and generalized Nyquist stability criterion. The impedance-based stability is visualized by the system eigenloci that is updated in real time. The method is highly modifiable and can be used, for example, to obtain accurate impedance-based stability margins or to provide rapid observations of the system stability under varying grid conditions.

[P4]
The paper presents a practical implementation of the adaptive PLL for the grid-connected inverters based on the real-time grid reactance measurements and the system sensitivity function. It is shown that the low-frequency sensitivity function of the grid-connected inverter

can be accurately evaluated by the measured grid-reactance and the inverter small-signal model. The PLL control parameters are adaptively re-adjusted based on the measured grid reactance so that the system sensitivity peak is kept constant. Very fast measurement methods are applied and the adaptive system is shown to react to drastic grid changes within a few tens of milliseconds. The adaptive method is shown to improve the overall control performance and to ensure stability of the grid-connected inverter under varying grid conditions.

[P5]

The paper considers adaptive control of the inverter current-control loop based on the online loop gain measurements. The grid impedance is shown to affect the loop stability and to decrease its bandwidth, which degrades the harmonic-mitigating ability of the current controller. The proposed adaptive methods can be divided into two main parts. First, the loop gain is measured by the MLBS, the grid-affected high-frequency resonance peak is observed, and parameters of the digital Notch filter are adjusted so that the observed resonance peak is effectively mitigated. This improves system stability and makes it possible to use higher gains in the current controller. In the second part, the bandwidth of the current-control loop is adaptively re-adjusted based on the online loop-gain measurements. This is shown to effectively mitigate the impact of the grid impedance from the current-control loop, thereby improving the control performance under various grid impedances.

[P6]

This paper introduces an adaptive method for improving the performance of the grid-voltage feedforward. The grid-voltage feedforward is shown to have a dualistic impact; it effectively mitigates distortions from the grid side, but magnifies inverter internal distortions. Therefore, the optimal feedforward gain depends on the local power quality. The adaptive method is based on the perturb-and-observe algorithm that observes the output current THD in real time and adjusts the feedforward gains so that THD is minimized, and thus enhances power quality. The method has a plug-and-play feature and is shown to effectively adjust the THD-minimizing feedforward gains without prior knowledge about the grid conditions.

REFERENCES

[1] *Paris Agreement*. United Nations Treaty Collection, Chapter XXVII 7. D. United Nations. 2015.

[2] *Global Warming of 1.5C. In An IPCC Special Report on the Impacts of Global Warming of 1.5C Above Pre-Industrial Levels and Related Global Greenhouse Gas Emission Pathways, in the Context of Strengthening the Global Response to the Threat of Climate Change, Sustainable Development, and Efforts to Eradicate Poverty*. The Intergovernmental Panel on Climate Change. United Nations. 2018.

[3] *The Sustainable Development Goals Report 2019*. Available Online: doi.org/10.18356/55eb9109-en. United Nations. New York, 2019.

[4] *Statistical Review of World Energy 2019*. Available Online: www.bp.com/en/global/corporate/energy-economics/statistical-review-of-world-energy. British Petrol (BP). 2019.

[5] D. Bogdanov et al. "Radical transformation pathway towards sustainable electricity via evolutionary steps," Nature Communications, vol. 10, no. 1107, pp. 1-16, 2019.

[6] *Directive (EU) 2018/2002 of the European Parliament and of the Council of 11 December 2018 amending Directive 2012/27/EU on energy efficiency*. European Union. 2018.

[7] *Global market outlook for solar power 2019-2023*. Tech. Rep. SolarPower Europe. 2019.

[8] *Renewables 2018, Market analysis and forecast from 2018 to 2023*. Available Online: www.iea.org/renewables2018/. International Energy Agency (IEA). 2018.

[9] P. Kundur. "Power System Stability and Control," McGraw-Hill, 1994.

[10] B. K. Bose. "Global Energy Scenario and Impact of Power Electronics in 21st Century," IEEE Transactions on Industrial Electronics, vol. 60, no. 7, pp. 2638-2651, 2013.

[11] B. Kroposki et al. "Achieving a 100 % Renewable Grid: Operating Electric Power Systems with Extremely High Levels of Variable Renewable Energy," IEEE Power and Energy Magazine, vol. 15, no. 2, pp. 61-73, 2017.

[12] F. Blaabjerg, Z. Chen and S. B. Kjaer. "Power electronics as efficient interface in dispersed power generation systems," IEEE Transactions on Power Electronics, vol. 19, no. 5, pp. 1184-1194, 2004.

[13] B. K. Bose. "Power Electronics, Smart Grid, and Renewable Energy Systems," Proceedings of the IEEE, vol. 105, no. 11, pp. 2011-2018, 2017.

[14] F. Blaabjerg, Y. Yang, D. Yang and X. Wang. "Distributed Power- Generation Systems and Protection," Proceedings of the IEEE, vol. 105, no. 7, pp. 1311-1331, 2017.

[15] T. Suntio, T. Messo and J. Puukko. "Power Electronic Converters," Wiley VCH, 2017.

[16] P. Fairley. "Customers seek 100-percent-renewable grids," IEEE Spectrum, vol. 54, no. 9, pp. 12-13, 2017.

[17] J. O'Sullivan et al. "Achieving the Highest Levels of Wind Integration— A System Operator Perspective," IEEE Transactions on Sustainable Energy, vol. 3, no. 4, pp. 819-826, 2012.

[18] C. Li. "Unstable operation of photovoltaic inverter from field experiences," IEEE Transactions on Power Delivery, vol. 33, no. 2, pp. 1013-1015, 2018.

[19] J. H. R. Enslin and P. J. M. Heskes. "Harmonic interaction between a large number of distributed power inverters and the distribution network," IEEE Transactions on Power Electronics, vol. 19, no. 6, pp. 1586-1593, 2004.

[20] X. Liang. "Emerging Power Quality Challenges Due to Integration of Renewable Energy Sources," IEEE Transactions on Industry Applications, vol. 53, no. 2, pp. 855-866, 2017.

[21] T. Suntio et al. "Impedance-based interactions in grid-tied three-phase inverters in renewable energy applications," Energies, vol. 12, no. 3, 31 pages, 2019.

[22] J. Sun. "Impedance-Based Stability Criterion for Grid-Connected Inverters," IEEE Transactions on Power Electronics, vol. 26, no. 11, pp. 3075-3078, 2011.

[23] M. Céspedes and J. Sun. "Impedance shaping of three-phase grid-parallel voltage-source converters," Annual IEEE Applied Power Electronics Conference and Exposition, pp. 754-760, 2012.

[24] T. Messo et al. "Time and frequency-domain evidence on power quality issues caused by grid-connected three-phase photovoltaic inverters," European Conference on Power Electronics and Applications, 9 pages, 2014.

[25] P. Belkin. "Event of 10/22/09," CREZ Technical Conference, Electrical Reliability Council of Texas, 2010.

[26] C. Buchhagen et al. "BorWin1 – First Experiences with harmonic interactions in converter dominated grids," International ETG Congress; Die Energiewende - Blueprints for the new energy age, pp. 27-33, 2015.

[27] L. Wang et al. "Investigation of SSR in practical DFIG-based wind farms connected to a series-compensated power system," IEEE Transactions on Power Systems, vol. 30, no. 5, pp. 2772-2779, 2015.

[28] L. Liang et al. "Variable-Generation Integration in China: An Update," IEEE Power and Energy Magazine, vol. 17, no. 6, pp. 99-107, 2019.

[29] J. Schoukens, K. Godfrey and M. Schoukens. "Nonparametric data-driven modeling of linear systems: Estimating the frequency response and impulse response function," IEEE Control Systems Magazine, vol. 38, no. 4, pp. 49-88, 2018.

[30] K. O. H. Pedersen, A. H. Nielsen and N. K. Poulsen. "Short-circuit impedance measurement," IEEE Proceedings - Generation, Transmission and Distribution, vol. 150, no. 2, pp. 169-174, 2003.

[31] K. R. Godfrey. "Perturbation Signals for System Identification," Prentice Hall, UK. 1993.

[32] T. Roinila, M. Vilkko and J. Sun. "Broadband methods for online grid impedance measurement," IEEE Energy Conversion Congress and Exposition, pp. 3003-3010, 2013.

[33] M. Céspedes and J. Sun. "Online grid impedance identification for adaptive control of grid-connected inverters," IEEE Energy Conversion Congress and Exposition, pp. 914-921, 2012.

[34] T. Messo et al. "Real-time impedance-based stability assessment of grid converter interactions," Workshop on Control and Modeling for Power Electronics, 8 pages, 2017.

[35] M. Liserre, R. Teodorescu and F. Blaabjerg. "Stability of photovoltaic and wind turbine grid-connected inverters for a large set of grid impedance values," IEEE Transactions on Power Electronics, vol. 21, no. 1, pp. 263-272, 2006.

[36] M. Céspedes and J. Sun. "Adaptive Control of Grid-Connected Inverters Based on Online Grid Impedance Measurements," IEEE Transactions on Sustainable Energy, vol. 5, no. 2, pp. 516-523, 2014.

[37] A. S. Morched and P. Kundur. "Identification and modeling of load characteristics at high frequencies," IEEE Transactions on Power System, vol. 2, pp. 153-160, 1987.

[38] A. A. Girgis and R. B. McManis. "Frequency domain techniques for modelling distribution transmission networks using capacitor switching induced transients," IEEE Transactions on Power Delivery, vol. 4, pp. 1882-1890, 1989.

[39] M. B. Harris et al. "Instrumentation for measurement of line impedance," IEEE Applied Power Electronics Conference and Exposition, pp. 887-893, 1994.

[40] J. P. Rhode, A. W. Kelley and M. E. Baran. "Complete characterization of utilization-voltage power system impedance using wideband measurement," IEEE Transactions on Industry Applications, vol. 33, no. 6, pp. 1472-1479, 1997.

[41] B. Palethorpe, M. Sumner and D. W. P. Thomas. "Power system impedance measurement using a power electronic converter," International Conference on Harmonics and Quality of Power, pp. 208-213, 2000.

[42] A. V. Timbus et al. "Online grid measurement and ENS detection for PV inverter running on highly inductive grid," IEEE Power Electronics Letters, vol. 2, no. 3, pp. 77-82, 2004.

[43] L. Asiminoaei et al. "A digital controlled PV-inverter with grid impedance estimation for ENS detection," IEEE Transactions on Power Electronics, vol. 20, no. 6, pp. 1480-1490, 2005.

[44] M. Jordan et al. "Frequency dependent grid-impedance determination with pulse-width-modulation-signals," International Conference-Workshop Compatibility and Power Electronics, pp. 131-136, 2011.

[45] T. Roinila, M. Vilkko and J. Sun. "Online Grid Impedance Measurement Using Discrete-Interval Binary Sequence Injection," IEEE Journal of Emerging and Selected Topics in Power Electronics, vol. 2, no. 4, pp. 985-993, 2014.

[46] T. Roinila, T. Messo and E. Santi. "Mimo-identification techniques for rapid impedance-based stability assessment of three-phase systems in dq domain," IEEE Transactions on Power Electronics, vol. 33, no. 5, pp. 4015-4022, 2018.

[47] M. Sumner, B. Palethorpe and D. W. P. Thomas. "Impedance measurement for improved power quality-Part 2: a new technique for stand-alone active shunt filter control," IEEE Transactions on Power Delivery, vol. 19, no. 3, pp. 1457-1463, 2004.

[48] A. Tarkiainen et al. "Identification of grid impedance for purposes of voltage feedback active filtering," IEEE Power Electronics Letters, vol. 2, no. 1, pp. 6-10, 2004.

[49] J. C. Vasquez et al. "Adaptive Droop Control Applied to Voltage-Source Inverters Operating in Grid-Connected and Islanded Modes," IEEE Transactions on Industrial Electronics, vol. 56, no. 10, pp. 4088-4096, 2009.

[50] J. D. Kooning et al. "Grid voltage control with distributed generation using online grid impedance estimation," Sustainable Energy, Grids and Networks, vol. 5, pp. 70-77, 2016.

[51] B. Arif et al. "Finite Set Model Predictive Control with a novel online grid inductance estimation technique," IET International Conference on Power Electronics, Machines and Drives, 6 pages, 2014.

[52] M. Sumner et al. "Real Time Parameter Estimation for Power Quality Control and Intelligent Protection of Grid-Connected Power Electronic Converters," IEEE Transactions on Smart Grid, vol. 5, no. 4, pp. 1602-1607, 2014.

[53] B. Wen et al. "Small-Signal Stability Analysis of Three-Phase AC Systems in the Presence of Constant Power Loads Based on Measured d-q Frame Impedan- ces," IEEE Transactions on Power Electronics, vol. 30, no. 10, pp. 5952-5963, 2015.

[54] A. Rygg and M. Molinas. "Real-time stability analysis of power electronic systems," IEEE Workshop on Control and Modeling for Power Electronics, 7 pages, 2016.

[55] D. K. Choi and D. H. K. nad K. B. Lee. "A novel gain scheduling method for distributed power generation systems with a LCL-filter by estimating grid impedance," IEEE International Symposium on Industrial Electronics, pp. 3438-3443, 2010.

[56] A. Ghanem et al. "Grid impedance estimation for islanding detection and adaptive control of converters," IET Power Electronics, vol. 10, no. 11, pp. 1279-1288, 2017.

[57] D. Martin and E. Santi. "Autotuning of Digital Deadbeat Current Controllers for Grid-Tie Inverters Using Wide Bandwidth Impedance Identification," IEEE Transactions on Industry Applications, vol 50, no. 1, pp. 441-451, 2014.

[58] X. Chen et al. "Hybrid damping adaptive control scheme for grid-connected inverters in a weak grid," IET Power Electronics, vol. 9, no. 15, pp. 2760-2768, 2016.

[59] H. Abdollahi et al. "A Novel DC Power Distribution System Stabilization Method Based on Adaptive Resonance-Enhanced Voltage Controller," IEEE Transactions on Industrial Electronics, vol. 66, no. 7, pp. 5653-5662, 2019.

[60] A. Rygg et al. "On the Equivalence and Impact on Stability of Impedance Modeling of Power Electronic Converters in Different Domains," IEEE Journal of Emerging and Selected Topics in Power Electronics, vol. 5, no. 4, pp. 1444-1454, 2017.

[61] R. Teodorescu, M. Liserre and P. Rodríguez. "Grid Converters for Photovoltaic and Wind Power Systems," John Wiley Sons, Ltd, 2010.

[62] H. Akagi, E. H. Watanabe and M. Aredes. "Instantaneous Power Theory and Applications to Power Conditioning," Wiley-IEEE Press. 2017.

[63] M. Belkhayat. "Stability Criteria For AC Power Systems with Regulated Loads," PhD Thesis, Purdue University, 1997.

[64] S. Skogestad and I. Postlethwaite. "Multivariable Feedback Control: Analysis and Design, 2nd Edition," New York: Wiley, 2007.

[65] S. Vesti et al. "Impedance-Based Stability and Transient-Performance Assessment Applying Maximum Peak Criteria," IEEE Transactions on Power Electronics, vol. 28, no. 5, pp. 2099-2104, 2013.

[66] C. Moler. "Numerical Computing with MATLAB," Society for Industrial and Applied Mathematics, 2004.

[67] L. Harnefors. "Modeling of Three-Phase Dynamic Systems Using Complex Transfer Functions and Transfer Matrices," IEEE Transactions on Industrial Electronics, vol. 54, no. 4, pp. 2239-2248, 2007.

[68] R. D. Middlebrook and S. Cuk. "A general unified approach to modelling switching-converter power stages," IEEE Power Electronics Specialists Conference, pp. 18-34, 1976.

[69] T. Messo. "Factors Affecting Stable Operation of Grid-Connected Three-Phase Photovoltaic Inverters," PhD Thesis, Tampere University of Technology, 2014.

[70] T. Messo, A. Aapro and T. Suntio. "Generalized multivariable small-signal model of three-phase grid-connected inverter in DQ-domain," IEEE Workshop on Control and Modeling for Power Electronics, 8 pages, 2015.

[71] R. Dorf and R. Bishop. "Modern Control Systems," Prentice-Hall, 2000.

[72] J. Kivimäki et al. "Revisited Perturbation Frequency Design Guideline for Direct Fixed-Step Maximum Power Point Tracking Algorithms," IEEE Transactions on Industrial Electronics, vol. 64, no. 6, pp. 4601-4609, 2017.

[73] T. Messo, R. Luhtala, A. Aapro and T. Roinila. "Accurate Impedance Model of a Grid-Connected Inverter for Small-Signal Stability Assessment in High-Impedance Grids", IEEJ Journal of Industry Applications, vol. 8, no. 3, pp. 488-496, 2019.

[74] C. M. Wu et al. "Analytical technique for calculating the output harmonics of an h-bridge inverter with dead time," IEEE Transactions on Circuits and Systems I, vol. 46, no. 5, pp. 617-626, 1999.

[75] H. Alenius, R. Luhtala, T. Messo and T. Roinila. "Autonomous reactive power support for smart photovoltaic inverter based on real-time grid-impedance measurements of a weak grid," Electric Power Systems Research, vol. 182, 14 pages, 2020.

[76] T. Messo et al. "Modeling the grid synchronization induced negative-resistor-like behavior in the output impedance of a three-phase photovoltaic inverter," IEEE International Symposium on Power Electronics for Distributed Generation Systems, 7 pages, 2013.

[77] R. Luhtala et al. "Adaptive Control of Grid-Voltage Feedforward for Grid-Connected Inverters based on Real-Time Identification of Grid Impedance," International Power Electronics Conference, pp. 547-554, 2018.

[78] J. Kukkola, M. Hinkkanen and K. Zenger. "Observer-Based State-Space Current Controller for a Grid Converter Equipped With an LCL Filter: Analytical Method for Direct Discrete-Time Design," IEEE Transactions on Industry Applications, vol. 51, no. 5, pp. 4079-4090, 2015.

[79] T. Reinikka et al. "PHIL Test Bench for Online-Identification Methods of Complex Power Grid," IFAC Symposium on System Identification, pp. 832-837, 2018.

[80] M. Liserre, F. Blaabjerg and S. Hansen. "Design and control of an LCL-filter-based three-phase active rectifier," vol. 41, no. 5, pp. 1281-1291, 2005.

[81] L. Harnefors et al. "Passivity-Based Stability Assessment of Grid-Connected VSCs—An Overview," IEEE Journal of Emerging and Selected Topics in Power Electronics, vol. 4, no. 1, pp. 116-125, 2016.

[82] A. Tan and K. Godfrey. "The generation of binary and near-binary pseudorandom signals: an overview," IEEE Transactions on Instrumentation and Measurement, vol. 51, no. 4, pp. 583-588, 2014.

[83] K. Godfrey. "Introduction to binary signals used in system identification," International Conference on Control, pp. 161-166, 1991.

[84] T. Roinila et al. "Rapid High-Frequency Measurements of Electrical Circuits by Using Frequency Mixer and Pseudo-Random Sequences," Modeling, Identification and Control, vol. 37, no. 2, pp. 113-119, 2016.

[85] A. Tan and K. Godfrey. "Industrial Process Identification: Perturbation Signal Design and Application," Springer, 2019.

[86] R. Luhtala et al. "Identification of Three-Phase Grid Impedance in the Presence of Parallel Converters," Energies, vol. 12, no. 14, 15 pages, 2019.

[87] H. Alenius, R. Luhtala and T. Roinila. "Amplitude Design of Perturbation Signal in Frequency-Domain Analysis of Grid-Connected Systems" IFAC World Congress, 6 pages, 2020.

[88] G. Chang et al. "Measuring power system harmonics and interharmonics by an improved fast Fourier transform-based algorithm," IET Generation, Transmission Distribution, vol. 2, no. 2, pp. 193-201, 2008.

[89] H. Wen et al. "Simple Interpolated FFT Algorithm Based on Minimize Sidelobe Windows for Power-Harmonic Analysis," IEEE Transactions on Power Electronics, vol. 26, no. 9, pp. 2570-2579, 2011.

[90] R. Luhtala et al. "Adaptive Method for Control Tuning of Grid-Connected Inverter Based on Grid Measurements During Start-Up," European Control Conference, pp. 417-422, 2019.

[91] H. Alenius, M. Berg, R. Luhtala and T. Roinila. "Stability and Performance Analysis of Grid-Connected Inverter Based on Online Measurements of Current Controller Loop," Annual Conference of the IEEE Industrial Electronics Society, 7 pages, 2019.

[92] M. Ciobotaru et al. "Adaptive notch filter based active damping for power converters using lcl filters," International Symposium on Power Electronics for Distributed Generation Systems, 7 pages, 2010.

[93] T. Messo et al. "Design of grid-voltage feedforward to increase impedance of grid-connected three-phase inverters with LCL-filter," IEEE International Power Electronics and Motion Control Conference, pp. 2675-2682, 2016.

[94] T. Messo et al. "Evaluation of Dead-Time Effect of Grid-Connected Inverters Using Broadband Methods," IFAC Symposium on System Identification, pp. 449-454, 2018.

[95] N. Femia et al. "Optimization of perturb and observe maximum power point tracking method," IEEE Transactions on Power Electronics, vol. 20, no. 4, pp. 963-973, 2005.

[96] L. Nousiainen et al. "Photovoltaic Generator as an Input Source for Power Electronic Converters," IEEE Transactions on Power Electronics, vol. 28, no. 6, pp. 3028-2038, 2013.

[97] T. Messo et al. "Using High-Bandwidth Voltage Amplifier to Emulate Grid-Following Inverter for AC Microgrid Dynamics Studies" Energies, vol. 12, no. 3, 18 pages, 2019.

[98] T. Roinila et al. "Hardware-in-the-Loop Methods for Real-Time Frequency-Response Measurements of on-Board Power Distribution Systems," IEEE Transactions on Industrial Electronics, vol. 66, no. 7, pp. 5769-5777, 2019.

PUBLICATIONS

PUBLICATION

I

Implementation of Real-Time Impedance-Based Stability Assessment of Grid-Connected Systems Using MIMO-Identification Techniques

R. Luhtala, T. Roinila and T. Messo

IEEE Transactions on Industry Applications, vol. 54, no. 5, pp. 5054-5063, 2018

Implementation of Real-Time Impedance-Based Stability Assessment of Grid-Connected Systems Using MIMO-Identification Techniques

Roni Luhtala, *Student Member, IEEE,* Tomi Roinila, *Member, IEEE,* and Tuomas Messo, *Member, IEEE*

***Abstract*—Grid impedance has a major effect on the operation of inverter-connected systems, such as renewable energy sources. Stability of such system depends on the ratio of the inverter output impedance and the grid impedance at the point of common coupling. Because the grid impedance varies over time with many parameters, online grid-impedance measurement acquired in real time is most preferred method for observing the stability. Recent studies have presented methods based on multiple-input-multiple-output (MIMO) identification techniques where the stability of grid-connected system is rapidly assessed in the dq domain. In the methods, orthogonal injections are used with Fourier techniques, and the grid impedance d and q components are measured. The Nyquist stability criterion is then applied to assess the stability. This paper extends previous studies, and presents a real-time implementation for the online stability analysis using MIMO-identification methods. The practical implementation is discussed in detail and experimental results based on a grid-connected three-phase inverter are provided to demonstrate the effectiveness of the methods.**

***Index Terms*—Frequency response, Impedance measurements, Inverters, MIMO systems, Power electronics, Stability, Real time systems**

I. Introduction

The global energy-production trend is based on environmentally friendly renewable energy. Most of the renewable energy sources, such as wind and photovoltaic farms, are connected to the utility grid through power electronic inverters. Rapidly increasing utilization of power electronics have started to affect the grid dynamics [1] and have already caused stability issues [2].

One of the emerging problems in grid-connected systems is harmonic resonance, which is caused by interactions between inverter output impedance and grid impedance. The harmonic resonance reduces the energy efficiency, and can even cause instability and inverter disconnection from a power system. [3]. These resonance phenomena are one of the main issues limiting the total share of renewable energy resources in power systems. Hence, new methods to identify the source of harmonic resonances and to mitigate them are important for both industry and academia.

The impedance-based stability can be assessed by the ratio between grid impedance and inverter output impedance. A grid-connected system will remain stable if the impedance ratio satisfies the Nyquist stability criterion [4]. The underlying problem of guaranteeing the impedance-based stability is grid impedance, seen by the inverter, which has become major parameter affecting the system stability. That is because the renewable energy sources are often located in remote areas with long grid-connecting cables, which introduces significant impedance that can cause stability issues. Thus, online measurements of the grid are required to guarantee stability in real-world conditions.

Energy distribution system will be more complex in the near future, including controllable loads, energy storage systems and large amount of weather-dependent renewable energy production [5]. Consequently, the grid impedance highly varies over time as the route for power flow to its consumption or energy storages change. Studies have already reported significant differences in grid impedance when comparing day and night-times [6]. This will necessitate online identification of the time-varying grid impedance performed in real time in order to accurately assess the system stability.

In recent years, there has been extensive research in online stability assessment of grid-connected inverters. Online grid or inverter impedance measurements for stability assessment have been implemented by using various methods, such as impulse response [7], multi-tone injections [8], sine sweeps [9] and maximum-length binary sequence (MLBS) [10].

A grid-connected system can be considered as a multiple-input-multiple-output (MIMO) system. Using Park transformation three-phase systems can be transformed to the synchronous reference frame (dq domain) [11], in which three AC signals are transformed into two DC signals (d and q components). To guarantee system stability, both components must be analyzed. Recent studies have introduced impedance-measurement method based on orthogonal pseudo-random sequences with which the (coupled) impedance d and q components can be rapidly measured using only one measurement cycle [12]. Similar techniques have also been applied in single- and multi-converter DC systems [13], [14]. Applying these methods reduces the total measurement time drastically compared to conventional measurement technique where the d and q components are measured separately. Another advantage of the methods is that the complete dq-domain impedance is measured under the same operating conditions, and thus, variations in both component can be simultaneously seen.

This paper extends the work in [12], and presents an implementation for real-time stability assessment of a grid-connected system by using MIMO-measurement method. The paper discusses the issues in practical real-time implementation, and presents steps to develop an informative diagnostic tool for stability analysis of grid-connected systems. The method is very versatile, and can be used for example in load

parameter estimation [15], adaptive control of grid-connected converters [16] or in grid-connected PV plants to enable effective post-fault diagnostics in a case of a disconnection due to high harmonic currents, such as in [2].

The remainder of the paper is organized as follows. Impedance-based stability analysis and modeling of the grid-connected inverters are reviewed in section II. Section III introduces methods for real-time MIMO-identification techniques for grid impedance. Section IV presents steps to develop practical implementation of real-time stability analysis tool. Section V shows the applied laboratory setup, practical implementation of real-time measurement system and experimental measurements. Section VI draws conclusions.

II. Stability Analysis of Inverter-Connected Systems

A. Impedance-Based Stability Analysis

Fig. 1 shows an equivalent small-signal circuit of a grid-connected inverter at the interconnection point with grid. The inverter is considered as ideal current source $\hat{\mathbf{i}}_{\mathrm{s}}$ with shunt impedance matrix $\mathbf{Z}_{\mathrm{o\text{-}dq}}$ describing the finite output impedance. The grid is modeled with ideal voltage sink $\hat{\mathbf{v}}_{\mathrm{L}}$ and series impedance matrix $\mathbf{Z}_{\mathrm{g\text{-}dq}}$ describing the effect of non-idealities.

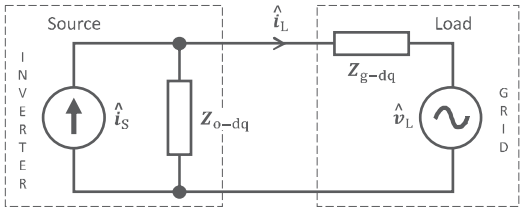

Fig. 1: Equivalent small-signal model of the interconnected source-load subsystem.

The stability analysis of interconnected system can be conducted applying the Nyquist stability criterion to the impedance ratio between load impedance and the source impedance [4]. Assuming that the unloaded source itself is stable and the load is stable when powered by an ideal source, the stability analysis of the load current $\hat{\mathbf{i}}_{\mathrm{L}}$ can be simplified by observing the transfer matrix

$$\mathbf{L}(s) = [\mathbf{I} + \mathbf{Z}_{\mathrm{g\text{-}dq}}(s)/\mathbf{Z}_{\mathrm{o\text{-}dq}}(s)]^{-1} \tag{1}$$

The interconnected system is stable if the eigenvalues of the return-ratio matrix $\mathbf{Z}_{\mathrm{g\text{-}dq}}(s)/\mathbf{Z}_{\mathrm{o\text{-}dq}}(s)$ satisfies the generalized Nyquist stability criterion. [17]

The AC component of a balanced three-phase systems can be presented in dq domain as two DC components, direct (d) and quadrature (q) which can be linearized around their steady-state operating point. The dq-domain impedance models for the inverter output impedance $\mathbf{Z}_{\mathrm{o\text{-}dq}}(s)$ and grid impedance $\mathbf{Z}_{\mathrm{g\text{-}dq}}(s)$ are basically 2 × 2 matrices which can be written as

$$\mathbf{Z}_{\mathrm{o\text{-}dq}}(s) = \begin{bmatrix} Z_{\mathrm{o\text{-}dd}}(s) & Z_{\mathrm{o\text{-}dq}}(s) \\ Z_{\mathrm{o\text{-}qd}}(s) & Z_{\mathrm{o\text{-}qq}}(s) \end{bmatrix} \tag{2}$$

$$\mathbf{Z}_{\mathrm{g\text{-}dq}}(s) = \begin{bmatrix} Z_{\mathrm{g\text{-}dd}}(s) & Z_{\mathrm{g\text{-}dq}}(s) \\ Z_{\mathrm{g\text{-}qd}}(s) & Z_{\mathrm{g\text{-}qq}}(s) \end{bmatrix} \tag{3}$$

where the dq transformation has introduced the cross-coupling (dq and qd) terms between the components. Thus the systems include individual impedances for both components and cross-coupling impedances between them. These local cross-couplings should not be confused with the cross-couplings used in nodal analysis, which is conventionally applied to analyze interconnected power systems [18], [19]. However, nodal analysis is based on the use of single-phase equivalent circuits, which effectively prevents including some control functions, such as the phase-locked-loop.

In this work the cross-coupling impedances are neglected from stability analysis because they are assumed to be small as the unity power factor is desired [20]. However in the case of decreased power factor, the cross-coupling impedances should be included in the analysis to avoid inaccuracy.

Considering the interconnection point with the grid, the inverter acts as a source and grid as a load. By neglecting the cross-coupling impedances, the (2) and (3) are reduced to diagonally dominant matrices. Using diagonally dominant forms, the resulting return-ratio matrix of (1) can be considered separately for both individual components. [20] The impedance ratios of the d and q components must satisfy the Nyquist stability criterion. The stability analysis is conducted by analyzing transfer functions

$$G_{\mathrm{dd}}(s) = \frac{1}{1 + Z_{\mathrm{g\text{-}dd}}(s)/Z_{\mathrm{o\text{-}dd}}(s)} \tag{4}$$

$$G_{\mathrm{qq}}(s) = \frac{1}{1 + Z_{\mathrm{g\text{-}qq}}(s)/Z_{\mathrm{o\text{-}qq}}(s)} \tag{5}$$

The grid impedances Z_{g-dd} and Z_{g-qq} are measured simultaneously in this paper. The inverter output impedances Z_{o-dd} and Z_{o-qq} are modeled analytically in the following subsection.

B. Inverter Impedance Model

Fig. 2 shows the power stage of the grid-connected inverter with a DC-capacitor, control system, and passively-damped LCL output filter. Detailed modeling of such current-fed three-phase inverter in dq-domain is derived in [21]. This paper focuses on the real-time measurements and analysis, and thus, only the main points of the inverter modeling are introduced.

In the methods, an average state-space model of the inverter is derived and linearized around the DC operating point which appears after transformation to the dq domain. Variables $\hat{i}_{\mathrm{dc}}$, $\hat{v}_{\mathrm{Cfd}}$, $\hat{v}_{\mathrm{Cfq}}$, $\hat{d}_{\mathrm{d}}$ and $\hat{d}_{\mathrm{q}}$ are considered as input variables ($\mathbf{U}(s)$) whereas $\hat{i}_{\mathrm{Ld}}$, $\hat{i}_{\mathrm{Lq}}$ and $\hat{v}_{\mathrm{dc}}$ as output variables ($\mathbf{Y}(s)$) of the system. Resulting state matrices $\mathbf{A}$, $\mathbf{B}$, $\mathbf{C}$, and $\mathbf{D}$ are introduced in the Appendix. According to [22], open-loop transfer functions between input and output variables for such state-space model can be written as

$$\mathbf{Y}(s) = \left[\mathbf{C}(s\mathbf{I} - \mathbf{A})^{-1}\mathbf{B} + \mathbf{D}\right] \mathbf{U}(s) \tag{6}$$

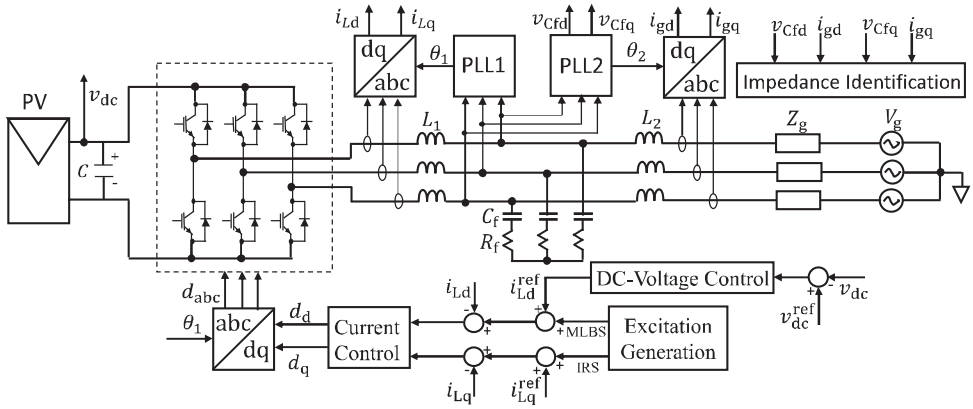

Fig. 2: Three-phase grid-connected inverter.

$$\begin{bmatrix}\hat{i}_{Ld}\\ \hat{i}_{Lq}\\ \hat{v}_{dc}\end{bmatrix} = \begin{bmatrix}G_{iod\text{-}o} & -Y_{d\text{-}o} & -Y_{qd\text{-}o} & G_{eod\text{-}o} & G_{eoqd\text{-}o}\\ G_{ioq\text{-}o} & -Y_{dq\text{-}o} & -Y_{q\text{-}o} & G_{eodq\text{-}o} & G_{eoq\text{-}o}\\ Z_{iin\text{-}o} & T_{iod\text{-}o} & T_{ioq\text{-}o} & G_{eid\text{-}o} & G_{eiq\text{-}o}\end{bmatrix}\begin{bmatrix}\hat{i}_{dc}\\ \hat{v}_{Cfd}\\ \hat{v}_{Cfq}\\ \hat{d}_d\\ \hat{d}_q\end{bmatrix} \quad (7)$$

The cascaded control system of the grid-connected inverter using PI-type controllers is implemented in the dq domain as depicted in Fig. 2. The DC-voltage control adjusts the PV generator operating point to the maximum power point (MPP) and sets the reference for the d-component current controller. Unity power factor is desired, and therefore current controllers regulate the current q component to zero and the d component to the reference value that depends on power produced by the PV generator. Grid synchronization is implemented using a conventional synchronous reference frame phase-locked-loop (SRF-PLL), which regulates the observed voltage q component to zero [23], thus not affecting the d-component variables when cross-couplings are neglected. By closing these control loops, the analytical closed-loop model of the inverter can be constructed.

TABLE I: Parameters of the inverter.

V_{dc}	414.3 V	I_{dc}	6.577 A	ω	2π·60 rad/s
V_{od}	$\sqrt{2}$·120 V	V_{oq}	0 V	f_{sw}	8 kHz
I_{Ld}	10.6375 A	D_d	0.4122	D_q	0.0213
C	1.5 mF	r_{L_1}	0.1 Ω	L_1	2.2 mH
R_f	1.8 Ω	C_f	10 μF	L_2	0.6 mH

Studied operating point and resulting steady-state parameters of the PV inverter are shown in Table I. The inverter feeds power to a balanced (60 Hz, 120 V) grid. Analytical closed-loop model of the inverter output admittances have been previously derived in [21]. For both admittance components, the LCL filter can be seen as passive-damped LC-filter, containing damping resistance R_f, capacitor C_f and inverter-side inductor L_1, whereas grid-side inductor L_2 can be included in the grid impedance. With that consideration, the output admittance d component ($\hat{v}_{Cfd} \rightarrow -\hat{i}_{Ld}$) can be given as

$$Y_{o\text{-}dd} = \frac{Y_{d\text{-}o}}{(1+L_{in})(1+L_{out\text{-}d})} + \left(\frac{L_{in}}{1+L_{in}}\right)\left(Y_{d\text{-}o} + \frac{G_{eod\text{-}o}T_{iid\text{-}o}}{(1+G_{eid\text{-}o})}\right) + \frac{C_f s}{(1+R_f C_f s)} \quad (8)$$

where $L_{out\text{-}d}$ is the current control loop gain and L_{in} is the DC-voltage control loop gain, which are derived in the Appendix.

The output admittance q component ($\hat{v}_{Cfq} \rightarrow -\hat{i}_{Lq}$) can be given as [21]

$$Y_{o\text{-}qq} = \frac{Y_{q\text{-}o}}{(1+L_{out\text{-}q})} - \frac{I_{od}}{V_{od}}\left(\frac{L_{out\text{-}q}}{(1+L_{out\text{-}q})}\right)\left(\frac{L_{PLL}}{(1+L_{PLL})}\right) - \frac{D_d}{V_{od}}\left(\frac{G_{eoq\text{-}o}}{(1+L_{out\text{-}q})}\right)\left(\frac{L_{PLL}}{(1+L_{PLL})}\right) + \frac{C_f s}{(1+R_f C_f s)} \quad (9)$$

where $L_{out\text{-}q}$ is the current control loop gain and L_{PLL} is the SRF-PLL loop gain, which are derived in the Appendix.

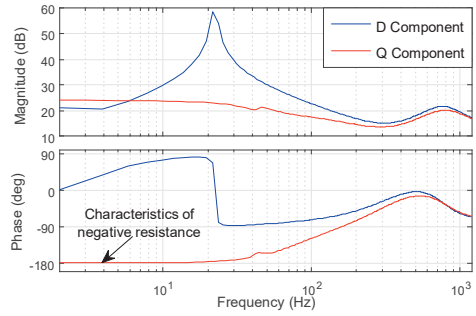

Fig. 3: D and q components of inverter output impedance.

Fig. 3 shows the resulting analytical output impedances of the d ($Z_{o\text{-}dd} = 1/Y_{o\text{-}dd}$) and q ($Z_{o\text{-}qq} = 1/Y_{o\text{-}qq}$) components at the operating point defined in Table I. It is important to note that $Z_{o\text{-}qq}$ has lost the passivity at low frequencies which

may cause stability issues when connected to a weak grid. The passivity is lost because L_{PLL} dominates the low-frequency dynamics of $Z_{\text{o-gq}}$ by resembling the characteristics of negative resistance ($-V_{\text{od}}/I_{\text{od}}$) below the PLL crossover which is set here as high as 100 Hz. [24] High crossover is adjusted in order to emphasize the effect of PLL on the impedance-based stability and to test proposed real-time stability assessment methods when studied inverter is connected to a relatively weak grid.

III. Implementation of Grid-Impedance Measurements

A. Orthogonal Pseudo-Random Sequences

Systems that include more than one inputs and/or outputs that correlate with each other are considered to be coupled multiple-input-multiple-output (MIMO) systems. Usually all the input and output couples (components) have to be measured when guaranteeing the stability of a MIMO system. Components of the system can be measured one by one but as the number of them increases, this approach may become time-consuming. In addition, highly time-varying operating conditions or values of the measured parameters may change in one component while they are measured from another. Fortunately, it is possible to produce signals that do not have energy at same frequencies; these are known as uncorrelated signals. [25] By applying such injections to MIMO system, the responses of each perturbation can be separated. Hence, frequency response functions of multiple coupled components can be obtained during a single measurements cycle. This reduces the total measurement time and guarantees that the data is not lost during the measurement cycles.

Considering the grid-connected systems in dq domain, two uncorrelated signals are required for simultaneous measurements of the grid-impedance d and q components. A technique to generate uncorrelated sequences is presented in [25]. This technique starts by generating a conventional maximum-length binary sequence (MLBS). The uncorrelated signal with respect to the generated MLBS is obtained by doubling the MLBS and then inverting every other digit of the doubled sequence. The resulting second sequence is orthogonal with respect to the MLBS and is known as the inverse-repeated sequence (IRS). The IRS is a periodic signal, with sequence length of $N_{\text{IRS}} = 2N_{\text{MLBS}}$, where N_{MLBS} is the length of the original MLBS. Hence, as two MLBS periods are injected during one IRS period, the responses of the MLBS should be averaged over two periods.

The power spectrum of both MLBS and IRS follow $sinc^2$ function [25] in which the power drops to zero at the generation frequency (f_{gen}) of the sequences. The measurable bandwidth is usually considered to be $0.45 f_{\text{gen}}$ where power content has drop 3 dB compared to highest value of the sequence. Fig. 4 shows power spectra of two orthogonal sequences, including a 31-bit-length MLBS (blue) and corresponding IRS (red). Both sequences are generated at 4 kHz. The energy values are scaled to facilitate the difference between the MLBS and the IRS. Due to orthogonality, the produced sequences have power at different frequencies and thus they are uncorrelated over their common period of N_{IRS}.

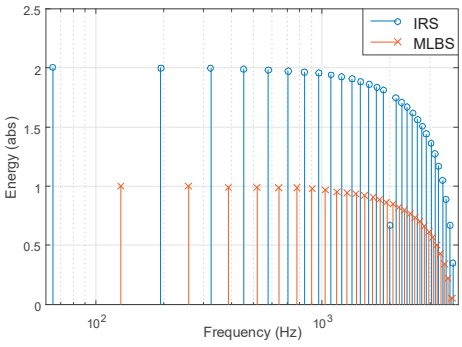

Fig. 4: Power spectra of two uncorrelated sequences.

It is possible to produce uncorrelated signals by using other techniques as well; for example, using the sum of sinusoids. However, the MLBS-based technique is applied in the paper because of its attractive features for real-time frequency-response identifications. The sequences are straightforward to generate by using a shift register with an XOR-feedback loops and their binary forms allow implementation even with a low-cost application which output can only cope with a small number of signal levels. The sequences are deterministic which allows the use of relatively low signal amplitude of perturbations, and thus, the normal system operation and power quality are not disturbed noticeably during the identification. [24]

B. Impedance Measurement

For the dq-domain grid-impedance measurements, the perturbation sequences are injected to the inverter output current d and q components. The responses from grid-side currents and voltages are measured as three-phase waveforms which are transformed to the dq-domain using Park transformation. Park transformation requires estimation of the grid phase angle from SRF-PLL, which should have relatively high crossover to provide fast dynamics. The SRF-PLL tracks the phase angle by regulating the observed voltage q component to zero effectively below its crossover. Hence, information of the voltage q component for impedance calculations is lost within that frequency band. This issue is solved by implementing second SRF-PLL with lower crossover to decouple impedance identification from the inverter control dynamics.

Fig. 2 shows that the system includes two PLLs, for different purposes. PLL1 provides phase angle estimation θ_1 for the control system, thus higher crossover provides better transient performance. PLL2 provides the phase angle estimation θ_2 for the dq-domain impedance calculations and its crossover must be adjusted lower than the lowest measured frequency from the q component. By using PLL2, the transformed grid-side waveforms of v_{Cfd} and i_{gd} from d component and v_{Cfq} and i_{gq} from q component can be collected properly for providing accurate estimation of dq-domain grid impedance.

The grid impedance is computed as a ratio of Fourier-transformed voltage and current of both components using cross-correlation technique. The impedance of linear system

can be presented as a convolution from current to voltage in time domain, and thus, according to basic Fourier theory, as multiplication in the frequency domain. The cross-energy spectrum from current to voltage is defined as [26]

$$R_{iu}(\omega) = Z(\omega)R_{ii}(\omega) \tag{10}$$

where ω is angular frequency, $Z(\omega)$ is the impedance and $R_{ii}(\omega)$ energy spectrum of current. $R_{iu}(\omega)$ and $R_{ii}(\omega)$ are defined by applying Fourier-transformed measurements, as presented in [25]. The frequency-domain impedance can be calculated from the ratio $R_{iu}(\omega)/R_{ii}(\omega)$.

IV. Practical Implementation

Fig. 2 shows the MIMO-identification setup for simultaneously measuring the d and q components of grid impedance. The control system of the three-phase inverter is configured to inject orthogonal sequences on top of the output-current references, enabling online identification without using any external perturbation signal. As the response of the MLBS can be averaged over two periods during the injection of the IRS, one may optimize the setup by applying the MLBS to the input that has the greater noise level. The power flows mainly on d component when unity power factor is desired; thus, the d component is assumed to have greater noise level and measured using MLBS.

Fig. 5 shows a block diagram for continuous generation of two orthogonal sequences in the inverter control system. The MLBS is generated using a seven-bit-length shift register. The injection amplitudes can be independently defined changing K_{MLBS} and K_{IRS}. The MLBS and IRS are generated by mapping two logical levels as K and $-K$ to produce a time-domain injection with an average value close to zero.

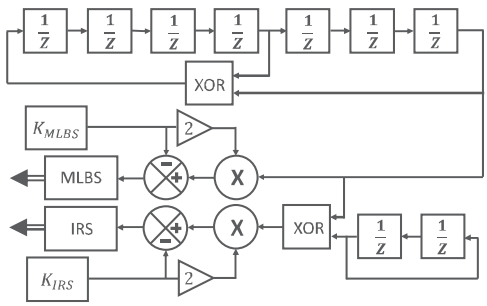

Fig. 5: Block diagram to continuous generation of 127-bit-length MLBS and corresponding IRS.

When the inverter itself is producing the perturbation sequences through its switches, selection of their sampling frequency (f_s) is bounded to inverter operating as

$$f_s = \frac{f_{sw}}{r} \tag{11}$$

where (f_{sw}) is the switching frequency of the inverter and r is positive integer defining the actual selection. In this practical implementation, the highest possible sampling frequency ($r = 1$) is used because of relatively low switching frequency of 8 kHz, yielding $f_s = f_{sw}$. As switching frequency increases, the sampling frequency of sequences should be limited in order to ease the computational burden. The sampling frequency of the MLBS and IRS has to be a multiple (at least twice) of their generation frequency f_{gen} to avoid aliasing effects. Therefore, the selection of generation frequency is also bounded to switching frequency as

$$f_{gen} = \frac{f_s}{e} = \frac{f_{sw}}{e \cdot r} \tag{12}$$

where e is a positive integer, equal or more than two, which is used to define suitable generation frequency for desired measurable bandwidth.

The ratio of the inverter and grid impedance is computed in real-time by utilizing the measured grid-impedance components and the analytical impedance model of the inverter. The visualization of stability analysis is implemented by plotting Nyquist contours based on the impedance ratio of each component. The Nyquist stability criterion states that the system is unstable if the Nyquist curve encircles clockwise the critical point (-1,0) in the complex-plane [22]. Bode plots of the impedances are shown to analyze certain impedances as a function of frequency. These tools provide extensive diagnostic tools for impedance-based stability of grid-connected systems.

V. Experiments and Performance Evaluation

A. Experimental Setup

The effectiveness of the presented MIMO-identification techniques of grid-connected systems are proven by implementing the methods to power hardware-in-the-loop (PHIL) test setup. Fig. 6 shows a block-diagram representation of a three-phase inverter feeding the power from a photovoltaic source to the grid. The PV emulator PVS7000 is operated at MPP (3 kW). The Spitzenberger Spies PAS 15000 Grid Emulator acts as an three-phase AC-load of the system repeating reference waveforms generated by the dSPACE 1103 real-time simulator. The internal control system of the used IGBT inverter is bypassed and replaced by simulated control system in the dSPACE.

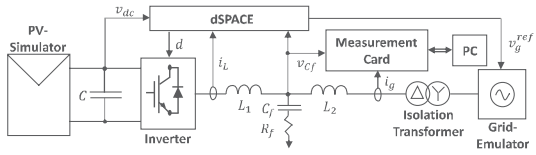

Fig. 6: Block diagram of the experimental setup.

The implementation was set up by using parallel a measurement card NI USB-6363, PC (MATLAB/Data Acquisition Toolbox) and dSPACE. The three-phase inverter was configured to continuously inject the MLBS and IRS on top of the current references. The injection system was implemented to the dSPACE-driven control system in Simulink model as shown in Fig. 5. The resulting waveforms of grid-side currents and voltages were captured using the NI USB-6363

measurement card, operated by MATLAB/Data Acquisition Toolbox. The impedance-based stability analysis is continuously performed during the data collection by using Matlab.

The switching frequency of the inverter is 8 kHz, which limits the generation frequency of perturbations. Applying (12), the generation frequencies of the injections can be set to 4 kHz. In these practical implementations the amplitude of the sequences are minimized in order not to disturb produced power quality. The 3 dB drop of the power content at $0.45 f_{\text{gen}}$ may significantly affect to results at high frequencies when the amplitude is strictly limited. Therefore, the measurable bandwidth in these experiments is considered to end at 1.2 kHz (20th harmonic) meaning only 1.3 dB drop of the power content compared to highest power value of the sequence.

Three sets of experiments are shown to demonstrate the efficiency of the proposed methods. The first experiment shows how the proposed methods can be used to accurately measure the grid impedance with a very high frequency resolution and low injection amplitude. This measurement setup could continuously identify resonance peaks and other unpredictable dynamics of the grid and their effects on the system stability. The second experiment will compare two measurement setups for adaptive control systems of grid-connected converters when using different injection amplitudes. In this experiment the frequency resolution is sacrificed to increase measurement speed. The last experiment shows an unstable case in order to show that the accuracy of the analytical model of grid impedance and the measured grid impedance are decent to perform reliable stability analysis.

B. Experiment 1: High Frequency Resolution

In first experiment, two orthogonal sequences are generated as shown in Fig. 5. The MLBS is generated using an 11-bit-length shift register for producing a sequence with a length of 2047 for the MLBS and 4094 for the corresponding IRS. Both sequences are generated at 4 kHz, yielding a frequency resolution of 1.95 Hz. The first harmonic of the IRS power spectrum is located at 0.98 Hz, hence the crossover of PLL2 is set to 0.9 Hz.

The MLBS responses are averaged over 116 periods (IRS over 58 periods) yielding $T_{\text{meas}} = 60.20$ s which is the refresh rate for new results in continuous measurements. Due to averaging, the injection amplitude for both the MLBS and the IRS can be set very low. An amplitude of 0.05 A (representing less than 0.5 % of nominal output current) is considered as the best trade-off between measurement accuracy and effects on the power quality.

Fig. 7 shows the inverter output impedance and measured grid impedance d component as Bode plot and computed stability assessment as Nyquist contour. Fig. 8 shows the simultaneously performed analysis for the q component. The results show a clear trend for the grid impedances above the fundamental frequency (60 Hz). Harmonics in grid waveforms are considered as a drastic disturbances for measurements, and thus, the measurement system is not able to provide accurate results at the frequencies where significant harmonics occur. However, using this high frequency resolution (1.95 Hz), inaccurate frequency points can be reliably distinguished between a real resonance peaks and negligible results due to harmonics.

The bode plots show the phase margins of the system at the frequency where the impedances overlap in magnitude. The phase margins and Nyquist contours indicate that q component has relatively low impedance-based stability margins, while the d component has sufficient margins. Low stability margins in q component at relatively low frequency indicate issues with overly high crossover (100 Hz) of the PLL1, which resembles negative resistance -like behavior in the inverter output impedance q component. Negative resistance -like behavior causes stability issues with the weak grid [27].

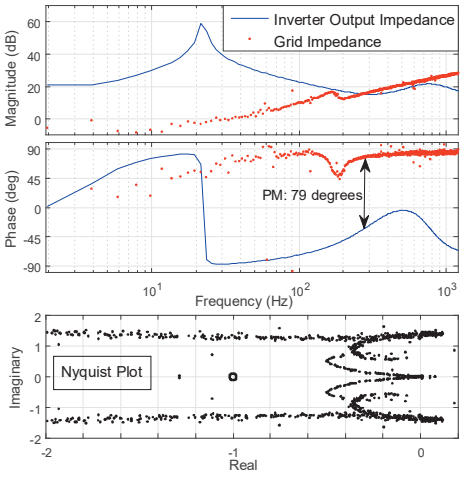

Fig. 7: Stability assessment for d component.

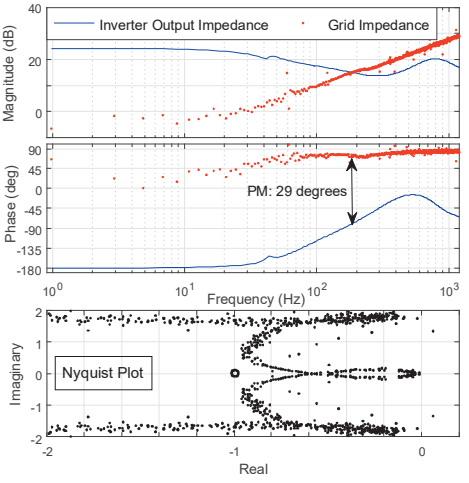

Fig. 8: Stability assessment for q component.

C. Experiment 2: Short Measurement Time

In order to achieve a faster measurement system, relatively short sequences and less averaging must be used. A shorter sequence weakens frequency resolution. To provide sufficient SNR, the injection amplitude has to be increased when the number of averaged periods is reduced. Table II shows the designed MLBS parameters for two different measurement setups $Meas_1$ and $Meas_2$. Both MLBS injections have a sequence length of 127, yielding a measurement time of 0.03175 s for one period and frequency resolution of 31.5 Hz. The corresponding IRS is produced from the MLBS as shown in Fig. 5. The first harmonic (IRS) of power spectrum is located at 15.7 Hz; thus, the crossover of PLL2 can be set to 10 Hz.

TABLE II: MLBS parameters.

	n	f_{gen}	P	K	T_{meas}
$Meas_1$	7	4 kHz	10	0.3 A	0.313 s
$Meas_2$	7	4 kHz	156	0.03 A	4.953 s

Fig. 9 shows the effect of a 0.3 A injection amplitude (used in $Meas_1$) to the inverter output current. Fig. 10 shows the effect of a 10-times-smaller (0.03 A) injection amplitude (used in $Meas_2$), which is almost negligible by representing less than 0.3 % of the nominal current.

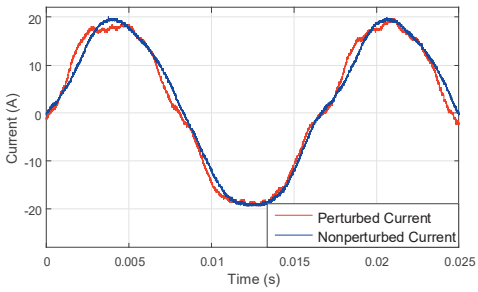

Fig. 9: Perturbed phase A current with MLBS and IRS using 0.3 A amplitude.

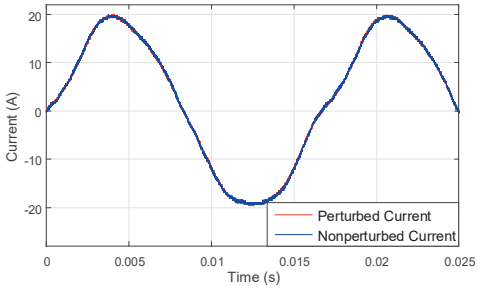

Fig. 10: Perturbed phase A current with MLBS and IRS using 0.03 A amplitude.

Fig. 11 shows simultaneous impedance-based stability assessment for both d and q components using measurement setup $Meas_1$. The measurement setup is designed to apply only 10 averaged periods for single measurement, thus providing a refresh rate of 0.313 s. The measurement setup is not optimal for continuous measurements because of the large injection amplitude (shown in Fig. 9), but could be used for example in the start-up routine of a system.

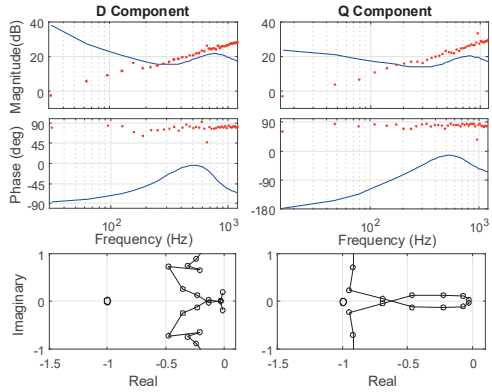

Fig. 11: Visualization of stability assessment (refresh rate 0.313 s) using grid impedances (red dots), inverter output impedances (blue line) and Nyquist contours of the ratios.

Fig. 12 shows similar stability assessment for both d and q components using measurement setup $Meas_2$. More averaging (P = 156) increases the refresh rate to almost 5 s but it reduces the required injection amplitude to one-tenth compared to $Meas_1$. Relatively accurate results using low amplitude (shown in Fig. 10) mean that $Meas_2$ is an effective tool for continuous grid-impedance measurements.

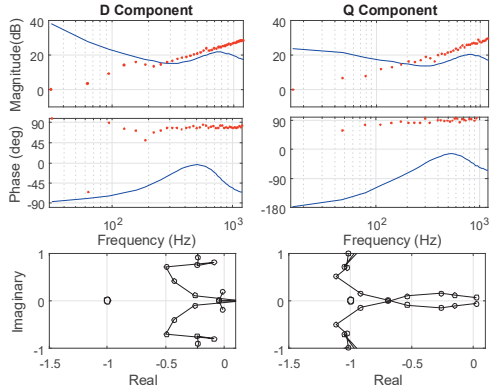

Fig. 12: Visualization of stability assessment (refresh rate 4.953 s) using grid impedances (red dots), inverter output impedances (blue line) and Nyquist contours of the ratios.

Grid harmonics represent drastic disturbances for the measurement system by causing inaccurate results at those frequencies. Fortunately, the frequency of harmonics are known in 60 Hz grid, making it possible to design the sequences in a way that avoid measuring the frequencies where significant

harmonics occur. Measurement setups $Meas_1$ and $Meas_2$ avoid measuring second (120 Hz) and third (180 Hz) harmonic frequencies, that is satisfied by designing the MLBS and IRS not having energy at frequencies that are closer than 6 Hz to those frequencies. Figures 11 and 12 show that the grid impedance have a clear trend and there is no unacceptable points, caused by grid harmonics, above the fundamental frequency.

D. Experiment 3: Unstable Case

The unstable case was constructed by first measuring the grid impedance when inductance was large and then deriving overly high PLL1 crossover which would cause instability, according to theory of impedance-based stability. The crossover is changed online and the real-time Nyquist curve of the q component in Fig. 13 shows instability because the impedance ratio encircles the critical point (-1,0). Fig. 14 shows phase A current when impedance-based instability occurs at the inverter and grid interconnection point. The PLL1 crossover is changed at 0.14 s and the uncontrolled oscillations start immediately. The inverter internal protection system reacts to the unstable phase currents at 0.35 s by disconnecting device from the grid.

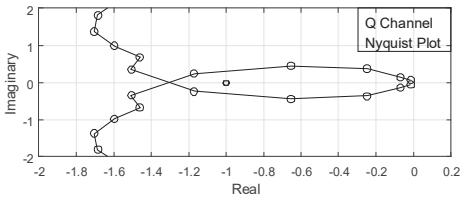

Fig. 13: Unstable Nyquist curve of q component.

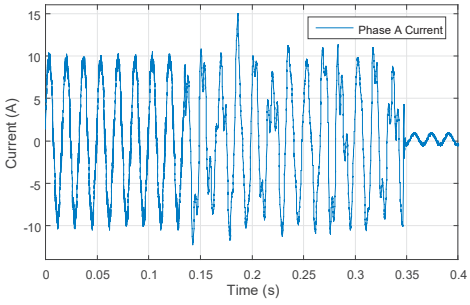

Fig. 14: Phase A current when stability margins are negative.

The source of instability is confirmed to originate from impedance mismatches in the q component by increasing PLL1 crossover so that the impedance-based stability margins go negative. The Nyquist curve in Fig. 13 is measured during instability, and the appearance of uncontrolled oscillations in the inverter output current in these conditions ensures that the accuracy of the methods are sufficient to perform reliable stability analysis in real-time.

VI. Conclusions

Time-varying grid impedance is important parameter for the operation of grid-connected inverter. Thus, the grid-impedance identification methods performed in real-time provide important benefits for example in adaptive control, start-up routines, and post-fault diagnostics of grid-connected systems. This paper has shown a practical implementation of stability analysis for d and q components in completely real time by measuring the grid-impedance of both components simultaneously. Orthogonal sequences are injected on top of the inverter output currents to enable simultaneous measurements without using an external circuit or device to generate small-signal excitations. The responses are measured from the grid side through additional low-bandwidth PLL, to preserve accuracy also at low frequencies. The impedance-based stability assessment is monitored by applying real-time measurements of grid impedance and the analytical model of inverter output impedance. Moreover, it has been demonstrated, using PHIL-test setup, that the real-time grid impedance measurements can be performed without significantly perturbing the grid currents and voltages.

Acknowledgements

This work was supported by the Academy of Finland.

Appendix

State matrices:

$$A = \begin{bmatrix} -\frac{r_L}{L_1} & \omega_s & \frac{D_d}{L_1} \\ -\omega_s & -\frac{r_L}{L_1} & \frac{D_q}{L_1} \\ -\frac{3}{2}\frac{D_d}{C} & -\frac{3}{2}\frac{D_q}{C} & 0 \end{bmatrix}$$

$$B = \begin{bmatrix} 0 & -\frac{1}{L_1} & 0 & \frac{V_{dc}}{L_1} & 0 \\ 0 & 0 & -\frac{1}{L_1} & 0 & \frac{V_{dc}}{L_1} \\ \frac{1}{C} & 0 & 0 & -\frac{3}{2}\frac{I_{Ld}}{C} & -\frac{3}{2}\frac{I_{Lq}}{C} \end{bmatrix}$$

$$C = \begin{bmatrix} 1 & 0 & 0 \\ 0 & 1 & 0 \\ 0 & 0 & 1 \end{bmatrix}$$

$$D = \begin{bmatrix} 0 \end{bmatrix}$$

where derived steady-state parameters from average model of the inverter and studied operating point are shown in Table I.

Open-loop transfer functions used in analytical inverter output impedance model and following control loops:

$$Y_{d\text{-}o} = \frac{2CLs^2 + 2Cr_L s + 3D_q^2}{den}$$

$$Y_{q\text{-}o} = \frac{2CLs^2 + 2Cr_L s + 3D_d^2}{den}$$

$$T_{od\text{-}o} = \frac{3D_d Ls + 3D_d r_L - 3D_q L\omega}{den}$$

$$G_{cod\text{-}o} = \frac{2CLV_{in}s^2 - (3D_d I_d L - 2CV_{in} r_L)s + 3(D_q{}^2 V_{in} - D_d I_d r_L - D_q I_d L\omega)}{den}$$

$$G_{\text{cod-o}} = \frac{2CLV_{\text{in}}s^2 - (3D_{\text{q}}I_{\text{q}}L - 2CV_{\text{in}}r_{\text{L}})s + 3(D_{\text{d}}{}^2V_{\text{in}} - D_{\text{q}}I_{\text{q}}r_{\text{L}} - D_{\text{d}}I_{\text{q}}L\omega)}{den}$$

$$G_{\text{cid-o}} = \frac{-3I_{\text{d}}L^2s^2 - 3(2I_{\text{d}}Lr_{\text{L}} + D_{\text{d}}V_{\text{in}}L)s - 3(I_{\text{d}}(L^2\omega^2 + r_{\text{L}}{}^2) - D_{\text{q}}V_{\text{in}}L\omega + D_{\text{d}}V_{\text{in}}r_{\text{L}})}{den}$$

where denominator den of every open-loop transfer function is characteristic polynomial of the state matrix $\mathbf{A}$, which defines the order of transfer functions and can be derived as

$$den = det(s\mathbf{I} - \mathbf{A}) = 2CL^2s^3 + 4CLr_{\text{L}}s^2 + (3(D_{\text{d}}{}^2 + D_{\text{q}}{}^2)L + 2CL^2\omega^2 + 2Cr_{\text{L}}{}^2)s + 3(D_{\text{d}}{}^2 + D_{\text{q}}{}^2)r_{\text{L}}$$

Control loop gains:

$$L_{\text{out-d}} = G_{\text{cod-o}}G_{\text{PI-od}}$$

$$L_{\text{out-q}} = G_{\text{coq-o}}G_{\text{PI-oq}}$$

$$L_{\text{in}} = \frac{G_{\text{cid-o}}}{G_{\text{cod-o}}}\frac{L_{\text{out-d}}}{(1 + L_{\text{out-d}})}G_{\text{PI-dc}}$$

$$L_{\text{PLL}} = -G_{\text{PI-PLL}}\frac{-V_{\text{od}}}{s}$$

where V_{od} is the grid voltage d component, and PI-controller transfer functions are derived using proportional K_{p} and integral gains K_{i} as

$$G_{\text{PI}} = K_{\text{p}} + \frac{K_{\text{p}}}{s}$$

.

REFERENCES

[1] J. L. Agorreta, M. Borrega, J. Lpez, and L. Marroyo, "Modeling and control of n -paralleled grid-connected inverters with lcl filter coupled due to grid impedance in pv plants," *IEEE Transactions on Power Electronics*, vol. 26, no. 3, pp. 770–785, March 2011.

[2] C. Li, "Unstable operation of photovoltaic inverter from field experiences," *IEEE Transactions on Power Delivery*, no. 99, pp. 1–1, 2017.

[3] T. Messo, R. Luhtala, R. Roinila, D. Yang, X. Wang, and F. Blaabjerg, "Real-time impedance-based stability assessment of grid converter interactions," in *the Eighteenth IEEE Workshop on Control and Modeling for Power Electronics, IEEE COMPEL 2017*, July 2017.

[4] J. Sun, "Impedance-based stability criterion for grid-connected inverters," *IEEE Transactions on Power Electronics*, vol. 26, no. 11, pp. 3075–3078, Nov 2011.

[5] B. Kroposki, B. Johnson, Y. Zhang, V. Gevorgian, P. Denholm, B. M. Hodge, and B. Hannegan, "Achieving a 100systems with extremely high levels of variable renewable energy," *IEEE Power and Energy Magazine*, vol. 15, no. 2, pp. 61–73, March 2017.

[6] L. Jessen and F. W. Fuchs, "Modeling of inverter output impedance for stability analysis in combination with measured grid impedances," in *2015 IEEE 6th International Symposium on Power Electronics for Distributed Generation Systems (PEDG)*, June 2015, pp. 1–7.

[7] M. Cespedes and J. Sun, "Online grid impedance identification for adaptive control of grid-connected inverters," in *2012 IEEE Energy Conversion Congress and Exposition (ECCE)*, Sept 2012, pp. 914–921.

[8] A. Rygg and M. Molinas, "Real-time stability analysis of power electronic systems," in *2016 IEEE 17th Workshop on Control and Modeling for Power Electronics (COMPEL)*, June 2016, pp. 1–7.

[9] J. Jokipii, T. Messo, and T. Suntio, "Simple method for measuring output impedance of a three-phase inverter in dq-domain," in *2014 International Power Electronics Conference (IPEC-Hiroshima 2014 - ECCE ASIA)*, May 2014, pp. 1466–1470.

[10] T. Roinila, M. Vilkko, and J. Sun, "Broadband methods for online grid impedance measurement," in *2013 IEEE Energy Conversion Congress and Exposition*, Sept 2013, pp. 3003–3010.

[11] A. Yazdani and R. Iravani, *Voltage-Sourced Converters in Power Systems: Modeling, Control, and Applications*. Wiley-IEEE Press, 2010.

[12] T. Roinila, T. Messo, and E. Santi, "Mimo-identification techniques for rapid impedance-based stability assessment of three-phase systems in dq domain," *IEEE Transactions on Power Electronics*, vol. 33, no. 5, pp. 4015–4022, May 2018.

[13] T. Roinila, J. Huusari, and M. Vilkko, "On frequency-response measurements of power-electronic systems applying mimo-identification techniques," *IEEE Trans. on Industrial Electronics*, vol. 60, no. 11, pp. 5270–5276, 2013.

[14] T. Roinila, H. Abdollahi, S. Arrua, and E. Santi, "Online measurement of bus impedance of interconnected power electronics systems: Applying orthogonal sequences," *in Proc. IEEE Energy Conversion Congress and Exposition*, pp. 5783–5788, 2017.

[15] Tushar, S. Pandey, A. K. Srivastava, P. Markham, and M. Patel, "Online estimation of steady-state load models considering data anomalies," *IEEE Transactions on Industry Applications*, vol. 54, no. 1, pp. 712–721, Jan 2018.

[16] S. Sahoo, S. Prakash, and S. Mishra, "Power quality improvement of grid-connected dc microgrids using repetitive learning-based pll under abnormal grid conditions," *IEEE Transactions on Industry Applications*, vol. 54, no. 1, pp. 82–90, Jan 2018.

[17] T. Messo, J. Jokipii, A. Aapro, and T. Suntio, "Time and frequency-domain evidence on power quality issues caused by grid-connected three-phase photovoltaic inverters," in *2014 16th European Conference on Power Electronics and Applications*, Aug 2014, pp. 1–9.

[18] X. Wang, F. Blaabjerg, and W. Wu, "Modeling and analysis of harmonic stability in an ac power-electronics-based power system," *IEEE Transactions on Power Electronics*, vol. 29, no. 12, pp. 6421–6432, Dec 2014.

[19] F. Wang, J. L. Duarte, M. A. M. Hendrix, and P. F. Ribeiro, "Modeling and analysis of grid harmonic distortion impact of aggregated dg inverters," *IEEE Transactions on Power Electronics*, vol. 26, no. 3, pp. 786–797, March 2011.

[20] B. Wen, R. Burgos, D. Boroyevich, P. Mattavelli, and Z. Shen, "Ac stability analysis and dq frame impedance specifications in power-electronics-based distributed power systems," *IEEE Journal of Emerging and Selected Topics in Power Electronics*, vol. 5, no. 4, pp. 1455–1465, Dec 2017.

[21] T. Suntio, T. Messo, and J. Puukko, *Power Electronic Converters: Dynamics and Control in Conventional and Renewable Energy Applications*. Wilwy-VCH, 2017.

[22] R. Dorf and R. Bishop, *Modern Control Systems*. Prentice-Hall, 2000.

[23] R. Teodorescu, M. Liserre, and P. Rodriguez, *Grid Converters for Photovoltaic and Wind Power Systems*. Wiley-IEEE Press, 2011.

[24] R. Luhtala, T. Messo, T. Roinila, T. Reinikka, J. Sihvo, and M. Vilkko, "Adaptive control of grid-connected inverters based on real-time measurements of grid impedance: Dq-domain approach," in *2017 IEEE Energy Conversion Congress and Exposition (ECCE)*, Oct 2017, pp. 69–75.

[25] K. R. Godfrey, *Perturbation Signals for System Identification*. Prentice Hall, UK, 1993.

[26] Z. Sharif and A. Z. Sha'ameri, "The application of cross correlation technique for estimating impulse response and frequency response of wireless communication channel," in *2007 5th Student Conference on Research and Development*, Dec 2007, pp. 1–5.

[27] T. Messo, J. Jokipii, A. Makinen, and T. Suntio, "Modeling the grid synchronization induced negative-resistor-like behavior in the output impedance of a three-phase photovoltaic inverter," in *2013 4th IEEE International Symposium on Power Electronics for Distributed Generation Systems (PEDG)*, July 2013, pp. 1–7.

PUBLICATION
II

Online Frequency Response Measurements of Grid-Connected Systems in Presence of Grid Harmonics and Unbalance

R. Luhtala, H. Alenius, T. Messo and T. Roinila

IEEE Transactions on Power Electronics, vol. 35, no. 4, pp. 3343-3347, 2020

Online Frequency-Response Measurements of Grid-Connected Systems in Presence of Grid Harmonics and Unbalance

Roni Luhtala, Henrik Alenius, Tuomas Messo, and Tomi Roinila

***Abstract*—Grid characteristics have a drastic impact on the stability and control performance of grid-connected systems. Because the grid conditions typically vary over time, online measurements are most desirable for the stability assessment, protection design, and control-system optimization of the systems. Previous studies have presented methods based on Fourier techniques and broadband sequences with which the frequency responses of the grid-connected systems, such as the grid impedance or inverter control loops, can be measured. However, online measurements under unbalanced grids with harmonic voltages have not been comprehensively considered. The present paper demonstrates how the previously applied online-measurement methods fail in the presence of unbalanced grid and voltage harmonics due to the spectral leakage caused by Fourier transform. This work also proposes a simple signal-design method to avoid the leakage. Experimental results based on a high-power grid-connected system are shown to demonstrate the effectiveness of the proposed method.**

I. Introduction

The performance and stability of grid-connected power-electronics applications are significantly affected by the interfaced grid [1]–[4]. Since the grid conditions vary over time, online measurements of the grid impedance and the load-affected converter AC-side dynamics are most desirable for obtaining the system stability margins in the grid-connection point. Additionally, online measurements acquired in real time allow novel control strategies such as adaptive control or adjustment of the protection parameters. Such measurements have become popular in power-electronics applications, including grid-connected converters [5]–[8]. In most of the presented methods, a broadband perturbation such as pseudo-random binary sequence (PRBS) is injected into the system, and Fourier analysis is applied to extract the corresponding frequency components in the responses.

A single converter may face unpredictable grid conditions such as a weak grid or poor grid voltages [2], [9]. The disturbances in grid voltages, such as voltage harmonics, may cause errors in the frequency-response measurements. Although the issues related to unbalanced or harmonic-polluted grid voltages are widely known, the impact of the voltage waveforms on the online measurements has not been previously considered. The present study discusses the measurement issues under the unbalanced grid with a high harmonic content and introduces a design procedure of the perturbation signal to suppress the issues.

The grid harmonics appear as periodic oscillations in the measured samples. When the discrete Fourier transform (DFT) is applied, the periodic oscillations may leak to other frequencies through two undesired features known as spectral leakage and the picket-fence effect (PFE) [5], [10]. The PFE appears if the discrete spectrum, produced by the DFT, does not include exactly the frequencies of periodic oscillations. This results in leaking to the nearest available frequency bins [11]. The spectral leakage occurs when the DFT is applied on samples that contain non-integer periods of periodic signals, causing those frequencies to leak over a wide frequency band [12].

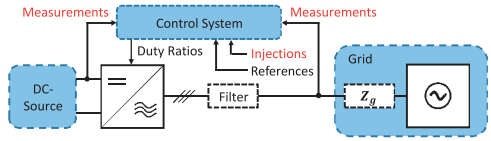

Fig. 1: Grid-connected inverter.

The grid fundamental and its harmonics appear at specific frequencies. This means they can be taken into account when adjusting the measurement time so that each measured sample contains integer periods of the grid fundamentals, and thereby, also its harmonics. This suppresses the spectral leakage caused by grid harmonics and unbalance.

This paper shows how the spectral leakage deteriorates the online frequency-response measurements under grid harmonics and unbalance. It also introduces a design procedure to remove the spectral leakage from the measurements.

The reminder of the paper is organized as follows. Section II reviews the online frequency-response measurements and issues related to the spectral leakage. Section III introduces the applied broadband perturbations that are suitable for the dq-domain measurements and proposes a design procedure for measurements under the grid unbalance and harmonics. Section IV shows high-power experimental results in which spectral leakage occurs and how the proposed design procedure can be used to remove the leakage. Section V draws conclusions.

II. Online Measurements of Grid-Connected Systems

Fig. 1 shows a three-phase grid-connected inverter. The inverter is controlled based on measurements from the DC- and AC-side waveforms. The same measurements can be used for frequency-response identification, which usually requires an excitation signal to be injected into the system. A typical frequency-response measurement setup for multi-input-multi-output (MIMO) identification is illustrated in Fig. 2. In this

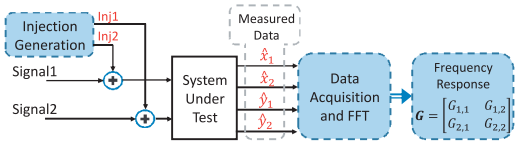

Fig. 2: Typical frequency-response measurement setup.

example, two signals are perturbed, the system responses are measured, and the frequency response is computed using Fourier techniques [7]. The online measurements can be performed either for the grid- or the inverter-side transfer functions, thus obtaining, for example, the grid impedance or inverter control loops.

Three-phase grid-connected systems are often analyzed in the dq domain, where three-phase AC quantities can be transformed into two DC quantities, d and q components [1]. In the dq domain, full-order transfer functions are represented as 2 x 2 matrices that include direct (dd and qq) and crosscoupling (dq and qd) components. The dq-domain measurements can be performed in accordance with the setup shown in Fig. 2, where Signal1 and Signal2 correspond to the d and q components. In the computed frequency-response matrix, the diagonal components ($G_{1,1}$ and $G_{2,2}$) usually refer to direct components (G_{dd} and G_{qq}) and the off-diagonal components ($G_{1,2}$ and $G_{2,1}$) refer to crosscouplings (G_{dq} and G_{qd}).

In online measurements of the grid-connected systems, the grid cannot be considered as an ideal three-phase voltage source, due to the occurence of non-idealities such as harmonics, unbalance, or noise. The measurement noise is usually relatively low and can be mitigated by simply increasing the signal-to-noise ratio (SNR) of the measurements by applying higher perturbation amplitude or by averaging the measurements over multiple measurement cycles [10].

The grid harmonics and unbalance appear as periodic oscillations in the measured data. When the discrete Fourier transformation (DFT) is applied, two unwanted features may appear: spectral leakage and picket-fence effect (PFE) [12]. These features deteriorate the spectral estimation and may cause drastic errors in the frequency-response measurements [5], especially at frequencies near the grid-voltage harmonics. The PFE results from non-coherent sampling as a discrete spectrum of the DFT does not include exactly the same frequencies that appear in the measured data, causing these frequencies to leak to the nearest frequency bins. The spectral leakage appears if the measured time-domain data does not include exact integer periods of each periodic signal components, such as the grid-voltage fundamental and its harmonics. If the DFT sample contains fractional periods of periodic signals, the DFT interprets them as discontinuations that cause spectral leakage over a wide frequency band.

III. Measurement Design

A. Orthogonal Pseudo-Random Sequences

A maximum-length binary sequence (MLBS) is a widely applied broadband excitation in the frequency-response measurements of power-electronics systems [5]. The MLBS can be easily modified, the sequence has lowest possible crest factor, and is periodic over its length $N = n^2 - 1$, where n is an integer [10]. Considering the measurement setup shown in Fig. 2, one can apply orthogonal binary sequences for simultaneously measuring the full impedance matrix [6], [7]. In the method, two orthogonal sequences are simultaneously injected into d and q channels. As the injections have energy at different frequencies, several (coupled) impedance components can be measured during a single measurement cycle.

The work in [6] and [7] applied a method based on Hadamard modulation for generating orthogonal binary sequences. In the method, the conventional MLBS is used as a first injection. The second (orthogonal) injection is obtained by doubling the MLBS and inverting every other digit. Due to inverse-repeated characteristics of the second injection, the power of the even-order harmonics equals to zero, and thus, must be neglected from the frequency-response measurements [6].

B. Measurement Parameters

The optimal online-measurement design avoids unnecessarily long measurement time and high injection amplitude, while still providing sufficient SNR. Averaging reduces the effect of the noise, but the spectral leakage may still remain. The leakage can be minimized by designing the measurement setup so that an integer number of the grid fundamental cycles (and, thereby, also its harmonics) occurs in the measured sample. The number of the grid fundamental cycles that occur during the measurement time can be given as

$$\frac{N}{f_{\mathrm{gen}}} P f_{\mathrm{g}} = (R + r) \tag{1}$$

where P is a number of averaged MLBS (generated at f_{gen}) periods, and f_{g} is a grid fundamental frequency. The number of grid fundamental cycles is separated to its integer part (R) and fractional part (r), from which the non-zero r causes the spectral leakage. The time difference ΔT between the measurement time and the nearest multiple of the periodic cycle can be given as

$$\Delta T = \mathrm{abs}\left[\frac{N}{f_{\mathrm{gen}}} P f_{\mathrm{g}} - \mathrm{round}\left(\frac{N}{f_{\mathrm{gen}}} P f_{\mathrm{g}}\right)\right] \frac{1}{f_{\mathrm{g}}} \tag{2}$$

where the operator $round$ gives the nearest integer of the grid fundamental. By varying the averaged periods, the local minimum of the spectral leakage is expected when $\Delta T(P)$ (and r) is minimized, representing the proposed measurement design. The following design procedure yields parameters to minimize the spectral leakage.

1) Adjust $f_{\mathrm{gen}} = m(2f_{\mathrm{g}})$, where m is an integer.
   - Converter switching frequency f_{sw} restricts the possible choices as $f_{\mathrm{gen}} = f_{\mathrm{sw}}/e$, where e is an integer.
2) Choose $P = f_{\mathrm{gen}}/f_{\mathrm{g}}$ or multiple of it.
   - $T_{\mathrm{meas}} = P(N/f_{\mathrm{gen}}) = a(1/f_{\mathrm{g}})$, where a is an integer.
   - This results in $a = N$, and thus, T_{meas} includes exactly $R = N$ fundamental grid cycles and r =0.
3) N can be chosen without restrictions to satisfy the desired measurement characteristics.

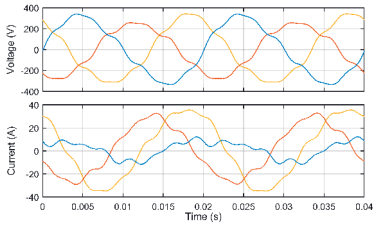

Fig. 3: Polluted grid waveforms without injection.

As a result of the proposed design procedure, an integer amount of the grid fundamental cycles (and consequently, its harmonics) is measured. Therefore, the spectral leakage caused by grid-voltage harmonics is avoided.

C. Measurement Accuracy

The measurement accuracy can be assessed by its variance σ^2. Higher values indicate increased variability between consecutive measurements and errors around the reference, thus making the measurement system unreliable. In this paper, a smooth impedance Z_{Fit} is used as a reference, produced by a MATLAB's curve-fitting tool from a measurement under ideal grid voltages. The variance can be computed as

$$\sigma^2 = \sum_{f=1}^{\infty} \left[Z_{\text{Fit}}(f) - Z_{\text{meas}}(f) \right]^2 \tag{3}$$

where the variance of the reference is considered as zero. It may be assumed that each dq-domain channel (including crosscouplings) has approximately equal SNR during measurements, and they can be taken equally into account when comparing the measurement results to each other. Thus, the total variance of measurement is computed over the entire dq-domain impedance matrix as

$$\sigma^2_{\text{DQ}} = \sigma^2_{\text{dd}} + \sigma^2_{\text{dq}} + \sigma^2_{\text{qd}} + \sigma^2_{\text{qq}} \tag{4}$$

IV. Experiments

The experiments are performed using a high-power PHIL setup in accordance with Fig. 1. The system is implemented by two 200 kVA Egston voltage amplifiers and the grid impedance by three-phase inductors. The amplifiers are used to emulate a three-phase grid and a grid-connected converter. The measurement system is described in detail in [8]. In the following experiments the grid impedance is measured in the dq domain. The currents and voltages are measured from the output terminal of the inverter emulator and the data is captured by a measurement card (NI USB-6363). The data is operated by the MATLAB/Data Acquisition Toolbox.

Fig. 3 shows samples of the highly-distorted grid voltages (230 V, 50 Hz) under which the experiments are performed. One of the phases is in 20 % unbalance and all phases include 5 % of the positive sequence 2^{nd} and 7^{th} harmonics as well as negative sequence 2^{nd} and 5^{th} harmonics.

A. Grid-Impedance Measurements

Two orthogonal sequences were designed and injected into the references of the current controller. The first sequence had 2047 bits and the second had 4094 bits. Both sequences were generated at 5 kHz, providing 2.44 Hz (5000/2047 Hz) frequency resolution. The number of averaged periods varied between the measurements in order to achieve desired measurement time that minimizes ΔT. The unbalance occurs at 50 and 100 Hz in the dq domain, and the present harmonics at 50, 150, and 300 Hz. As the frequency resolution of the measurements does not produce the discrete spectral line at 50 Hz, the PFE occurs and the harmonics leak to the nearest discrete spectrum frequencies, given in Table I.

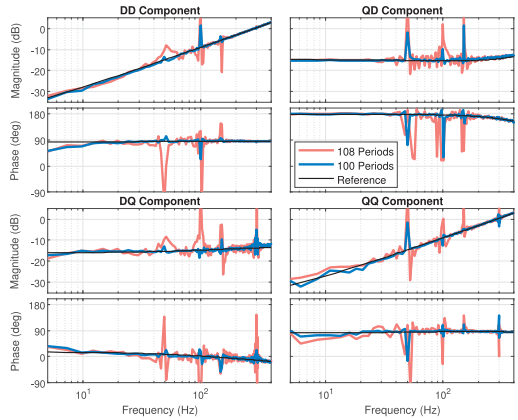

Fig. 4: MIMO-measurements of the grid impedance with different averaging.

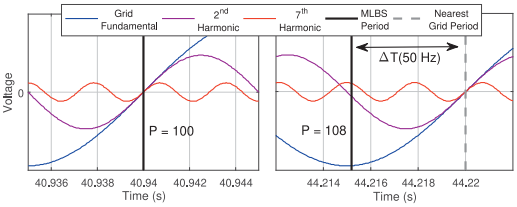

Fig. 5: Time difference between applied MLBS periods P = 100 (left), P = 108 (right), and grid-voltage components.

TABLE I: Nearest discrete spectrum frequency points to the grid harmonics.

f (Hz)	50	100	150	300
Below	48.85	97.70	149.00	298.00
Above	51.29	100.15	151.44	300.44

Fig. 4 shows the measured grid impedance with two different number of averaged periods. The blue line represents one of the proposed measurement designs (P = 100), where the measured data includes an integer amount of the fundamental grid cycles (R = 2047, r = 0, ΔT = 0). Therefore, the grid-impedance measurement does not show any spectral leakage, only the PFE distort the measurement near the grid harmonics, which can be predicted. Red line (P=108) represents design without considering the spectral leakage minimization as the fractional part of grid fundamental cycle occurs in the measured data (R = 2210, r = 0.76, ΔT = 4.8 ms). Fig. 5 illustrates the time difference between the measurement time for different number of averaged periods and the nearest full period of fundamental grid voltage. When P = 100 (left), the time difference equals to zero and no spectral leakage occurs.

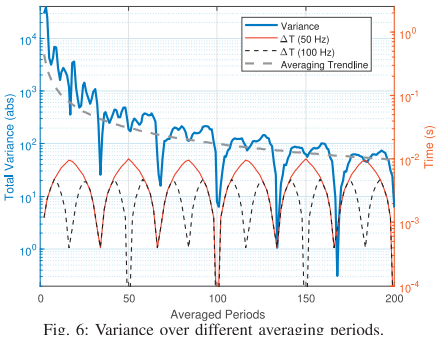

Fig. 6: Variance over different averaging periods.

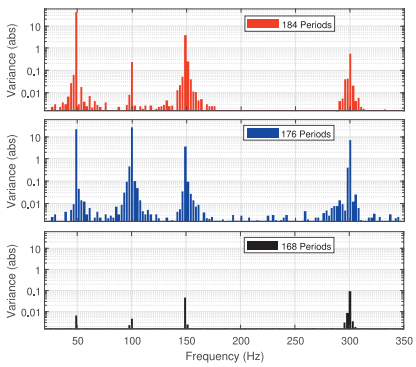

Fig. 7: Variance over frequency spectrum for different numbers of averaged periods.

The time difference with P = 108 (right) produces spectral leakage which deteriorates the measurements, as shown in Fig. 4.

Fig. 6 shows the variance, averaging trend line, and the time difference to the grid fundamental cycle ΔT(50 Hz) and its second harmonic ΔT(100 Hz) with varying number of averaged periods. The local minimums of ΔT(50 Hz) give the proposed parametrization to minimize the spectral leakage. The variance follows the averaging trend line otherwise, but the variance is significantly decreased at the local minimums of ΔT(50 Hz).

To illustrate the appearance of the spectral leakage, Fig. 7 shows the measurement variance as a function of frequency with three different P, given as

- P = 184 (red bars), chosen from local minimum of ΔT(100 Hz), which mitigates the spectral leakage of even-order grid harmonics (here 100 and 300 Hz).
- P = 176 (blue bars) representing design not considering the spectral leakage.
- P = 168 (black bars), chosen from local minimum of both ΔT(50 Hz) and ΔT(100 Hz), which mitigates the spectral leakage from all grid-harmonic frequencies.

V. Conclusions

Wideband identification methods have become popular in the analysis of grid-connected systems. However, recent studies have not considered the undesired spectral leakage that deteriorates the measurements under unbalanced grid conditions or under high harmonic content in the grid voltages. The unbalance and harmonics occur as periodic oscillations in the measured data and leak over a wide frequency band during the signal post-processing. This paper has presented methods to mitigate the spectral leakage by adjusting the measurement parameters such that an integer amount of grid-fundamental cycles is included in the measured data. Consequently, the spectral leakage caused by signal processing is avoided, and the frequency responses are obtained with significantly more accuracy. The proposed method is well applicable both in dq- and sequence-domain measurements. Experimental measurements based on a high-power PHIL system were shown to demonstrate the effectiveness of the proposed method.

Acknoledgment

This research and testing has been performed using the ERIGrid Research Infrastructure and is part of a project that has received funding from the European Union's Horizon 2020 Research and Innovation Programme under Grant Agreement No. 654113. The support of the European Research Infrastructure ERIGrid and its partner DNVGL is much appreciated. The work was also supported by the Academy of Finland.

References

[1] A. Rygg and M. Molinas, "Apparent impedance analysis: A small-signal method for stability analysis of power electronic-based systems," *IEEE Journal of Emerging and Selected Topics in Power Electronics*, vol. 5, no. 4, pp. 1474–1486, Dec 2017.

[2] T. Messo, R. Luhtala, A. Aapro, and T. Roinila, "Accurate impedance model of grid-connected inverter for small-signal stability asssessment in high-impedance grids," in *IEEJ Journal of Industry Applications*, vol. 8, 2019, pp. 488–492.

[3] L. Jessen and F. W. Fuchs, "Modeling of inverter output impedance for stability analysis in combination with measured grid impedances," in *2015 IEEE 6th International Symposium on Power Electronics for Distributed Generation Systems (PEDG)*, 2015.

[4] M. Cespedes and J. Sun, "Online grid impedance identification for adaptive control of grid-connected inverters," in *2012 IEEE Energy Conversion Congress and Exposition (ECCE)*, 2012, pp. 914–921.

[5] J. Schoukens, K. Godfrey, and M. Schoukens, "Nonparametric data-driven modeling of linear systems: Estimating the frequency response and impulse response function," *IEEE Control Systems Magazine*, vol. 38, no. 4, pp. 49–88, Aug 2018.

[6] T. Roinila, T. Messo, and E. Santi, "Mimo-identification techniques for rapid impedance-based stability assessment of three-phase systems in dq domain," *IEEE Transactions on Power Electronics*, vol. 33, no. 5, pp. 4015–4022, 2018.

[7] R. Luhtala, T. Roinila, and T. Messo, "Implementation of real-time impedance-based stability assessment of grid-connected systems using mimo-identification techniques," *IEEE Transactions on Industry Applications*, 2018.

[8] T. Roinila, T. Messo, R. Luhtala, R. Scharrenberg, E. de Jong, A. Fabian, and Y. Sun, "Hardware-in-the-loop methods for real-time frequency-response measurements of on-board power distribution systems," *IEEE Transactions on Industrial Electronics*, 2018.

[9] C. Li, "Unstable operation of photovoltaic inverter from field experiences," *IEEE Transactions on Power Delivery*, vol. 33, no. 2, 2018.

[10] K. R. Godfrey, *Perturbation Signals for System Identification*. Prentice Hall, UK, 1993.

[11] G. W. Chang, C. I. Chen, Y. J. Liu, and M. C. Wu, "Measuring power system harmonics and interharmonics by an improved fast fourier transform-based algorithm," *IET Generation, Transmission Distribution*, vol. 2, no. 2, pp. 193–201, March 2008.

[12] H. Wen, Z. Teng, Y. Wang, B. Zeng, and X. Hu, "Simple interpolated fft algorithm based on minimize sidelobe windows for power-harmonic analysis," *IEEE Transactions on Power Electronics*, vol. 26, no. 9, pp. 2570–2579, Sep. 2011.

PUBLICATION

III

Improved Real-Time Stability Assessment of Grid-Connected Converters Using MIMO-Identification Methods

R. Luhtala, T. Reinikka, T. Roinila, T. Messo and J. Sihvo

IEEE Energy Conversion Congress and Exposition, pp. 5322-5329, 2018

Improved Real-Time Stability Assessment of Grid-Connected Converters Using MIMO-Identification Methods

Roni Luhtala*, Tommi Reinikka, Tomi Roinila
Laboratory of Automation and Hydraulics
Tampere University of Technology
Tampere, Finland
*roni.luhtala@tut.fi

Tuomas Messo*, Jussi Sihvo
Laboratory of Electrical Energy Engineering
Tampere University of Technology
Tampere, Finland
*tuomas.messo@tut.fi

***Abstract*—Several stability and power quality problems have been reported recently in power systems, which experience a high penetration of power electronics converters, such as renewable energy inverters. The problems are often caused by the interaction between the converter and the grid impedance. Stability monitoring tools have been presented to gain insight into the stability margin of the power system. Online methods are most favorable since the power system has many parameters that vary with time. However, the online methods that have been presented may produce inaccurate estimate of the stability margin due to several simplifications, such as using reduced-order impedance models. This paper introduces an improved dq-domain stability analysis that takes into account the time-varying grid impedance in real time and also the multivariable inverter output impedance, including the crosscouplings.**

***Index Terms*—Generalized Nyquist Stability Criterion, Real-Time Identification, Grid-Connected Converters, MIMO Systems**

I. Introduction

A rapidly increasing amount of distributed renewable energy production is being connected to the power grid using power-electronic converters with relatively high switching frequencies. This kind of grid-connected system is more prone to stability issues than conventional synchronous generators. [1] The stability issues are usually caused by interactions between the inverter output impedance and a relatively high grid impedance. As the renewables are often located in remote areas with long grid-connection cables, introducing a significant grid impedance, the stability issues may arise more often. [2]

The stability of grid-connected systems can be assessed using the generalized impedance-based stability analysis by examining the grid impedance and the converter output impedance [3]. This assessment method is shown to be effective in predicting the unstable interactions between the grid and converter, and thus, the stability and operation of the grid-connected systems [4], [5]. By implementing accurate stability analysis using online identifications, the method can also be used to fine tune the converter control loops in order to provide sufficient stability margins and performance in different grid-connection points [6], [7].

The impedance-based stability of three-phase systems can be evaluated in the dq domain, which allows the model linearization around the steady-state operating point and straightforward tuning of conventional PI-type controllers. The dq-domain impedance is a matrix, including diagonal and non-diagonal (crosscoupling) components. The analysis is very often simplified and the crosscouplings are assumed to be small enough to be neglected. However, the crosscouplings may have as important a role for stability as the diagonal components, as reactance in the grid impedance increases, reactive power flow increases, or the control system of the converter becomes more complex. Thus for accurate stability assessment, the multiple-input-multiple-output (MIMO) analysis must be applied and the crosscouplings must be taken into account.

The underlying problem in accurate impedance-based stability assessment is the unpredictable grid impedance, which depends on the connection point. Online measurements from the connection point have greatly improved stability assessment techniques. Recent research has introduced measurement techniques such as applying an impulse response [8], or a maximum-length binary sequence [9]. However, for accurate stability analysis, the complete dq-domain matrix has to be measured under the same operating conditions. Simultaneous online measurement of all the components in the dq-domain impedance matrix requires uncorrelated injections to both components, the direct and quadrature. Recent studies have shown an implementation, suitable for dq-domain MIMO measurements, which applies orthogonal binary sequences [10]. Using similar methods, the complete dq-domain grid-impedance matrix can be simultaneously measured.

In renewable-energy dominant grids with load conditioning or during grid faults, the grid impedance, seen by a single grid-connection point, may vary widely over time. The unpredictable and highly time-variant grid impedance will play an important role in the stability of future power systems. As complex grid impedance is difficult to model, the use of real-time measurement of grid impedance and analytical converter impedance models may be the best basis for accurate stability assessments. Studies have demonstrated real-time methods to

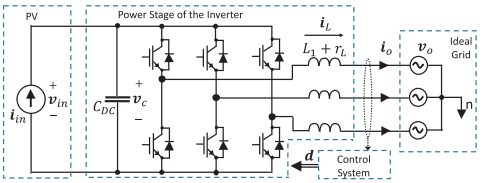

Fig. 1: Photovoltaic generator connected to the ideal grid through inverter.

measure the dq-domain grid-impedance components one by one [11], [12], and more recently to measure both diagonal components simultaneously [13]. This paper extends the work in [13] by including the effect of crosscouplings.

This paper introduces an improved assessment of the impedance-based small-signal stability in the dq domain that applies the multivariable small-signal model of the grid-connected converter and real-time measurements of the complete grid-impedance matrix. The complete grid-impedance matrix is measured continuously using a technique that applies orthogonal binary sequences. The stability is monitored continuously by plotting the characteristic loci of the return-ratio from the grid-connection point. The methods are implemented in a real-world converter as a part of a power hardware-in-the-loop (PHIL) test bench.

The remainder of the paper is organized as follows. Modeling of the grid-connected inverter, the basics of the time-varying grid impedance, and the impedance-based stability analysis are reviewed in Section II. Section III introduces the applied methods for real-time measurements and improved stability assessment. Section IV shows the applied setup, practical implementation and experimental results. Section V draws conclusions.

II. Theory

A. Analytical Inverter Model

Fig. 1 presents the three-phase inverter, connecting a photovoltaic generator to the ideal grid v_o. By using Park's transformation, the three-phase AC system can be represented in the dq domain, which includes two DC-valued components (dd and qq) with crosscouplings (dq and qd) between them. Due to the DC-valued steady-state operating point, the dq domain allows linearization around the operating point and the derivation of an accurate small-signal model. The modeling in this paper is based on [14].

To produce the small-signal model of the inverter in the dq domain, first the open-loop average model is derived. The AC-side inductor currents (i_{Ld}, i_{Lq}) and voltage over the DC capacitor (v_C) are considered as state variables whose derivatives are zero in the steady state. From the average model with state-variable derivatives set to zero are derived the steady-state values for state variables and input variables, including grid voltage (V_{gd}, V_{gq}), duty ratios (D_d, D_q), and DC-side input current for the power stage (I_{in}).

The dq-domain model is linearized around the steady-state operating point and transformed to the frequency domain, from which the open-loop transfer functions between input

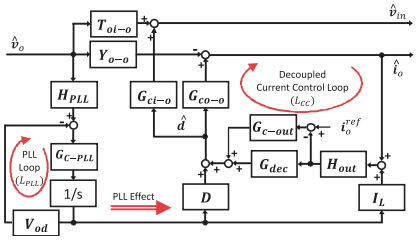

Fig. 2: Inverter dynamics as PLL and current control loops are closed.

and output variables can be numerically solved, as shown in [15].

$$\mathbf{Y}(s) = \left[\mathbf{C}(s\mathbf{I} - \mathbf{A})^{-1}\mathbf{B}\right]\mathbf{U}(s) \tag{1}$$

The linearized state-space matrices $\mathbf{A}$, $\mathbf{B}$ and $\mathbf{C}$ are given in the Appendix. From (1), the open-loop transfer functions between the input and output variables are collected into a matrix form as

$$\mathbf{Y}(s) = \begin{bmatrix} \mathbf{Z}_{\text{io-o}} & \mathbf{T}_{\text{oi-o}} & \mathbf{G}_{\text{ci-o}} \\ \mathbf{G}_{\text{io-o}} & -\mathbf{Y}_{\text{o-o}} & \mathbf{G}_{\text{co-o}} \end{bmatrix} \mathbf{U}(s) \tag{2}$$

where all the open-loop transfer functions are 2 x 2 matrices, representing the MIMO characteristics of the system. These transfer functions are given in detail in the Appendix.

The closed-loop transfer functions are derived by closing the control loops, including the phase-locked loop (PLL), DC-voltage control, and decoupled output-current control. In a cascaded control scheme, the DC-voltage control provides a reference value for the output current's d component; the q component is regulated to zero for achieving the unity power factor. The PLL synchronizes the control system with the grid voltages. For modeling the AC-side inverter output admittance, the small-signal effect of the DC-side current can be neglected from the analysis as the DC-side voltage is controlled to a maximum-power point (MPP) based on the IV-curve of the PV generator. Thus, the DC-side current is taken into account by its steady-state value.

First the AC-side control loops, including the decoupled current control and PLL, are closed. Fig. 2 shows the block diagram, which represents the input and output dynamics of the inverter as 2 x 2 transfer matrices (introduced in the Appendix) when PLL, and current control are closed. The decoupled current control (derived as [14]) and PLL loops, respectively, can be written as

$$\mathbf{L}_{\text{CC}} = \mathbf{G}_{\text{co-o}}(\mathbf{G}_{\text{c-out}} - \mathbf{G}_{\text{dec}})\mathbf{H}_{\text{out}} \tag{3}$$

$$\mathbf{L}_{\text{PLL}} = \mathbf{G}_{\text{c-PLL}}(s^{-1})\mathbf{V}_{\text{od}} \tag{4}$$

where $\mathbf{G}_{\text{c-out}}$ is the transfer function of an actual current controller, $\mathbf{G}_{\text{dec}}$ is the decoupling gain, and $\mathbf{G}_{\text{c-PLL}}$ is the actual controller of the PLL loop.

Using loop gains of (3) and (4), the PLL transfer matrix is solved as

$$\mathbf{G}_{\text{PLL}} = (\mathbf{L}_{\text{CC}}\mathbf{I}_{\text{L}} - \mathbf{G}_{\text{co-o}}\mathbf{D})\mathbf{L}_{\text{PLL}}\mathbf{H}_{\text{PLL}} \tag{5}$$

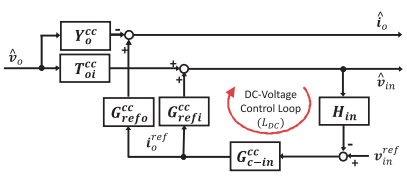

Fig. 3: Inverter input and output dynamics as AC-side control loops are included to transfer functions and DC-voltage control loop is closed.

The output dynamics can be solved as transfer functions from the output voltage $\mathbf{v}_o$, and the output-current reference $\mathbf{i}_o^{ref}$, to the output current $\mathbf{i}_o$, respectively, as

$$\begin{aligned}\mathbf{Y}_{o}^{cc} &= (\mathbf{I}+\mathbf{L}_{CC})^{-1}(\mathbf{Y}_{o\text{-}o}+\mathbf{G}_{PLL})\\ \mathbf{G}_{refo}^{cc} &= (\mathbf{I}+\mathbf{L}_{CC})^{-1}\mathbf{G}_{c\text{-}out}\mathbf{G}_{co\text{-}o}\end{aligned} \tag{6}$$

Derivation of the input dynamics requires solving the duty ratio $\mathbf{d}$. The dynamics of the decoupled current control is gathered into a matrix as

$$\mathbf{G}_{cc} = \mathbf{L}_{CC}(\mathbf{I}+\mathbf{L}_{CC})^{-1} \tag{7}$$

The input dynamics can be solved from $\mathbf{v}_o$ and $\mathbf{i}_o^{ref}$ to the input voltage $\mathbf{v}_{in}$, respectively, as

$$\begin{aligned}\mathbf{T}_{oi}^{cc} &= \mathbf{T}_{io\text{-}o}+\mathbf{G}_{ci\text{-}o}(\mathbf{G}_{co\text{-}o})^{-1}(\mathbf{G}_{cc}(\mathbf{Y}_{o\text{-}o}\mathbf{G}_{PLL})-\mathbf{G}_{PLL})\\ \mathbf{G}_{refi}^{cc} &= \mathbf{G}_{ci\text{-}o}(\mathbf{G}_{co\text{-}o})^{-1}(\mathbf{I}-\mathbf{G}_{cc})\mathbf{G}_{c\text{-}out}\mathbf{G}_{co\text{-}o}\end{aligned} \tag{8}$$

Finally the DC-voltage control loop is closed. However, only the AC-side dynamics are considered here because the stability of the grid-connection point is the focus of this paper. Thus, complete DC-side dynamics are not included in this analysis. Fig. 3 shows the block diagram of the output and input dynamics when all control loops are closed; the transfer functions include AC-side controllers, as derived in (6) and (8).

The DC-voltage control loop gain is

$$\mathbf{L}_{DC} = \mathbf{G}_{refi}^{cc}\mathbf{G}_{c\text{-}in}\mathbf{H}_{in} \tag{9}$$

where $\mathbf{G}_{c\text{-}in}$ is the actual DC-voltage controller.

The inverter output admittance can be solved from Fig. 3 as the transfer function from $\mathbf{v}_o$ to $\mathbf{i}_o$ as

$$\mathbf{Y}_{o\text{-}c} = \mathbf{Y}_{o}^{cc}+\mathbf{G}_{refo}^{cc}\mathbf{G}_{c\text{-}in}\mathbf{H}_{in}(\mathbf{I}+\mathbf{L}_{DC})^{-1}\mathbf{T}_{oi}^{cc}+\mathbf{Y}_{f} \tag{10}$$

where $\mathbf{Y}_f$ is a parallel admittance (passively damped C-branch of the filter) including damping resistance r_f and capacitance C_f; the matrix is presented in the Appendix. Due to parallel connection, the filter admittance can be added directly to the inverter small-signal model.

The complete dq-domain inverter output-admittance matrix,

$$\mathbf{Y}_{o\text{-}c} = \begin{bmatrix} Y_{o\text{-}dd} & Y_{o\text{-}qd} \\ Y_{o\text{-}dq} & Y_{o\text{-}qq} \end{bmatrix} \tag{11}$$

includes diagonal (dd and qq) and crosscoupling (qd and dq) components.

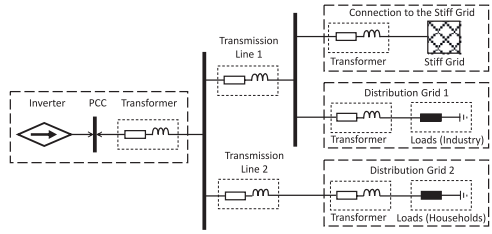

Fig. 4: Example of a power grid topology.

B. Time-Varying Grid Impedance

Distributed PV generation is often located in remote areas, due to space requirements. As the length of the grid-connection cables increases, the grid impedance seen by a single grid-connecting inverter becomes significant. High grid impedance may interact with the inverter output admittance, causing excessive harmonics in the grid currents. The observed grid impedance depends highly on the grid-connection point of the single converter and is hard to model from a complex grid topology. Additionally, the changing load profiles and possible grid faults produce highly time-variant characteristics for the grid impedance. Thus, the grid impedance for every single connection point at a certain time cannot be accurately predicted without measurements. [16]

Fig. 4 shows an example of the inverter point of common coupling (PCC) with the grid. The simple grid topology includes two transfer lines (1 and 2) to the different kinds of load centers (distribution grid 1 and 2) and to the stiff-grid connection. The transformers and the transfer lines are mainly inductive, increasing the grid impedance. The stiff grid is a very low-impedance part that can consume or produce power as much as required. Distribution grid 1 includes mainly heavy industry that may vary considerably as the industry consumes power during the day and possibly shuts down during the night and weekends. Distribution grid 2 includes mainly households, which introduce capacitive characteristics [17], causing resonance peaks with the inductive parts. The resonance peaks are damped when active power is consumed in households but may be significantly high when less power is consumed. Overall, this simple grid is difficult to model accurately as the loading conditions at certain times are unpredictable. [18]

The possibility of grid faults should also be considered. The parallel connection of the two transfer lines in Fig. 4 decreases the total grid impedance, seen from the inverter PCC, compared to that with one grid-connection cable. However, grid faults in transfer lines can cause a sudden increase in the total grid impedance. This high grid impedance may start to interact with the inverter output admittance, causing stability issues such as excessive harmonics, and thus spreading the grid fault.

The reactance and consumption/production of reactive power increase the crosscoupling components in the dq-domain grid impedance. Thus, the complete dq-domain grid impedance matrix,

$$\mathbf{Z}_{g} = \begin{bmatrix} Z_{g\text{-}dd} & Z_{g\text{-}qd} \\ Z_{g\text{-}dq} & Z_{g\text{-}qq} \end{bmatrix} \tag{12}$$

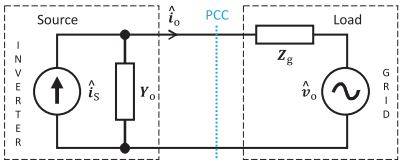

Fig. 5: Equivalent circuit of inverter grid-connection point.

must be considered in the stability studies, and the crosscouplings cannot be neglected in weak grids.

C. Impedance-Based Stability Analysis

The small-signal stability issues and the interactions between the grid and inverter at the PCC can be predicted by an impedance-based stability analysis [14]. Fig. 5 shows an equivalent small-signal circuit diagram of the PCC. The inverter (source) is modeled as a Norton equivalent, by an ideal current source $\mathbf{i}_s$ with a non-zero shunt admittance $\mathbf{Y}_o$. The grid (load) is modeled as a Thevenin equivalent, by an ideal voltage sink $\mathbf{v}_o$ and a non-zero series impedance $\mathbf{Z}_g$.

The impedance-based stability analysis is based on applying the Nyquist stability criterion to the return-ratio formed by the source and load impedance. [3]e Assuming that the source is stable when unloaded and the load is stable when powered by an ideal source, the stability analysis of the current flowing from the source to the load can be simplified by observing only the transfer matrix:

$$\mathbf{L}_s(s) = [\mathbf{I} + \mathbf{Y}_o(s)\mathbf{Z}_g(s)]^{-1} \tag{13}$$

The PCC is stable if a characteristic loci of the return-ratio matrix $\mathbf{Y}_o(s)\mathbf{Z}_g(s)$ satisfy the generalized Nyquist stability criterion. Satisfying that criterion is similar to a conventional eigenvalue analysis and ensures that the system eigenvalues have non-positive real parts. [19] The complete dq-domain matrices are fully identified in this paper by analytically modeling the inverter (11) and measuring the grid (12) in real time.

III. Methods

A. MIMO Measurements Applying Orthogonal Binary Sequences

The dq-domain impedance matrix can be considered as a clear MIMO system with two individual components and the crosscouplings between them. Conventionally, all components of such a MIMO system are identified one by one. That is time consuming and the system operation or parameters may vary between the measurement cycles in time-variant systems. However, all the components can be simultaneously measured by applying uncorrelated sequences, which do not interfere with each other, as the sequences include energy at different frequencies. Two uncorrelated sequences are required for simultaneous identification of the complete dq-domain impedance matrix, one to perturb the current d component and another the q component. By perturbing both output-current components, the grid-impedance matrix can be identified as ratios of voltage and current components, as follows

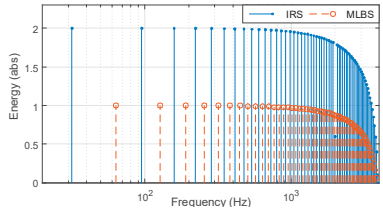

Fig. 6: Power spectra of orthogonal sequences.

$$\mathbf{Z}_g(s) = \begin{bmatrix} v_{g\text{-}d}(s)/i_{o\text{-}d}(s) & v_{g\text{-}d}(s)/i_{o\text{-}q}(s) \\ v_{g\text{-}q}(s)/i_{o\text{-}d}(s) & v_{g\text{-}q}(s)/i_{o\text{-}q}(s) \end{bmatrix} \tag{14}$$

The output currents are perturbed by uncorrelated sequences, and voltage responses are gathered from the grid side; the waveforms are transformed to the frequency domain using a Fourier transformation. From the voltage transformed to the frequency-domain, the responses of the current d and q components can be separated accurately if the system is linear around its steady state [10]. In the case of highly non-linear systems, the methods will fail as the responses from certain frequencies leak to near frequencies, and thus, the responses of the uncorrelated sequences cannot be separated. However, the grid is assumed to consist of passive components, and thus, it can be considered as a linear system.

The maximum-length binary sequence (MLBS) is a broadband signal and is the most common form of the pseudo-random binary sequences (PRBS). The periodic MLBS is easy to generate with the use of a shift register and XOR feedback. The sequence length is based on the applied number of stages in the shift register n as $N_{\text{MLBS}} = 2^n - 1$. The frequency resolution depends on the generation frequency f_{gen} as $f_{\text{res}} = f_{\text{gen}}/N_{\text{MLBS}}$. [20] The required time for a single measurement cycle is given as $T_{\text{cycle}} = N_{\text{MLBS}}/f_{\text{gen}}$. Due to the periodicity of the sequence, the response can be averaged over P periods to increase the accuracy of the measurements but that tactic also increases the total measurement time as $T_{\text{meas}} = P \times T_{\text{cycle}}$.

It is possible to generate two (or more) orthogonal binary sequences from the conventional MLBS, which are uncorrelated over their common period. As two uncorrelated sequences are required to fully identify the dq-domain impedance matrix, the inverse-repeated sequence (IRS) is generated from the conventional MLBS by doubling the sequence and then inverting every other digit. Thus, the sequence length of the IRS is twice the original length of the MLBS, as $N_{\text{IRS}} = 2N_{\text{MLBS}}$, and the required time for a single IRS cycle is increased by the same factor. Fig. 6 shows the power spectra (power values are scaled to illustrate differences) of the 63-bit-length MLBS and the corresponding IRS, generated at 4 kHz. Due to inverse-repeat characteristics, the even-order harmonics of the IRS are suppressed, and thus, the MLBS and IRS have a similar frequency resolution, with the MLBS starting from f_{res} and the IRS from $f_{\text{res}}/2$. The power content of both sequences follows

a $sinc^2$ function, which is halved approximately at $0.45f_{gen}$ which is usually considered the ending of the measurable bandwidth.

B. Real-Time Stability Assessment

The generalized Nyquist stability assessment applies the complete dq-domain matrices of the grid impedance and the inverter output admittance. The orthogonal pseudo-random sequences (MLBS and IRS) have energy at different frequencies. This is a practical issue for the generalized Nyquist stability analysis as a characteristic loci of the return-ratio matrix (13) are identified as a function of $s = j2\pi f$ where f is a certain frequency. That issue is solved by perturbing both components using the MLBS and the IRS which have different frequency contents. First the MLBS perturbs the d-component and the IRS perturbs the q component for P_1 periods, which corresponds to IRS periods. After that, the sequence order is changed and the IRS perturbs the d component and MLBS the q component for P_2 (IRS) periods. Thus, $P_1 + P_2$ IRS periods are required to identify every grid-impedance component from similar frequencies. Control of the sequences is driven by a measurement device that sends a trigger for an injection generator (implemented in the inverter control system) to change which current component is perturbed by the MLBS and which by the IRS. Thus, the data gathering can be synchronized with the injection generator, and the responses of certain sequences can be separated from each other. That feature enables accurate computation of the complete dq-domain grid-impedance matrix.

Along with the analytical small-signal model of the complete inverter output-admittance matrix from similar frequencies that the measured grid-impedance matrix includes, the characteristic loci of the return-ratio matrix (13) can be calculated. For the calculations, the variable $\lambda(s)$ is introduced. Its solution represents the characteristic locus of the return-ratio matrix at a certain frequency as (in this paper) the s sweeps the positive imaginary axis. [19] Negative frequencies are not considered in this implementation. The interconnection point of the inverter and grid (as shown in Fig. 5) can be thought of as a MIMO-feedback system. The characteristic loci of such system can be solved from the determinant [14]:

$$det\left[\lambda(s)\mathbf{I} + \mathbf{Y}_o(s)\mathbf{Z}_g(s)\right] = \mathbf{0} \tag{15}$$

The determinant of 2 x 2 matrices yields a second-order equation in function of $\lambda(s)$, and thus, two solutions are proposed, representing two separate characteristic loci. The equation is solved after every measurement of the grid-impedance matrix and the characteristic loci are drawn to the complex plane in order to monitor the stability in the real time. The stability is ensured if the loci do not encircle the critical (-1 + j0) point clockwise.

IV. Experiments

A. Experimental PHIL Setup

The proposed methods are implemented by applying a three-phase grid-connected inverter as part of a PHIL test bench.

TABLE I: Parameters of the inverter.

V_{dc}	414.3 V	I_{dc}	6.6 A	ω	$2\pi{\cdot}60$ rad/s
V_{od}	$\sqrt{2}{\cdot}120$ V	V_{oq}	0 V	f_{sw}	8 kHz
I_{Ld}	10.6 A	D_d	0.4122	D_q	0.0213
C	1.5 mF	r_L	0.1 Ω	L_1	2.2 mH
r_f	1.8 Ω	C_f	10 μF		

TABLE II: Controller parameters.

AC-current controller	$K_{p\text{-}AC}$	0.0149	$K_{i\text{-}AC}$	23.4423
DC-voltage controller	$K_{p\text{-}DC}$	0.0962	$K_{i\text{-}DC}$	1.2092
100 Hz PLL	$K_{p\text{-}100PLL}$	3.3157	$K_{i\text{-}100PLL}$	1000
20 Hz PLL	$K_{p\text{-}20PLL}$	0.6723	$K_{i\text{-}20PLL}$	38.0189

The PHIL setup includes a three-phase grid emulator, a PV simulator, and an inverter connecting the PV to the grid through an LCL-type filter and an isolating transformer. The grid-connecting inverter is controlled by a dSPACE real-time simulator, which is also configured to inject the perturbations on top of the output currents as introduced in [13]. The measurement card NI-USB 6363 sends trigger signals to the injection generator and continuously collects the grid-side waveforms, which are transformed to the dq domain inside the simulation model executed by dSPACE.

B. Inverter Output Admittance

The operating point of the inverter is given in Table I. Additionally, the proportional gains K_p and the integral gains K_i of the applied PI controllers are given in Table II. Similar AC-current controllers are implemented for the d and q components. Using the introduced parameters, the complete dq-domain admittance matrix (12) of the studied inverter can be computed using equations (3)-(10) and the open-loop model. Fig. 7 shows the analytical output admittances of diagonal components with two different PLLs. The PLL parameters affect only the admittance qq component. Fig. 8 shows the crosscoupling components with and without decouplings. It should be noted that the output filter is dominating the crosscouplings.

C. Grid-Impedance Measurements

The grid impedance is increased by connecting an extra inductance to the grid side. The setup itself introduces 0.4 Ω resistance and 0.3 mH inductance. L_2 (= 0.6 mH) of the LCL filter is included into Z_g because grid-side waveforms are gathered from a point between L_1 and L_2, which is considered as the PCC for the stability studies.

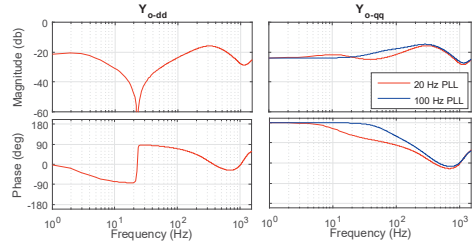

Fig. 7: Diagonal components (dd and qq) of inverter output admittance with 20 and 100 Hz PLL crossovers.

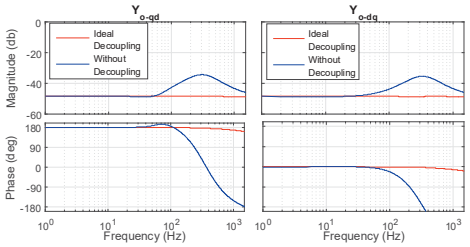

Fig. 8: Crosscoupling components (qd and dq) of inverter output admittance with and without decoupling gains in control system.

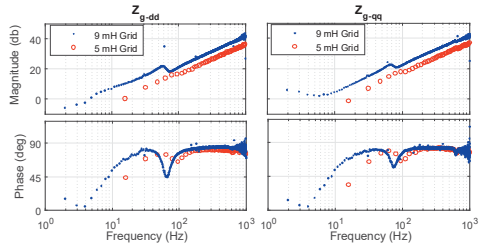

Fig. 9: Diagonal components (dd and qq) of grid impedance with 5 and 9 mH extra inductance.

Fig. 9 shows the diagonal and Fig. 10 the crosscoupling components of the measured grid impedances (with 5 and 9 mH extra inductance). All the components of the complete grid-impedance matrix are measured simultaneously by applying MIMO techniques, presented in Section III. In Figures 9 and 10, the red circles represent a 5 mH grid which is measured using a 127-bit-long MLBS and a corresponding IRS with 4 kHz generation frequency, yielding 15.75 Hz frequency resolution. The blue dots represent measurements from a 9 mH grid, identified using a 2047-bit-long MLBS and a corresponding IRS. A generation frequency of 4 kHz yields 0.98 Hz frequency resolution.

D. Generalized and Reduced-Order Nyquist Stability Analysis

Fig. 11 shows an experimental characteristic loci computed from (15). The studied inverter with 20 Hz PLL and decoupling gains (admittances shown in Figures 7 and 8) is connected to a weak grid as the 9 mH extra inductance is connected to the grid side. For accurate analysis, the grid-impedance matrix is measured in real time by a 2047-bit-long MLBS and a corresponding IRS with 4 kHz generation frequency, providing the frequency resolution of 0.977 Hz.

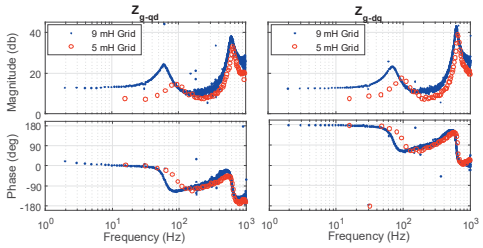

Fig. 10: Crosscoupling components (qd and dq) of grid impedance with 5 and 9 mH extra inductance.

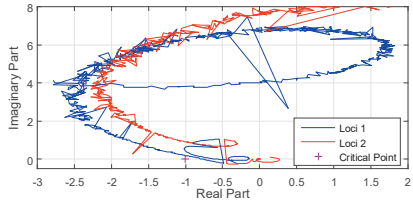

Fig. 11: Full-order characteristic loci in weak grid.

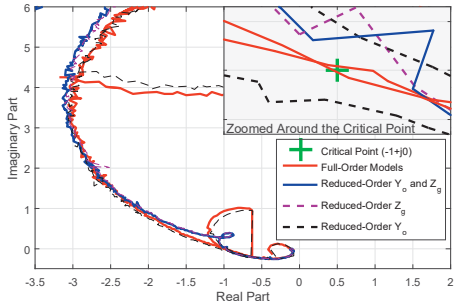

Fig. 12: Comparison of full-order and three differently simplified Nyquist stability-assessment methods.

The stability predictions by the reduced order and the generalized Nyquist stability assessment methods are compared in Fig. 12, which shows four characteristic loci in similar conditions. Only the loci that are more prone to instability are shown (similar to the blue line in Fig. 11), and the critical point (-1+j0) is studied in the zoomed-in view. The red line represents the analysis where the full-order matrices are applied (generalized Nyquist stability), the blue line represents a purely diagonal-dominant analysis where all crosscouplings are neglected, in the black dashed line only the crosscouplings from the inverter model are neglected, and in the magenta dashed line only the crosscouplings from the grid impedance are neglected.

Fig. 12 shows that the analysis applying the full-order grid-impedance matrix predicts slightly unstable operation (red and black lines), but the analysis that neglects the crosscouplings from the grid impedance (blue and magenta lines) predicts stable operation. Lower stability margins, predicted by taking the grid-impedance crosscouplings into account, could have been expected when analysing the measured grid impedances in Figures 9 and 10. The dimensions of the crosscoupling components are close to the diagonal components, and the higher grid impedance (achieved by not setting the significant crosscouplings to zero) is known to decrease the stability margins. However, by including the crosscoupling components of the inverter output admittance to the analysis, there is only a marginal effect on the predicted stability margins compared to the reduced-order analysis. The crosscoupling components of the inverter output admittance have much lower dimensions

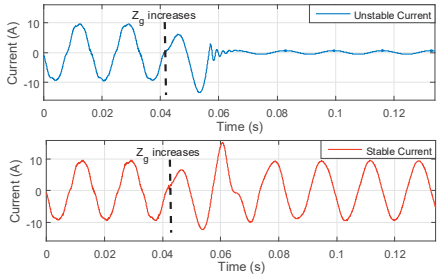

Fig. 13: Grid currents when grid impedance increases, two different PLLs.

than the diagonal components, and thus, their effects are small in this case.

Fig. 13 shows currents that are recorded in similar conditions with different controls. After the increase in grid impedance, the blue line represents the case in which stability is predicted in Fig. 12. The instability occurs after the grid impedance is increased (as the analysis with full-order model predicted) and over-current protection shuts the inverter. Unstable currents confirm that the full-order analysis predicts the stability better than the fully diagonal-dominant analysis. The current, represented in the red line, is recorded during the similar change in grid impedance but with more conservative control parameters, in order to prove that the instability does not occur because of the sudden change in grid impedance. Hence, the use of reduced-order matrices for the stability assessment may produce inaccurate predictions, and thus, the generalized Nyquist stability assessment methods are recommended.

E. Real-Time Stability Assessment

The real-time stability analysis may reveal the stability issues right after an operation condition change. Thus, rapid measurements are required. The grid impedance is measured by a 127-bit-long MLBS and corresponding IRS (f_{gen} = 4 kHz), and the results are averaged only over 20 periods, providing the 15.75 Hz frequency resolution for the characteristic loci which are updated once in 1.27 seconds.

Fig. 14 shows three real-time characteristic loci when the grid impedance suddenly increases. The red line represents the characteristic loci when the grid impedance is still low. The black (dashed) line shows the transient case. As the new characteristic loci are plotted to the complex plane once in 1.27 seconds, the one set of characteristic locus is computed during the change in grid impedance, and thus, may have mixed information about the low- and high-impedance grids. That characteristic loci are computed during the transient case, where the small-signal stability analysis does not apply, and thus they are not informative and should be neglected. The blue line represents the stability analysis in the high-impedance grid that has the widely known stability issues with the high-crossover PLL. The loci approach the critical (-1+j0) point when the grid inductance increases, indicating poor stability margin. Fig. 15 shows the phase current when the transient from low-impedance to high-impedance grid happens. At the

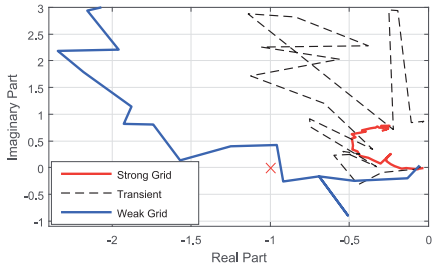

Fig. 14: Real-time stability assessment when grid impedance increases.

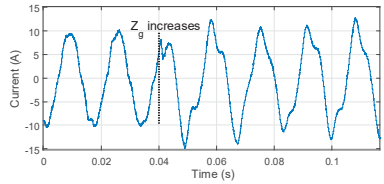

Fig. 15: Phase current when grid impedance suddenly increases.

time of increase in grid impedance, the low stability margins (predicted by the blue characteristic loci) are confirmed as the current starts immediately to suffer from a high harmonic content in output currents.

V. Conclusion

To achieving accurate predictions of stability of a grid-connected inverter in the dq domain, the complete inverter output-admittance and grid-impedance matrices must be considered. The inverter admittance matrix can be analytically modeled using a multivariable model. However, the time-varying characteristics of the grid impedance require real-time identifications and measuring the complete dq-domain matrix. By using the analytical model of the inverter and the real-time measurements of grid impedance, computation of the generalized Nyquist stability criterion can be executed in real time. After each measurement cycle of the grid impedance, the stability is monitored by plotting the impedance-based characteristic loci of the return-ratio matrix to the complex plane. By observing the distance to the critical point (-1+j0), stability margins are accurately predicted. Comparison to reduced-order stability analyses revealed those analyses' faulty predictions about stability margins. To prove the accuracy of the methods, the experimental results were obtained using a real three-phase inverter and the PHIL test bench.

Acknowledgements

This work was supported by the Academy of Finland.

Appendix

State vector, output vector and input vector respectively:

$$\mathbf{X} = \left[\hat{\mathbf{i}}_{\text{L}}^{\mathbf{T}}, \hat{\mathbf{v}}_{\text{c}}^{\mathbf{T}}\right]^T = \left[\hat{i}_{\text{Ld}}, \hat{i}_{\text{Lq}}, \hat{v}_{\text{c}}, 0\right]^T$$

$$\mathbf{Y} = \left[\hat{\mathbf{v}}_{\text{in}}^{\mathbf{T}}, \hat{\mathbf{i}}_{\text{o}}^{\mathbf{T}}\right]^T = \left[\hat{v}_{\text{in}}, 0, \hat{i}_{\text{od}}, \hat{i}_{\text{oq}}\right]^T$$

$$\mathbf{U} = \left[\hat{\mathbf{i}}_{\text{in}}^{\mathbf{T}}, \hat{\mathbf{v}}_{\text{o}}^{\mathbf{T}}, \hat{\mathbf{d}}^{T}\right]^{T} = \left[\hat{i}_{\text{in}}, 0, \hat{v}_{\text{od}}, \hat{v}_{\text{oq}}, \hat{d}_{\text{d}}, \hat{d}_{\text{q}}\right]^{T}$$

State matrices:

$$A = \begin{bmatrix} -\frac{r_{\text{L}}}{L_{\text{l}}} & \omega_s & \frac{D_{\text{d}}}{L_{\text{l}}} & 0 \\ -\omega_s & -\frac{r_{\text{L}}}{L_{\text{l}}} & \frac{D_{\text{q}}}{L_{\text{l}}} & 0 \\ -\frac{3}{2}\frac{D_{\text{d}}}{C} & -\frac{3}{2}\frac{D_{\text{q}}}{C} & 0 & 0 \\ 0 & 0 & 0 & 0 \end{bmatrix}$$

$$B = \begin{bmatrix} 0 & 0 & -\frac{1}{L_{\text{l}}} & 0 & \frac{V_{\text{dc}}}{L_{\text{l}}} & 0 \\ 0 & 0 & 0 & -\frac{1}{L_{\text{l}}} & 0 & \frac{V_{\text{dc}}}{L_{\text{l}}} \\ \frac{1}{C} & 0 & 0 & 0 & -\frac{3}{2}\frac{I_{\text{Ld}}}{C} & -\frac{3}{2}\frac{I_{\text{Lq}}}{C} \\ 0 & 0 & 0 & 0 & 0 & 0 \end{bmatrix}$$

$$C = \begin{bmatrix} 0 & 0 & 1 & 0 \\ 0 & 0 & 0 & 0 \\ 1 & 0 & 0 & 0 \\ 0 & 1 & 0 & 0 \end{bmatrix}$$

Transfer matrices of the open-loop model:

$$\mathbf{Z}_{\text{in-o}} = \begin{bmatrix} Z_{\text{in-o}} & 0 \\ 0 & 0 \end{bmatrix}, \mathbf{T}_{\text{oi-o}} = \begin{bmatrix} T_{\text{oid-o}} & T_{\text{oiq-o}} \\ 0 & 0 \end{bmatrix}, \mathbf{G}_{\text{ci-o}} = \begin{bmatrix} G_{\text{cid-o}} & G_{\text{ciq-o}} \\ 0 & 0 \end{bmatrix}$$

$$\mathbf{G}_{\text{io-o}} = \begin{bmatrix} G_{\text{iod-o}} & 0 \\ G_{\text{ioq-o}} & 0 \end{bmatrix}, \mathbf{Y}_{\text{o-o}} = \begin{bmatrix} Y_{\text{od-o}} & Y_{\text{oqd-o}} \\ Y_{\text{odq-o}} & Y_{\text{oq-o}} \end{bmatrix}, \mathbf{G}_{\text{co-o}} = \begin{bmatrix} G_{\text{cod-o}} & G_{\text{coqd-o}} \\ G_{\text{codq-o}} & G_{\text{coq-o}} \end{bmatrix}$$

Sensing-gain matrices for output voltage (for PLL), output current, and input voltage:

$$\mathbf{H}_{\text{PLL}} = \begin{bmatrix} 0 & 0 \\ 0 & 1 \end{bmatrix}, \mathbf{H}_{\text{out}} = \begin{bmatrix} 1 & 0 \\ 0 & 1 \end{bmatrix}, \mathbf{H}_{\text{in}} = \begin{bmatrix} 1 & 0 \\ 0 & 0 \end{bmatrix}$$

Transfer functions describing the PLL effect on output current, and duty ratios:

$$\mathbf{D} = \begin{bmatrix} 0 & -D_{\text{q}} \\ 0 & D_{\text{d}} \end{bmatrix}, \mathbf{I}_{\text{L}} = \begin{bmatrix} 1 & I_{\text{Lq}} \\ 0 & -I_{\text{Ld}} \end{bmatrix}$$

The decoupling gain, output current control, and DC-voltage control matrices:

$$\mathbf{G}_{\text{dec}} = \begin{bmatrix} 0 & -\frac{\omega L_{\text{l}}}{V_{\text{in}}} \\ \frac{\omega L_{\text{l}}}{V_{\text{in}}} & 0 \end{bmatrix}, \mathbf{G}_{\text{c-out}} = \begin{bmatrix} G_{\text{co-d}} & 0 \\ 0 & G_{\text{co-q}} \end{bmatrix}, \mathbf{G}_{\text{c-in}} = \begin{bmatrix} G_{\text{ci-d}} & 0 \\ 0 & 1 \end{bmatrix}$$

PI-controller transfer functions are derived using proportional K_{p} and integral gains K_{i} as

$$G_{\text{PI}} = K_{\text{p}} + \frac{K_{\text{p}}}{s}$$

Small-signal admittance of filter C branch ($\mathbf{Y}_{\text{f}} = (\mathbf{Z}_{\text{f}})^{-1}$)

$$\mathbf{A}_{\text{c}} = \begin{bmatrix} 0 & \omega_s \\ -\omega_s & 0 \end{bmatrix}, \mathbf{B}_{\text{c}} = \begin{bmatrix} 1/C_{\text{f}} & 0 \\ 0 & 1/C_{\text{f}} \end{bmatrix}, \mathbf{C}_{\text{f}} = \begin{bmatrix} 1 & 0 \\ 0 & 1 \end{bmatrix}$$

$$\mathbf{D}_{\text{f}} = \begin{bmatrix} r_{\text{f}} & 0 \\ 0 & r_{\text{f}} \end{bmatrix}, \mathbf{Z}_{\text{f}}(s) = \left[\mathbf{C}_{\text{f}}(s\mathbf{I} - \mathbf{A}_{\text{f}})^{-1}\mathbf{B}_{\text{f}} + \mathbf{D}_{\text{f}}\right]$$

REFERENCES

[1] C. Li, "Unstable operation of photovoltaic inverter from field experiences," *IEEE Transactions on Power Delivery*, vol. 33, no. 2, pp. 1013–1015, 2018.

[2] T. Messo, J. Jokipii, A. Aapro, and T. Suntio, "Time and frequency-domain evidence on power quality issues caused by grid-connected three-phase photovoltaic inverters," in *2014 16th European Conference on Power Electronics and Applications*, Aug 2014, pp. 1–9.

[3] J. Sun, "Impedance-based stability criterion for grid-connected inverters," *IEEE Transactions on Power Electronics*, vol. 26, no. 11, pp. 3075–3078, Nov 2011.

[4] B. Wen, R. Burgos, D. Boroyevich, P. Mattavelli, and Z. Shen, "Ac stability analysis and dq frame impedance specifications in power-electronics-based distributed power systems," *IEEE Journal of Emerging and Selected Topics in Power Electronics*, vol. 5, no. 4, pp. 1455–1465, Dec 2017.

[5] T. Messo, R. Luhtala, A. Aapro, and T. Roinila, "Accurate impedance model of grid-connected inverter for small-signal stability asssessment in high-impedance grids," in *IPEC-Niigata 2018 -ECCE ASIA*, 2018.

[6] R. Luhtala, T. Messo, and T. Roinila, "Adaptive control of grid-voltage feedforward for grid-connected inverters based on real-time identification of grid impedance," in *IPEC-Niigata 2018 -ECCE ASIA*, 2018.

[7] T. Roinila, H. Abdollahi, S. Arrua, and E. santi, "Adaptive control of dc power distribution systems: Applying pseudo-random sequences and fourier techniques," in *IPEC-Niigata 2018 -ECCE ASIA*, 2018.

[8] M. Cespedes and J. Sun, "Online grid impedance identification for adaptive control of grid-connected inverters," in *2012 IEEE Energy Conversion Congress and Exposition (ECCE)*, Sept 2012, pp. 914–921.

[9] T. Roinila, M. Vilkko, and J. Sun, "Broadband methods for online grid impedance measurement," in *2013 IEEE Energy Conversion Congress and Exposition*, Sept 2013, pp. 3003–3010.

[10] T. Roinila, T. Messo, and E. Santi, "Mimo-identification techniques for rapid impedance-based stability assessment of three-phase systems in dq domain," *IEEE Transactions on Power Electronics*, vol. 33, no. 5, pp. 4015–4022, May 2018.

[11] T. Messo, R. Luhtala, R. Roinila, D. Yang, X. Wang, and F. Blaabjerg, "Real-time impedance-based stability assessment of grid converter interactions," in *the Eighteenth IEEE Workshop on Control and Modeling for Power Electronics, IEEE COMPEL 2017*, July 2017.

[12] R. Luhtala, T. Messo, T. Roinila, T. Reinikka, J. Sihvo, and M. Vilkko, "Adaptive control of grid-connected inverters based on real-time measurements of grid impedance: Dq-domain approach," in *2017 IEEE Energy Conversion Congress and Exposition (ECCE)*, Oct 2017, pp. 69–75.

[13] R. Luhtala, T. Roinila, and T. Messo, "Implementation of real-time impedance-based stability assessment of grid-connected systems using mimo-identification techniques," *IEEE Transactions on Industry Applications*, 2018.

[14] T. Messo, A. Aapro, and T. Suntio, "Generalized multivariable small-signal model of three-phase grid-connected inverter in dq-domain," in *2015 IEEE 16th Workshop on Control and Modeling for Power Electronics (COMPEL)*, 2015, pp. 1–8.

[15] R. Dorf and R. Bishop, *Modern Control Systems*. Prentice-Hall, 2000.

[16] L. Jessen and F. W. Fuchs, "Modeling of inverter output impedance for stability analysis in combination with measured grid impedances," in *2015 IEEE 6th International Symposium on Power Electronics for Distributed Generation Systems (PEDG)*, June 2015, pp. 1–7.

[17] J. Enslin and P. Heskes, "Harmonic interaction between a large number of distributed power inverters and the distribution network," *IEEE Transactions on Power Electronics*, vol. 19, no. 6, pp. 1586–1593, Nov 2004.

[18] H. Alenius, T. Reinikka, T. Messo, and T. Roinila, "Modeling, sensitivity analysis, and power hardware-in-the-loop emulation of grid impedance," in *2018 IEEE Energy Conversion Congress and Exposition (ECCE)*, Sept 2018.

[19] M. Belkhayat, "Stability criteria for ac power systems with regulated loads," Ph.D. dissertation, Purdue University, Dec 1997.

[20] K. R. Godfrey, *Perturbation Signals for System Identification*. Prentice Hall, UK, 1993.

PUBLICATION
IV

Practical Implementation of Adaptive SRF-PLL for Three-Phase Inverters Based on Sensitivity Function and Real-Time Grid-Impedance Measurements

R. Luhtala, H. Alenius and T. Roinila

Energies, vol. 13, no. 1173, pp. 1-18 , 2020

energies

MDPI

Article

Practical Implementation of Adaptive SRF-PLL for Three-Phase Inverters Based on Sensitivity Function and Real-Time Grid-Impedance Measurements

Roni Luhtala [1,*], Henrik Alenius [2] and Tomi Roinila [2]

[1] Tampere University Faculty of Engineering and Natural Sciences, 33720 Tampere, Finland
[2] Tampere University Faculty of Information Technology and Communication Sciences, 33720 Tampere, Finland; henrik.alenius@tuni.fi (H.A.); tomi.roinila@tuni.fi (T.R.)
* Correspondence: roni.luhtala@tuni.fi

Received: 13 January 2020; Accepted: 27 February 2020; Published: 4 March 2020

Abstract: Rapidly increasing demand for renewable energy has created a need for the photovoltaic and wind farms to be placed in various locations that have diverse and possibly time-variant grid conditions. A mismatch between the grid impedance and output admittance of an inverter causes impedance-based stability issues, which appear as power quality problems and poor transient performance. Grid synchronization with phase-locked loop (PLL) introduces a negative-resistance-like behavior to inverter output admittance. High control bandwidth of the PLL makes the system sensitive to impedance-based stability issues when the inverter is connected to a weak grid that has high impedance. However, very conservative tunings lead to overly damped dynamic responses in strong grids, where the control performance and power quality can be improved by applying higher PLL control bandwidths. Continuous evaluation of grid conditions makes it possible to avoid the risk of instability and poor dynamic responses, as the inverter output admittance can be re-shaped online to continuously match the grid conditions. The present work proposes method for adaptive control of the PLL based on the real-time measurements of the grid impedance, applying pseudo-random binary sequence (PRBS) injections. The method limits the PLL bandwidth in weak grids to avoid stability issues and increases the control bandwidth in strong grids to improve voltage-tracking, and thus overall control performance. The method is verified through simulations and experimental laboratory tests in a kW-scale system. The results show that optimizing the PLL bandwidth with respect to the grid conditions is highly beneficial for system performance and stability.

Keywords: power electronics; phase locked loops; impedance measurement; stability analysis; control systems; system identification

1. Introduction

The increasing penetration level of the inverter-connected renewable energy has caused stability and power-quality issues in power grids [1,2]. One of the main problems is the harmonic resonance triggered by the mismatch between the grid impedance and the inverter output admittance. The harmonic resonance is an indication of insufficient stability margins; it increases the system sensitivity and may even cause instability [3,4]. To avoid these issues, the control system is often designed to have very conservative stability margins, leading to overly damped dynamic responses in robust systems where faster responses are desired.

The impedance-based stability of the grid-connected inverter can be assessed from a return ratio matrix of the dq-domain grid impedance and inverter output admittance [5]. The grid impedance may vary over time, due to, for example, load changes [6–9] or various grid faults and clearance of these faults [10–13]. As the grid impedance varies over time, online measurements performed in real-time are desirable for accurate stability assessment [14–16]. Recent studies have presented a number of online measurement methods based on broadband injections, such as impulse [17], multitone sinewaves [18], and pseudo-random binary sequence (PRBS) [15,16,19]. Particularly the PRBS has become popular, as the signal is easy to implement, it has the lowest possible crest factor, and a largely controllable spectral-energy content [20].

Grid synchronization using phase-locked loop (PLL) introduces negative-resistance-like behavior below the PLL crossover frequency [21], which causes the inverter output admittance to lose its passivity, and thus a possibility for stability issues occurs [22,23]. Recent research has introduced methods to improve the PLL performance [24] and stability in weak grids [25,26]. However, the PLL crossover should be limited to minimize the frequency region of the negative-resistance-like behavior to avoid impedance-based stability issues when the grid impedance increases.

Improved stability and performance of grid synchronization can be achieved by adaptive control of the PLL, where its control bandwidth is limited when the grid-impedance increases [27–30]. Existing studies of the adaptive PLLs have proposed methods that improve the impedance-based stability under various grid impedances. However, a practical implementation for adaptive PLL that systematically optimizes the control performance in varying grid conditions still lacks from the literature. This paper extends the research in [28] by introducing a practical implementation of the adaptive PLL that optimizes the trade-off between the system robustness and PLL control performance based on continuous evaluation of the impedance-based sensitivity function. In this paper, the system sensitivity function is evaluated by applying real-time grid-reactance measurements based on the PRBS methods. The measurement methods can be used to rapidly detect and react the changes in grid impedance in order to ensure impedance-based stability. In the proposed methods, the PLL bandwidth is controlled so that the maximum value of the system sensitivity function is kept constant regardless of the grid conditions. This is equivalent to constant stability margins with the highest possible PLL bandwidth, satisfying the desired system robustness. Therefore, more sophisticated and systematic adaptive control of the PLL is provided that considers the optimal control performance in addition to the system stability. This results in improved power quality and overall dq-domain control performance under varying grid conditions.

The rest of this paper is organized as follows. Section 2 briefly reviews the modeling of three-phase grid-connected inverters, PLL control design, and theory behind the impedance-based stability with the use of sensitivity functions. Section 3 presents methods for continuously measuring the grid impedance using PRBS injections and presents the flowchart of the adaptive process. Section 4 presents the design of the adaptive PLL in detail for a small-scale prototype. In Section 5, the adaptive PLL is implemented in MATLAB/Simulink, where the improvements on the control performance and system stability are demonstrated. Section 6 shows the experimental implementation of the adaptive PLL controller for laboratory hardware with 2.7 kW power level, and verifies the enhanced performance. Finally, the conclusions are drawn in Section 8.

2. Modeling Grid-Connected Inverter

2.1. Impedance-Based Stability Analysis and System Sensitivity

Small-signal stability at point of common coupling (PCC) of interconnected systems can be assessed by applying impedance-based stability analysis [3]. The analysis is performed in synchronous reference frame (dq domain) in this paper. In the dq domain, the three-phase variables are represented as two equivalent DC signals, and the impedance can be considered as two components (dd and qq) with cross-couplings (dq and qd) between them. Due to the cross-couplings, the components cannot be

analyzed separately and the generalized Nyquist stability criterion (GNC) for multi-input multi-output (MIMO) systems has to be applied [5,31].

Figure 1a shows an equivalent small-signal circuit of source-load interconnection, representing the inverter as a source and the grid as a load at their PCC. The grid impedance and inverter output admittance matrices can be defined as

$$\mathbf{Z}_{\mathrm{g}} = \begin{bmatrix} Z_{\mathrm{g\text{-}dd}} & Z_{\mathrm{g\text{-}qd}} \\ Z_{\mathrm{g\text{-}dq}} & Z_{\mathrm{g\text{-}qq}} \end{bmatrix}, \mathbf{Y}_{\mathrm{o}} = \begin{bmatrix} Y_{\mathrm{o\text{-}dd}} & Y_{\mathrm{o\text{-}qd}} \\ Y_{\mathrm{o\text{-}dq}} & Y_{\mathrm{o\text{-}qq}} \end{bmatrix} \tag{1}$$

Figure 1b illustrates the control system equivalent for the interconnected subsystems, as the current equation resembles a negative feedback system. Therefore, the stability analysis can be simplified to observe only the eigenvalues of the return-ratio matrix $\mathbf{L}_{\mathrm{s}}(s) = \mathbf{Y}_{\mathrm{o}}(s)\mathbf{Z}_{\mathrm{g}}(s)$ as:

$$\det\left[\mathbf{I} + \mathbf{Y}_{\mathrm{o}}(s)\mathbf{Z}_{\mathrm{g}}(s)\right] = \det\left[\mathbf{I} + \mathbf{L}_{\mathrm{s}}(s))\right] = 0 \tag{2}$$

The stability of the PCC is preserved if the return-ratio matrix satisfies the Nyquist criterion [5].

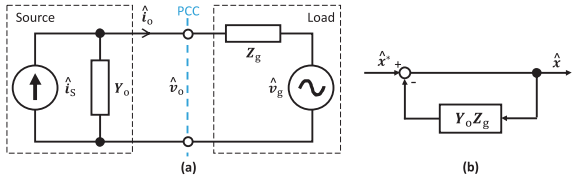

Figure 1. Interconnected source-load subsystem (**a**) and its simplified feedback-system equivalence (**b**).

Power quality issues may occur even in stable systems, if the stability margins are low. Insufficient stability margins can be identified by using a sensitivity function as presented in [32] for DC systems. The system sensitivity function is based on the Nyquist stability criterion and can be considered as an inverse of the Nyquist eigenloci's distance to the critical point $(-1, 0)$. Similar analysis applies for MIMO systems but they require the use of generalized Nyquist criterion (GNC) of the return-ratio matrix [33]. Thus, robustness of the MIMO systems can be analyzed by observing a system sensitivity function, which can be given as

$$S(s) = \frac{1}{\det\left[\mathbf{I} + \mathbf{L}_{\mathrm{s}}(s)\right]} \tag{3}$$

The sensitivity function appears in closed-loop transfer functions of the system seen from the PCC. Thus, the control performance and power quality can be estimated from $S(s)$ as it also describes the transfer function from external disturbances to the output currents [34].

The maximum absolute value of $S(s)$ is denoted as a sensitivity peak:

$$S_{\mathrm{peak}} = \max_{0 \le s \le \infty} |S(s)| = \max_{0 \le s \le \infty} \left| \frac{1}{\det\left[\mathbf{I} + \mathbf{L}_{\mathrm{s}}(s)\right]} \right| \tag{4}$$

The sensitivity peak rises to infinity when the system approaches instability. Low values for S_{peak} are desired to avoid harmonics and stability issues. However, to achieve a low sensitivity peak in weak grids, the inverter control bandwidths must be modified.

2.2. Small-Signal Modeling of Three-Phase Inverter with PLL

Figure 2 shows the studied photovoltaic (PV) inverter, and Figure 3 shows a block diagram representing the inverter dynamics. The multivariable small-signal model of such a three-phase grid-connected inverter in the dq domain has already been introduced in [35], so the present paper only considers the PLL and its optimal control tunings in more detail. The synchronous-reference-frame PLL (SRF-PLL) synchronizes the dq-control frame to the grid waveforms (grid reference frame) by

regulating the sensed output voltage q component to zero. Because only the voltage q component is regulated, the PLL loop gain can be given as a scalar transfer function:

$$L_{\text{PLL}} = G_{\text{c-PLL}} G_{\text{PLL-Plant}} = (K_{\text{p-PLL}} + \frac{K_{\text{i-PLL}}}{s}) \frac{V_{\text{od}}}{s} \tag{5}$$

where $G_{\text{c-PLL}}$ is the internal PI-type controller of the PLL.

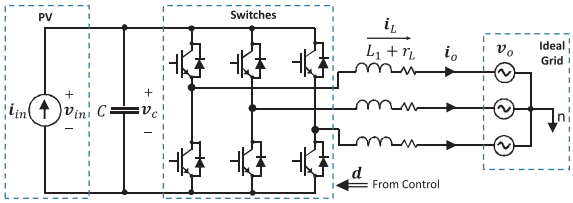

Figure 2. Three-phase inverter connected to ideal grid.

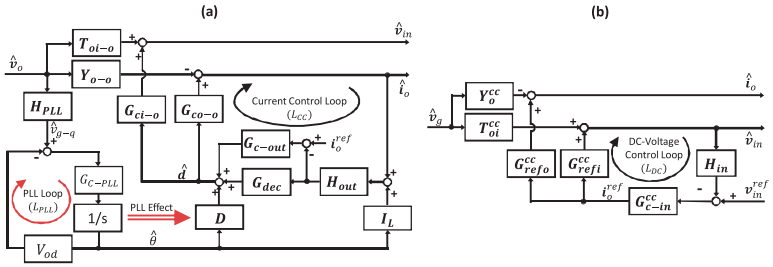

Figure 3. Inverter dynamics including (**a**) phase-locked loop (PLL) and current-control loops, and (**b**) closed-loop transfer functions and DC-voltage control loop.

The PLL plant consists of an integrator with a constant gain (V_{od}), which makes it possible to provide simple control-tuning procedure, where the PLL loop gain's phase margin (Θ_{PM}) and crossover frequency (f_{co}) can be fixed. The procedure considers the loop characteristics at f_{co}, where the loop magnification is 0 dB and $s = j2\pi f_{\text{co}}$. This yields the following equation group,

$$\begin{cases} \cot(-180^\circ + \Theta_{\text{PM}}) = \dfrac{\left(\dfrac{V_{\text{od}}}{4\pi^2 f_{\text{co}}^2}\right) K_{\text{i-PLL}}}{\left(\dfrac{V_{\text{od}}}{2\pi f_{\text{co}}}\right) K_{\text{p-PLL}}} \\ 1\angle(-180^\circ + \Theta_{\text{PM}}) = \left(K_{\text{p-PLL}} + \dfrac{K_{\text{i-PLL}}}{2\pi f_{\text{co}}}\right) \dfrac{V_{\text{od}}}{2\pi f_{\text{co}}} \end{cases} \tag{6}$$

where the desired phase margin Θ_{PM} determines the ratio between the imaginary and real parts of the PLL loop gain, whereas the final control gains set the loop magnification (0 dB) at f_{co}. By solving the equation group, the controller gains can given as

$$\begin{cases} K_{\text{i-PLL}} = K_{\text{p-PLL}} 2\pi \cot(-180^\circ + \Theta_{\text{PM}}) f_{\text{co}} \\ K_{\text{p-PLL}} = \dfrac{2\pi}{V_{\text{od}} \sqrt{\cot(-180^\circ + \Theta_{\text{PM}})^2 + 1}} f_{\text{co}} \end{cases} \tag{7}$$

The complete PLL transfer matrix is solved as

$$\mathbf{G}_{\text{PLL}} = \left[\mathbf{L}_{\text{cc}} \mathbf{I}_{\text{L}} - \mathbf{G}_{\text{co-o}} \mathbf{D}\right] \left[\frac{L_{\text{PLL}}}{V_{\text{od}}(1 + L_{\text{PLL}})} \mathbf{H}_{\text{PLL}}\right] \tag{8}$$

which affects the admittance qq and dq components through $\mathbf{D}$, $\mathbf{I}_{\mathrm{L}}$, and sensing gain $\mathbf{H}_{\mathrm{PLL}}$. The derivation and related transfer functions of the impedance model are given in the Appendix A.

2.3. PLL Design Based on System Sensitivity Function

The PLL dominates the qq component of the inverter output-admittance below the control bandwidth of L_{PLL}. Below the PLL bandwidth, phase response of the output admittance stays at 180 degrees with constant magnitude. The effect is usually referred as the negative resistance, which dominates the inverter output admittance at low frequencies [21]. When the interfaced grid is inductive, the impedance is mainly reactance and the phase is close to 90 degrees. This results in maximal phase difference to the inverter output impedance. The PLL dominates the qq component of the inverter output-admittance below the control bandwidth of L_{PLL}. Below the PLL bandwidth, phase response of the output admittance stays at 180 degrees with constant magnitude. The effect is usually referred as the negative resistance, which dominates the inverter output admittance at low frequencies [21]. When the interfaced grid is inductive, the impedance is mainly reactance and the phase is close to 90 degrees. This results in maximal phase difference to the inverter output impedance.

Figure 4 illustrates the impact of the inductive grid reactance (a), grid resistance (b), and the PLL bandwidth (c) to the system sensitivity function (3) below 300 Hz. The grid reactance and resistance are increased in the same proportion with the X/R ratio of 5, which is typical for example for the impedance of grid-interfacing transformers. When the inverter control system is kept constant, higher grid reactance clearly increases the sensitivity peak (maximum of the function), but the resistance has a negligibly small effect that actually slightly decrease the sensitivity peak. Additionally, the higher PLL bandwidth in constant grid conditions increases the sensitivity peak. The increased PLL bandwidth improves directly the voltage-tracking performance, and thus, the entire dq-domain control performance. However, high PLL bandwidth and increased grid reactance decrease the system robustness which can be seen from the increased sensitivity functions. The trade-off between the robustness and control performance should be optimized by limiting the system sensitivity peak, but at the same time, overly conservative PLL tunings should be avoided. From this, it is evident that the PLL bandwidth has to be decreased when grid reactance increases. On the other hand, higher bandwidths are allowed when grid reactance is decreased.

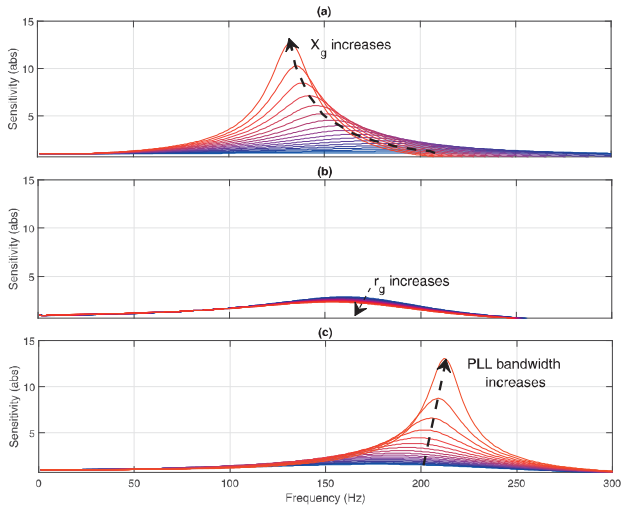

Figure 4. System sensitivity functions as (**a**) inductive grid reactance increases, (**b**) grid resistance increases, and (**c**) PLL bandwidth increases.

3. Real-Time Impedance Measurements for Adaptive PLL

3.1. Maximum-Length Binary Sequence

Recent studies have presented methods based on Fourier techniques and broadband perturbations for measuring the grid impedance in real-time [15]. In the methods, the impedance was measured by the inverter itself: the inverter injects a perturbation current on top of the reference d or q current, measures the resulting responses in the grid voltage, and applies Fourier analysis to extract the corresponding frequency components in both the voltage and current. The grid impedance is then determined by the ratio between the perturbation voltage and current. The signal sampling process can be implemented without any additional data-acquisition units as the output voltages and current are sensed anyway.

A maximum-length binary sequence (MLBS) is the most common form of the PRBS signals, and has been applied as a perturbation in many previous studies. The MLBS is a widely used periodic sequence that is easy to generate with a shift register and XOR feedback [36]. The MLBS is a wide-band sequence that exists for $N = 2^n - 1$, where n is the applied number of stages in the shift register. The frequency resolution of the sequence is $f_{\text{res}} = f_{\text{gen}}/N$, where f_{gen} is the generation frequency [19]. The required time for the measurement is given as $T_{\text{cycle}} = PN/f_{\text{gen}}$, where P denotes the number of averaged periods. The binary sequences also have the lowest possible peak factor, so a relatively low injection amplitude can be used when applying such sequences [20].

3.2. Grid-Reactance Estimation

The inverter control system is configured to continuously inject the small-amplitude MLBS on top of the current reference d component, and responses from grid-side voltage and current are gathered. The responses are transformed to the frequency domain and the grid impedance is calculated in real-time as a ratio of grid current to voltage, as $Z_{\text{g}}(\omega) = r + jX(\omega) = U_{\text{g}}(\omega)./I_{\text{g}}(\omega)$ where r is the resistance and $X(\omega)$ the reactance. The d component is measured because the measurements of the q component are deteriorated inside the PLL bandwidth [37].

The adverse interactions between the negative-resistance-like behavior of inverter impedance (induced by PLL) and grid impedance can be evaluated by examining the grid reactance. The reactance represents the imaginary part of the grid impedance, which is frequency-dependent. Thus, to compare stiffness of different grids, the grid reactance is given at the fundamental frequency $X_{\text{g}} = X(60\text{ Hz})$. The grid impedance typically resembles inductive characteristics below 400 Hz [6]. Thus, the grid reactance is assumed mainly inductive, which is proportional to frequency and the grid inductance. Thus, X_{g} can be estimated from the broadband grid-impedance measurement, performed for example by the MLBS-based methods. The fundamental-frequency grid reactance can be computed from the measured grid impedance by

$$X_{\text{g}} = \frac{\text{Im}[Z_{\text{g}}(\omega)]}{\omega} \times \omega_{\text{g}} \tag{9}$$

where the $\text{Im}[Z_{\text{g}}(\omega)]$ is the imaginary part (reactance) of the measured grid impedance, ω is the angular frequency, and ω_{g} is the fundamental frequency ($2\pi 60$ Hz).

A 31 bit long MLBS, generated at 1 kHz, provides a frequency resolution of 32.3 Hz. From the measured grid impedance, X_{g} is estimated from five different frequencies, so they all can be considered as different estimates and are not polluted by the same disturbance such as the oscillation after the transient. The frequencies, applied in the grid-reactance estimation should be chosen so that they are not affected by the system's most dominating periodic distortions, which in the dq domain are the grid-voltage unbalance and harmonics [38]. In the dq domain, the unbalanced grid voltages appear as oscillations at 120 Hz, the third (in-phase) harmonic occur only in zero component, not affecting the measured d component, and the fifth harmonic appears at 360 Hz. Thus, the five frequencies for the grid-reactance estimation are chosen as 193.5 Hz, 225.8 Hz, 258.1 Hz, 290.3 Hz, and 322.6 Hz. These frequencies are below 400 Hz, and are not significantly polluted by neither 120 Hz nor 360 Hz

oscillations. The final X_g value is given as a median of these five estimates. By taking the median from the five estimates, the measurement errors are significantly reduced and the measurement time is not increased as is the case when using a conventional averaging over many measurement cycles.

3.3. Adaptive PLL

The design of the adaptive PLL in the work is based on the system sensitivity function. The sensitivity function can be applied as an indicator for the robustness, and in this case also for the control performance. By adaptively adjusting the PLL bandwidth based on changes in the grid impedance, the sensitivity peak can be kept at a constant value which should be chosen as a good trade-off between the control performance and robustness.

The applied design method is based on continuous functions from the measured grid reactance to the internal PI-controller parameters of the PLL. Figure 5 shows a flowchart of the design process and application of the adaptive PLL. The design process begins by modeling the inverter output admittance over a wide range of PLL bandwidths and the grid impedance over wide range of the inductive reactance values. The sensitivity peak is computed for each pair of the PLL bandwidth and grid-reactance value. Next, the value for maximum-peak criterion (MPC) is chosen. The MPC determines the desired sensitivity peak and operates as a design rule for the adaptive PLL. Based on the chosen MPC, the optimal PLL bandwidth for each grid-reactance value is selected from the computed sensitivity peaks so that the MPC is satisfied. In the last step of the design process, a continuous function is fitted to the discrete pairs of the PLL bandwidth and grid-reactance values. In the application, the PLL parameters can be adaptively tuned based on the real-time grid-reactance measurement.

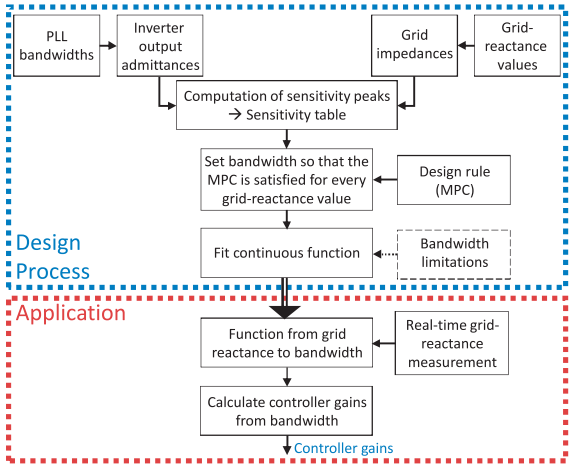

Figure 5. Flowchart of adaptive PLL design process and application.

4. Implementation of Adaptive PLL Design

In this section, the adaptive PLL is implemented for a small-scale (2.7 kVA) prototype of a grid-connected inverter. The control-design procedure (7) is applied to provide a continuous function from the PLL bandwidth (considered here as f_{co}) to the controller gains, so that the phase margin of the PLL loop gain remains at 65 degrees for every bandwidth. The inverter is connected to the 120 V grid. Therefore, substituting $\Theta_{PM} = 65^\circ$ and $V_{od} = \sqrt{2} \times 120V$ into (7), the controller gain can be computed as

$$\begin{aligned} K_{\text{p-PLL}} &= 0.0336 f_{co} \\ K_{\text{i-PLL}} &= 0.0983 f_{co}^2 \end{aligned} \tag{10}$$

where the proportional gain ($K_{\text{p-PLL}}$) is linearly depended on the desired crossover frequency, whereas the integral gain ($K_{\text{i-PLL}}$) has squared dependency.

Next, the function from the grid reactance to the PLL bandwidth is determined based on the system sensitivity function. The inverter output admittance is modeled with the PLL tunings from work in (10) with crossover resolution of 1 Hz, and it is denoted as $\mathbf{Y}_{\text{o-c}}(f_{\text{co}})$. Other model parameters are given in Tables 1 and 2. The grid impedance $\mathbf{Z}_{\text{g}}(X_{\text{g}})$ is modeled for the small-scale prototype (120 V, 2.7 kVA), where the grid reactance is varied from 0.038 to 4.0 Ω with a resolution of 0.038 Ω and the grid resistance (r_{g} = 0.1 Ω) is kept constant due to its negligibly small impact to the sensitivity. The grid-impedance model is given in the Appendix A. The grid-reactance is varied in the model by ranging the grid inductance (L_{g}) from 0.1 to 10.6 mH, with a resolution of 0.1 mH. The equivalent short-circuit ratio (SCR) range is from 150 to 4, which approximately corresponds to a reactance range of 0.29 to 10.8 mΩ for a large-scale 1 MW inverter (in low voltage level). For every grid-reactance value, the f_{co} that satisfies the chosen MPC is computed from (4). Figure 6 shows the PLL bandwidths that satisfy most accurately the MPC limits of two (red line) and three (blue line), with varying grid reactances from 0.038 to 4.0 Ω.

Here, the MPC = 3 is applied as the design rule, representing blue line in Figure 6 to which the continuous function is fitted. The least-square regression is applied in the curve fitting process. A third-order function is fitted into modeled grids (with 106 different reactance values) and corresponding PLL bandwidths that satisfy the MPC = 3 most accurately. Figure 7 shows the fitted third-order function (black dashed line).

$$f_{\text{co}} = -13.43X_{\text{g}}^3 + 111.24X_{\text{g}}^2 - 327.03X_{\text{g}} + 357.90 \tag{11}$$

which accurately follows the individually adjusted pairs of the X_{g} and the optimal PLL crossover frequency. For the final implementation, the PLL bandwidth is limited to reasonable range, which can be chosen arbitrarily. Black line includes the used upper (180 Hz) and lower (1 Hz) limits for the PLL bandwidth. With the chosen bandwidth limitations, pure adaptive characteristics occur in grid reactance ranging from 0.68 Ω to 3.4 Ω. In that range, the system sensitivity peak can be kept constant (S_{peak} = 3). The system becomes more robust ($S_{\text{peak}} < 3$) when grid reactance lies below 0.68 Ω. With grid reactances higher than 3.4 Ω, the sensitivity peak starts to increase but small-signal instability will be avoided also in extremely weak (SCR < 2, translates here to $X_{\text{g}} > 8$ Ω) grids [26].

The final controller gains are generated by substituting (11) into (10) as

$$\begin{aligned} K_{\text{p-PLL}} &= 0.0336(-13.43X_{\text{g}}^3 + 111.24X_{\text{g}}^2 - 327.03X_{\text{g}} + 357.90) \\ K_{\text{i-PLL}} &= 0.0983(-13.43X_{\text{g}}^3 + 111.24X_{\text{g}}^2 - 327.03X_{\text{g}} + 357.90)^2 \end{aligned} \tag{12}$$

Real-time measurement of the grid reactance is required for the adaptive control. In the implementation, the applied MLBS amplitude is 0.1 A (< 1 % of the nominal current), the reactance value is refreshed every 31 ms. The grid-reactance measurement is filtered through a first-order low-pass filter with a time constant of 1 s, to reduce the undesired fluctuations of the PLL bandwidth at the steady state. However, a rapid change in grid impedance may destabilize the system relatively fast. To tackle this challenge, an auxiliary trigger is implemented to the adaptive controller. If the measured grid reactance (prior filtering) is 0.6 Ω greater than the filter output, the control interprets this as an rapid grid-impedance change, and injects an impulse-like signal to the measured grid reactance. This decreases the PLL bandwidth within tens of ms, so that the stability is preserved even in drastic grid impedance changes, such as grid faults. In this work, the impulse-like signal is generated by multiplying the latest reactance-estimation value by a factor of ten, so long that an overshoot into the filter output is produced, which, in a sense, bypasses the slow time-domain filtering.

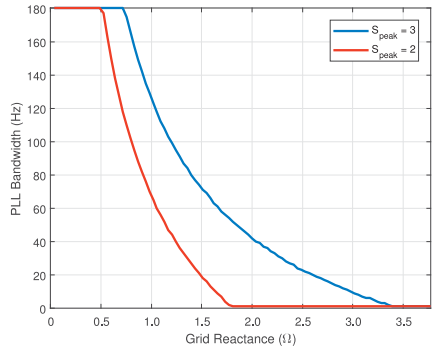

Figure 6. PLL bandwidths which satisfy maximum-peak criterion (MPC) as a function of grid reactance.

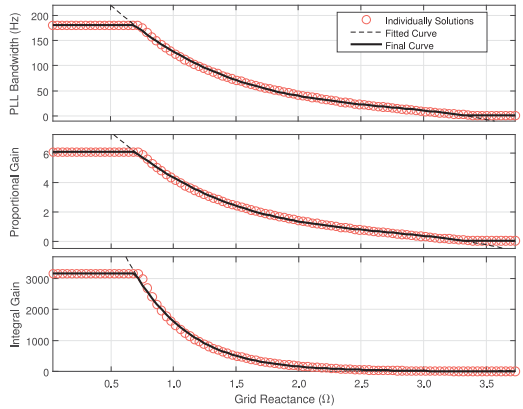

Figure 7. Fitted functions from grid reactance to PLL bandwidth and control parameters.

5. Simulations

The presented approach for adaptive control of the PLL is validated by implementing the method in MATLAB/Simulink. Figure 8 shows a three-phase inverter with the adaptive PLL structure and real-time grid-reactance measurement system, which are implemented to a 2.7 kW three-phase inverter that is connected into the 120 V/60 Hz grid. The model parameters are given in Table 1, which replicates the experimental small-scale set-up. The inverter control parameters are given in Table 2. The performance of the adaptive PLL is illustrated in changing grid conditions, where rapid changes are made to the grid impedance or grid voltage phase angle.

Table 1. Parameters of small-scale prototype.

V_g	120 V	f_q	60 Hz	f_{sw}	8 kHz
V_{dc}	414 V	I_{dc}	6.52 A	D_d	0.412
V_{od}	$120\sqrt{2}$ V	V_{oq}	0 V	D_q	0.0213
I_{Ld}	10.6 A	r_L	0.1 Ω	L_1	2.2 mH
C_{dc}	1.5 mF				

Table 2. Control parameters.

AC-current controller	$K_{p\text{-}AC}$ = 0.0149	$K_{i\text{-}AC}$ = 23.4423
DC-voltage controller	$K_{p\text{-}DC}$ = 0.0962	$K_{i\text{-}DC}$ = 1.2092

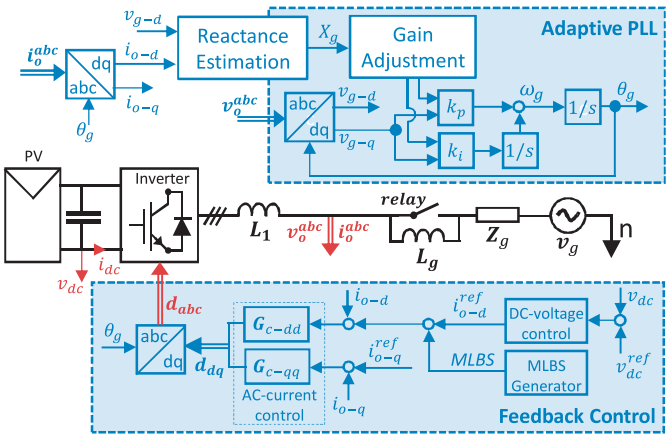

Figure 8. Three-phase inverter with adaptive synchronous-reference-frame PLL (SRF-PLL).

5.1. Adaptive PLL in Varying Grid Conditions

The adaptive adjustment of the PLL control parameters is based on the real-time measurements of the grid reactance. Figure 9 illustrates the basic operation of the adaptive control in significantly varying grid conditions. The inverter is placed in a remote location, where two equal transmission lines (inductive, X_{TL} = 3.0 Ω) are used for a connection to the main grid. Thus, the transmission lines mainly characterize the grid impedance. As two equal lines are occur, the grid-impedance is half (X_g = 1.5 Ω) of the individual line impedance. At 0 s, the inverter is connected this grid, and the grid reactance is measured during the inverter start-up. From the grid-reactance measurement, the PLL bandwidth is computed as in 11 and the controller gains as in 12. The PLL bandwidth is adaptively set to 72 Hz after the start-up process. Suddenly at 10 s, the second transmission line is disconnected due to, for example, grid fault or maintenance. The rapid increase in the grid impedance triggers the impulse to the filter and overshoot in the measurement appears. Due to the filter overshoot, the PLL bandwidth is decreased close to 1 Hz, and the possible stability issues are avoided. Once the adaptive system is recovered from the drastic change in grid impedance, approximately 1 s after the transient, the PLL bandwidth is set 15 Hz. At 20 s, the second transmission line is reconnected, and the PLL bandwidth is increased back to 72 Hz.

5.2. Performance in Weak Grid

In this simulation, a comparison between the conventional PLL and the adaptive implementation in weakening grid conditions is performed. Figure 10 shows phase currents, current q components, and bandwidths of the compared PLLs. The SCR decreases from 11.5 to 5.1 at 0.02 s, which translates to grid-reactance values of 1.4 and 3.2 Ω, respectively. The conventional PLL is optimized to 1.4 Ω grid (constant 80 Hz bandwidth is applied) in which the inverter is connected in the beginning of the test run. When the constant 80 Hz PLL is applied during the grid-impedance transient, oscillations around 130 Hz appear in currents. This is an indication of insufficient stability margins. Figure 11 shows the analytical sensitivity function for the inverter (80 Hz PLL) connected to the weak (X_g = 3.2 Ω) grid and the Fourier-transformed I_{oq} during the oscillations. The analytical sensitivity peak rises close to 100 at 130 Hz, thus accurately predicting poor stability margins and oscillations around the peak frequency.

These impedance-based stability issues between high PLL bandwidth and weak grids can be avoided by the adaptive control of the PLL. The rapid increase in the grid impedance is noticed approximately 8 ms after the transient, and the PLL bandwidth is decreased from 80 Hz to 10 Hz. This readjustment mitigates the oscillations in the currents and significantly improves system stability margins.

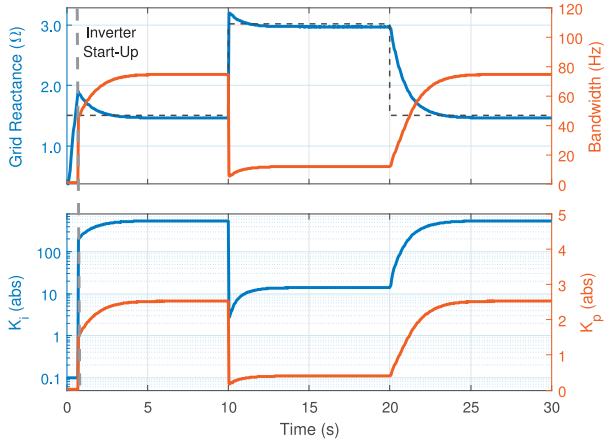

Figure 9. Real-time measurement (blue) of grid reactance, its known value (black dashed), and adaptively adjusted PLL parameters.

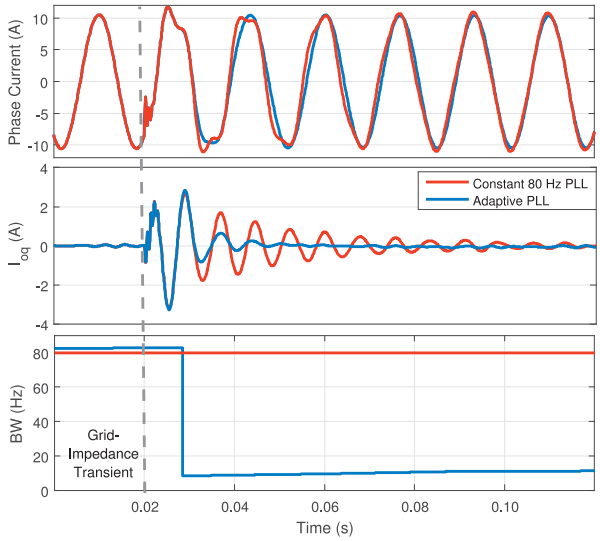

Figure 10. Performance comparison of adaptive and 80 Hz PLL in weakening grid conditions.

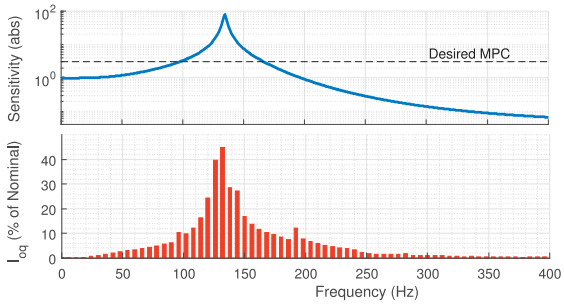

Figure 11. Predicted sensitivity function and produced distortions during grid transient.

6. Experiments

6.1. Experimental Set-Up

A power hardware-in-the-loop (PHIL) set-up for the three-phase grid-connected PV inverter is used to test the adaptive control system in downscaled conditions with relatively high amount of background harmonics and distortions. The PHIL setup includes a three-phase grid emulator, a PV emulator, a three-phase inverter, and an isolation transformer. A real-time simulator (dSPACE) runs the control system of the inverter, which enables testing of the proposed control schemes to the real hardware. The inverter operating point and control system are equivalent to the simulations, given in Tables 1 and 2. The grid-side impedance is changed by switching on or off the bypass relays of the additional inductor located between the inverter and the grid emulator.

6.2. Adaptive Control during Grid Transients

Figure 12 illustrates the operation of the adaptive control. The upper part shows the grid-reactance measurement and the lower part shows the adaptively adjusted PLL bandwidth. The system is connected to a relatively strong grid, as grid-reactance measurement is settled around 1.7 Ω (SCR ≈ 9.4) and the PLL bandwidth is adaptively adjusted approximately to 57 Hz. At 2 s, a sudden increase in grid impedance occurs that triggers the impulse to the measurement filter. The grid-reactance measurement settles around the 2.3 Ω (SCR ≈ 6.9) after an overshoot that decreases the PLL bandwidth rapidly. Next, the PLL bandwidth is adaptively set to 29 Hz. The grid reactance decreases back to 1.7 Ω at 6.5 s, and the original steady-state bandwidth (57 Hz) is obtained after two seconds.

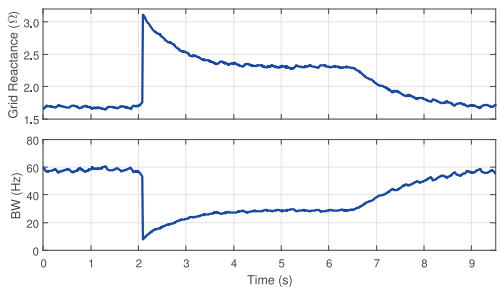

Figure 12. Adaptive control during changes in grid impedance.

6.3. Performance Comparison in Weak Grids

Figure 13 shows the performance comparison between the constant and adaptive PLLs. First, the grid is stronger, with approximately 2.0 Ω grid reactance (SCR ≈ 8.0) where the PLL bandwidth

is adaptively adjusted approximately to 40 Hz. The conventional PLLs with constant bandwidths (40 and 50 Hz) are applied as a comparison to the adaptive implementation. In the experiments, the grid reactance is suddenly increased to approximately 3.4 Ω (SCR ≈ 4.7) at 0.1 s, where the adaptive control proposes 1 Hz PLL bandwidth. The rapid increase in the grid impedance is noticed 50 ms after the transient, and the adaptive implementation (blue lines) decreases the bandwidth from 40 Hz to 1 Hz. With this adaptive readjustment, the oscillations in I_{oq} and V_q (blue lines) are effectively mitigated. With a constant 40 Hz PLL (red lines), the voltages and currents remain oscillating after the transient, which indicates insufficient stability margins. The inverter with a constant 50 Hz PLL (gray lines) becomes unstable (or marginally stable) after the transient, extremely high oscillations appear in the waveforms, and the system cannot recover from the grid-impedance transient.

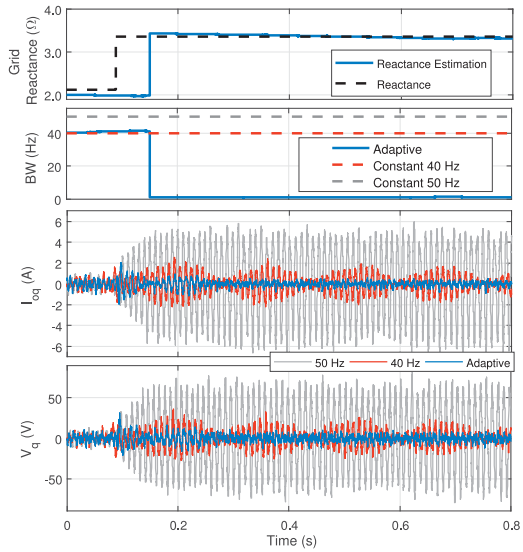

Figure 13. Performance comparison of adaptive PLL and conventional high-bandwidth PLLs in weak grid.

6.4. PLL Performance during Phase Jump

Voltage-tracking performance of the PLL decreases when low bandwidths are applied. However, too high PLL bandwidth produces oscillating responses or even unstable operations especially in the weak grids. Here, this clear trade-off is optimized by using the sensitivity-function-based analysis. Figure 14 shows the transient response in V_q during a 30 degree phase jump in grid voltages. Different PLL bandwidths are compared in a grid with approximately 2.1 Ω grid reactance (SCR ≈ 7.6). The adaptive control proposes approximately 38 Hz PLL bandwidth, to provide the sensitivity-peak value of 3 under the present grid impedance. The adaptive PLL is compared to higher (50 and 70 Hz) and lower (1, 10, and 20 Hz) bandwidths. As shown in the figure, oscillations are magnified when higher PLL bandwidths are applied. This indicates increased value for the sensitivity functions, and thus, insufficient stability margins. The oscillations are mitigated by using a lower PLL bandwidth. However, a lower bandwidth decreases the voltage-tracking performance as the settling time of V_q is increased. Here, the non-zero V_q means a momentary loss of the optimal grid synchronization that affects the whole dq-domain control performance of the inverter. Therefore, a good trade-off between high and low bandwidths can be achieved by considering the desired value of the system sensitivity peak.

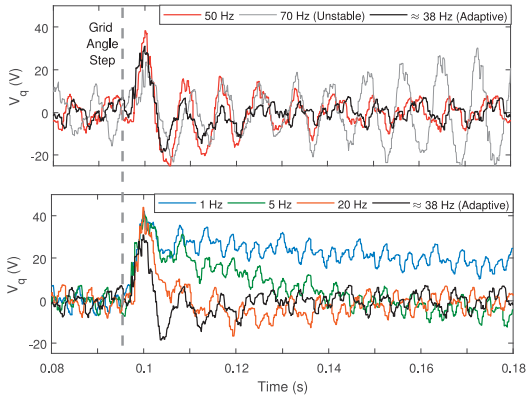

Figure 14. Performance comparison of different PLLs during phase jump in grid voltages.

7. Discussion

The grid impedance changes are chosen to demonstrate the performance of the proposed adaptive optimization of the PLL bandwidth. Consequently, this work does not consider any specific fault types, but instead, demonstrates the behavior of the proposed adaptive PLL in more general level. The presented work is a proof-of-concept for the adaptively tuned PLL based on real-time grid impedance measurements, and more specific case studies with certain grid-fault types remain a future topic.

In this work, the grid estimation algorithm for the adaptive control assumes the grid connection to be mainly resisitive-inductive, which typically is the case for remote PV inverters, where the grid impedance consists of mainly transmission lines and transformers. However, the applied reactance estimation also takes into account the capacitive characteristics of the grid, but a thorough analysis of the operation in LC-resonant grids is not included in the scope of this paper. For example, poorly damped low-frequency LC resonances may deteriorate the estimation and adaptation process. However, in normal systems these resonances rarely take place below 400 Hz, where the grid estimation takes place.

8. Conclusions

This paper has presented a method to adaptively adjust the PLL parameters of grid connected inverters based on real-time measurements of the grid impedance. To optimize the PLL controller parameters to match current grid conditions, a continuous function from the measured grid impedance to the optimal PLL bandwidth is created. In the method, the PLL control system is continuously readjusted by considering the optimal sensitivity peak of the system. A maximum-length binary sequence (MLBS) perturbation is applied to obtain the grid-impedance estimates in real time. Based on the measurements, the PLL parameters were readjusted to the current operating conditions, thus avoiding instability, excessive system sensitivity to external disturbances, and overly conservative control tunings. Simulation results and experiments based on power hardware-in-the-loop tests of a three-phase photovoltaic inverter show significant improvements in the PLL and overall control performance under varying grid conditions. Adaptive control of the PLL also increases fault ride-through capability as the inverter disconnection can be avoided during drastic grid transients and faults. Adjusting the PLL parameters to match the grid conditions ensures both good control performance in strong grids, and robust operation in weak grids.

Author Contributions: Conceptualization, R.L.; Methodology, R.L., H.A., and T.R.; Software, R.L., H.A., and T.R.; Validation, H.A. and R.L.; Writing—original draft preparation, R.L.; Writing—review and editing, T.R., R.L., and H.A.; Visualization, H.A.; Supervision, T.R.; Project Administration, T.R. All authors have read and agreed to the published version of the manuscript.

Funding: This research received no external funding.

Conflicts of Interest: The authors declare no conflict of interest.

Appendix A

In the inverter model, the state vector and output and input vectors are defined (respectively) as:

$$\mathbf{X} = \left[\hat{i}_{\mathrm{Ld}}, \hat{i}_{\mathrm{Lq}}, \hat{v}_{\mathrm{c}}\right]^T, \mathbf{Y} = \left[\hat{v}_{\mathrm{in}}, 0, \hat{i}_{\mathrm{od}}, \hat{i}_{\mathrm{oq}}\right]^T, \mathbf{U} = \left[\hat{i}_{\mathrm{in}}, 0, \hat{v}_{\mathrm{od}}, \hat{v}_{\mathrm{oq}}, \hat{d}_{\mathrm{d}}, \hat{d}_{\mathrm{q}}\right]^T$$

State-space matrices:

$$\mathbf{A} = \begin{bmatrix} -\frac{r_{\mathrm{L}}}{L_1} & \omega_S & \frac{D_{\mathrm{d}}}{L_1} & 0 \\ -\omega_S & -\frac{r_{\mathrm{L}}}{L_1} & \frac{D_{\mathrm{q}}}{L_1} & 0 \\ -\frac{3}{2}\frac{D_{\mathrm{d}}}{C} & -\frac{3}{2}\frac{D_{\mathrm{q}}}{C} & 0 & 0 \\ 0 & 0 & 0 & 0 \end{bmatrix}, \mathbf{B} = \begin{bmatrix} 0 & 0 & -\frac{1}{L_1} & 0 & \frac{V_{\mathrm{in}}}{L_1} & 0 \\ 0 & 0 & 0 & -\frac{1}{L_1} & 0 & \frac{V_{\mathrm{in}}}{L_1} \\ \frac{1}{C} & 0 & 0 & 0 & -\frac{3}{2}\frac{I_{\mathrm{Ld}}}{C} & -\frac{3}{2}\frac{I_{\mathrm{Lq}}}{C} \\ 0 & 0 & 0 & 0 & 0 & 0 \end{bmatrix}, \mathbf{C} = \begin{bmatrix} 0 & 0 & 1 & 0 \\ 0 & 0 & 0 & 0 \\ 1 & 0 & 0 & 0 \\ 0 & 1 & 0 & 0 \end{bmatrix}$$

where upper letters denote the steady-state values.

Applying $\mathbf{Y}(s) = \left[\mathbf{C}(s\mathbf{I} - \mathbf{A})^{-1}\mathbf{B}\right]\mathbf{U}(s)$, the 2 × 2 transfer matrices from input to output are collected together as

$$\mathbf{Y}(s) = \begin{bmatrix} \mathbf{Z}_{\text{in-o}} & \mathbf{T}_{\text{oi-o}} & \mathbf{G}_{\text{ci-o}} \\ \mathbf{G}_{\text{io-o}} & -\mathbf{Y}_{\text{o-o}} & \mathbf{G}_{\text{co-o}} \end{bmatrix} \mathbf{U}(s)$$

The decoupling matrix:

$$\mathbf{G}_{\mathrm{dec}} = \begin{bmatrix} 0 & -\omega_S L_1 / V_{\mathrm{in}} \\ \omega_S L_1 / V_{\mathrm{in}} & 0 \end{bmatrix}$$

The decoupled current-control loop gain and the loop:

$$\mathbf{L}_{\mathrm{CC}} = \mathbf{G}_{\text{co-o}}(\mathbf{G}_{\text{c-out}} - \mathbf{G}_{\mathrm{dec}})\mathbf{H}_{\mathrm{out}}$$
$$\mathbf{G}_{\mathrm{cc}} = \mathbf{L}_{\mathrm{CC}}(\mathbf{I} + \mathbf{L}_{\mathrm{CC}})^{-1}$$

The closed-loop output dynamics:

$$\mathbf{Y}_{\mathrm{o}}^{\mathrm{cc}} = (\mathbf{I} + \mathbf{L}_{\mathrm{CC}})^{-1}(\mathbf{Y}_{\text{o-o}} + \mathbf{G}_{\mathrm{PLL}})$$
$$\mathbf{G}_{\mathrm{refo}}^{\mathrm{cc}} = (\mathbf{I} + \mathbf{L}_{\mathrm{CC}})^{-1}\mathbf{G}_{\text{c-out}}\mathbf{G}_{\text{co-o}}$$

The input dynamics:

$$\mathbf{T}_{\mathrm{oi}}^{\mathrm{cc}} = \mathbf{T}_{\text{io-o}} + \mathbf{G}_{\text{ci-o}}\mathbf{G}_{\text{co-o}}^{-1}(\mathbf{G}_{\mathrm{cc}}(\mathbf{Y}_{\text{o-o}} + \mathbf{G}_{\mathrm{PLL}}) - \mathbf{G}_{\mathrm{PLL}})$$
$$\mathbf{G}_{\mathrm{refi}}^{\mathrm{cc}} = \mathbf{G}_{\text{ci-o}}(\mathbf{G}_{\text{co-o}})^{-1}(\mathbf{I} - \mathbf{G}_{\mathrm{cc}})\mathbf{G}_{\text{c-out}}\mathbf{G}_{\text{co-o}}$$

The DC-voltage control loop gain:

$$\mathbf{L}_{\mathrm{DC}} = \mathbf{G}_{\mathrm{refi}}^{\mathrm{cc}}\mathbf{G}_{\text{c-in}}\mathbf{H}_{\mathrm{in}}$$

The transfer matrices related to the PLL effect:

$$\mathbf{D} = \begin{bmatrix} 0 & -D_{\mathrm{q}} \\ 0 & D_{\mathrm{d}} \end{bmatrix}, \mathbf{I}_{\mathrm{L}} = \begin{bmatrix} 0 & I_{\mathrm{Lq}} \\ 0 & -I_{\mathrm{Ld}} \end{bmatrix}, \mathbf{H}_{\mathrm{PLL}} = \begin{bmatrix} 0 & 0 \\ 0 & 1 \end{bmatrix}$$

The inverter output admittance:

$$\mathbf{Y}_{\text{o-c}} = \mathbf{Y}_{\text{o}}^{\text{cc}} + \mathbf{G}_{\text{refo}}^{\text{cc}}\mathbf{G}_{\text{c-in}}\mathbf{H}_{\text{in}}(\mathbf{I} + \mathbf{L}_{\text{DC}})^{-1}\mathbf{T}_{\text{oi}}^{\text{cc}}$$

where the PLL transfer matrix (8) is included to $\mathbf{Y}_{\text{o}}^{\text{cc}}$ and $\mathbf{T}_{\text{oi}}^{\text{cc}}$.

The expanded form of the inverter output admittance:

$$\begin{aligned}\mathbf{Y}_{\text{o-c}} = (\mathbf{I} + \mathbf{L}_{\text{CC}})^{-1}\left(\mathbf{Y}_{\text{o-o}} + (\mathbf{L}_{\text{CC}}\mathbf{I}_{\text{L}} - \mathbf{G}_{\text{co-o}}\mathbf{D})\left[\frac{L_{\text{PLL}}}{V_{\text{od}}(1+L_{\text{PLL}})}\mathbf{H}_{\text{PLL}}\right]\right) + \\ \mathbf{G}_{\text{refo}}^{\text{cc}}\mathbf{G}_{\text{c-in}}\mathbf{H}_{\text{in}}(\mathbf{I} + \mathbf{L}_{\text{DC}})^{-1}[\mathbf{T}_{\text{io-o}} + \mathbf{G}_{\text{ci-o}}\mathbf{G}_{\text{co-o}}^{-1}(\mathbf{G}_{\text{cc}}(\mathbf{Y}_{\text{o-o}} + (\mathbf{L}_{\text{CC}}\mathbf{I}_{\text{L}} - \mathbf{G}_{\text{co-o}}\mathbf{D})\times \\ \left[\frac{L_{\text{PLL}}}{V_{\text{od}}(1+L_{\text{PLL}})}\mathbf{H}_{\text{PLL}}\right]) - (\mathbf{L}_{\text{CC}}\mathbf{I}_{\text{L}} - \mathbf{G}_{\text{co-o}}\mathbf{D})\left[\frac{L_{\text{PLL}}}{V_{\text{od}}(1+L_{\text{PLL}})}\mathbf{H}_{\text{PLL}}\right])]\end{aligned}$$

The resistive-inductive grid impedance in dq domain:

$$\mathbf{Z}_{\text{g}}(L_{\text{g}}) = \begin{bmatrix} r_{\text{g}} + L_{\text{g}}s & L_{\text{g}}\omega \\ -L_{\text{g}}\omega & r_{\text{g}} + L_{\text{g}}s \end{bmatrix}$$

References

1. Li, C. Unstable Operation of Photovoltaic Inverter from Field Experiences. *IEEE Trans. Power Deliv.* **2018**, *33*, 1013–1015. [CrossRef]
2. Liang, X. Emerging Power Quality Challenges Due to Integration of Renewable Energy Sources. *IEEE Trans. Ind. Appl.* **2012**, *53*, 855–866. [CrossRef]
3. Sun, J. Impedance-Based Stability Criterion for Grid-Connected Inverters. *IEEE Trans. Power Electron.* **2011**, *26*, 3075–3078. [CrossRef]
4. Suntio, T.; Messo, T.; Berg, M.; Alenius, H.; Reinikka, T.; Luhtala, R.; Zenger, K. Impedance-Based Interactions in Grid-Tied Three-Phase Inverters in Renewable Energy Applications. *Energies* **2019**, *12*, 464. [CrossRef]
5. Belkhayat, M. Stability Criteria For AC Power Systems with Regulated Loads. Ph.D. Thesis, Purdue University, West Lafayette, Indiana, 1997.
6. Jessen, L.; Fuchs, F. Modeling of Inverter Output Impedance for Stability Analysis in Combination with Measured Grid Impedances. In Proceedings of the 2015 IEEE 6th International Symposium on Power Electronics for Distributed Generation Systems (PEDG), Aachen, Germany, 22–25 June 2015. [CrossRef]
7. Jessen, L.; Fuchs, F. Investigation of Renewable Energy Generation and Load Impact on the Grid Impedance at Different Points of Connection in Public Low-Voltage Grids to Support Grid Integration of Renewable Energies. In Proceedings of the 2016 18th European Conference on Power Electronics and Applications (EPE'16 ECCE Europe), Karlsruhe, Germany, 5–9 September 2016. [CrossRef]
8. Hallak, G.; Bumiller, G. Impedance Measurement of Electrical Equipment Loads on the Power Line Network. In Proceedings of the 2017 IEEE International Symposium on Power Line Communications and its Applications (ISPLC), Madrid, Spain, 3–5 April 2017. [CrossRef]
9. Alenius, H.; Reinikka, T.; Messo, T.; Roinila, T. Modeling, Sensitivity Analysis, and Power Hardware-in-the-Loop Emulation of Grid Impedance. In Proceedings of the 2018 IEEE Energy Conversion Congress and Exposition (ECCE), Portland, OR, USA, 3–7 September 2018; pp. 4179–4186. [CrossRef]
10. Jia, K.; Bi, T.; Li, W.; Yang, Q. Ground Fault Distance Protection for Paralleled Transmission Lines. *IEEE Trans. Ind. Appl.* 2015, *51*, 5228–5236. [CrossRef]
11. Milioudis, A.; Andreou, G.; Labridis, D. Enhanced Protection Scheme for Smart Grids Using Power Line Communications Techniques—Part I: Detection of High Impedance Fault Occurrence. *IEEE Trans. Smart Grid* **2012**, *3*, 1621–1630. [CrossRef]
12. Izykowski, J.; Rosolowski, E.; Saha, M. Locating Faults in Parallel Transmission Lines under Availability of Complete Measurements at one End. *IEE Proc. Gener. Transm. Distrib.* **2004**, *151*, 268–273.:20040163. [CrossRef]
13. Funabashi, T.; Otoguro, H.; Mizuma, Y.; Dube, L.; Ametani, A. Digital Fault Location for Parallel Double-Circuit Multi-Terminal Transmission Lines. *IEEE Trans. Power Deliv.* **2000**, *2*, 531–537. [CrossRef]

14. Roinila, T.; Messo, T.; Luhtala, R.; Scharrenberg, R.; de Jong, E.; Fabian, A.; Sun, Y. Hardware-in-the-Loop Methods for Real-Time Frequency-Response Measurements of on-Board Power Distribution Systems. *IEEE Trans. Ind. Electron.* **2019**, *66*, 5769–5777. [CrossRef]
15. Luhtala, R.; Roinila, T.; Messo, T. Implementation of Real-Time Impedance-Based Stability Assessment of Grid-Connected Systems Using MIMO-Identification Techniques. *IEEE Trans. Ind. Appl.* **2018**, *54*, 5054–5063. [CrossRef]
16. Messo, T.; Luhtala, R.; Roinila, T.; Yang, D.; Wang, X.; Blaabjerg, F. Real-time Impedance-Based Stability Assessment of Grid Converter Interactions. In Proceedings of the 2017 IEEE 18th Workshop on Control and Modeling for Power Electronics (COMPEL), Stanford, CA, USA, 9–12 July 2017. [CrossRef]
17. Cespedes, M.; Sun, J. Online grid impedance identification for Adaptive Control of Grid-Connected Inverters. In Proceedings of the 2012 IEEE Energy Conversion Congress and Exposition (ECCE), Raleigh, NC, USA, 15–20 September 2012; pp. 914–921. [CrossRef]
18. Kamala, S.; Kanakesh, V.K.; Panda, S.K.; Amaratunga, G. D-Q Frame Impedance Measurement and Small Signal Stability Improvement in a 3-phase System with Constant Power Loads by an Active Control Method. In Proceedings of the 2018 IEEE International Telecommunications Energy Conference (INTELEC), Torino, Italy, 7–11 October 2018. [CrossRef]
19. Roinila, T.; Messo, T.; Santi, E. MIMO-Identification Techniques for Rapid Impedance-based Stability Assessment of Three Phase Systems in DQ Domain. *IEEE Trans. Power Electron.* **2017**, *3*. [CrossRef]
20. Roinila, T.; Vilkko, M.; Sun, J. Broadband Methods for Online Grid Impedance Measurement. *IEEE Energy Convers. Congr. Expo.* **2013**, 3003–3010. [CrossRef]
21. Messo, T.; Jokipii, J.; Mäkinen, A.; Suntio, T. Modeling the Grid Synchronization Induced Negative-Resistor-Like Behavior in the Output Impedance of a Three-Phase Photovoltaic Inverter. In Proceedings of the 2013 4th IEEE International Symposium on Power Electronics for Distributed Generation Systems (PEDG), Rogers, AR, USA, 8–11 July 2013. [CrossRef]
22. Harnefors, L.; Wang, X.; Yepes, A.G.; Blaabjerg, F. Passivity-Based Stability Assessment of Grid-Connected VSCs—An Overview. *IEEE J. Emerg. Sel. Top. Power Electron.* **2016**, *4*, 116–125. [CrossRef]
23. Wen, B.; Dong, D.; Boroyevich, D.; Burgos, R.; Mattavelli, P.; Shen, Z. Impedance-Based Analysis of Grid-Synchronization Stability for Three-Phase Paralleled Converters. *IEEE Trans. Power Electron.* **2016**, *31*, 26–38. [CrossRef]
24. Messo, T.; Sihvo, J.; Yang, D.; Wang, X.; Blaabjerg, F. Improved Delayed Signal Cancellation-Based SRF-PLL for Unbalanced Grid. In Proceedings of the 2017 IEEE Energy Conversion Congress and Exposition (ECCE), Cincinnati, OH, USA, 1–5 October 2017; pp. 3103–3110. [CrossRef]
25. Davari, M.; Mohamed, Y. Robust Vector Control of a Very Weak-Grid-Connected Voltage-Source Converter Considering the Phase-Locked Loop Dynamics. *J. IEEE Trans. Power Electron.* **2017**, *32*, 977–994. [CrossRef]
26. Zhou, J. Impact of Short-Circuit Ratio and Phase-Locked-Loop Parameters on the Small-Signal Behavior of a VSC-HVDC Converter. *IEEE Trans. Power Deliv.* **2014**, *29*, 2287–2296. [CrossRef]
27. Cespedes, M.; Sun, J. Adaptive Control of Grid-Connected Inverters Based on Online Grid Impedance Measurements. *IEEE Trans. Sustain. Energy* **2014**, 516–523. [CrossRef]
28. Luhtala, R.; Messo, T.; Reinikka, T.; Sihvo, J.; Roinila, T.; Vilkko, M. Adaptive Control of Grid-Connected Inverters Based on Real-Time Measurements of Grid Impedance: DQ-Domain Approach. *IEEE Energy Convers. Congr. Expo.* **2017**, 69–75. [CrossRef]
29. Xu, J.; Qian, Q.; Xie, S. Adaptive control Method for Enhancing the Stability of Grid-Connected Inverters under Very Weak Grid Condition. In Proceedings of the 2018 IEEE Applied Power Electronics Conference and Exposition (APEC), San Antonio, TX, USA, 4–8 March 2018; pp. 1141–1146. [CrossRef]
30. Luhtala, R.; Reinikka, T.; Alenius, H.; Roinila, T.; Messo, T. Adaptive Method for Control Tuning of Grid-Connected Inverter Based on Grid Measurements During Start-Up. In Proceedings of the 2019 18th European Control Conference (ECC), Naples, Italy, 25–28 June 2019; pp. 417–422. [CrossRef]
31. Wen, B.; Boroyevich, D.; Burgos, R.; Mattavelli, P.; Shen, Z. Small-Signal Stability Analysis of Three-Phase AC Systems in the Presence of Constant Power Loads Based on Measured d-q Frame Impedances. *IEEE Trans. Power Electron.* **2015**, *30*, 5952–5963. [CrossRef]
32. Vesti, S.; Suntio, T.; Oliver, J.A.; Prieto, R.; Cobos, J.A. Impedance-Based Stability and Transient-Performance Assessment Applying Maximum Peak Criteria. *IEEE Trans. Power Electron.* **2013**, *28*, 2099–2104. [CrossRef]

33. Luhtala, R.; Reinikka, T.; Roinila, T.; Messo, T.; Sihvo, J. Improved Real-Time Stability Assessment of Grid-Connected Converters Using MIMO-Identification Methods. In Proceedings of the 2018 IEEE Energy Conversion Congress and Exposition (ECCE), Portland, OR, USA, 23–27 September 2018; pp. 5322–5329. [CrossRef]
34. Reinikka, T.; Roinila, T.; Luhtala, R.; Messo, T. Impedance-Based Sensitivity-Criterion for Grid-Connected Three-Phase Inverters. *IEEE Energy Convers. Congr. Expo.* **2018**, 4173–4178. [CrossRef]
35. Messo, T.; Aapro, A.; Suntio, T. Generalized Multivariable Small-Signal Model of Three-Phase Grid-Connected Inverter in DQ-Domain. In Proceedings of the IEEE 16th Workshop on Control and Modeling for Power Electronics (COMPEL), Vancouver, BC, Canada, 12–15 July 2015. [CrossRef]
36. Godfrey, K. *Perturbation Signals for System Identification*; Prentice Hall: Englewood Cliffs, NJ, USA, 1993.
37. Luhtala, R.; Messo, T.; Lenius, H.A.; Roinila, T.; de Jong, E.; Burstein, A.; Fabian, A. Identification of Three-Phase Grid Impedance in the Presence of Parallel Converters. *Energies* **2019**, *12*, 2674. [CrossRef]
38. Luhtala, R.; Alenius, H.; Messo, T.; Roinila, T. Online Frequency-Response Measurements of Grid-Connected Systems in Presence of Grid Harmonics and Unbalance. *IEEE Trans. Power Electron.* **2020**, *35*, 3343–3347. [CrossRef]

PUBLICATION

V

Adaptive Optimization of AC-Current Control Loop for Grid-Connected Inverters

R. Luhtala, H. Alenius and T. Roinila

IEEE Applied Power Electronics Conference and Exposition, 6 pages, 2020

Adaptive Optimization of Current-Control Loop for Grid-Connected Inverters

1st Roni Luhtala
Faculty of Engineering and Natural Sciences
Tampere University
Tampere, Finland
roni.luhtala@tuni.fi

2nd Henrik Alenius
Faculty of Information Technology and Communication Sciences
Tampere University
Tampere, Finland
henrik.alenius@tuni.fi

3rd Tomi Roinila
Faculty of Information Technology and Communication Sciences
Tampere University
Tampere, Finland
tomi.roinila@tuni.fi

***Abstract*—The amount of grid-connected power electronics is rapidly increasing and their effect to power quality becomes important especially in areas with high penetration levels. In weak grids with significant grid impedance, the inverter control performance usually decreases and the impedance-based stability issues may arise. A method to analyze the stability issues and to improve the inverter control performance is to consider the grid as a load effect in the small-signal model of the grid-connected inverter. Studies have shown that the bandwidth of the inverter current-control loop decreases in the weak grids through the load effect, and consequently, the controller ability to mitigate harmonics is weakened. This work introduces an adaptive method that keeps the bandwidth of the control loop constant under varying grid conditions. Additionally, an adaptive Notch filter is added into the current-control loop in order to avoid possible stability issues caused by the interactions with the LC-filter resonance and the grid impedance. Improved control performance and stability under various grid conditions are demonstrated through power hardware-in-the-loop tests with a kW-scale three-phase inverter.**

I. Introduction

The amount of the grid-connected inverters have been rapidly increasing, mainly through growing interests into the renewable energy [1]. In many areas the instantaneous power generation through the inverters may increase temporarily over 50 %. As a consequence, the power system operation has become highly depended on control performance and stability of the grid-connected inverters [2], [3]. The grid characteristic, especially high grid impedance, has a major impact on the inverter control performance and the system stability [4]–[6]. The impact of the grid impedance can be included into the inverter dynamic model as a load effect [7]. The load-affected models include an additional term that resembles a negative feedback loop and contains information about the present grid impedance. These models have similar information about the stability that is usually achieved from the impedance-based stability assessment [5].

By applying the load-affected inverter models, the system stability and performance can be accurately predicted under a certain grid impedance [7], [8]. Consequently, those models should be applied in the inverter optimization process when the grid impedance is a known parameter. However, the grid impedance is often an unknown parameter that usually varies between the connection points and time [9], [10]. This makes the online frequency-response measurements, performed during the normal operation under the present grid conditions, the most desired when analyzing the system stability and the control performance of a grid-connected inverter [11]–[13].

This paper considers a load-affected current-control loop, which usually acts as the innermost control loop in the grid-following inverters. In weak grids, where the grid impedance is significant, the bandwidth of the current-control loop decreases through the load effect [8]. This weakens the control performance, for example by increasing settling times and decreasing the ability to mitigate low-order harmonics from the produced currents. The grid impedance also affects the magnitude and frequency of the high-frequency resonance peak, that is caused by a grid-side filter [6], [14]. These effects are analyzed through analytical models and online frequency-response measurements under various grid conditions.

To improve the inverter control performance under varying grid conditions, this paper introduces adaptive methods for optimizing the current-control loop. In the methods, an adaptively-adjusted Notch filter mitigates the stability issues arising from the AC filter, and load-affected bandwidth of the current-control loop is kept constant by re-adjusting the controller parameters to match the present grid conditions. The methods are based on online frequency-response measurements of the inverter current-control loop. In the measurements, a small-amplitude sine wave is applied as a perturbation for continuously re-adjusting the current control loop, and a pseudo-random binary sequence (PRBS) is applied for adjusting the Notch filter. The measurements and adaptive processes are performed by utilizing the control system of the existing inverter, and thus, no additional sensors are required. Online measurements and the improved control performance in various grid conditions are shown from a power hardware-in-the-loop test setup, which include a kW-scale three-phase inverter.

The reminder of this paper is organized as follows. Section II presents the load-affected small-signal modeling of the grid-connected inverter, and introduces methods for measuring the current-control loop online. Section III introduces the adaptive process, which includes parametrization of the Notch

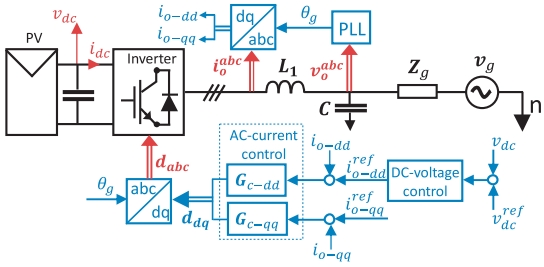

Fig. 1: Grid-connected three-phase inverter.

filter and continuous re-adjustment of the controller gains to match present grid conditions. Section IV demonstrates the implementation of the adaptive process in MATLAB/Simulink simulation. In Section V, experiments with power hardware-in-the-loop setup show online measurements of the current-control loop and illustrates the improved control performance in weak grids. Section VI draws the conclusion.

II. Grid-Connected Inverter

A. Load-Affected Small-Signal Model

Fig. 1 shows a simplified block diagram of a grid-connected three-phase PV inverter with an LC-type filter. A DQ-domain control system is applied, which is synchronized to the voltages over the LC-filter capacitors, and a feedback for the current control is measured from the inductor currents. The inverter open-loop small-signal transfer functions (2 x 2 matrices) can be represented as [4]

$$\begin{bmatrix} \hat{\mathbf{v}}_{\text{DC}} \\ \hat{\mathbf{i}}_{\text{o}} \end{bmatrix} = \underbrace{\begin{bmatrix} \mathbf{Z}_{\text{in-o}} & \mathbf{T}_{\text{oi-o}} & \mathbf{G}_{\text{ci-o}} \\ \mathbf{G}_{\text{io-o}} & -\mathbf{Y}_{\text{o-o}} & \mathbf{G}_{\text{co-o}} \end{bmatrix}}_{\mathbf{G}} \begin{bmatrix} \hat{\mathbf{i}}_{\text{dc}} \\ \hat{\mathbf{v}}_{\text{o}} \\ \hat{\mathbf{d}} \end{bmatrix} \tag{1}$$

where $\mathbf{G}$ is a transfer-function matrix from input to output variables, which are shown in Fig. 1.

As the inverter is connected to the real grid, the grid impedance is present and results in a load effect. The load effect appears as the output current affects the grid voltage through the grid impedance $\mathbf{Z}_{\text{g}}$. Consequently, the grid voltage affects the currents through the inverter output admittance ($\mathbf{Y}_{\text{o-o}}$). As a combination of these two effects, an additional term appears in the inverter transfer functions. This term resembles a feedback loop and can be written as $[\mathbf{I} + \mathbf{Y}_{\text{o-o}}\mathbf{Z}_{\text{g}}]^{-1}$. Similar transfer function is analyzed in the impedance-based stability analysis [5]. The load-affected modeling becomes practical option to assess the system stability and to predict its control performance, as it can be added to the open-loop transfer functions. For example, the load-affected transfer function from the duty ratios to the output current ($\mathbf{G}_{\text{co-o}}$) can be written as [7]

$$\mathbf{G}_{\text{co-o-L}} = \mathbf{G}_{\text{co-o}} \left[\mathbf{I} + \mathbf{Y}_{\text{o-o}}\mathbf{Z}_{\text{g}}\right]^{-1} \tag{2}$$

To produce complete closed-loop small-signal model of the inverter, the closed control loops must be included to

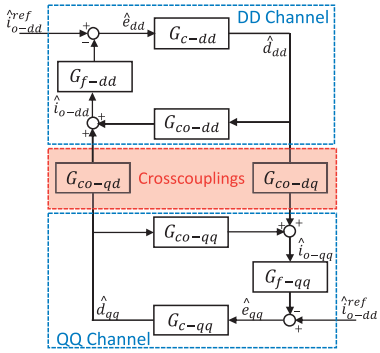

Fig. 2: Small-signal model of current-control loop.

the model. The grid-following PV inverter (shown in Fig. 1) is used as an example in this paper. The inverter can be controlled with a cascaded control scheme in the DQ domain. In such control scheme, an outer loop adjusts the inverter DC voltage to the maximum-power point of the PV generator. The controller applies relatively low bandwidths and removes the need for an additional DC-DC converter. The innermost loop, controlling the three-phase output currents, applies a controller with a higher bandwidth. Additionally, a phase-locked loop (PLL) is applied to synchronize the inverter control frame to the grid voltages, which is required when the DQ-domain control system is applied.

B. AC-Current Control Loop

Fig. 2 shows the block-diagram representation of the load-affected current-control loops, where the transfer matrices are divided to direct (dd and qq) and crosscoupling components (dq and qd). Sensing gains and a pulse-width modulator are replaced by a time delay $T_{\text{d}} = 1.5/f_{\text{sw}}$, where f_{sw} is the converter switching frequency. A third-order Pade approximation of the time delay is included to $\mathbf{G}_{\text{co-o-L}}$. The controllers are denoted as $G_{\text{c-dd}}$ and $G_{\text{c-qq}}$ for dd and qq channels, respectively. Additional digital filters, implemented into the loop, are denoted by $G_{\text{f-dd}}$ and $G_{\text{f-qq}}$. The DC-voltage controller and grid-synchronization are neglected from the model as they have significantly lower bandwidth than the current-control loop. The current-control loop gains can be written as

$$L_{\text{ACC-dd}} = G_{\text{c-dd}}G_{\text{co-dd-L}}G_{\text{f-dd}} - \frac{G_{\text{c-dd}}G_{\text{co-dq-L}}G_{\text{f-qq}}G_{\text{c-qq}}G_{\text{co-qd-L}}G_{\text{f-dd}}}{(1 + G_{\text{c-qq}}G_{\text{co-qq-L}}G_{\text{f-qq}})} \tag{3}$$

$$L_{\text{ACC-qq}} = G_{\text{c-qq}}G_{\text{co-qq-L}}G_{\text{f-qq}} - \frac{G_{\text{c-qq}}G_{\text{co-qd-L}}G_{\text{f-dd}}G_{\text{c-dd}}G_{\text{co-dq-L}}G_{\text{f-qq}}}{(1 + G_{\text{c-dd}}G_{\text{co-dd-L}}G_{\text{f-dd}})} \tag{4}$$

C. LC Filter with Grid Impedance

The LC filter and an interfaced grid inductance (L_{g}) form an LCL circuit, whose properties depends on the filter design and the grid impedance. Its resonant pole appears at

$$\omega_{\text{p-LCL}} = \sqrt{\frac{L_{\text{i}} + L_{\text{g}}}{C L_{\text{i}} L_{\text{g}}}} \tag{5}$$

where L_g is usually unknown. The value of L_g depends on the connection point, and may vary over time. This pole appears as a resonant peak in the current-control loop gain, and is affected by the grid impedance similar to the load-affected transfer functions. The peak is usually located at significantly higher frequencies than the inverter control bandwidths. In high frequencies, the control delay has usually decreased the phase below -180 degree, which may cause stability issues at high frequencies. These stability issues may arise especially in weak grids with significant L_g. The issues can be avoided by adjusting the current-control loop characteristics not to interact with the high grid impedances.

D. Online Measurements of Loop Gain

A method for the online current-control loop measurements is introduced in [8]. In the proposed method, perturbations are injected on top of the current reference, loop responses are measured from both sides of the injection point, and the frequency response is computed as a relation of the responses. The resulting online curren-control loop-gain measurement includes information about the control dynamics and the LC filter through the load effect. Thus, the same dynamic interactions between the grid and the inverter can be predicted as from the conventional impedance-based stability analysis, where the grid impedance and inverter output impedance have to be modeled or separately measured [15]. This makes the online loop measurement practical in assessing the inverter stability during its normal operation under the present grid conditions [7], [8].

In the frequency-response measurements, the applied perturbation signal determines the properties of the measurement. The sine waves can be applied to excite one frequency at time or a sweep of sines over many frequencies [16]. This method provides accurate results but is quite slow when a wide frequency band has to be measured. An alternative is to use a broadband perturbations, with which a number of frequencies can be simultaneously analyzed within a single measurement cycle. A maximum-length binary sequence (MLBS) is a widely applied broadband perturbation, which is easy to generate and have many attractive characteristics in both time and frequency domains [12], [15], [17].

III. Adaptive Control

A. Adaptive Notch Filter

The LC-filter and the grid impedance form a resonance peak to the load-affected current-control loop. The frequency where the peak appears depends on the grid inductance as shown in (5). In weak grids the grid inductance is significant and the resonance peak is magnified through the load effect which may result in stability issues [6]. Additionally, the current-controller gains proportionally magnify the resonance peak. Consequently, the resonance peak sets upper limit for the controller gains that can be applied in the AC-current controller. This is an issue especially in weak grids where the resonance peak is already magnified by the grid inductance, and higher gains should be applied in the current-control loop to increase the load-affected bandwidth.

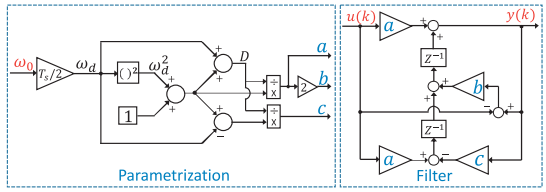

Fig. 3: Parametrization and implementation of adaptive Notch filter.

To increase the gain limits in the AC-current controller, a digital Notch filter is added to the current-control loop to introduce damping at the LC-resonance frequency [14]. In this work, a second-order Notch filter, with a unity quality factor is applied. The filter transfer function can be written as

$$\mathbf{G}_{\text{f-c}} = \frac{s^2 + \omega_0^2}{s^2 + \omega_0 s + \omega_0^2} \tag{6}$$

where ω_0 is center frequency of the filter. For a practical implementation of a digital filter, (6) must be discretized. This can be performed by using, for example, the Tustin approximation, yielding

$$\mathbf{G}_{\text{f-d}} = u(k)\left[a - bZ^{-1} + aZ^{-2}\right] - y(k)\left[-bZ^{-1} + cZ^{-2}\right] \tag{7}$$

where Z^{-1} is the unit delay, determined by the sampling time T_s of the control system. The parameters for the digital Notch filter are computed as

$$\begin{aligned} \omega_d &= \omega_0 T_s/2 \\ D &= 1 + \omega_d + \omega_d^2 \\ a &= \frac{1+\omega_d^2}{D} \\ b &= \frac{2(1+\omega_d^2)}{D} \\ c &= \frac{1-\omega_d+\omega_d^2}{D} \end{aligned} \tag{8}$$

The frequency and magnitude of the resonance peak depend on the grid inductance, which is usually an unknown parameter. This makes the use of the online current-contol loop measurements practical when adjusting the Notch filter. In this work, the MLBS is applied as a perturbation to achieve fast measurement over a wide frequency band. From the resulting broadband measurement, the resonance peak is observed as a local maximum at frequencies higher than the control bandwidths. The frequency of the resonance peak is set as a center frequency ω_0 in the Notch-filter adjustment process. Fig. 3 shows a block-diagram presentation of the parametrization process of the discrete Notch filter, where the center frequency ω_0 is observed from the online measurement and fed to the parametrization (8).

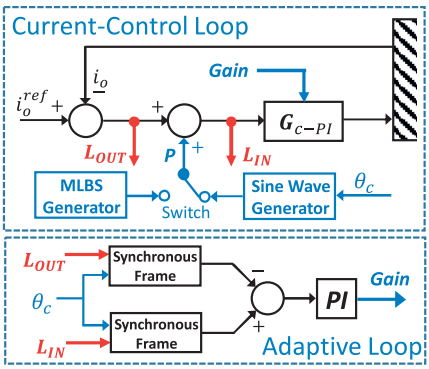

Fig. 4: Implementation of adaptive current-control loop.

B. Adaptive AC-current control

The adaptive procedure adjusts the controller parameters so that the loop magnification is 0 dB at the selected bandwidth frequency (f_c), that is, the bandwidth is kept constant. The selection of the bandwidth can be made arbitrarily, depending on the desired loop characteristics. System delays and the LCL resonance between the filter and the grid impedance set the upper limit for the gains. However, the upper limit can be significantly increased by applying the proposed Notch filter [14].

Fig. 4 shows a practical implementation of the adaptive method. During the inverter start-up the Notch filter is adjusted (possibility to re-adjust) with the use of the MLBS measurements. After this the adaptive process can be launched. The loop is continuously perturbed by a small-amplitude sinusoidal current at a frequency of f_c (θ_c) and the corresponding loop responses (L_{IN} and L_{OUT}) are measured. The responses are fed to the adaptive loop where they are compared in a synchronous frame, rotating at f_c. The error signal is fed to the PI-controller, whose output continuously adjusts the current-controller gains. Consequently, magnification of the current-control loop is regulated to 0 dB at f_c. Symmetrical controllers are applied in the d and q channels, thus the adaptive process adjusts the parameters in both controllers $G_{c\text{-}dd}$ and $G_{c\text{-}qq}$.

IV. Analytical Model and Simulations

The analytical modeling and the simulations are performed to illustrate the load-affected current-control loop and its adaptive optimization method. A three-phase inverter with a 2.7 kW nominal power is connected into the 120 V/60 Hz grid. The LC-type filter is applied where L_1 = 2.2 mH and C = 10 μF. Table I in Appendix shows the other applied parameters, which are approximations from the experimental setup.

Fig. 5 shows the modeled AC-current control loop gains (dd component) in different grids. Blue line (ideal grid) represents the current-control loop gain when the load effect is not included in the model and the loop bandwidth is set to 300 Hz. The same control parameters are applied under various grid impedances, from relatively strong (inductance 2 mH) to weak (10 mH) grids, and the load effect (2) is taken into account. It is clearly shown that the grid impedance reduces the loop bandwidth through the load effect. For example under the 10 mH grid, the bandwidth is 80 Hz which strongly affects the inverter performance, as the harmonics are mitigated effectively only inside the bandwidth.

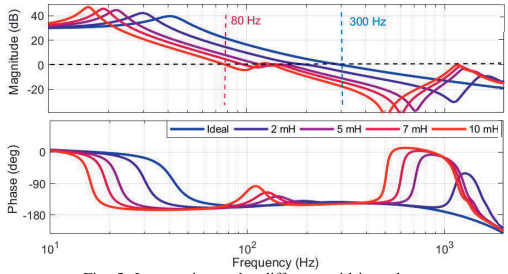

Fig. 5: Loop gains under different grid impedances.

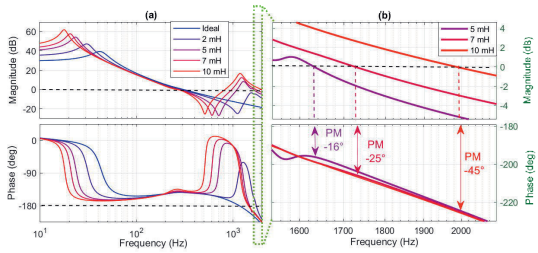

Fig. 6: Loop gains with adaptive gain adjustment.

The bandwidth can be increased by using higher gains in the current controller. However, the LCL-resonance peak (located around 1200 - 1400 Hz in Fig. 5) is also magnified when the gains are increased. The phase of the current-control loop is decreased below -180 degrees around the peak which causes stability issues if the magnitude rises above 0 dB around those frequencies. Fig. 6 (a) shows the analytical loops, when the gains are increased so that the load-effect is compensated to achieve the 300 Hz bandwidth in every grid. Fig. 6 (b) shows the magnified resonance peaks under weak grids (5, 7 and 10 mH). As the peak is magnified above 0 dB with negative phase margins, the unstable operations and harmonic resonances at high frequencies are predicted. However, the proposed Notch filter may damp the resonance peak and increase the gain limits (illustrated in the experiments).

Fig. 7 shows the adaptive operation during the inverter start up, where the Notch filter is adjusted at 1 s to increase the gain limits. Here the desired AC-loop bandwidth is set to 300 Hz. Thus, the current reference is perturbed at 300 Hz. By comparing the 300 Hz amplitudes of L_{OUT} (grey line) and L_{IN} (blue line) signals in the synchronous frame, the PI-controller is able to adjust the AC-controller gains so that the desired control bandwidth is obtained. The suitable controller gains are found approximately at 3 s when the amplitude of L_{OUT} equals to L_{IN} amplitude, and the load effect is compensated.

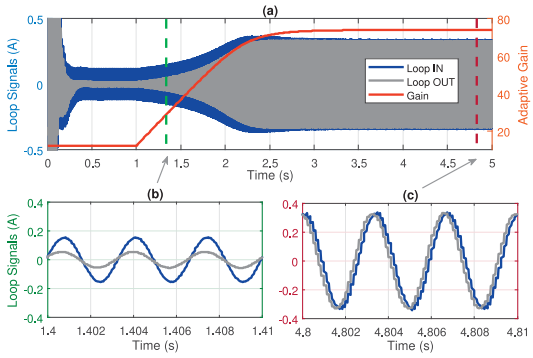

Fig. 7: Operation of the adaptive control.

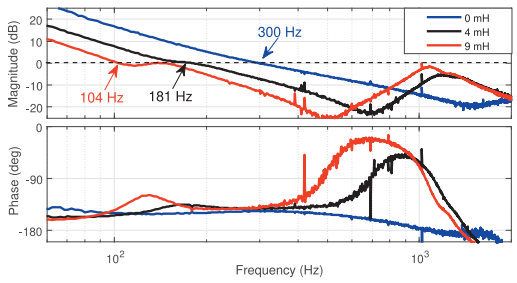

Fig. 8: Effect of the different grid impedances.

The lower parts of the figure show the amplitude difference at 1.4 s (b) and at 4.8 s (c) to illustrate the error signal applied in the adaptive loop that is regulated to zero by adjusting the current-controller gains.

V. Experiments

The experimental tests are performed with a power hardware-in-the-loop setup, which consists of a three-phase grid emulator (voltage amplifier), a PV emulator, and a 2.7 kW three-phase inverter. The inverter is connected to the grid emulator through an isolation transformer and various three-phase inductors that emulate different grid impedances. The inverter control system is implemented in a real-time simulator. The applied control parameters and hardware parameters are given in Table I in Appendix.

A. Load-Affected Current-Control Loop Measurements

A 2047-bit long MLBS was generated at 4 kHz, thus providing a frequency resolution of 1.95 Hz (4000/2047 Hz). The MLBS is injected to the loop in accordance with Fig. 4, and the same responses (L_{IN} and L_{OUT}) are measured as done in the adaptive process, where the single-sine injection was applied. These MLBS-based measurements are applied in the Notch filter parametrization, where the LCL-resonance peak frequency is required.

Fig. 8 shows current-control loop measurements under three different grid impedances. The bandwidth of the current-control loop is adjusted to 300 Hz when the loop is designed for an ideal grid. Blue line represents the current-control loop measurement under a strong grid where the grid impedance is negligibly small, and the load effect has a negligible impact on the loop bandwidth. Black and red lines represent the loop gains when a significant grid impedance is present, and the decrease in the bandwidth is clear in both cases. For example, when the inverter is connected to a weak grid (L_g = 9 mH), the bandwidth is decreased to as low as 104 Hz. Additionally, the effect of L_g to the high-frequency resonance peak is shown. Due to the grid impedance, the resonance is magnified and the peak appears at lower frequency.

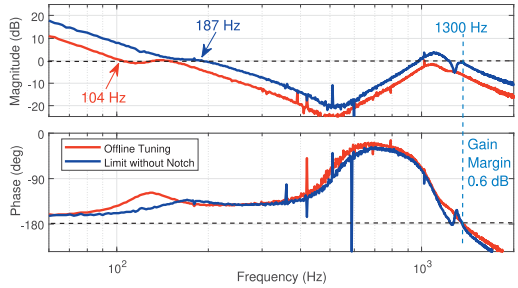

Fig. 9: Practical controller gain limit under 9 mH grid impedance without Notch filter.

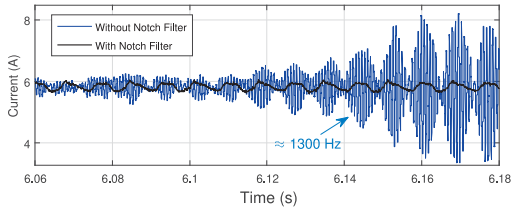

Fig. 10: Currents in d channel with and without optimized Notch filter.

Under a weak grid, the high-frequency resonance peak limits the controller gains. Fig. 9 shows online current-control loop measurements under 9 mH grid inductance with two different controller gains. Red line represents the same measurement as in Fig. 8, and blue line represents the loop when the controller gains are increased to their practical limits. In this case, the bandwidth can be increased from 104 Hz to 187 Hz by simply re-adjusting the controller gains. However, further bandwidht increase is not possible by simple controller gain tuning, because the gain margin already becomes very low (0.6 dB) around 1300 Hz. The system has became relatively sensitive to high-frequency disturbances due to low stability margins. By increasing the controller gains without applying the proposed Notch filter, stability issues will arise. Fig. 10 shows the d-channel current (blue line) when the controller gain is increased above the limit, and excessive harmonic resonances appear around 1300 Hz. Black line shows the current when similar controller gains are applied, but the

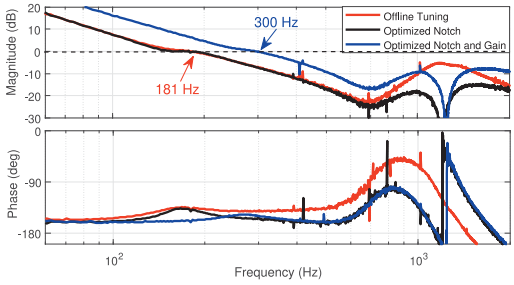

Fig. 11: Loop optimization under 4 mH grid impedance.

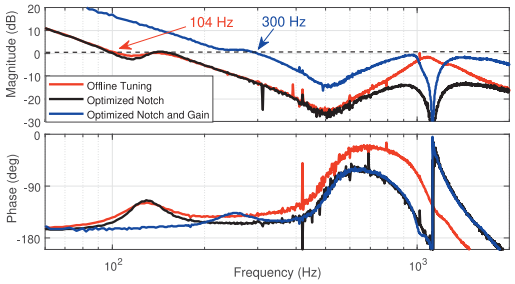

Fig. 12: Loop optimization under 9 mH grid impedance.

resonance peak is mitigated by the optimized Notch filter. By adding the optimized Notch filter, the controller gains can be increased without destabilizing system around the high-frequency resonance peak.

B. Adaptive Loop Optimization

Figs. 11 and 12 show effect of the adaptive optimization process to the current-control loops under two different grid impedances. Red lines (in both figures) show the loop measurements during the inverter start-up, when the adaptive process is not started yet. The current-controllers are tuned offline for a 300 Hz bandwidth in ideal grid. However, the load effect decreases the bandwidth significantly when the grid impedance is present. To increase the practical limits for the controller gains, the Notch filter is adjusted to damp the high-frequency resonance peak. As the filter parameters are known, the resonance peak is not expected to appear below 1 kHz. Thus, the local maximum of the measured loop is observed above 1 kHz, and the maximum is chosen as the central frequency of the Notch filter. The central frequency of the Notch filter is set approximately to 1300 Hz under 4 mH grid and to 1150 Hz under 9 mH grid. Black lines show the loop measurements when the optimized Notch filters are added to the loops. The filters clearly mitigate the resonance peaks, and consequently, increase the upper limit for the controller gains. After adjusting the Notch filters, the adaptive optimization of the bandwidth is performed as illustrated in Fig. 7. The desired bandwidth is set to 300 Hz in both experiments. Blue lines show the final current-control loops, when the adaptive process has adjusted the controller gains so that the 300 Hz bandwidth is achieved. It can be seen that the use of the Notch filter enables to adjust the controller gains that provide 300 Hz bandwidth. As Fig. 9 showed, the practical limit for the bandwidth is around 187 Hz in 9 mH grid when the Notch filter is not applied

C. Harmonic Mitigation with Adaptive Loop

In the next experiment, the inverter is connected to a weak grid (9 mH inductance) where a slight unbalance (2 %) and third harmonic (2 %) are present in the grid voltages. Under such grid conditions, the performance of different current-control loops are illustrated by testing their ability to mitigate

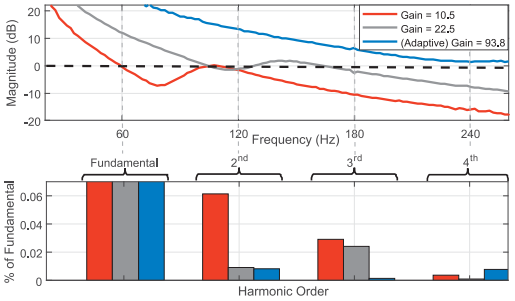

Fig. 13: Effect of the loop gain under weak grid with 3rd harmonic and voltage unbalance.

low-order harmonics from the produced currents. Upper part of Fig. 13 shows magnitudes of the applied current-control loops, from which the control bandwidths can be observed. Blue line represents the loop that is adjusted by the proposed methods, and the bandwidth is adaptively set to 300 Hz. The grey line represents an offline tuning where the load effect is not taken into account. The effect of lower bandwidth is illustrated by a loop shown with red line. The resonance around the bandwidth is produced through the load effect, but is damped relatively well when higher controller gains are applied. The lower part of the figure shows the harmonic content in the produced currents, where the colors match to the loops in the upper part of the figure. It can be seen that the harmonics are effectively mitigated inside the bandwidth of the current-control loop. With the lowest controller gains (red line), the bandwidth is approximately 60 Hz. Thus, significant amount of second (120 Hz) and third harmonics (180 Hz) are produced. The loop (grey line) with a 160 Hz bandwidth is able to mitigate second harmonic but not the third harmonic. The adaptive loop (blue line) effectively mitigates all the low-order harmonics as its bandwidth is re-adjusted to match the weak grid.

VI. Conclusions

A properly designed grid-connected inverter typically mitigates the undesired low-order harmonics from the inverter output current within the bandwidth of the inverter current-control loop. In a weak grid, however, the grid impedance decreases

the bandwidth of the current-control loop. The bandwidth may be increased simply by re-adjusting the controller gains but this typically magnifies the LCL-resonance peak through the grid-side filter and the grid impedance. The resonance peak may cause high-frequency stability issues especially in weak grids, and sets practical limits for the controller gains. In this work, an adaptive Notch filter is added into the current-control loop for enabling to use higher controller gains. The filter parameters are automatically adjusted to damp the resonance peak the frequency of which depends on the grid impedance. To optimize the performance of the current-control loop under varying grid conditions, an adaptive process is applied to re-adjusts the controller gains to continuously match the present grid impedance. The adaptive method bases on the online measurements of the current-control loop, and is able to keep the control bandwidth constant in varying grid conditions. Therefore, a decrease in the control bandwidth is avoided, and the inverter ability to mitigate low-order harmonics is improved. The power hardware-in-the-loop experiments clearly show the improved control performance of the current-control loop when the proposed adaptive optimization methods are applied.

VII. Appendix

TABLE I: Parameters for inverter and grid in simulations and experiments.

Parameter	Symbol	Value
Grid frequency	f_{n}	60 Hz
Nominal power	P_{n}	2.7 kW
Nominal grid voltage	V_{n}	120 V
Switching frequency	f_{sw}	8 kHz
DC voltage reference	V_{dc}^{*}	414 V
Current references	i_{d}^{*}	10.6 A
	i_{q}^{*}	0 A
DC capacitance	C_{dc}	1.5 mF
Filter inductance	L_{1}	2.2 mH
Inverter-side resistance	R_{L1}	100 mΩ
Filter capacitance	C	10 μF
Damping resistance	R_{C}	1.8 Ω
Current-controller (Offline)	$K_{\mathrm{P\text{-}CC}}$	0.0144
	$K_{\mathrm{I\text{-}CC}}$	22.500
DC-voltage control	$K_{\mathrm{P\text{-}VC}}$	0.0962
	$K_{\mathrm{I\text{-}VC}}$	1.2092
PLL control	$K_{\mathrm{P\text{-}PLL}}$	0.39
	$K_{\mathrm{I\text{-}PLL}}$	9.77

References

[1] B. K. Bose, "Global energy scenario and impact of power electronics in 21st century," *IEEE Transactions on Industrial Electronics*, vol. 60, no. 7, pp. 2638–2651, 2013.

[2] B. Kroposki, B. Johnson, Y. Zhang, V. Gevorgian, P. Denholm, B. M. Hodge, and B. Hannegan, "Achieving a 100 renewable grid: Operating electric power systems with extremely high levels of variable renewable energy," *IEEE Power and Energy Magazine*, vol. 15, no. 2, pp. 61–73, 2017.

[3] C. Li, "Unstable operation of photovoltaic inverter from field experiences," *IEEE Transactions on Power Delivery*, vol. 33, no. 2, pp. 1013–1015, 2018.

[4] T. Messo, R. Luhtala, A. Aapro, and T. Roinila, "Accurate impedance model of grid-connected inverter for small-signal stability asssessment in high-impedance grids," in *IEEJ Journal of Industry Applications*, vol. 8, 2019, pp. 488–492.

[5] J. Sun, "Impedance-based stability criterion for grid-connected inverters," *IEEE Transactions on Power Electronics*, vol. 26, no. 11, pp. 3075–3078, 2011.

[6] M. Liserre, R. Teodorescu, and F. Blaabjerg, "Stability of photovoltaic and wind turbine grid-connected inverters for a large set of grid impedance values," *IEEE Transactions on Power Electronics*, vol. 21, no. 1, pp. 263–272, 2006.

[7] T. Suntio, T. Messo, M. Berg, H. Alenius, T. Reinikka, R. Luhtala, and K. Zengeri, "Impedance-based interactions in grid-tied three-phase inverters in renewable energy applications," *Energies*, vol. 12, no. 464, 2019.

[8] H. Alenius, M. Berg, R. Luhtala, and T. Roinila, "Stability and performance analysis of grid-connected inverter based on online measurements of current controller loop," in *45th Annual Conference of the IEEE IES (IECON 2019)*, 2019, pp. 1–7.

[9] L. Jessen and F. W. Fuchs, "Modeling of inverter output impedance for stability analysis in combination with measured grid impedances," in *2015 IEEE 6th International Symposium on Power Electronics for Distributed Generation Systems (PEDG)*, 2015, pp. 1–7.

[10] A. N. Milioudis, G. T. Andreou, and D. P. Labridis, "Enhanced protection scheme for smart grids using power line communications techniques—part i: Detection of high impedance fault occurrence," *IEEE Transactions on Smart Grid*, vol. 3, no. 4, pp. 1621–1630, Dec 2012.

[11] M. Cespedes and J. Sun, "Adaptive control of grid-connected inverters based on online grid impedance measurements," *IEEE Trans. on Sustainable Energy*, vol. 5, pp. 516–523, 2014.

[12] T. Roinila, T. Messo, and E. Santi, "Mimo-identification techniques for rapid impedance-based stability assessment of three-phase systems in dq domain," *IEEE Transactions on Power Electronics*, vol. 33, no. 5, pp. 4015–4022, 2018.

[13] R. Luhtala, H. Alenius, T. Messo, and T. Roinila, "Online frequency-response measurements of grid-connected systems in presence of grid harmonics and unbalance," *IEEE Transactions on Power Electronics*, pp. 1–5, 2019 (Early Access).

[14] M. Ciobotaru, A. Rosse, L. Bede, B. Karanayil, and V. G. Agelidis, "Adaptive notch filter based active damping for power converters using lcl filters," in *2016 IEEE 7th International Symposium on Power Electronics for Distributed Generation Systems (PEDG)*, June 2016, pp. 1–7.

[15] R. Luhtala, T. Roinila, and T. Messo, "Implementation of real-time impedance-based stability assessment of grid-connected systems using mimo-identification techniques," *IEEE Transactions on Industry Applications*, vol. 54, no. 5, pp. 5054–5063, 2018.

[16] L. Jessen, S. Gunter, F. W. Fuchs, M. Gottschalk, and H. Hinrichs, "Measurement results and performance analysis of the grid impedance in different low voltage grids for a wide frequency band to support grid integration of renewables," in *2015 IEEE Energy Conversion Congress and Exposition (ECCE)*, Sep. 2015, pp. 1960–1967.

[17] J. Schoukens, K. Godfrey, and M. Schoukens, "Nonparametric data-driven modeling of linear systems: Estimating the frequency response and impulse response function," *IEEE Control Systems Magazine*, vol. 38, no. 4, pp. 49–88, Aug 2018.

PUBLICATION VI

Adaptive Grid-Voltage Feedforward for Three-Phase Inverters applying Perturb and Observe Algorithm to minimize Current THD

R. Luhtala, T. Messo, T. Roinila and G. Spagnuolo

45th Annual Conference of the IEEE Industrial Electronics Society, pp. 1151-1156 , 2019

Adaptive Grid-Voltage Feedforward for Three-Phase Inverters applying Perturb and Observe Algorithm to minimize Current THD

1st Roni Luhtala
Faculty of Engineering and Natural Sciences
Tampere University
Tampere, Finland
roni.luhtala@tuni.fi

2nd Tuomas Messo
Faculty of Information Technology and Communication Sciences
Tampere University
Tampere, Finland
tuomas.messo@tuni.fi

3rd Tomi Roinila
Faculty of Engineering and Natural Sciences
Tampere University
Tampere, Finland
tomi.roinila@tuni.fi

4th Giovanni Spagnuolo
Dept. of Information and Electrical Eng. and Applied Mathematics
University of Salerno
Fisciano, Italy
gspagnuolo@unisa.it

***Abstract*—As the amount of renewable energy increases rapidly, power systems will face novel challenges to maintain power quality. Power quality issues, which usually arise from the grid connection through power-electronic devices, can be reduced by proper control strategies. Grid-connected devices are conventionally optimized into a single operating point, but real performance is affected by the interfaced grid conditions. As the grid conditions change over time, the control performance varies, as does the quality of the power produced. To tackle this issue, the adaptive grid-voltage feedforward is introduced to the control system. The adaptive method, applying a perturb-and-observe algorithm, improves the produced power quality in real time by taking the control system characteristics and the grid conditions into account. The results show the improved power quality in various grid conditions when comparing the adaptive grid-voltage feedforward and the conventional implementations.**

I. Introduction

Electrical energy production is moving, at an accelerated pace, towards climate-friendly distributed generation [1]. Conventional production will be replaced by renewable and distributed generation, which is connected to the grid through fast-switching power electronic converters. Responsibility for the system stability and power quality will move from big synchronous machines to power electronics in renewable-energy dominant grids. During this rapid change, power quality may decrease as the power electronics have been shown to introduce new challenges for power quality and stability issues [2], [3].

Power-electronic devices produce power through semiconductor switches that introduce distortions to the grid that conventional rotating generators did not [4]. The inverters' power quality can be improved by proper control strategies [5]–[7]. An additional control strategy for improving power quality is a proportional feedforward from measured grid voltages [8]. This strategy effectively increases the inverter output impedance and compensates the effect of the grid-voltage harmonics to the output current. [9] This simple implementation is effective at improving power quality when an inverter is operating under distorted grid voltages.

The mandatory dead time of the semiconductor switches distorts the output voltages, which creates a response to other waveforms [10]–[12]. High gain of the grid-voltage feedforward has been shown to magnify harmonics arising from the dead-time effect [13], which is relatively hard to model accurately [14]. Thus, the grid voltage feedforward has a dualistic impact on the power quality; high feedforward gain mitigates the power quality issues arising from distorted grid voltage, but at the same time magnifies harmonics caused by the internal dead-time effect of the inverter [9]. This paper shows that the feedforward gain that minimizes the output current harmonics depends on the time-varying grid conditions and can be found adaptively.

While the literature has reported on adaptive control of the grid-voltage feedforward [8], [15], it has only done so from an impedance-based stability perspective. In the present paper, the grid-voltage feedforward gains are adaptively adjusted to minimize the total harmonic distortion (THD) of the inverter output current. The implementation includes the use of a perturb-and-observe (P&O) algorithm, which perturbs the feedforward gain and observes response from the output current THD. The P&O algorithm is most commonly the maximum-power-point tracking (MPPT) algorithm in the DC side of PV-systems [16]–[18], but it is applied here for the first time in the AC side. The simulation results show that the adaptive grid-voltage feedforward is an effective and simple method for improving the power quality over conventional implementations, especially in varying grid conditions.

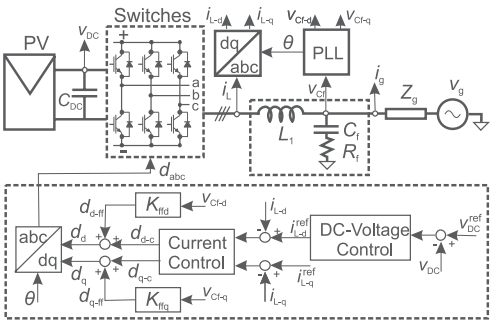

Fig. 1: Dq-domain control of grid-connected inverter.

The remainder of this paper is organized as follows. Section II provides some background to the grid-connected converter control strategy and the impact of its dead time. Section III introduces the use of the P&O algorithm in the converter AC side to adaptively adjust the feedforward gain to minimize the THD of the output current. Section IV shows the simulation results of the applied adaptive feedforward, which is capable of adjusting gains so that the output current THD is also minimized in rapidly changing grid conditions. Section V concludes.

II. Theory

A. Control of Grid-Connected Inverter

Three-phase AC systems can be analyzed in the synchronous-reference frame (dq domain) where the AC waveforms are transferred to two DC-valued signals by applying Park's transformation. The signals are referred to as direct (d) and quadrature (q), and the transformation also introduces crosscouplings between the two channels. The DC-valued signals allow linearization around the steady-state operating point, and thus the derivation of small-signal model with which the controllers can be designed [19].

Fig. 1 shows a three-phase grid-connected inverter with a cascaded control system, where d and q channels have separate control schemes. Inverter open-loop small-signal transfer functions can be represented as [20]

$$\begin{bmatrix} \hat{\mathbf{v}}_{\text{DC}} \\ \hat{\mathbf{i}}_{\text{L}} \end{bmatrix} = \begin{bmatrix} \mathbf{Z}_{\text{in-o}} & \mathbf{T}_{\text{oi-o}} & \mathbf{G}_{\text{ci-o}} \\ \mathbf{G}_{\text{io-o}} & -\mathbf{Y}_{\text{o-o}} & \mathbf{G}_{\text{co-o}} \end{bmatrix} \begin{bmatrix} \hat{\mathbf{i}}_{\text{DC}} \\ \hat{\mathbf{v}}_{\text{Cf}} \\ \hat{\mathbf{d}} \end{bmatrix} \tag{1}$$

The control is synchronized to grid voltages using a phase-locked loop (PLL) that provides synchronization angle (θ) for the dq-domain control. The outer control loop is a DC-voltage control, which provides the reference for d channel of the inner AC-current control loop, while its q channel regulates reactive current to zero for unity power factor. The grid-voltage feedforward is an additional control scheme that is used to improve the power quality.

The harmonics in the grid voltages circulate to inverter output currents through the inverter output admittance $Y_{o\text{-}o}$,

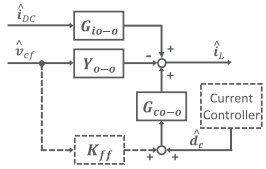

Fig. 2: Output dynamics of the grid-connected inverter.

thereby decreasing the power quality. The grid-voltage feedforward is used to mitigate the effect of low-order harmonics by adding the sensed grid voltages ($\hat{\mathbf{v}}_{\text{Cf-d}}$ and $\hat{\mathbf{v}}_{\text{Cf-q}}$) through an appropriate feedforward gain ($\mathbf{K}_{\text{ff}}$) to the duty ratios ($\mathbf{d}$). Fig. 2 shows the output dynamics of the inverter, from which the inverter output current can be derived as

$$\hat{\mathbf{i}}_{\text{L}} = \mathbf{G}_{\text{io-o}}\hat{\mathbf{i}}_{\text{DC}} - (\mathbf{Y}_{\text{o-o}} - \mathbf{G}_{\text{co-o}}\mathbf{K}_{\text{ff}})\hat{\mathbf{v}}_{\text{cf}} + \mathbf{G}_{\text{co-o}}\hat{\mathbf{d}}_{\text{c}} \tag{2}$$

The applied open-loop transfer functions are introduced in (1) and $\mathbf{K}_{\text{ff}}$ is a feedforward gain matrix. To fully compensate the $\mathbf{Y}_{\text{o-o}}\hat{\mathbf{v}}_{\text{cf}}$, the feedforward gain should be adjusted as $\mathbf{K}_{\text{ff}} = \mathbf{G}^{-1}_{\text{co-o}}\mathbf{Y}_{\text{o-o}}$. The equation may yield high-order transfer functions for $\mathbf{K}_{\text{ff}}$, which depends on the applied grid-side filter. However, high-order transfer functions as feedforward gains are sensitive for disturbances due to derivative terms. Fortunately, the equation is satisfied relatively accurate for L-filtered inverter (current feedback from inductor current, as shown in Fig. 1) by only the static gains ($1/V_{\text{DC}}$) in direct channels. Thus, the commonly applied transfer matrix for the grid-voltage feedforward is given as [9]

$$\mathbf{K}_{\text{ff}} = \begin{bmatrix} 1/V_{\text{DC}} & 0 \\ 0 & 1/V_{\text{DC}} \end{bmatrix} \tag{3}$$

In the ideal case, these gains remove the impact of the grid voltages from the produced output current, thus improving the power quality and decreasing the total harmonic distortion (THD) under distorted grid voltages.

B. Dead-Time

Three-phase inverters typically include six semiconductor switches, positive- and negative-leg switches for every phase. If both switches of the same phase are in the conductive mode, the DC link is short-circuited. The fact that real switches cannot change their state instantaneously must be taken into account to avoid short-circuiting the DC capacitor. Therefore, the dead time must be added into control system, which can be implemented by delaying the switch's turn-on signals by a certain amount of time to guarantee that the other switch always has time to change the mode to a non-conductive state. The dead time is usually a few percent of the inverter's switching cycle [13].

Apart from being important for avoiding short circuits, the dead time introduces momentary loss of controllability and reduces power quality [10]. Anti-parallel diodes are added to switching components to provide route for power flow during dead time. The conduction of the diodes causes distortion to the output voltages - mainly the 5th, 7th, 11th and 13th

harmonics - and their response to the output currents [11], [12]. The phenomena are relatively hard to model accurately because of non-linear characteristics and the complex dependency of many parameters [14].

It has been shown in [13] that the grid-voltage feedforward increases the harmonics caused by the dead-time effect when grid impedance is present. Because of the non-linear effect of the dead-time, it was not included in the linearized small-signal model of the inverter, from which the ideal gains for the feedforward were derived. Thus, the feedforward gain that minimizes the produced THD can be significantly lower than $1/V_{\text{DC}}$ as higher gains magnify the dead-time effect.

III. Methods

A. Perturb and Observe

The P&O algorithm is widely used in PV systems' maximum power-point tracking (MPPT) for optimizing the energy yield. The popularity of the algorithm is based on its simple implementation, where the PV-array voltage is perturbed and the output power is observed. If the output power increases, the next step is taken in the same direction; if the power is decreased, the next step is taken in the opposite direction. [17]

The P&O algorithm effectively finds the maximum or minimum value, at least the local one, of the observed variable in function of the perturbed one. However, a drawback of the algorithm is that it continues perturbations even when the maximum (minimum) value has been found. Thus, the algorithm makes the perturbed variable oscillate around the desired value. The oscillation amplitude is equal to the applied perturbation-step size (A_{pert}). [16] A lower step size indicates slow tracking in changing conditions, whereas higher steps increase oscillations. The step size should be high enough to perturb the system so that the increase or decrease in the observed value can be detected. Another critical value of the P&O algorithm is the time interval between the perturbations (T_{pert}), which should be longer than the system settling time, caused by the perturbation, to avoid misleading observations [18]. However, longer time intervals make the P&O algorithm slower in terms of finding the desired values after a change in operation conditions or during start-up. In changing conditions, a large step size with short time intervals between the perturbations is most desirable for fast performance. In steady conditions, an overly large step size and overly frequent perturbations increase oscillations around the desired values.

B. Adaptive Grid-voltage Feedforward to Minimize THD

The grid-voltage feedforward gains have a dualistic impact on the produced THD: higher gains mitigate the impact of the grid voltage harmonics and magnify the effect of the dead time. [9] Thus, highly distorted grid voltages endorse the use of high feedforward gains, while the ideal grid voltages endorse the gains near zero. A single inverter usually does not have information about the time-variant grid conditions. Additionally, the non-linear effect of the switches' dead time is not included in inverter models to accurately predict its impact on the produced THD, at least not yet. The ideal feedforward gain from the dead-time perspective equals to zero while it equals $1/V_{\text{DC}}$ to remove the impact of the grid-voltage harmonics. Thus, the feedforward gain that minimizes the produced THD depends on the operating conditions lies between zero and $1/V_{\text{DC}}$, and can be adaptively found by applying the P&O algorithm.

Due to time-varying and unpredictable operating conditions of the grid-connected inverter, the P&O algorithm is applied to adaptively adjust the grid-voltage feedforward gains to minimize the output current THD. Fig. 3 shows a block diagram of the adaptive-control scheme and the applied P&O algorithm in it. The grid-voltage feedforward gains are perturbed and the THD of the phase-domain output currents is observed. The direction of the next perturbation step in the feedforward gains is based on the observed THD. If the THD decreases because of the last taken step in feedforward gains, the next step is taken in the same direction. If the THD is increased, the direction of the perturbation steps is changed.

The feedforward gains are adaptively adjusted for d and q channels symmetrically. The perturbation size for adaptive feedforward gain is chosen as $A_{\text{pert}} = 0.05/V_{\text{DC}}$, the impact of which can be seen from the output current THD, but does not produce overly high oscillations when the THD-minimizing feedforward gains are found. Based on the approximated settling time of the system, the interval between perturbations is chosen as $T_{\text{pert}} = 0.2$ s, which determines the triggers executing the P&O algorithm. To avoid misleading disturbances, the THD is averaged over 0.15 s. It is observed after 0.2 s from the last perturbation and the direction of the next step is chosen.

IV. Experiments

The introduced approach for the grid-voltage feedforward is tested with a switching model of the three-phase grid-connected inverter in MATLAB/Simulink and compared to the conventional feedforward implementations. In all simulations, constant 2.7 kW DC power is fed to the (60 Hz/120 V) grid through the inverter and LC filter (C_{f}= 10 μF, L_{f} = 2.2 mH). The inverter dead time is included in the model by delaying the turn-on signals of the switches where the switching frequency equals 8 kHz. The grid impedance is passive (R_{g} = 0.4 Ω, L_{g} = 0.9 mH) and the grid-voltage disturbances are realized by introducing harmonics to grid-voltage reference, generated by an ideal voltage source. The DC voltage that affects the feedforward gains is kept at the maximum power point (414 V) in all simulations.

A. Dead-Time Effect

The required dead time of the semiconductor switches is usually a few percent of the switching cycle. Longer (safer) dead times distort the output voltages more, which increases the output current THD, especially when high gains in the grid-voltage feedforward are applied. Fig. 4 shows the output current THD when the feedforward gain is scanned from 0 to $1.1/V_{\text{DC}}$. Simulations in similar grid conditions (high harmoncis in grid voltages) with five inverters, in which only the dead time varies from 1 to 5 μs, equal 0.8-4 percent

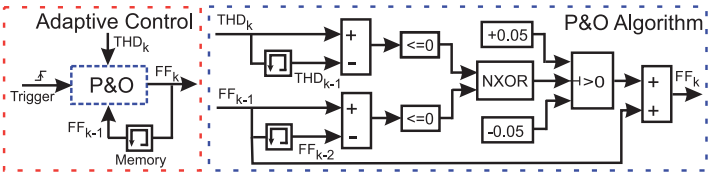

Fig. 3: Block diagram of the adaptive-control implementation.

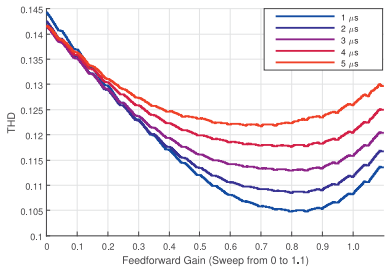

Fig. 4: Sweep of feedforward gain with different inverter dead times.

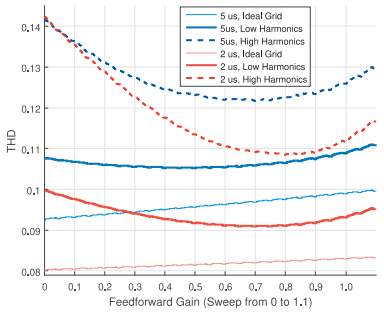

Fig. 5: Scan of feedforward gains with different dead times and grids.

of the applied switching cycle. Two important conclusions can be made from Fig. 4. First, the feedforward gains that minimize the output current THD can be found and they are not the conventionally adjusted 0 or $1/V_{\text{DC}}$; secondly, the THD increases with longer dead times when high feedforward gains are applied. The THD-minimizing gain is approximately $0.7/V_{\text{DC}}$ with 5 μs dead time and $0.85/V_{\text{DC}}$ with 1 μs. For example, with 1 μs dead time, the $0.85/V_{\text{DC}}$ feedforward gain produces approximately 26 percent lower output current THD than zero gain, and 3 percent lower than $1/V_{\text{DC}}$.

B. Grid Harmonics

As the grid-voltage feedforward has a dualistic impact on the power quality, the interfaced grid conditions and the dead time affect its performance. Fig. 5 shows the output current THD in three different grid conditions when the feedforward gains are varied from 0 to $1.1/V_{\text{DC}}$. Similar tests are made with two inverters applying 2 μs (red lines) and 5 μs (blue lines) dead times, equaling 1.6 and 4 percent of the switching cycle, respectively. The conditions are varied by changing the amount of harmonics in the grid voltages: ideal 60 Hz sinusoid (thin lines), low harmonic content (thick lines), and high harmonic content (dashed lines). Table I shows the THD-minimizing gains for every six cases. Under ideal 60 Hz grid voltages, the feedforward magnifies harmonics arising from the dead-time effect, and thus the THD-minimizing gain equals to zero. Under distorted grid voltages, the THD-minimizing gain is located between 0 and $1/V_{\text{DC}}$, which depends on both dead time and the amount of harmonics in grid voltages.

TABLE I: THD-minimizing gains

		Grid harmonics		
		Ideal	Low	High
Dead time	2 μs	0.00	$0.70/V_{\text{DC}}$	$0.85/V_{\text{DC}}$
	5 μs	0.00	$0.50/V_{\text{DC}}$	$0.70/V_{\text{DC}}$

Fig. 5 shows that longer dead time supports the use of lower feedforward gains, while increased grid-voltage harmonics endorse higher gains. The THD-minimizing gain under highly distorted grid voltages and 2 μs dead time is $0.85/V_{\text{DC}}$, with which the output current THD is decreased by approximately 23 percent compared to zero gain and 4 percent compared to $1/V_{\text{DC}}$. In this case, the THD-minimizing gain is high because of the relatively short dead time and highly distorted grid voltages. Under low grid harmonics and 5 μs dead time, the THD-minimizing gain ($0.50/V_{\text{DC}}$) is lower and the THD can be decreased 1 percent compared to zero gain and 2 percent compared to $1/V_{\text{DC}}$.

C. Perturb and Observe during Start-up

The P&O algorithm adaptively adjusts the feedforward gains to minimize the output current THD. The implementation has a plug-and-play feature during start-ups as the algorithm independently finds the gains that minimize the output current THD in interfaced grid conditions. Fig. 6 shows the THD of the output current and the feedforward gain during the inverter start up in two different grid conditions, with low (left) and high (right) harmonic content in the grid voltages. The inverter dead time is 5 μs in both cases. After an experimentally approximated settling time of the start-up (0.5 s), the P&O algorithm is enabled at 0.6 s. The feedforward gain increases by $A_{\text{pert}} = 0.05/V_{\text{DC}}$ in $T_{\text{pert}} = 0.2$ s intervals until the THD-minimizing gain is achieved. Those gains are $0.5/V_{\text{DC}}$ and $0.7/V_{\text{DC}}$ for grids with low and high harmonics, respectively. The THD is decreased by 3 percent when the inverter is interfacing to low-harmonic grid voltages, and 14 percent when there are high harmonics.

The drawback of the P&O algorithm is that the gains start oscillating around the THD-minimizing gain by A_{pert}. The

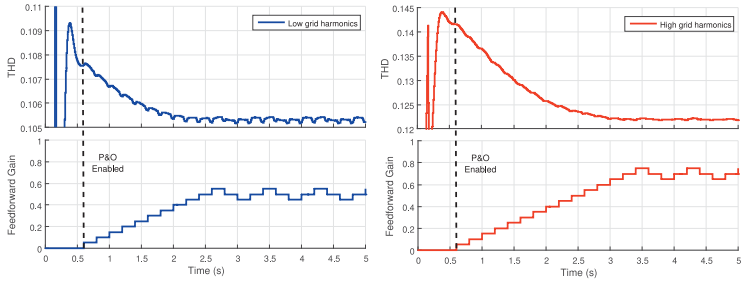

Fig. 6: Perturb and observe performance during start-ups in different grids.

feedforward gain remains at the THD-minimizing gain half of the oscillation cycle (4 T_{pert}), while the gain is improperly adjusted by A_{pert} during the other half of the cycle. However, the effect to the THD is negligible compared to the benefits of the adaptive grid-voltage feedforward compared to the conventional implementation with zero or $1/V_{\text{DC}}$ gains.

D. THD Minimization during Transient Cases

The grid conditions may significantly vary over time, especially the distortions in voltages when local production and loading profiles change [5], [6]. Fig. 7 shows the performance comparison between the conventional (constant zero and $1/V_{\text{DC}}$ gains) and the adaptive feedforward implementations under varying grid conditions. First, the inverter with 5 μs dead time is started up under ideal 60 Hz grid voltages, at 2 s and 10 s the harmonics in grid voltages are suddenly increased. Before 2 s, the adaptively adjusted feedforward gain oscillates around zero. It may be obvious that the THD is similar with the conventional zero gain. The THD is 5 percent higher with $1/V_{\text{DC}}$. After the first increase in grid-voltage harmonics, both constant gains $1/V_{\text{DC}}$ and zero gain produces approximately same amount of THD. It takes 2.4 s for the P&O to find the THD-minimizing gain ($0.6/V_{\text{DC}}$) under slightly distorted grid voltages; with that gain, the produced THD is 8 percent lower compared to constant zero and $1/V_{\text{DC}}$ gains. After the second transient in grid conditions, it takes 1.6 s for adaptive implementation to find the new THD-minimizing gain ($0.9/V_{\text{DC}}$). The THD-minimizing gain produces 21 percent lower THD than constant zero gain, and over 7 percent lower than $1/V_{\text{DC}}$ gain. Thus, it can be concluded that the presented adaptive implementation also improves the performance of the grid-voltages feedforward in changing grid conditions.

Figs. 8 and 9 take a closer look at the effect of the feedforward gains by showing a magnitude of the output current harmonics under low and high grid harmonics, which are measured between 7 - 9 s and 12 - 14 s, respectively, in the same simulation as analyzed in Fig. 7. The amount of harmonics are shown in Table II; the highest amounts are emboldened to highlight the clear effect of the feedforward gain. Higher feedforward gains effectively mitigate the low-order harmonics that arise from the grid voltages, especially 3 rd and 5 th. For example, during high grid harmonics (Fig. 9), the 3 rd harmonic can be mitigated over by 70 percent by using

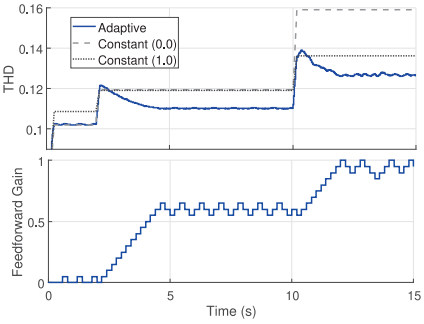

Fig. 7: Performance comparison during grid transients.

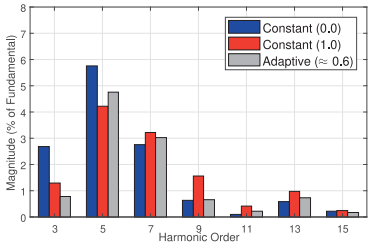

Fig. 8: Output current harmonics under slightly distorted grid.

$1/V_{\text{DC}}$ gain, and over 60 percent with adaptive ($\approx 0.9/V_{\text{DC}}$) gain when compared to the constant zero gain. However, high feedforward gain magnifies higher-order harmonics arising from the inverter dead-time effect. For example during low grid harmonics (Fig. 8), the 11 th harmonic increases by over 350 percent with $1/V_{\text{DC}}$ gain and by almost 150 percent with adaptive gain ($\approx 0.6/V_{\text{DC}}$) when compared to the constant zero gain. It should be noted that absolute values of the high-order harmonics remains significantly smaller than low-order harmonics. Thus, the percentage increment in the high-order harmonics has less impact in the output current THD than low-order harmonics.

The harmonics in grid voltages circulate to the inverter output currents. High feedforward gains effectively mitigate the impact of the grid-voltage harmonics by decreasing low-order harmonics in the output currents; at the same time, they magnify the dead-time effect, which appears as increased high-

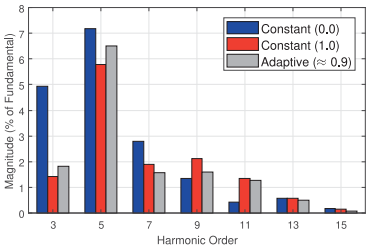

Fig. 9: Output current harmonics under highly distorted grid.

TABLE II: Amount of harmonics

	Grid harmonics					
	Low			High		
	0	1	≈ 0.60	0	1	≈ 0.90
3 rd	**2.688**	1.280	0.773	**4.942**	1.416	1.808
5 th	**5.747**	4.218	4.742	**7.176**	5.798	6.507
7 th	2.757	**3.223**	3.032	**2.791**	1.901	1.560
9 th	0.622	**1.560**	0.662	1.345	**2.121**	1.588
11 th	0.089	**0.421**	0.218	0.424	**1.341**	1.277
13 th	0.582	**0.973**	0.719	0.561	**0.567**	0.492
15 th	0.223	**0.244**	0.165	**0.179**	0.147	0.076

order harmonics. For every realistic case, there appears to be an optimal feedforward gain between zero and $1/V_{\mathrm{DC}}$, which balances the dualistic impact of the grid-voltage feedforward by minimizing the output current THD. The value of the optimal gain is based on the amount of the grid-voltage harmonics and can be found adaptively, without prior knowledge about the grid conditions, by using the proposed P&O algorithm.

V. Conclusions

This paper has presented an adaptive grid-voltage feedforward for grid-connected inverters. In the method, the feedforward gains are adaptively adjusted so that the output current THD is minimized, thus improving the power quality. The grid-voltage feedforward is shown to have dualistic impact on the produced power quality; it mitigates disturbances from grid voltages, but also magnifies the harmonics arising from the inverter dead-time effect. Hence, the optimal gain in perspective of minimizing the output current THD depends on the interfaced grid conditions, which may vary over time. This makes the feedforward gains attractive choice for including adaptive operations. The presented adaptive-control method includes the use of the P&O algorithm for the first time in AC sides. The presented method perturbs the feedforward gains and observes the impact on the produced power quality (current THD). This novel approach includes a plug-and-play feature during start-up and fast adaptivity to changes in grid conditions. Through simulations, the adaptive grid-voltage feedforward is shown to improve the system performance and the produced power quality in various grid conditions compared to conventional implementations.

References

[1] B. K. Bose, "Global energy scenario and impact of power electronics in 21st century," *IEEE Transactions on Industrial Electronics*, vol. 60, no. 7, pp. 2638–2651, 2013.

[2] C. Li, "Unstable operation of photovoltaic inverter from field experiences," *IEEE Transactions on Power Delivery*, vol. 33, no. 2, pp. 1013–1015, 2018.

[3] L. Wang, X. Xie, Q. Jiang, H. Liu, Y. Li, and H. Liu, "Investigation of ssr in practical dfig-based wind farms connected to a series-compensated power system," *IEEE Transactions on Power Systems*, vol. 30, no. 5, pp. 2772–2779, Sep. 2015.

[4] J. M. Carrasco, L. G. Franquelo, J. T. Bialasiewicz, E. Galvan, R. C. PortilloGuisado, M. A. M. Prats, J. I. Leon, and N. Moreno-Alfonso, "Power-electronic systems for the grid integration of renewable energy sources: A survey," *IEEE Transactions on Industrial Electronics*, vol. 53, no. 4, pp. 1002–1016, June 2006.

[5] Q. Zhong and T. Hornik, "Cascaded current–voltage control to improve the power quality for a grid-connected inverter with a local load," *IEEE Transactions on Industrial Electronics*, vol. 60, no. 4, pp. 1344–1355, April 2013.

[6] Q. Trinh and H. Lee, "An enhanced grid current compensator for grid-connected distributed generation under nonlinear loads and grid voltage distortions," *IEEE Transactions on Industrial Electronics*, vol. 61, no. 12, pp. 6528–6537, Dec 2014.

[7] Q. Yan, X. Wu, X. Yuan, and Y. Geng, "An improved grid-voltage feedforward strategy for high-power three-phase grid-connected inverters based on the simplified repetitive predictor," *IEEE Transactions on Power Electronics*, vol. 31, no. 5, pp. 3880–3897, May 2016.

[8] M. Cespedes and J. Sun, "Adaptive control of grid-connected inverters based on online grid impedance measurements," *IEEE Trans. on Sustainable Energy*, vol. 5, pp. 516–523, 2014.

[9] T. Messo, R. Luhtala, A. Aapro, and T. Roinila, "Accurate impedance model of grid-connected inverter for small-signal stability asssessment in high-impedance grids," in *IEEJ Journal of Industry Applications*, vol. 8, 2019, pp. 488–492.

[10] S.-G. Jeong and M.-H. Park, "The analysis and compensation of dead-time effects in pwm inverters," *IEEE Transactions on Industrial Electronics*, vol. 38, no. 2, April 1991.

[11] Z. Shen and D. Jiang, "Dead-time effect compensation method based on current ripple prediction for voltage-source inverters," *IEEE Transactions on Power Electronics*, vol. 34, no. 1, pp. 971–983, Jan 2019.

[12] G. Grandi, J. Loncarski, and R. Seebacher, "Effects of current ripple on dead-time distortion in three-phase voltage source inverters," in *2012 IEEE International Energy Conference and Exhibition (ENERGYCON)*, Sep. 2012, pp. 207–212.

[13] T. Messo, T. Roinila, A. Aapro, and P. Rasilo, "Evaluation of dead-time effect of grid-connected inverters using broadband methods," in *18th IFAC Symposium on System Identification*, 2018.

[14] I. Dolguntseva, R. Krishna, D. E. Soman, and M. Leijon, "Contour-based dead-time harmonic analysis in a three-level neutral-point-clamped inverter," *IEEE Transactions on Industrial Electronics*, vol. 62, no. 1, pp. 203–210, Jan 2015.

[15] R. Luhtala, T. Messo, and T. Roinila, "Adaptive control of grid-voltage feedforward for grid-connected inverters based on real-time identification of grid impedance," in *IPEC-Niigata 2018 -ECCE ASIA*, 2018, pp. 1–8.

[16] N. Femia, G. Petrone, G. Spagnuolo, and M. Vitelli, "Optimization of perturb and observe maximum power point tracking method," *IEEE Transactions on Power Electronics*, vol. 20, no. 4, pp. 963–973, July 2005.

[17] D. Sera, L. Mathe, T. Kerekes, S. V. Spataru, and R. Teodorescu, "On the perturb-and-observe and incremental conductance mppt methods for pv systems," *IEEE Journal of Photovoltaics*, vol. 3, no. 3, pp. 1070–1078, July 2013.

[18] M. A. Elgendy, B. Zahawi, and D. J. Atkinson, "Operating characteristics of the p o algorithm at high perturbation frequencies for standalone pv systems," *IEEE Transactions on Energy Conversion*, vol. 30, no. 1, pp. 189–198, March 2015.

[19] T. Messo, A. Aapro, and T. Suntio, "Generalized multivariable small-signal model of three-phase grid-connected inverter in dq-domain," in *2015 IEEE 16th Workshop on Control and Modeling for Power Electronics (COMPEL)*, 2015.

[20] R. Luhtala, T. Reinikka, T. Roinila, T. Messo, and J. Sihvo, "Improved real-time stability assessment of grid-connected converters using mimo-identification methods," in *2018 IEEE Energy Conversion Congress and Exposition (ECCE)*, 2018.